Synthesis, Characterization and Quantum-Chemical Analysis of {FeNO}^{7} and {Fe(NO)$_2$}^{9} Compounds and their Photo-induced Linkage Isomers

Areenan In-Iam

aus

Nai Mueang, Khon Kaen, Thailand

2020

Table of Contents

List of Figures

List of Tables

List of Schemes

Abbreviations and conventions

aptz	2-amino-4-(2-pyridyl)thiazole
ATR	attenuated total reflection
Bn	benzyl
bipzpy	2,6-di(1-pyrazolyl)pyridine
bpy	2,2'-bipyridine
br	broad
bs	broken symmetry
calcd.	calculated
conc.	concentrated
CV^+	crystal violet cation: $C_{25}N_3H_{30}^+$
CPCM	conductor-like polarizable continuum model
d	doublet
DFT	density functional theory
DNIC	dinitrosyl iron complex
DNIC-Br	dibromidodinitrosylferrate
DNIC-Cl	dichloridodinitrosylferrate
DNIC-I	diiodidodinitrosylferrate
EA	elemental analysis
EI	electron ionization
eNOS	endothelial nitric oxide synthase
EPR	electron paramagnetic resonance spectroscopy
ESR	electron spin resonance spectroscopy
eq.	equivalent
Exp.	experiment
FAB	fast atom bombardement
GTN	glyceryl trinitrate
h	hour
HS	high-spin
HOMO	highest occupied molecular orbital
HRMS	high resolution mass spectrometry
IR	infrared spectroscopy
L	ligand
LUMO	lowest unoccupied molecular orbital
LS	low-spin

m	medium (IR spectroscopy), multiplet (NMR spectroscopy)
Mephaz$^+$	methyphenazinium cation
MNIC	mononitrosyl iron complex
MNIC-Br	tribromidonitrosylferrate
MNIC-Cl	trichloridonitrosylferrate
MO	molecular orbital
MPA	mulliken population analysis
MS	mass spectrometry
NMR	nuclear magnetic resonance
NOS	nitric oxide synthase
*n*Pr	*n*-propyl
OC-6	octahedron (IUPAC polyhedral symbol)
PLI	photo-induced linkage isomerism
ppm	parts per million
PPN$^+$	bis(triphenylphosphane)iminium cation
q	quartet
QTAIM	quantum theory of atoms in molecules
rt	room temperature
s	strong (IR spectroscopy), singulet (NMR spectroscopy)
SNP	sodium nitroprusside
SQUID	superconducting quantum interference device magnetometry
T-4	tetrahedron (IUPAC polyhedral symbol)
TD-DFT	time dependent density functional theory
Tf	trifluoromethylsulfonyl
THF	tetrahydrofurane
TNIC	trinitrosyl iron compound
UV/Vis	ultraviolet/visible
$\tilde{\nu}$	wavenumber
vs	very strong (IR spectroscopy)
vw	very weak (IR spectroscopy)
w	weak (IR spectroscopy)
WFT	wave function theory

- All molecular structures are presented with the same color code. Atoms: arsenic (violet), bromine (brown-red), carbon (gray), chlorine (green), cobalt (pink), fluorine (turquoise), hydrogen (white), iron (orange), iodine (violet), nitrogen (blue), oxygen (red), phosphorus (yellow).

- Disordered or substitutional-disordered terms in the present work refer to the disorder between the nitrosyl (NO) ligand and mostly a chlorido ligand whereby the occupations are parted (see below). For example, an occupation of 8% Cl at the NO fragment means that this position is occupied to 92% by the NO ligand and to 8% by a Cl atom. The rest of the molecule is occupied to 100%.

disordered $[FeCl_3(NO)]^-$
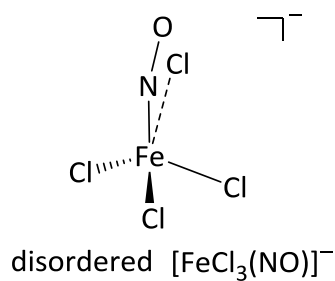
Overview of numbered compounds

Tetra-coordinated {FeNO}^{7} compounds

A $[Fe(CH_3OH)(NO)(\mu_4\text{-}SO_4)]_{n/n}$

1a $NMe_4[FeCl_3(NO)]$ from ferrous route

1b $NMe_4[FeCl_3(NO)]$ from ferric route

2a $NEt_4[FeCl_3(NO)]$ from ferrous route

2b $NEt_4[FeCl_3(NO)]$

3 $NBnMe_3[FeCl_3(NO)]$

4 $Mephaz[FeCl_3(NO)]$

5 $[Co(cp)_2][FeCl_3(NO)]$

6 $PPh_4[FeCl_3(NO)]$

7 $AsPh_4[FeCl_3(NO)]$

8 $PPN[FeCl_3(NO)]$

9 $[Fe(bpy)_3)][FeCl_3(NO)]_2$

10 $CV[FeCl_3(NO)]$

11 $PPh_4[FeBr_3(NO)]$

12 $AsPh_4[FeBr_3(NO)]$

13a $PPN[FeBr_3(NO)]$

Tetra-coordinated {Fe(NO)$_2$}^{9} compounds

14a $NMe_4[FeCl_2(NO)_2]$ from ferrous route

14b $NMe_4[FeCl_2(NO)_2]$ from ferric route

14c $PPN[FeCl_2(NO)_2]$

15a $PPN[FeBr_2(NO)_2]$

15b $PPN[FeBr_2(NO)_2]$

16 $PPN[FeI_2(NO)_2]$

17 $(PPN)_2[FeI_2(NO)_2](I_3)$

18 $AsPh_4[FeI_2(NO)_2]$

19 $PPh_4[FeI_2(NO)_2]$

Hexa-coordinated {FeNO}^{7} compounds

20a $[Fe(bipzpy)Cl_2(NO)]\cdot MeOH$ from ferrous route

20b $[Fe(bipzpy)Cl_2(NO)]\cdot MeOH$ from ferric route

20c $[Fe(bipzpy)Cl_3]\cdot MeOH$

23 $[Fe(aptz)_2Cl(NO)]Cl\cdot0.5\,MeOH$

Penta-coordinated {Fe(NO)$_2$}^{9} compounds

21 $[Fe(bipzpy)(NO)_2]BF_4$

22 $[Fe(bipzpy)(NO)_2]_3(BF_4)(NO_3)_2$

Overview of numbered compounds

$[FeCl_3(NO)]^-$

1–10

$[FeBr_3(NO)]^-$

11–13

$[FeCl_2(NO)_2]^-$

14a–c

$[FeBr_2(NO)_2]^-$

15a–b

$[FeI_2(NO)_2]^-$

16–19

$[Fe(bipzpy)Cl_2(NO)]$

20a–b

$[Fe(bipzpy)Cl_3]$

20c

$[Fe(bipzpy)(NO)_2]^+$

21–22

$[Fe(aptz)Cl(NO)]^+$

23

$[Fe(CH_3OH)(NO)(\mu_4\text{-}SO_4)]_{n/n}$
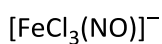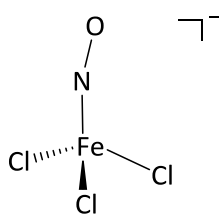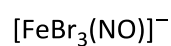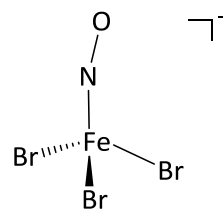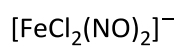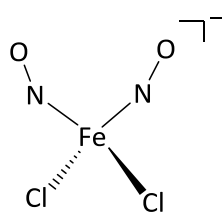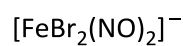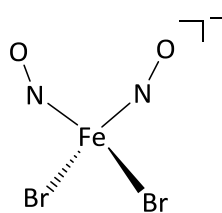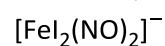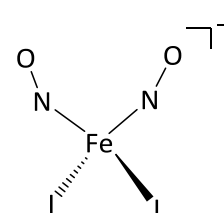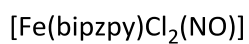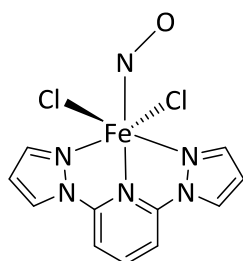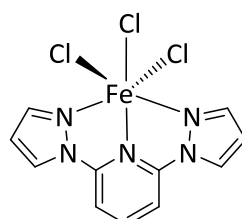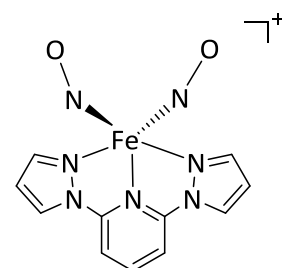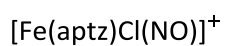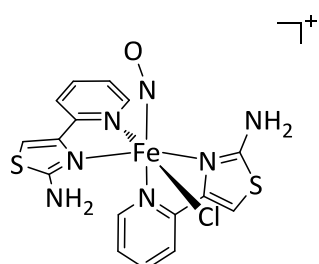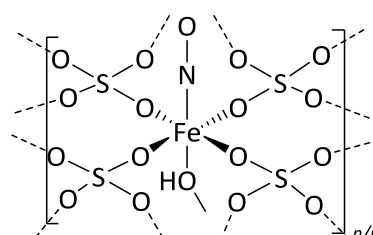
A

1   Introduction

Nitrogen gas, N_2 makes up nearly 80% of the Earth's atmosphere. Though it is one of the primary nutrients for life, N_2 cannot be used directly by plants, animals or humans. Thus, N_2 has to be converted into bioavailable nitrogen, NH_3. This nitrogen fixation is carried out mostly by prokaryotes. NH_3 is converted to other important inorganic compounds in the nitrification process $(NH_3{\rightarrow}NH_2OH{\rightarrow}NO_2^-{\rightarrow}NO_3^-)$. NO_3^- can be used by plants in their life cycle and N_2 is released back to the atmosphere by the denitrification process $(NO_3^-{\rightarrow}NO_2^-{\rightarrow}NO{\rightarrow}N_2O{\rightarrow}N_2)$.[1] Hence, N_2 and nitrogen oxide $(NO)_x$ species play an important role in the biological life processes.

An imbalance of the nitrogen cycle, especially from human activities, can lead to ecological problems. That includes the use of nitrogen-based fertilizers, burning fossil fuels or operating engines whereby $(NO)_x$ species $(NO, NO_2, N_2O$ etc.) are formed.[2] $(NO)_x$ species are air pollutants that, at high concentrations, cause serious health risks. Long-term exposure can decrease lung function, increase the risk of respiratory conditions and the responses to allergens. Furthermore, nitrous oxide (N_2O) is a greenhouse gas.[1]

However, nitric oxide (NO) is also produced in low concentration in mammals *via* the oxidation of L-arginine by the NO synthase (NOS) enzyme.[3,4] At such concentrations, NO acts as a signalling molecule in various physiological processes: smooth muscle relaxation, platelet reactivity, neurotransmission and blood-pressure regulation.[4–8] In contrast, the *in vivo* overproduction of NO is described as a carcinogenic source.[4,9] In 1992, NO was announced 'molecule of the year'. The Nobel Prize in medicine was awarded to Furchgott, Ignarro and Murad for the discovery of NO biosynthesis and its role as a blood-pressure regulator in 1998.[10,11] Nowadays, NO-donating drugs are widely used in medicine. Sodium nitroprusside (SNP, $Na_2[Fe(CN)_5(NO)]$), for example, is used for lowering blood pressure and glyceryl trinitrates (GTN) is used for prevention and treatment of chest pain, as well as lowering the blood pressure. NO-donor drugs such as GTN or NONOates (diazeniumdiolates) are also used in cancer therapy.[12]

1.1 NO as a ligand

For more than a century, many researchers have been working on the synthesis of metal-nitrosyl complexes. Different NO sources have been used to introduce the nitrosyl ligand.[13–18] Since the discovery of NO at the end of 1900s as a blood pressure regulator, the chemistry of NO has attracted even more interest.[19]

Nitrosyl-metal complexes have unique chemical, physical or biological properties, which can be studied using IR, UV/Vis, EPR, Mössbauer spectroscopy, SQUID magnetometry, X-ray diffraction and theoretical analysis. The coordination geometry and electronic properties can vary largely. Due to the fact that NO is a redox-active molecule and, thus a so-called 'non-innocent' ligand, it can bind to metal atoms as $NO^{.}$, NO^+ or NO^- so that it is difficult to state the formal oxidation number of the metal as well as the NO ligand. The Enemark-Feltham notation, in which the metal-nitrosyl complexes are described as $\{M(NO)_x\}^n$, simplifies this declaration.[20] In this notation, M is the metal in the coordination compound, x is the number of nitrosyl ligands and n is the total number of electrons in the metal-d and π^* orbitals of NO. M–N–O bond angles may vary from 120°–180° depending on the bonding situation between the metal center and the NO ligand: $M–^1NO^-$ is strongly bent (120°), $M–^2NO^0$ is noticeably bent (140°), $M–^3NO^-$ is slightly bent (150°–180°) and $M–^1NO^+$ is almost linear (180°). Accordingly, the mononitrosyl-iron compounds (MNICs) are found as $\{FeNO\}^{6–8}$ compounds whereas the dinitrosyl-iron compounds (DNICs) are found as $\{Fe(NO)_2\}^{9-10}$ species. Trinitrosyl-iron (TNICs)[21–25] and tetranitrosyl-iron compounds are rare. To date (09/2019), some TNICs are published but only one structure of a $[Fe(NO)_4]^-$ ion has been published.[26] In this work, $\{FeNO\}^7$ and $\{Fe(NO)_2\}^9$ compounds are of main interest. The following Sections 1.2–1.5 report the history of these nitrosyl-iron complexes.

1.2 Red compound $\{FeNO\}^7$ ($S = 3/2$)-type of $[FeSO_4(NO)]$ species

The qualitative nitrate test is practically performed, for example, by undergraduate students during their analytical course. As shown in Figure 1.1, both red and brown products can, apparently, be simultaneously observed from the reaction of an acidic aqueous solution of $FeSO_4$ and NO_3^- and concentrated sulfuric acid. During the reaction, NO_3^- ions are reduced to NO while Fe^{2+} is oxidized to Fe^{3+}. The *in situ*-produced NO binds to excessive $[Fe(H_2O)_6]^{2+}$ yielding the $[Fe(H_2O)_5(NO)]^{2+}$ ion which appears at the border region as a brown-colored chromophore, the so-called "brown ring" (Figure 1.1). Most recently, the $[Fe(H_2O)_5(NO)]^{2+}$ ion was successfully characterized *via* X-ray structural analysis by Monsch and Klüfers.[27] Their work describes a slightly bent Fe–N–O fragment with an angle of ≈160°. DFT and WFT calculations resemble the oxidation state of the Fe in the

$[Fe(H_2O)_5(NO)]^{2+}$ complex to be more likely $Fe^I(NO^+)$ than $Fe^{III}(NO^-)$. The brown-ring chromophore is described as a parent compound of $\{FeNO\}^7$ (S = 3/2) species.[27,28]

According to the aforementioned, the bottom layer of the brown-ring appears reddish.

$$3\ Fe^{2+} + NO_3^- + 4\ H^+ \longrightarrow 3\ Fe^{3+} + NO + 2H_2O$$

$$[Fe(H_2O)_6]^{2+} + NO \rightleftharpoons [Fe(H_2O)_5(NO)]^{2+} + H_2O$$
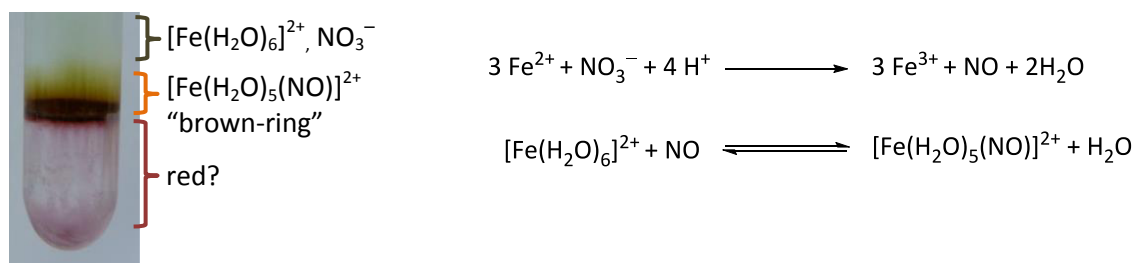
Figure 1.1: During the ring test for nitrate analysis a typical reddish-colored solution appears under the brown-ring layer. The top layer contains aqueous $FeSO_4$ and nitrate while the bottom layer is consisted mostly of concentrated H_2SO_4. The photo is modified from Reference [28].

The search for the "brown-ring" chromophore $[Fe(H_2O)_5(NO)]^{2+}$ and the unknown red compound described as $[(FeSO_4)NO]$ by Manchot and Huttner[14] has a long history. In 1910, Manchot and Huttner reported the synthesis of the "brown-ring" compound as follows: diluted sulfuric acid was added into a mixture aqueous of $FeSO_4$ and gaseous nitric oxide. The mixture solution turned homogeneously brown, and brown plate-shaped crystals were obtained by adding absolute alcohol into the reaction mixture. Those crystals were postulated to be $2(FeSO_4)(NO)\cdot13H_2O$ or more precisely one mole of $FeSO_4(NO)\cdot6H_2O$ co-crystallized with one mole $FeSO_4\cdot7H_2O$.[14,29,30] When concentrated sulfuric acid, instead of diluted sulfuric acid, was added to the solution, a homogeneous red solution was observed (sometimes described as blood-red or cherry-red, depending on the concentration of sulfuric acid).[13,15,29] Furthermore, when hydrochloric acid was added, instead, a green solution of a chlorido nitrosyl-iron compound was obtained. Scheme 1.1 shows the synthetic routes of the brown, red and green compounds.

FeSO$_4$(aq) + NO

⇅

[FeSO$_4$(NO)](aq)

diluted H$_2$SO$_4$ conc. H$_2$SO$_4$ conc. HCl   diluted HCl

brown solution   red solution   green solution   brown solution

abs. alcohol

brown plate-shaped crystals   red plate-shaped crystals

2 FeSO$_4$(NO)·13 H$_2$O   (FeSO$_4$)NO   (FeCl$_2$)NO
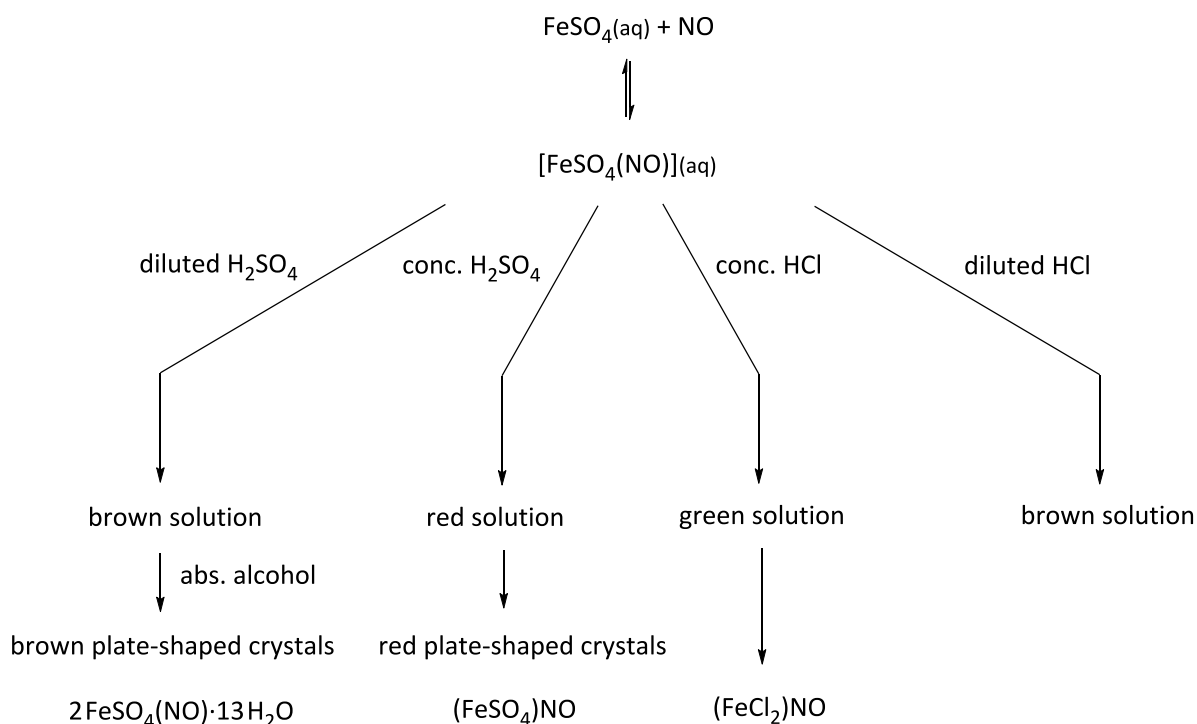
Scheme 1.1: Synthesis of iron-nirosyl complexes as proposed by Manchot.[13,14,29,31]

Manchot described the brown [FeSO$_4$(NO)](aq) solution as unstable against air and pressure, so that the reaction was reversible and in equilibrium as presented in Scheme 1.1. Upon addition of different diluted acids, different solution colors were observed but all these solutions were not stable in air and lost their colors upon application of pressure or hydrogen flow. This caused a loss of the NO ligand so that a reagent, for example, absolute alcohol, was used to precipitate those compounds. If concentrated acids were applied, the solutions were stable against air and pressure. Furthermore, the cherry-red solution from concentrated H$_2$SO$_4$ was, likewise, obtained from Fe$_2$(SO$_4$)$_3$ but needed two equivalents of nitric oxide, instead of one, to obtain the same intensive cherry-red color.[29] It was not possible to analyze this red plate-shaped crystalline compound assigned as "(FeSO$_4$)NO" due to its low stability.[14,31]

Later, in 2014, Kästele[32] used a synthetic route of Manchot[14,29] by reacting an aqueous solution of FeSO$_4$ in concentrated H$_2$SO$_4$ saturated with NO to obtain a solid as red, plate-shaped single crystals which were suitable for X-ray diffraction. The red crystals crystallized in the tetragonal space group *I*4/*mmm*. Their cell parameters were $a = 6.426$ Å, $c = 15.418$ Å and $V = 636.66$ Å^3. It was a coordination polymer with the formula reported as (H$_3$O)[{Fe(NO)(μ_4-SO$_4$)(μ_2-SO$_4$)$_{0.5}$}$_{n/n}$] The Fe center was coordinated with adjacent four μ_4-SO$_4$ groups, one nitrosyl ligand and a hydrogensulfate group, as an octahedral. In the crystal structure, a hydrogen-sulfate group was coordinated to the iron center in *trans* position to the nitrosyl group. However, this compound was very reactive and

quite unstable against air due to its oxonium cation and therefore could not be analyzed further.[32] Thus, the stability of such red compounds had to be improved in order to allow further investigations.

In order to contribute to the red derivate compound "[FeSO$_4$(NO)]" (Section 1.2), experiments that avoid an oxonium counterion were performed.

1.3 Green solution variants from ferrous precursor

Besides FeSO$_4$, other iron salts such as (NH$_4$)$_2$Fe(SO$_4$)$_2$, FeCl$_2$, FeCl$_3$ or FeBr$_2$ were tested as well by Manchot.[13,14] The addition of diluted HCl to the NO-mixture of aqueous FeCl$_2$ resulted brown solution. In contrast, concentrated HCl led to dark green solutions. Various solvents for FeCl$_2$ were used instead of water or hydrochloric acid resulting in green (abs. alcohol, acetone, acetonitrile, ethyl benzoate, diethyl malonates) or red-brown (hydrous pyridine) solutions on the action of NO.[14] Many attempts to crystallize iron-nitrosyl compounds from the aqueous ferrous solution were done but inhibited.

In competition to the Manchot group, in 1904 and 1907, the Kohlschütter group published reports on a green solution of iron-nitrosyl species from NO and FeCl$_2$ in concentrated HCl. This green species was formulated by Kohlschütter as 'Ferrochlorwasserstoff-säure' (chloridoiron(II) acid).[16,17] Later, in 1911, Kohlschütter summarized the experimental data and formulated the green species as [FeCl$_{2+x}$(NO)]$^{'x}$, *x* = 2. At that time the green species was not isolated as a solid. Electrochemical-transference experiments on a FeCl$_2$-NO solution in ethanol showed this species to be anionic.[18] In his formulation, Kohlschütter was one of the first persons who used the new ideas of coordination chemistry.[16,17,33]

1.4 Green solution variants from FeCl$_3$

During this time, Manchot *et al.* reported that a green solution was not observed if FeCl$_3$ in concentrated HCl was used. On the contrary, it succeeded when ferric or ferrous chloride was dissolved in an organic solvent such as ethanol and reacted with gaseous NO.[29] Manchot *et al.* identified nitric oxide as the reductant of a ferric precursor, but a full reaction equation was not given due to the "complicated side reactions of the organic solvents".

Fifty years later, Griffith *et al.* reported in 1958 that {FeNO}^{7} (*S* = 3/2) compounds could be prepared in ethanol as a solvent from FeCl$_3$ or FeCl$_2$ salts. The resulting complexes were described as [Fe(C$_2$H$_5$OH)$_5$(NO)]Cl$_3$ or [Fe(C$_2$H$_5$OH)$_5$(NO)]Cl$_2$ with infrared spectroscopic data indicating the NO stretching vibration frequency of 1775 cm^{-1} in MeOH and 1795 cm^{-1} in 3% HCl, respectively. The

UV/Vis absorption spectrum of both compounds is similar in the region 500–800 nm. At that time, there was no information about crystal structures available. However, the magnetic susceptibility of the species from the ferric route exceeded the expected value for a high-spin $\{FeNO\}^7$ ($S = 3/2$) compound.[34]

The results of Griffith and Manchot led to the assumption that they could have had the same product in their hands but it could not be isolated as a crystalline product.

Later, in 1976, Connelly and Gardner prepared the green solid $PPN[FeX_3(NO)]$ (X = Cl, Br) by reacting $PPN[Fe(CO)_3(NO)]$ with chlorine or bromine in dichloromethane.[35] The obtained solid products had an NO vibration at 1802 cm^{-1} and the magnetic moment indicated a spin $S = 3/2$ species which suggested a similar anion as observed by Kohlschütter. However, no crystal structure analysis was reported. The Connelly and Gardner synthetic route was later repeated by Böttcher resulting in Cl/NO disorder which was caused by the co-crystallization of $PPN[FeCl_3(NO)]$ and the oxidized $[FeCl_4]^-$ species.[33]

An X-Ray diffraction analysis was reported in 1983 by the Beck group on the green compound $AsPh_4[FeCl_3(NO)]$ by means of Weissenberg film techniques.[36] The synthetic route was described as follows: a red Roussin salt $(AsPh_4)_2[Fe_2(NO)_4S_2]$ was reacted with gaseous HCl in pentane, a brown compound claimed as $AsPh_4[FeCl_2(NO)_2]$ was first formed which afterward transformed to solid $AsPh_4[FeCl_3(NO)]$. The crystalline product was obtained after recrystallization from THF/pentane. Beck assigned these brown needles to the space group $P\bar{4}$; the unit-cell metrics were $a = 18.335(6)$ Å, $c = 7.507(2)$ Å, $Z = 4$ and $V = 2524$ Å^3. The complex anion had a fairly linear Fe1–N1–O1 moiety with an angle of 177° and the Fe–Cl mean bond length of 2.2366 Å, Fe1–N1 1.70(1) Å and N1–O1 1.12(2) Å.[36] In 2011, Wilfer synthesized the same compound but used a modified Kohlschütter method and reported $AsPh_4[FeCl_3(NO)]$ as green crystals in the monoclinic space group $P2_1/n$.[37] The difference among space groups and crystal colors of the same product question whether statement is accurate.

In 2014, Akutsu *et al.* reported the crystal structure of brown crystals of $PPh_4[FeCl_2(NO)_2]$ using a modification of Beck's method.[38] The crystal structure was reported in the tetragonal space group $P\bar{4}$ with $a = 18.181(4)$ Å, $c = 7.4559(14)$ Å, $Z = 4$ and $V = 2464.6(8)$ Å^3, similar to Beck's $AsPh_4[FeCl_3(NO)]$[36] compound. After closer inspection of the molecular structure from the Akutsu group, there is major disorder between chlorido and nitrosyl ligands. The disorder caused one of Fe–N–O bond angles to be almost linear of 175° (normally $\approx$160°, see DNIC-Cl in Section 2.11). Furthermore, the magnetic moment was reported too high for the dichlorido-DNIC $\{Fe(NO)_2\}^9$ ($S = 1/2$) but close to the trichlorido-MNIC $\{FeNO\}^7$ ($S = 3/2$). This indicated that in Akutsu's brown

crystals (DNIC-Cl), a substantial amount of green crystals of $PPh_4[FeCl_3(NO)]$ were co-crystallized. Both groups (Beck and Akutsu) results clearly suffered from NO/Cl disorder. Coincidental with Akutsu work group, the Lippard group reported on a cationic MNIC with $[FeCl_3(NO)]^-$ ion as the counter ion. That anion had unresolved residual electron density of 2.5 $e\text{Å}^{-3}$.[39] Besides that, the most recent work on disorder (2016) was published within another crystal structure of the $[FeCl_3(NO)]^-$ ion.[40]

In 2016, Wolf published a well-ordered crystal structure of $PPN[FeCl_3(NO)]$ as green crystals prepared from $Fe(OTf)_2$, chloride salt and gaseous nitric oxide.[41]

Although some data of chlorido, bromido and iodido nitrosyl-iron compounds were previously reported, no data of fluorido nitrosyl-iron species $[FeF_x(NO)]^-$ are available.

1.5   Towards halogenido dinitrosyl-iron complexes

Dinitrosyl-iron complexes (DNICs) have been prepared since the early 1900s. Even though simple halogenidodinitrosyl anions like $[FeCl_2(NO)_2]^-$, $[FeBr_2(NO)_2]^-$ or $[FeI_2(NO)_2]^-$ ions were already analyzed using ESR and IR spectroscopy and described in literature many years ago,[35,42] the only structure of a $[FeI_2(NO)_2]^-$ anion was published in 1992.[43] Recently, as mentioned earlier, a crystal-structure analysis of $PPh_4[FeCl_2(NO)_2]$ was claimed in 2014 but this analysis suffered from disorder.[38] Furthermore, no structural data are available for $[FeBr_2(NO)_2]^-$ or $[FeF_2(NO)_2]^-$. In our working group, Wolf reported, in 2016, on the synthesis of the well-ordered compound $(PPN)[FeCl_2(NO)_2]$ (**14c**)[41] which was accessible by the addition of two equivalents of PPNCl into $(PPN)[Fe(NO)_2(ONO)_2]$ as precursor.[41] In addition, Wolf synthesized $(PPN)_2[FeI_2(NO)_2]I_3$ whereby the I_3^- ion crystallized as a counterion. Wolf's $[FeI_2(NO)_2]^-$ ion is isostructural to that of $(PPN)[FeI_2(NO)_2]$, published in 1992.

Furthermore, Böttcher prepared the previously mentioned DNIC-Cl by the Connelly and Gardner method.[44] This route contained several steps: first the synthesis of $PPN[Fe(CO)_3(NO)]$ as a precursor which was afterwards, treated optionally by adding of I_2, NOCl or *n*-PrCl or with SO_2Cl_2 and EtBr to form $[FeI_2(NO)_2]^-$, $[FeCl_2(NO)_2]^-$ and $[FeBr_2(NO)_2]^-$, respectively. The addition of Cl_2 or Br_2 yielded $PPN[FeCl_3(NO)]$ and $PPN[FeBr_3(NO)]$ instead. Connelly and Gardner used IR spectroscopy, as well as elemental analysis, melting-point determination, EPR and conductance measurement to describe their compounds.[35] Böttcher obtained these compounds in crystalline form. However, they contained the disorder $[FeCl_4]^-$ or $[FeBr_4]^-$ ions that were co-crystallized with the product.[45]

1.6 Photo-induced linkage isomerism (PLI)

For half a century, $Na_2[Fe(CN)_5(NO)]$, SNP, has attracted much interest since long-lived metastable states were detected by irradiation with a green laser at low temperature. Upon irradiation, two excited-state isomers are formed, namely a κO-bonded isonitrosyl (MS1) and a $\kappa^2 N,O$-bonded side-on nitrosyl (MS2) (Figure 1.2). Furthermore, irradiation can also induce NO-release which is of therapeutic importance.[46–48] Photo-induced linkage isomers have been detected in the solid state, as well as in aqueous solutions, [48–50] due to the fact that the SNP is a low–spin complex, d^6 Fe^{II}–NO^+ or $\{FeNO\}^6$ ($S = 0$) compound, and has a diamagnetic ground state. Thus, its PL isomers have been detected at room temperature. Along with SNP, other metal nitrosyl complexes have been demonstrated to show PLI as well. Remarkably, all currently known cases are diamagnetic compounds. As one exception, Cheng *et al.* reported the rare example of a paramagnetic iron-nitrosyl complex $\{FeNO\}^7$ ($S = 1/2$) which showed an MS1 state.[51]
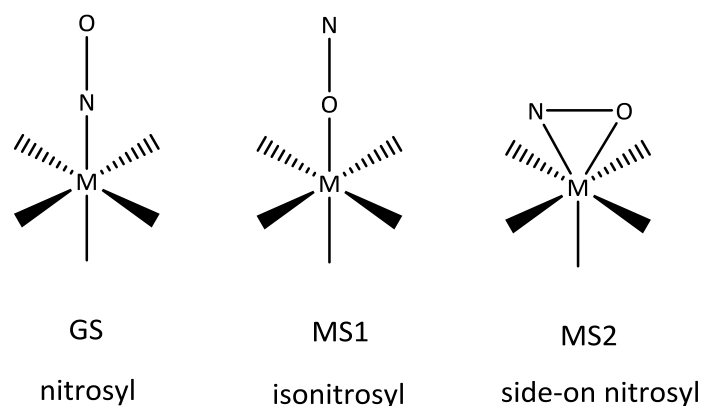
Figure 1.2: Bonding modes of metal-nitrosyl compound in the metastable states.[49]

The search for paramagnetic iron-nitrosyl compounds that show PLI has been an aim of our working group. However, PLI measurements of $\{FeNO\}^7$ ($S = 3/2$) compounds with aminocarboxylato ligands, namely, $[Fe(ida)(H_2O)(NO)]$, $[Fe(H_2O)(NO)(phida)]$ and $[Fe(bnida)(H_2O)_2(NO)]$ did not show PLI at a measurement temperature of 80 K.[41] Experiments at low temperature (9 K, 635 nm irradiation) allowed the observation of a new metastable state (photo-induced charge transfer) in the $PPN[FeCl_3(NO)]$ salt, indicated by an unusual new NO stretching vibration band at 1868 cm^{-1}. Wolf proved this result by means of DFT calculations and assigned the new NO band as a photo-oxidized state, which means that one electron of the $[FeCl_3(NO)]^-$ anion was transferred and shorty localized at the PPN^+ cation.[33] As the temperature was increased to 40 K, the localized electron returned to its ground state.

1.7 Aims of this work

In order to study photo-induced linkage isomerism (PLI) in the MNIC or DNIC species, pure products are required. All the histories of synthetic routes towards MNIC-X and DNIC-X (X: F, Cl, Br and I) compounds described in Sections 1.2–1.5 showed that the MNIC and DNIC species were mostly coincidently prepared and, thus contained co-crystallized products causing disorder in crystal structures. Therefore, routes such as the Connelly and Gardner method would not be suitable to obtain a pure compound. However, the Kohlschütter[16,17] and Wolf[41] method revealed well-ordered crystals and, thus, were used as a guide for the synthetic work in this thesis.

Thus, the main objective has been to synthesize and analyze pure products of the simple classes of MNICs [FeX$_3$(NO)]$^-$ and DNICs [FeX$_2$(NO)$_2$]$^-$ (X = F, Cl, Br, I) as the basis to study the PLI behavior of paramagnetic iron-nitrosyl compounds. To supplement the synthetic work, quantum-chemical calculations were used to characterize such metastable states. In addition, new {FeNO}^{7} and {Fe(NO)$_2$}^{9} compounds with bi- and tridentate ligands were prepared and characterized.

In order to contribute to the red compound "[FeSO$_4$(NO)]" (Section 1.2), experiments that avoid oxonium counterions were performed.

2 Results

The first part of this Chapter presents the characterization of derivates of the red compound "(FeSO$_4$)NO" which was mentioned first in the early 1900s.[13,29] Subsequently, the synthetic routes of green MNIC-X as well as brown DNIC-X (X: Cl, Br, I) are shown including crystal structures of all obtained products (Section 2.10–2.13). Well-ordered crystalline products were studied by means of PLI experiments and the results are illustrated in Section 2.15. Lastly, the quantum-chemical calculations are presented and compared to the experimental data.

2.1 Synthesis of the red [Fe(CH$_3$OH)(NO)(μ_4-SO$_4$)]$_{n/n}$: a {FeNO}^{7} (S = 3/2)-type compound

In this work, synthetic routes of derivatives of the red compound "(FeSO$_4$)NO" were developed and the products were analyzed based on previous results by Kästele.[32] To improve the stability of the Kästele compound (H$_3$O)[{Fe(NO)(μ_4-SO$_4$)(μ_2-SO$_4$)$_{0.5}$}$_{n/n}$][32] against exposure to air, the syntheses in this work were performed in methanolic solution instead of concentrated sulfuric acid. Iron(II) sulfate was used primarily as the starting salt. By treatment of the reaction mixture with gaseous NO, the solution turned dark green and a red, amorphous precipitate of a nitrosyl-iron compound was obtained. IR- and UV/Vis-spectroscopic analysis resulted in an N–O stretching vibration of 1840 cm^{-1} and UV/Vis absorption spectra with λ_{max} at 447, 583 nm (MeOH) and 236, 290, 473, 590 nm (solid). Crystallization of this compound succeeded by using iron(II) perchlorate as a reactant and adding magnesium sulfate as the SO$_4^{2-}$ source (Scheme 2.1). In addition, an auxiliary ligand such as citric acid (preferably), tartaric acid, maleic acid, 2-furoic acid or azelaic acid was added to the reaction mixture to avoid the formation of amorphous products. Furthermore, using acetone as the antisolvent accelerated the crystallization. Red, plate-shaped single crystals were obtained with its N–O stretching vibration was 1835 cm^{-1}, suitable for X-ray diffraction. Structure analysis revealed the formula [Fe(CH$_3$OH)(NO)(μ_4-SO$_4$)]$_{n/n}$ (**A**). According to the Enemark-Feltham notation, **A** is a {FeNO}^{7} (S = 3/2) compound.

$$\text{Fe(ClO}_4)_2\cdot\text{H}_2\text{O} + \text{MgSO}_4\cdot\text{7H}_2\text{O} + \text{NO} \xrightarrow[\text{rt}]{\text{L, MeOH}} \text{[Fe(CH}_3\text{OH)(NO)}(\mu_4\text{-SO}_4)_4]_{n/n} + \text{Mg(ClO}_4)_2 + 8\,\text{H}_2\text{O}$$

A
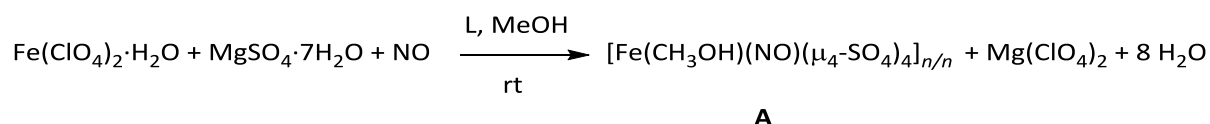
L: citric acid, tartaric acid, maleic acid, 2-furoic acid or azelaic acid.

Scheme 2.1: Synthesis of [Fe(CH$_3$OH)(NO)(μ_4-SO$_4$)]$_{n/n}$ (**A**).

A crystallized in the tetragonal space group *P*4/*nmm* with the lattice parameters *a* = 6.396 Å, *c* = 9.335 Å and *V* = 381.91 Å^3 with two formula units in the primitive cell. The lattice constant *a* was similar to that in Kästele's report but the lattice constant *c* was not. Other batches showed similar lattice constant *a* but different values of the lattice constant *c*, together with different centering types. As an example, a lattice constant of *c* = 22.27 Å with *V* = 905.52 Å^3 in space group *I*4/*mmm*. The differences could have been caused by different *trans* ligands to the nitrosyl group. However, both [Fe(CH$_3$OH)(NO)(μ_4-SO$_4$)]$_{n/n}$ (**A**) and (H$_3$O)[{Fe(NO)(μ_4-SO$_4$)(μ_2-SO$_4$)$_{0.5}$}$_{n/n}$][32] shared the same plate-like crystal habitus and the red color (Figure 2.1).
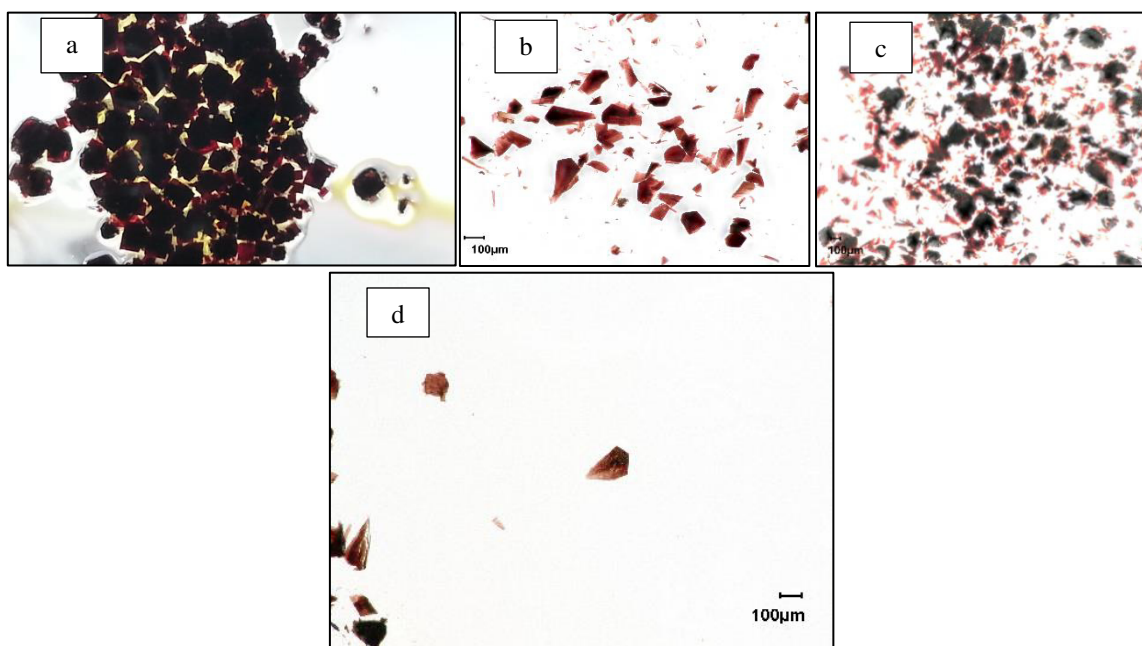
Figure 2.1: Photos of red [Fe(CH$_3$OH)(NO)(μ_4-SO$_4$)]$_{n/n}$ (**A**) at different magnifications. (b, c and d).

In contrast to Kästele's product, compound **A** bore a methanol ligand coordinated in *trans* position to the nitrosyl ligand. Furthermore, **A** was electroneutral. The absence of the reactive counterion H$_3$O$^+$ seemed to be responsible for the enhanced stability of **A** against air. Thus, further investigations such as IR, UV/Vis, SQUID and Mössbauer measurements were possible. Figure 2.2 (top) shows the SQUID measurements of **A** which is paramagnetic with χ_MT $\approx$ 2 cm$^3\cdot$K$\cdot$mol^{-1} and $\mu_{eff} \approx$ 4 (see Section 2.14) corresponding to three unpaired electrons in the formula unit of **A**, in line with the {FeNO}^{7}(*S* = 3/2) formulation. In addition, Figure 2.2 (bottom) shows the Mössbauer spectrum of **A** with an isomer shift (δ) of δ = 0.828(4) mm s^{-1} and a quadrupole splitting (ΔE_Q) of ΔE_Q = 1.879(7) mm s^{-1} (black line). These values are similar and agree very well with data recently published for the {FeNO}^{7}(*S* = 3/2)-[Fe(H$_2$O)$_5$(NO)]$^{2+}$ ion, namely δ = 0.655(3) mm s^{-1} and ΔE_Q = 2.031(8) mm s^{-1}.[27] The depicted spectrum shows a minor component (gray line) a yet unidentified compound, possibly a decomposition product of **A**.
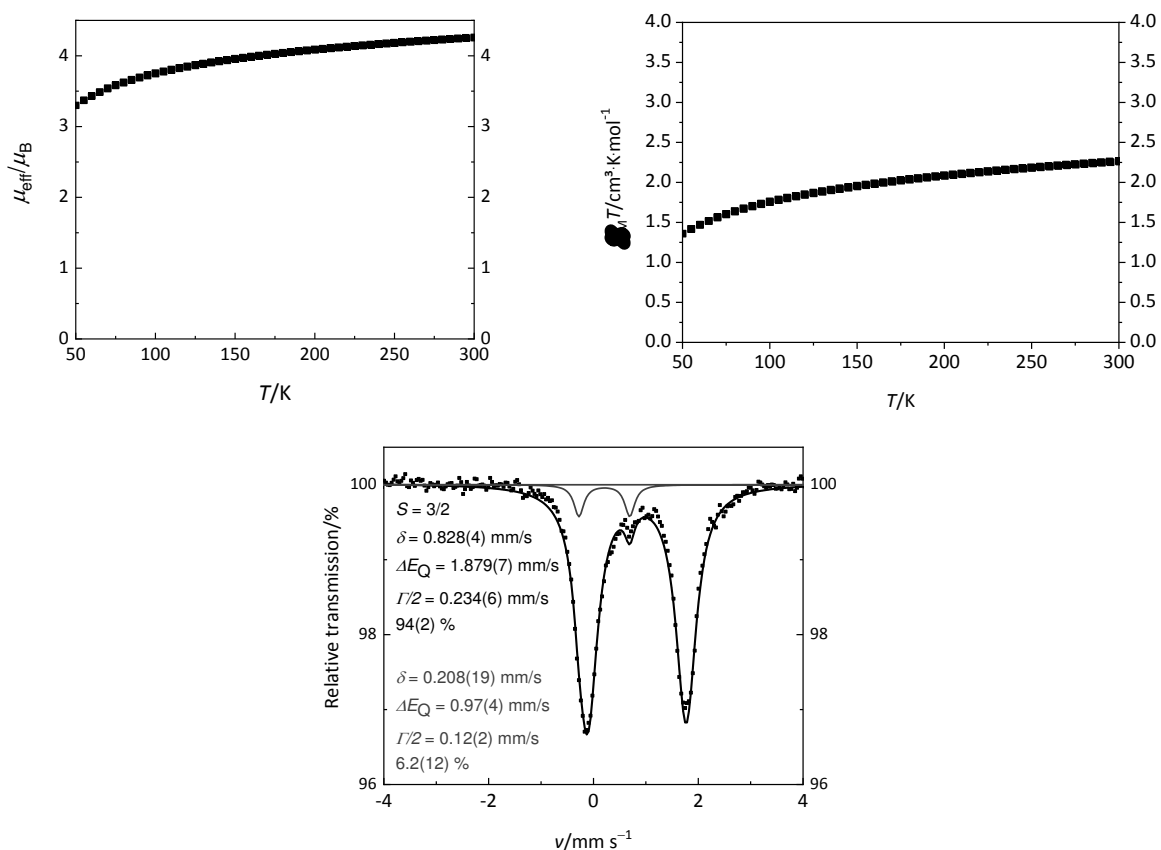
Figure 2.2: SQUID (top) and Mössbauer (bottom) measurements of $[Fe(CH_3OH)(NO)(\mu_4\text{-}SO_4)]_{n/n}$ (**A**).

Figure 2.3 illustrates the crystal structure of **A**. Four bridging oxygen atoms (μ_4-SO_4) coordinate to an iron center in a horizontal plane while a nitrosyl group coordinates in axial position opposite to a methanol ligand. Thus, each iron center is surrounded by μ_4-sulfato ligands. Figure 2.3 shows details of the two-dimensional polymer of the *ab* plane. In the bottom part of the figure, the bonding situation is highlighted for a couple of adjacent iron central atoms. The nitrosyl ligands alternate above and below the $FeSO_4$ plane. As is shown in Figure 2.3 (top), the Fe–N–O moiety has a bond angle of ≈180° with the bond length of Fe1–N1 1.769(8) Å and N1–O1 1.110(11) Å, If no attempt is made to resolve a tentative disorders which is indicated by the flat thermal ellipsoid of the nitrosyl-O-atom (Figure 2.3). A methanol group is coordinated in *trans* position to the nitrosyl group. Its methyl group is heavily disordered.
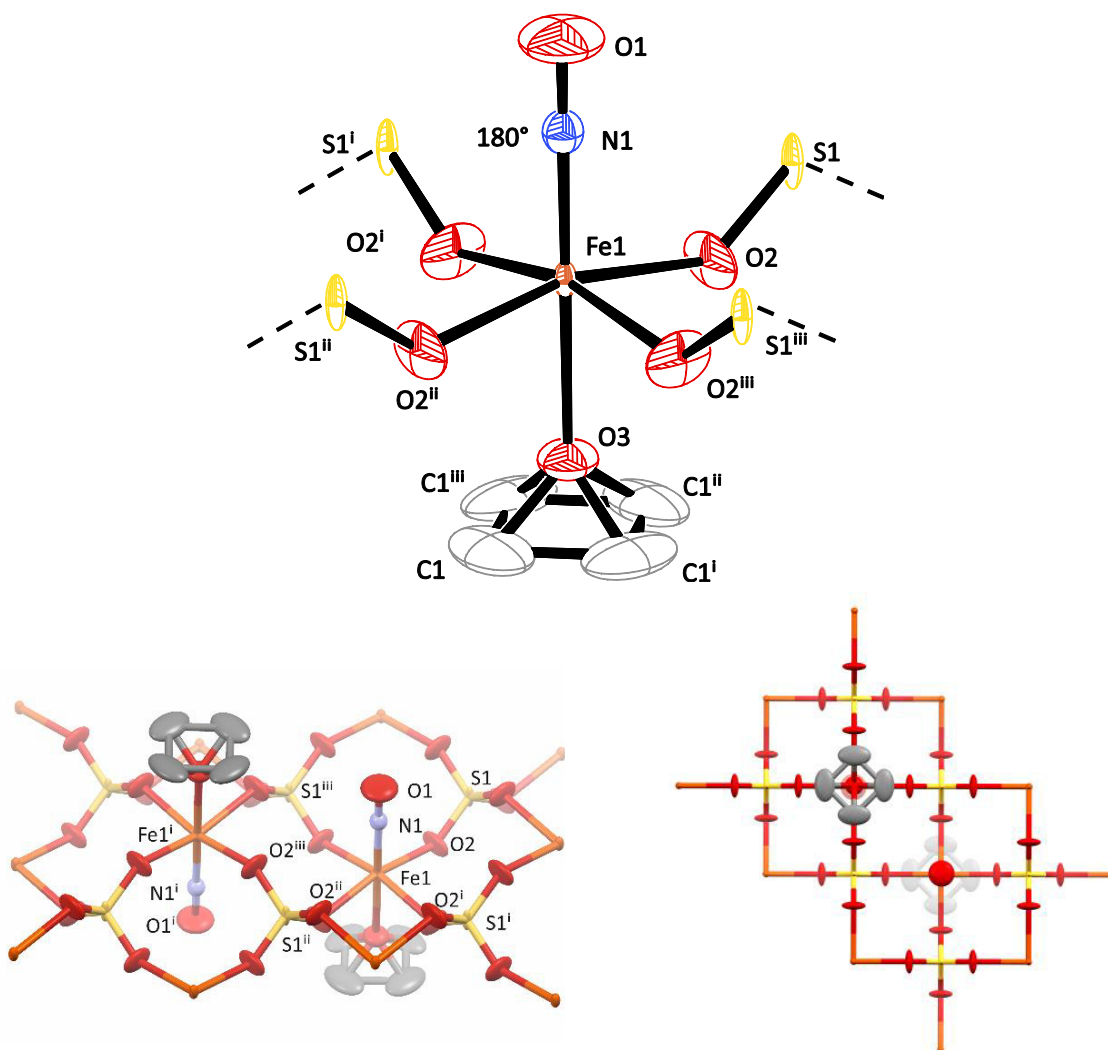
Figure 2.3: (Top) ORTEP plot of the compound [Fe(CH$_3$OH)(NO)(μ_4-SO$_4$)]$_{n/n}$ (**A**) (50% probability level at 100 K). Space group *P4/nmm*. Interatomic distances (Å) and angles (°) with the standard deviation of the last digit is given in parentheses : Fe1–N1 1.769(8), N1–O1 1.110(11), Fe1–O2 2.058(3), Fe1–O3 2.155(7), S1–O2 1.458(3), C1–O3 1.35(3), Fe1–N1–O1 180.0°, N1–Fe1–O2 98.59(10)°, O2–Fe1–O3 81.41(10)°, O2^{iii}–Fe1–O2 162.8(2)°, O2–S1–O2^{i} 105.93(3)°, O2–S1–O2^{ii} 111.27(14)°. Hydrogen atoms are omitted in Figure 2.3 for clarity reasons. (Bottom) MERCURY plot of **A**, view along [001] shows a square-like arrangement (right). Symmetry code: ^{i} 1/2–*y*,+*x*,+*z*, ^{ii} 1/2–*x*,1/2–*y*,+*z*, ^{iii} +*y*, 1/2–*x*,+*z*.

On closer inspection, there is similarity between **A**, (H$_3$O)[{Fe(NO)(μ_4-SO$_4$)(μ_2-SO$_4$)$_{0.5}$}$_{n/n}$]$^{[32]}$, [Fe(H$_2$O)$_5$(NO)]$^{2+,[27]}$, [{Fe(H$_2$O)(NO)(μ_2-ox)}$_{n/n}$·H$_2$O]$^{[32]}$ and [Fe(H$_2$O)$_2$(oda)(NO)]$^{[41]}$ concerning the coordination of the iron by five oxygen atoms and one nitrosyl group, {Fe(NO)(O)$_5$}. A following comparison of interatomic distances and angles as well as the experimental Fe–NO stretching vibration of these compounds illustrates the similarity (Table 2.1).

In conclusion, [Fe(CH$_3$OH)(NO)(μ_4-SO$_4$)]$_{n/n}$ (**A**) and (H$_3$O)[{Fe(NO)(μ_4-SO$_4$)(μ_2-SO$_4$)$_{0.5}$}$_{n/n}$]$^{[32]}$ have a similar crystal habitus and color as described by Manchot. At that time, no crystal-structure analysis

was available. However, it seems reasonable to assume that $(H_3O)[\{Fe(NO)(\mu_4\text{-}SO_4)(\mu_2\text{-}SO_4)_{0.5}\}_{n/n}]$[32] is the product described by Manchot and **A** is a derivate of Manchot's red compound, bearing the same 2D-coordination polymer in their $Fe(NO)SO_4$ part. Both are $\{FeNO\}^7$ (S = 3/2) compounds.
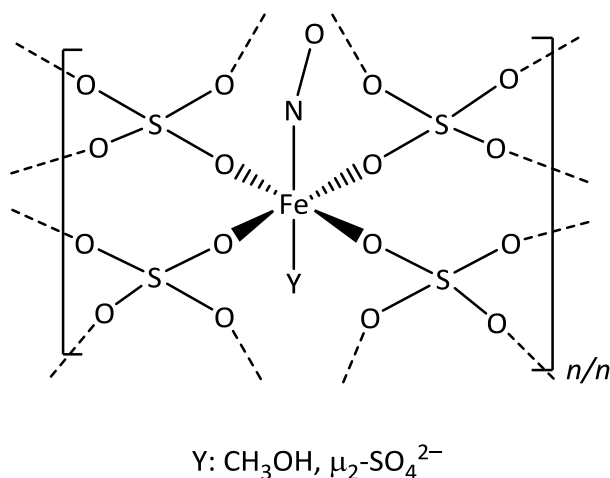
Y: CH_3OH, $\mu_2\text{-}SO_4^{2-}$

Figure 2.4: Coordination pattern of the red compound **A** with Y = CH_3OH, and $(H_3O)[\{Fe(NO)(\mu_4\text{-}SO_4)(\mu_2\text{-}SO_4)_{0.5}\}_{n/n}]$[32] (Y = $\mu_2\text{-}SO_4^{2-}$).

Table 2.1: Comparison of **A**, $(H_3O)[\{Fe(NO)(\mu_4\text{-}SO_4)(\mu_2\text{-}SO_4)_{0.5}\}_{n/n}]$[32], $[Fe(H_2O)_5(NO)]^{2+}$,[27] $[\{Fe(H_2O)(NO)(\mu_2\text{-}ox)\}_{n/n}\cdot H_2O]$[32] and $[Fe(H_2O)_2(NO)(oda)]$[41]. Note the Fe–N distances in **A** and Manchot's compound were differed. The shorter distance in **A** goes along with positional disorders of the O-atom, which has been resolved in a split mode in the analysis of Manchot's compound.

Coordination entity	$[Fe(CH_3OH)(NO)$-$(\mu_4\text{-}SO_4)]_{n/n}$ (**A**)	$(H_3O)[\{Fe(NO)(\mu_4\text{-}SO_4)$-$(\mu_2\text{-}SO_4)_{0.5}\}_{n/n}]$[32]	$[Fe(H_2O)_5(NO)]^{2+}$,[27]	$[\{Fe(H_2O)(NO)$-$(\mu_2\text{-}ox)\}_{n/n}\cdot H_2O]$[32]	$[Fe(H_2O)_2(NO)(oda)]$[41]
Fe1–N1/Å	1.769(8)	1.776	1.786(4)	1.784(6)	1.769(4)
N1–O1/Å	1.110(11)	1.172	1.143(5)	1.135(8)	1.146(5)
Fe1–OH(CH$_3$)/Å	2.155(7)	Fe1–O(μ_2-SO$_4$)$_{0.5}$ 2.136	Fe1–O95 2.120(4)	2.166(4)	Fe1–O2 2.123(4)
Fe1–N1–O1/°	≈180°	164.38°	160.6(4)°	155.6(6)	164.6(4)°
N1–Fe1–O3/°	180.0°	180°	178.88(16)°		180.00°
O2–Fe1–O2^i/°	88.72(3)°	88.49°	87.50(15)°		O21–Fe1–O91 90.25(5)°
O2–Fe1–O2^{ii}/°	162.8(2)°	161.32°	170.53(16)°		O21–Fe1–O91^i 177.02(7)°
O2^{ii}–Fe1–O3(CH$_3$)/°	81.41(10)°	80.66°	84.65(14)°		O91–Fe1–O2 88.51(5)°
Fe1–O2$_{sulfate}$/Å	2.058(3)	2.073	Fe1–O91 2.105(4)	2.083(5)	Fe1–O21 2.0663(13)
			Fe1–O92 2.067(3)	2.084(5)	Fe1–O91 2.0757(11)
			Fe1–O93 2.064(3)	2.108(4)	
			Fe1–O94 2.031(4)	2.035(5)	
Color, IR (solid, $\tilde{\nu}$)	red, 1837 cm^{-1}	red, 1840 cm^{-1}	brown, 1843 cm^{-1}	brown, 1823cm^{-1}	green, 1799 cm^{-1}

2.2 Synthesis of crystalline tetra-coordinated halogenidonitrosylferrates [FeX$_3$(NO)]$^-$ (X: F, Cl and Br)

Some of the results of this part were published in *Chem. Eur. J.* **2019**, *25*, 1304–1325 with the title *{FeNO}^{7}-Type Halogenido Nitrosyl Ferrates: Syntheses, Bonding, and Photo-induced Linkage Isomerism* (DOI:10.1002/chem.201804565).

Tetra-coordinated halogenidonitrosylferrates with various cations (**1–19**) were obtained by the following general procedure under an argon atmosphere. Iron salts such as FeCl$_2$·4H$_2$O, Fe(OTf)$_2$ or FeCl$_3$ were dissolved in methanol, followed by the addition of one or three equivalents of halide salt of the respective cation. The resulting yellow solutions were then treated with excess gaseous nitric oxide, whereupon they turned dark green.

Chloridonitrosylferrate, [FeCl$_3$(NO)]$^-$, compounds **1–11** were synthesized by the reaction of FeCl$_2$·4H$_2$O with one equivalent of chloride salt in methanol and an excess of gaseous nitric oxide. The clear-yellow solution turned dark green upon exposure to NO. The dark green crystalline products were formed immediately with voluminous cations such as PPh$_4$$^+$, AsPh$_4$$^+$ or PPN$^+$ (**6–8**), while products with smaller cations such as NMe$_4$$^+$, NEt$_4$$^+$, Co(cp)$_2$$^+$ (**1–5**) were formed by storing the solution at 5 °C for at least one day or up to several weeks without using an antisolvent. The exception was complex **4** with NBnMe$_3$$^+$ as the cation which formed when diethyl ether was used as an antisolvent. Products with other reactively small cations, namely K$^+$, Rb$^+$, Cs$^+$, NH$_4$$^+$ and NBu$_4$$^+$ could not be crystallized either by cooling the samples at 5 °C, or by using either diethyl ether or acetone as antisolvents. These green solutions were stable under nitric-oxide atmosphere for years. Nevertheless, Cs[FeCl$_3$(NO)] was obtained as a green amorphous solid not suitable for single crystal X-ray crystallography.

Some other starting iron salts, namely Fe(OTf)$_2$ and Fe(OTs)$_2$ were tested as well and used for synthesizing such complexes. In these cases, three equivalents of halide salt were required to obtain the attempted complex. Unlike the chloridonitrosylferrates, bromidonitrosylferrate, [FeBr$_3$(NO)]$^-$, salts (**11–13**) were crystallized only with voluminous cations. The application of the same procedure using iodide salts did not result in the formation of the [FeI$_3$(NO)]$^-$ anion. Instead, a redox reaction took place, iodine was produced and led to the formation of brown [FeI$_2$(NO)$_2$]$^-$ (**17–20**) complexes, which, according to the Enemark-Feltham[20] notation, are {Fe(NO)$_2$}^{9} compounds. The reaction equations of the synthesis of halogenido mononitrosyl-iron complexes are shown in Scheme 2.2.

$$\text{FeCl}_2 \cdot 4\text{H}_2\text{O} + \text{A}^+\text{Cl}^- + \text{NO} \xrightarrow[\text{rt}]{\text{MeOH}} \text{A}^+[\text{FeCl}_3(\text{NO})]^- + 4\,\text{H}_2\text{O}$$

$$\text{Fe(OTf)}_2 \cdot 4\text{MeOH} + 3\,\text{A}^+\text{X}^- + \text{NO} \xrightarrow[\text{rt}]{\text{MeOH}} \text{A}^+[\text{FeX}_3(\text{NO})]^- + 2\,\text{A(OTf)} + 4\,\text{MeOH} \quad (\text{X = Cl, Br})$$

$$2\,\text{Fe(OTf)}_2 \cdot 4\text{MeOH} + 6\,\text{A}^+\text{I}^- + 2\,\text{NO} \xrightarrow[\text{rt}]{\text{MeOH}} 2\,\text{A}^+[\text{FeI}_2(\text{NO})_2]^- + \text{I}_2 + 4\,\text{A(OTf)} + 8\,\text{MeOH}$$

A: NMe_4^+, NEt_4^+, NBnMe_3^+, Mephaz^+, Co(cp)_2^+, PPh_4^+, AsPh_4^+, PPN^+, $\text{C}_{25}\text{N}_3\text{H}_{30}^+$, $\{\text{Fe(bpy)}_3\}^{2+}$
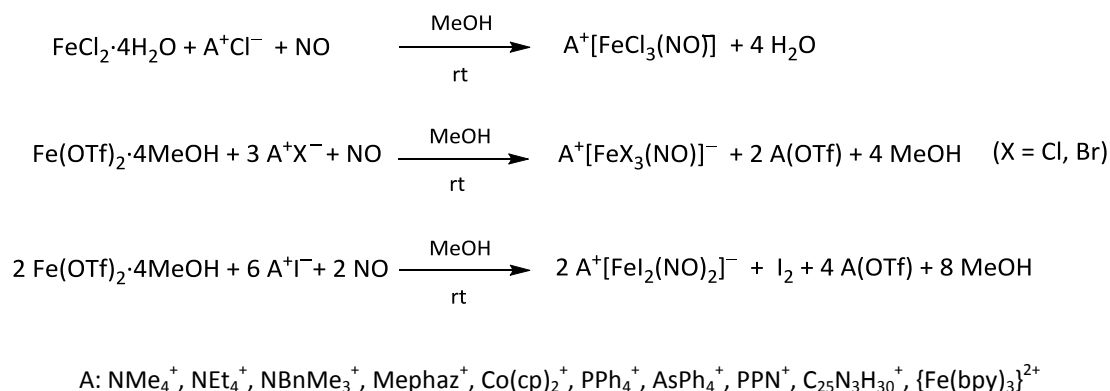
Scheme 2.2: Synthesis of halogenidonitrosylferrates.

2.3 Synthesis of mixed halogenidonitrosylferrates PPN[FeX$_a$Y$_{3-a}$(NO)] compounds.

The following syntheses were done in a similar fashion as those for unmixed halogenidonitrosylferrates. The resulting products were analyzed by IR spectroscopy. As shown in Scheme 2.3, the reaction of FeCl$_2$ and one equivalent of bromide salt led to a mononitrosyl-iron complex. This PPN[FeCl$_2$Br(NO)]* complex was different from PPN[FeCl$_3$(NO)] (**8**) or PPN[FeBr$_3$(NO)] (**13**). The NO stretching vibration band of this compound shifted to 1760 cm^{-1} while **8** and **13** had their NO stretching vibration at about 1790 cm^{-1}. When using the iodide (PPN)I, two NO stretching vibration bands were observed (1704 and $\approx$1760 cm^{-1}), indicating the formation of a dinitrosyl-iron complexes. However, mixed halide salts could produce disordered complexes.

$$\text{FeCl}_2 \cdot 4\text{H}_2\text{O} + (\text{PPN})\text{Br} + \text{NO} \xrightarrow[\text{rt}]{\text{MeOH}} \text{PPN}[\text{FeCl}_2\text{Br(NO)}]^* + 4\,\text{H}_2\text{O} \quad \text{green crystals, } \tilde{\nu}(\text{NO}) = 1760\ \text{cm}^{-1}$$

$$\text{FeCl}_2 \cdot 4\text{H}_2\text{O} + (\text{PPN})\text{I} + \text{NO} \xrightarrow[\text{rt}]{\text{MeOH}} \text{PPN}[\text{FeCl}_a\text{I}_{2-a}(\text{NO})_2] + 4\,\text{H}_2\text{O} \quad \text{green-brown crystals, } \tilde{\nu}(\text{NO}) = 1759, 1704\ \text{cm}^{-1}$$

$$\text{FeBr}_2 + (\text{PPN}) + \text{NO} \xrightarrow[\text{rt}]{\text{MeOH}} \text{PPN}[\text{FeBr}_a\text{I}_{2-a}(\text{NO})_2] \quad \text{brown crystals, } \tilde{\nu}(\text{NO}) = 1763, 1704\ \text{cm}^{-1}$$
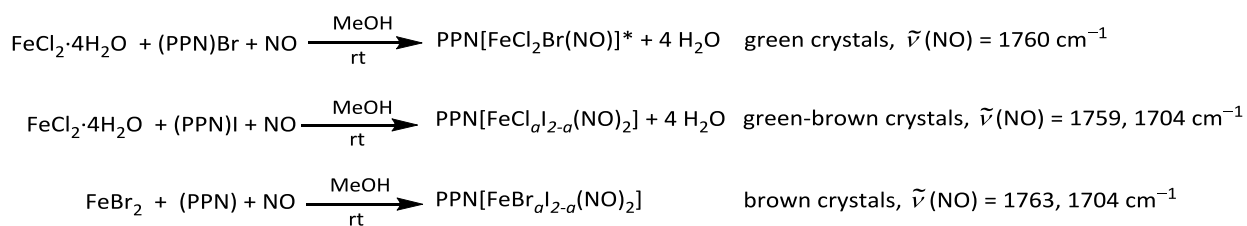
* Cl/Br disordered crystal structures

Scheme 2.3: Synthesis of mixed halogenidonitrosylferrates.

2.4 Synthesis of crystalline trichloridonitrosylferrates from FeCl$_3$

In this thesis, the preparations of such complexes from the ferric precursor FeCl$_3$ were successfully developed and confirmed by X-ray diffraction analysis, IR and UV/Vis spectroscopy. According to Manchot, nitric oxide was assigned as the reductant in the presence of an organic solvent and a ferric precursor. The reduction mechanism was considered complicated by Manchot who did not give a balanced equation.[13,52]

Various conditions for the synthesis of $\{FeNO\}^7$ compounds from $FeCl_3$ were investigated, whereby the Fe:Cl molar ratio was varied. Whichever iron starting salt ($FeCl_2$ or $FeCl_3$) was used, an excess of chloride had no negative impact on the outcome of the reaction leading to the formation of compound **8** (Scheme 2.4). As an example, the following reaction was performed: $FeCl_3$ was mixed with two equivalents of (PPN)Cl, resulting in a clear yellow solution with a light yellowish precipitate. Some of this solution was isolated and kept at 5 °C for a few days. From this batch, yellow crystals were obtained and analyzed by X-ray diffractometry. As a result, the compound was identified as $PPN[FeCl_4]$.

$$FeCl_3 + (PPN)Cl \xrightarrow{\text{MeOH}} PPN[FeCl_4]$$
$$\text{yellow solid}$$

$$\downarrow \text{NO, rt}$$

$$PPN[FeCl_3(NO)]$$
$$\mathbf{8}$$
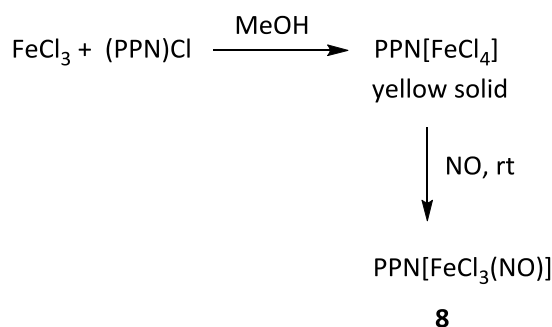
Scheme 2.4: Synthesis of trichloridonitrosylferrate from tetrachloridoferrate(III).

The remaining solution including a yellowish suspension of the tetrachloridoferrate(III) was treated with gaseous nitric oxide for ten minutes at room temperature whereby the product formed immediately. As the only product, the compound $PPN[FeCl_3(NO)]$ (**8**) was obtained. It can be concluded from this observation that chloridoferrate(III) formation does not prohibit the reaction to the nitrosylated complex and that there is no tendency to form $[FeCl_n(NO)]^-$ anions with $n > 3$.

2.5 Attempts at the synthesis of fluoridonitrosylferrates

Attempts to synthesize fluoridonitrosylferrates were unsuccessful. Various fluoride salts were tested such as KF, $(NMe_4)F$, $(NBnMe_3)F$, $(NBu_4)F$ and (PPN)F. The stoichiometry of fluoride to iron was varied, as well as the iron precursor. Hence, iron(II) triflate instead of iron(II) chloride or iron(II) bromide was used to avoid the formation of the known halogenidonitrosylferrates. Other precursors were excluded, since they did not dissolve well in methanol: $FeBr_2$, FeF_2, FeF_3, FeI_2. Table 2.2 summarizes the results of the reaction of ferrous triflate with various amounts of fluoride in terms of (a) a color change of the solution on treatment with nitric oxide and (b) the pH values (in methanol) of the mixture before it was treated with nitric oxide. The following table shows the reaction color and the pH values of the various batches.

Table 2.2: Comparison of experiments with Fe(OTf)$_2$·4MeOH and (NMe$_4$)F/KF salts. The pH values of the reaction mixtures and color changes within one day of the mixtures after treatment with NO are given. In the 1:10 experiment, KF was used instead of (NMe$_4$)F.

Molar ratio Fe: F	pH value before NO	Color changes after NO-gas treatment
1:0	2	pale yellow → dark green
1:1	3	pale yellow → dark green
1:2	3–4	pale yellow → brown → dark green
1:3	5–6	pale yellow → orange → brown → green → yellow/green
1:4	7–8	pale yellow → orange → brown → green → yellow/green
1:5	8	pale yellow → orange → brown → green → yellow/green
1:10	10	colorless (turbid) → pale-brown (turbid)

As shown in Table 2.2, the initial pH value of the reaction mixtures increased with the amount of fluoride. If pure Fe(OTf)$_2$ dissolved in methanol and, was treated with gaseous nitric oxide, a dark green color was observed indicating the formation a mononitrosyl-iron complex. The solution was stable under nitric oxide atmosphere for years, but lost its green color immediately on exposure to inert gas, which caused loss of NO and restored the initial color. For pH>4, the color of the reaction mixture turned light brown, then light yellow-green, indicating that other species formed. The light brown color was similar to the one of a dinitrosyl-iron complex solution (see the following section 2.6). At a high pH of 8 and 10, no reaction with nitric-oxide gas took place. This was also observed when FeCl$_2$ or FeCl$_3$ were mixed with fluoride salt because the resulting pH value of more than 5 was too high. The exposure of the mixture to nitric oxide thus showed no color change. That would mean that a higher amount of F$^-$ in solution could lead to the formation of unknown iron–fluoride species which did not react with gaseous nitric oxide. However, Maigut *et al.* reported the exchange of F$^-$ and NO in an aqueous solution of the [Fe(edta)]$^{2-}$ complex.[53] They indicated that an F$^-$ ligand can be replaced by an NO ligand.

In addition, FeF$_2$ and FeF$_3$ were tested as starting material dissolved in 1-butyl-3-methyl-imidazole-3-ium hexafluoridophosfate ((BMIM)-PF$_6$), an ionic liquid. These experiments were inspired by van Eldik *et al.* who prepared tetrahedral iron complexes with chloride and nitrosyl ligands in ionic liquids.[54,55] However, FeF$_2$ and FeF$_3$ did not sufficiently dissolve in the ionic liquid to react with gaseous NO, as indicated by the absence of a color change. On the contrary, FeCl$_3$ reacted with gaseous NO and the solution turned green, indicating the formation of a nitrosyl-iron complex. In conclusion, the set-up with the ionic liquid (BMIM)-PF$_6$ was not suitable for the synthesis of fluoridonitrosylferrates.

Apart from methanol and ionic liquids, acids such as FSO_3H, HBF_4 (48 wt.% in H_2O), HF (40 wt.% in H_2O) and CF_3SO_3H were used to improve the solubility of the iron fluorides. FeF_2 and FeF_3 dissolved very well in HF or HBF_4 and a clear solution was obtained. When NO gas was passed through the solution, it remained colorless, indicating that no reaction took place. Even storing the solution under NO atmosphere for a long period (from several months up to a year), did not lead to a color change.

The hygoscopic triflic acid was tested as a solvent as well. Table 2.3 shows the color change of the reaction mixture on NO treatment with different iron salts as starting materials. While combining the different reactants in the acid under the argon gas stream, a gas formation (colorless) was observed (in all cases of $FeCl_2$, $FeCl_3$, FeF_2, FeF_3 and $Fe(OTf)_2$). After NO treatment the initially green-white suspension (in the case of FeF_2 and FeF_3) changed to deep blue. On strong shaking or stirring of the reaction mixture during the nitric oxide exposure, the deep blue color intensified with simultaneous strong colorless smoke formation. After the removal of the nitric oxide atmosphere, the deep blue suspension turned colorless. After the reexposure of the reaction mixture to nitric oxide, the colorless suspension changed to deep blue again.

Table 2.3: Color changes of reaction mixtures upon NO treatment with different pure iron salts in anhydrous triflic acid.

Iron salt	Color
FeF_2	deep blue
FeF_3	deep blue
$FeCl_3$	pink blue
$FeCl_2$	deep blue
$Fe(OTf)_2$	pink blue

Comparing all of these results with those in literature, it was found that the colorless precipitate was, supposedly nitrosyl trifluoromethanesulfonate ($NOCF_3SO_3$) according to Noftle and Cady.[56] That salt was described as hygroscopic colorless solid, which could be synthesized *via* the reaction of $CF_3SO_2OSO_2CF_3$ with an excess of NO or *via* the reaction of CF_3SO_3H with an excess NOCl. Furthermore, it was described that $NOCF_3SO_3$ hydrolyzed rapidly in cold water to give an initially blue-colored solution which slowly decolorized. As was shown in Table 2.3, a deep blue (pink blue) color was also observed during the reaction with NO gas. This could be described as a formation of the byproduct $NOCF_3SO_3H$, which could be hydrolyzed with crystal water from the starting iron salt. However, no analysis of such colorless or deep blue precipitates was performed from triflic acid or hydrofluoric acid because of its corrosivity. In conclusion, the use of CF_3SO_3H, FSO_3H, HBF_4 and HF as solvent for the synthesis of fluoridonitrosylferrate compounds turned out to be unsuitable.

2.6 Synthesis of crystalline dihalogenidodinitrosylferrate [FeX$_2$(NO)$_2$]$^-$ complexes (X: Cl, Br and I)

As mentioned earlier, the reaction of Fe(OTf)$_2$ and iodide, which is itself redox-active, and gaseous NO resulted in the formation of dinitrosyl-iron complexes (DNICs) instead of mononitrosyl-iron complexes (MNICs). The reaction seemed to proceed according to the following equation:

$$Fe^{2+} + 3.5\ I^- + 2\ NO \rightarrow [FeI_2(NO)_2]^- + 0.5\ I_3^-$$
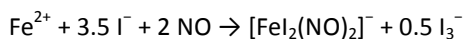
Scheme 2.5: Proposed formation of [FeI$_2$(NO)$_2$]$^-$.[33]

In the present thesis, pure dihalogenidodinitrosylferrates were successfully prepared employing a 'one-pot-synthesis' using Fe(OTf)$_2$ or FeCl$_2$ or FeCl$_3$ as the starting materials. By using of Fe(OTf)$_2$ mixed with one equivalent of PPNCl and NEt$_3$ as a base, and, finally, gaseous NO, resulted in the formation of PPN[FeCl$_2$(NO)$_2$] (**14c**). The use of bases such as NEt$_3$, NaOCH$_3$ and TMEDA in order to synthesize dihalogenidodinitrosyl–metal complexes had been described before in the 1970s,[35,43,57] and complexes such as [CoCl$_2$(NO)$_2$][58] and HNEt$_3$[FeCl$_2$(NO)$_2$][58] were analyzed by IR spectroscopy. It was proved herein that not only NEt$_3$ can be used as a base but also fluoride salts. The synthesis of the A[FeCl$_2$(NO)$_2$] compounds succeeded from the reaction of one equivalent of FeCl$_3$ and three equivalents (NMe$_4$)F or from one equivalent of FeCl$_2$ and two equivalents of (NMe$_4$)F (Scheme 2.6). The latter method was preferably used, as the main product could be obtained in high yields. The dichloridodinitrosylferrate (DNIC-Cl) synthesis is a consecutive reaction: with the trichloridomononitrosylferrate-MNIC (MNIC-Cl) formation followed by the subsequent DNIC-Cl formation (this point will be discussed later in Section 2.7). Furthermore, FeCl$_3$ as the starting salt led to the co-crystallization of [FeCl$_3$(NO)]$^-$ as a byproduct for some cations. Both DNIC reactions using of FeCl$_2$ and FeCl$_3$ reactants produced a redox by-product: methyl nitrite (). The frequent observation of methyl-nitrite formation during the treatment with gaseous NO was best monitored by UV/Vis spectroscopy and exemplarily shown in Figure 2.5. In case of dibromidodinitrosylferrate (DNIC-Br), only the PPN[FeBr$_2$(NO)$_2$] (**15a**) salt was obtained unexpectedly alongside green crystals of PPN[FeBr$_3$(NO)] as the main product, which was prepared from Fe(OTf)$_2$ and PPNBr (1:1) without the use of base. More detail will be discussed later in Chapter 2.11.

$$FeCl_2 + 2\ (NMe_4)F + 3\ NO + MeOH \longrightarrow NMe_4[FeCl_2(NO)_2] + MeONO + (NMe_4)HF_2$$

$$FeCl_3 + 2\ (NMe_4)F + 4\ NO + 2\ MeOH \longrightarrow NMe_4[FeCl_2(NO)_2] + (NMe_4)Cl + 2\ MeONO + 2\ HF$$
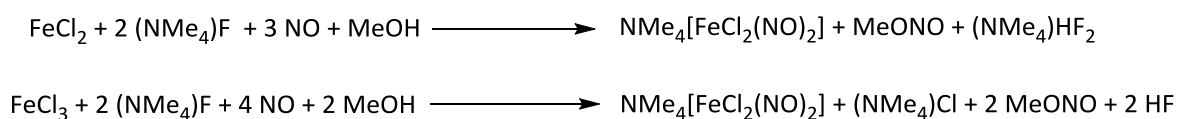
Scheme 2.6: Synthesis of dichloridodinitrosylferrates from FeCl$_2$ and FeCl$_3$ salt.
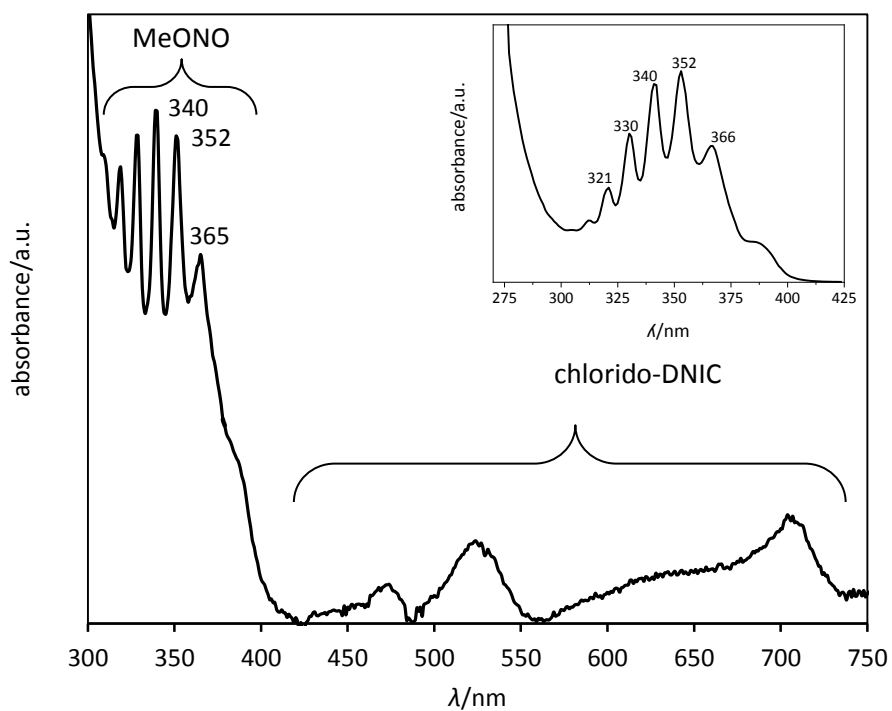
Figure 2.5: UV/Vis spectrum of a methanolic solution chlorido-DNIC containing MeONO after the reaction of FeCl$_3$ and (NMe$_4$)F with NO. The MeONO absorption bands are found at 319, 329, 340, 352 and 365 nm. The insert (top right) is a UV/Vis spectrum of a methanolic solution of NOBF$_4$ (0.2 M).

2.7 Consecutive MNIC-to-DNIC-transformation in the presence of base

The MNIC-to-DNIC transformation was best monitored by *in situ* IR (REACTIR 15) spectroscopy. The time-resolved spectra are depicted in Figure 2.6.

Upon the contact of gaseous NO with a methanolic solution of $FeCl_2$, MNIC-$[FeCl_3NO)]^-$ was rapidly formed ($\tilde{v}$(NO) $\approx$ 1790 cm^{-1}, Figure 2.6) and was completed within about five minutes whereby a small signal of $[FeCl_2(NO)_2]^-$ at 1720 cm^{-1} arose. After about one hour, no further change in the concentration of MNIC and DNIC species was observed. At this point (black arrow in Figure 2.6, right) the methanolic solution of two equivalents of $(NMe_4)F$ was added to the green reaction solution, leading to a decay of the MNIC absorption band within a few minutes with simultaneous increase of two characteristic DNIC bands at 1770 cm^{-1} and 1720 cm^{-1} these bands reached their maxima within ten minutes. The green solution turned brown immediately upon addition of $(NMe_4)F$.
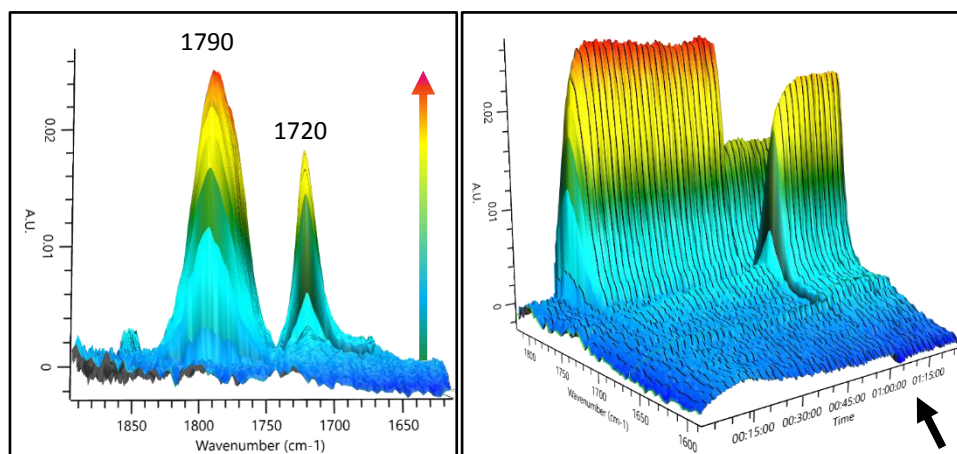
Figure 2.6: IR spectra of MNIC-to-DNIC transformation, as monitored using REACTIR 15 spectroscopy.

When repeating this reaction but starting in the presence of fluoride salt, at the beginning of the reaction the MNIC band first formed along with some DNIC species (see the blue gradient in Figure 2.7). Afterwards, the asymmetric Fe(N–O) absorption band at 1720 cm^{-1} increased drastically and the formation of DNIC was completed, in terms of IR spectroscopy, within about four minutes. The red solution darkened and was air- and under inert-gas atmosphere stable. Conversely, the green MNIC solution was very sensitive to air and even under inert gas atmosphere. When it was exposed to air, the solution turned back to its initial light-yellow color, indicating loss of the nitrosyl ligand.
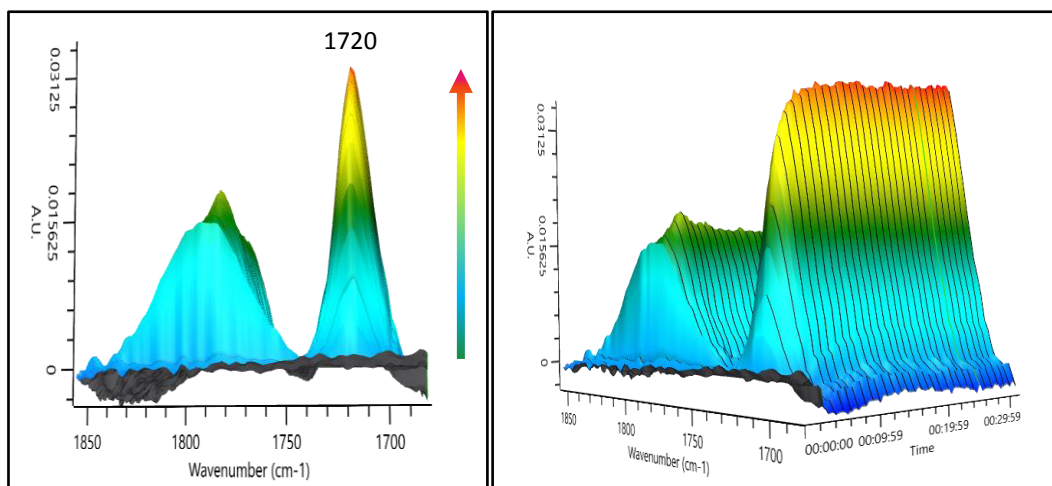
Figure 2.7: IR spectra of MNIC-to-DNIC transformation, monitored using REACTIR 15 spectroscopy.

2.8 IR spectroscopic characterization

$\{FeNO\}^7$ complexes have a typical N–O stretching vibration in a range of about 1750 to 1850 cm^{-1}. Specifically, A[FeX$_3$(NO)] (X = Cl, Br) solid compounds showed a strong single NO band at approximately 1800 cm^{-1}. For A[FeX$_2$(NO)$_2$] (X = Cl, Br, I), $\{Fe(NO)_2\}^9$ solid compounds, two NO stretches occurred at around 1700$_{(asym)}$ and 1770$_{(sym)}$ cm^{-1} (Figure 2.8). Solutions of chlorido and bromido mononitrosyl-iron compounds were not stable on exposure to air. An *OMNI cell* was then used to obtain IR spectra. Solutions of DNICs were stable when exposed to air, so that they were measured directly on an ATR. In summary, IR as well as crystallographic data of salts with the [FeCl$_3$(NO)]$^-$, [FeBr$_3$(NO)]$^-$, [FeCl$_2$(NO)$_2$]$^-$, [FeBr$_2$(NO)$_2$]$^-$ and [FeI$_2$(NO)$_2$]$^-$ anions (**1**−**19**) are listed in Table 2.4.
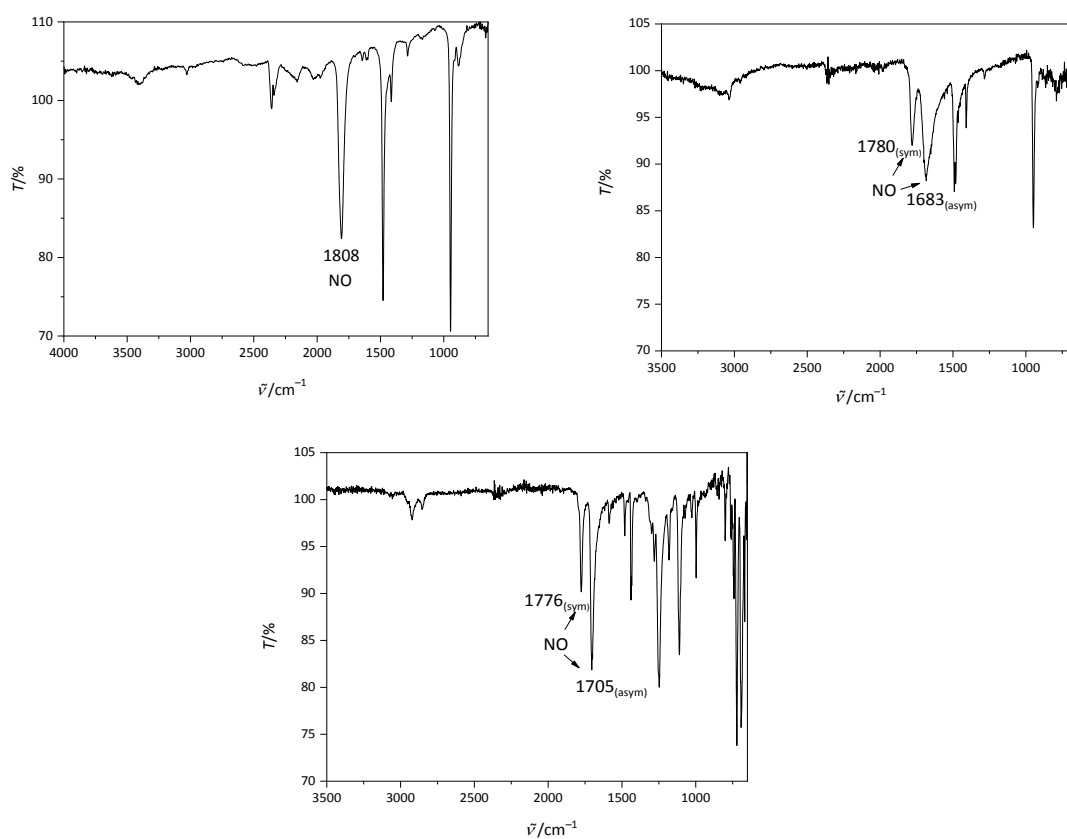
Figure 2.8: IR spectra of crystalline NMe$_4$[FeCl$_3$(NO)] (**1**) (top left), NMe$_4$[FeCl$_2$(NO)$_2$] (**14a**) (top right) and PPN[FeCl$_2$(NO)$_2$] (**14c**) (bottom).

Table 2.4: Spectroscopic and structural parameters for selected anionic MNICs {FeNO}[7] and DNICs {Fe(NO)$_2$}[9] complexes.

	Code	Cation	Space group	dFe–Cl/Å	dFe–N/Å	dN–O/Å	Fe–N–O/°	$\tilde{v}$(N–O)/cm^{-1}	Min. and Max. Resd. Dens.[e/Å^3]
1a	tq006	NMe$_4$$^+$	$Pca2_1$	2.2370	1.710(7)	1.154(9)	175.2(6)	1806	−0.30, 0.37
1b	tv242	NMe$_4$$^+$	$Pca2_1$	2.2394	1.729(7)	1.1452(12)	174.1(3)	1810	−0.16, 0.29
2a	vv686	NEt$_4$$^+$	$Pca2_1$	2.2379	1.7677(16)	1.103(2)	172.62(16)	1780	−0.14, 0.26
2b	uo104	NEt$_4$$^+$	$Pca2_1$	2.2305	1.728(7)	1.149(15)	173.1(3)	1776	−0.26, 0.21
3	tv136	NBnMe$_3$$^+$	$P\bar{1}$	2.2296	1.732(4)	1.134(5)	173.5(4)	1805	−0.41, 0.61
4	vv064	Mephaz$^+$	$P2_1/n$	2.2414	1.734(2)	1.152(3)	170.12(17)	1792	−0.22, 0.35
5	tv206	Co(cp)$_2$$^+$	$Pca2_1$	2.2467	1.715(6) 1.710(6)	1.161(9) 1.157(9)	176.8(5) 176.3(6)	1793	−0.56, 0.75
6	tv135	PPh$_4$$^+$	$P\bar{4}$	2.2329	1.724(3)	1.158(4)	174.3(3)	1794	−0.23, 0.26
7	vv505	AsPh$_4$$^+$	$P2_1/n$	2.2457	1.734(3)	1.150(3)	171.0(2)	1797	−0.58, 0.69
8	tq012	PPN$^+$	$C2/c$	2.2277	1.7407(19)	1.133(3)	170.97(19)	1791	−0.41, 0.46
9	tv406	[Fe(bpy)$_3$]$^{2+}$	$P2_1/c$	2.2240	1.835(6)	0.928(8)	175.7(6)	1780	−0.57, 0.56
					1.717(19)	1.15(3)	173.3(9)		
					1.760(6)	1.102(8)	163.4(6)		
					1.801(5)	1.004(8)	173.4(6)		
					1.813(7))	0.964(10)	160.2(8)		
10	uv295	(C$_{25}$N$_3$H$_{30}$$^+$)$_2$	$Pca2_1$	2.2538	1.756(11)	1.071(16)	163.1(12)	1771	−0.47, 0.56
11	uv505	PPh$_4$$^+$	$P\bar{4}$	2.377	1.724(12)	1.158(15)	169.9(10)	1795	−1.17, 1.82
12	uv591	AsPh$_4$$^+$	$P\bar{4}$	2.371	1.732(5)	1.145(7)	173.5(5)	1794	−0.60, 0.44
13a	wv365	PPN$^+$	$P\bar{1}$	2.3752	1.729(9)	1.150(4)	169.5(3)	1800	−0.79, 0.96
13b[41]	tv137	PPN$^+$	$C2/c$	2.362	1.725(5)	1.168(7)	171.2(5)		−1.02, 0.84
14a	vv661	NMe$_4$$^+$	$Pbcm$	2.2811(5)	1.7074(11)	1.1567(14)	160.84(10)	1779, 1695	−0.26, 0.48
		X=Cl		2.2784(5)					
14b	uo024	NMe$_4$$^+$	$Pbcm$	2.2797(8)	1.7088(18)	1.146(2)	160.75(16)	1783, 1687	−0.34, 0.40
		X=Cl		2.2751(7)					
14c	vv643	PPN$^+$	$P\bar{1}$	2.2772(5)	1.6986(17)	1.168(2)	165.64(15)	1775, 1696	−0.31, 0.37
				2.2714(5)	1.7121(16)	1.147(2)	161.25(15)		
15a	vv286	PPN$^+$	$P\bar{1}$	2.4061(4)	1.691(3)	1.181(4)	163.4(3)	1777, 1710	−0.53, 1.02
		X=Br		2.4128(4)	1.689(4)	1.177(5)	166.4(4)		
15b	tv280	PPN$^+$	$P\bar{1}$	2.4108(4)	1.7077(19)	1.144(2)	162.76(17)	1776, 1709	−0.36, 1.02
		X=Br		2.4128(4)	1.686(4)	1.182(5)	166.1(4)		
16	tv038	PPN$^+$	$P\bar{1}$	2.5882(4)	1.686(2)	1.163(3)	164.75(19)	1758, 1709	−0.35, 0.58
		X=I		2.5982(4)	1.685(2)	1.165(3)	166.9(2)		
17	to029	PPN$^+$	$Ibca$	2.584(6)8	1.693(2)	1.163(3)	166.7(2)	1760, 1711	−0.89, 1.17
		X=I							
18	uv122	AsPh$_4$$^+$	$P2/n$	2.590(3)	1.6869(15)	1.172(2)	164.88(14)	1754, 1705	−0.59, 0.54
19	uv222	PPh$_4$$^+$	$P2/n$	2.5911(3)	1.687(13)	1.1740(19)	165.24(14)	1753, 1704	−0.57, 0.44

2.9 UV/Vis-spectroscopic characterization

Due to the green and brown color of $\{FeNO\}^7$ and $\{Fe(NO)_2\}^9$ compounds, respectively, UV/Vis spectra were collected from both crystalline samples and solutions. In general, both kinds of spectra agree in terms of the Λ_{max} values. Typical absorption maxima in the visible range of the green $\{FeNO\}^7$ compounds were found in three regions, namely around 400, 480 and 600 nm, while the brown solutions of $\{Fe(NO)_2\}^9$ compounds show absorption maxima at around 510 and 710 nm (see Figure 2.9, left). Table 2.5 shows a summary of the relevant results.
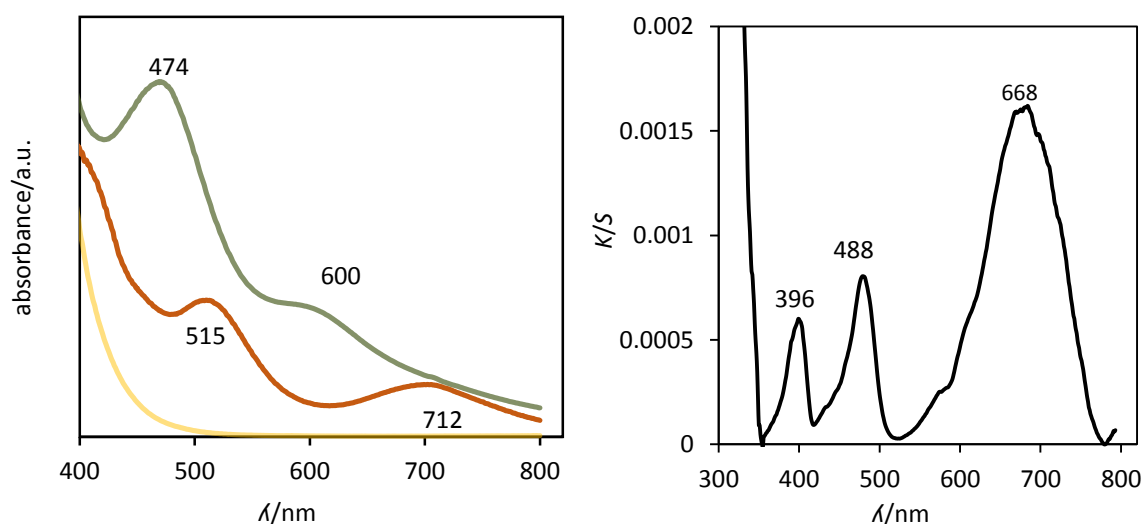
Figure 2.9: Left: UV/Vis-spectroscopic comparison of MNIC and DNIC solutions with the spectrum of methanolic FeCl$_2$ solution before treatment with NO gas (yellow line). MNIC [FeCl$_3$(NO)]$^-$ (green line) and DNIC [FeCl$_2$(NO)$_2$]$^-$ (brown line). Right: UV/Vis spectrum of crystalline **6**, diluted with BaSO$_4$. *K/S* refers to the Kubelka–Munk function: $K/S = (1-R)^2/2R$.[59]

Table 2.5: UV/Vis-spectroscopic data of MNIC and DNIC compounds. Λ/nm (MeOH) column: spectrum of a reaction batch using MeOH as the solvent; the label 'acetone' refers to re-dissolved solid precipitated during the reaction. Λ/nm(crys) column: K/S maxima of the solid samples.

Compound	Λ/nm (MeOH)	Λ/nm (crys)
$[Fe(MeOH)_5(NO)]Cl_2$	477, 518, 611, 708	no crystalline product
$[Fe(CH_3OH)(NO)(\mu_4\text{-}SO_4)]_{n/n}$ (**A**)	442, 579	464, 573
$HNMe_3[FeCl_3(NO)]$	465, 601	no crystalline product
$NMe_4[FeCl_3(NO)]$ (**1**)	472, 604	399, 476, 711
	323, 356, 475, 650 (acetone)	
$NEt_4[FeCl_3(NO)]$ (**2**)	-	246, 316, 388, 488, 668
$NBnMe_3[FeCl_3(NO)]$ (**3**)	461, 601	-
$NBnEt_3[FeCl_3(NO)]$	477, 606	216, 247, 316, 360, 448, 487, 659 (**)
$Mephaz[FeCl_3(NO)]$ (**4**)	425, 460, 604	-
$[Co(cp)_2][FeCl_3(NO)]$ (**5**)	340, 352, 417, 600, 687	269, 322, 396, 477, 689
$PPh_4[FeCl_3(NO)]$ (**6**)	358, 476, 646 (acetone)	231, 274, 399, 480, 684
$AsPh_4[FeCl_3(NO)]$ (**7**)	-	369, 395, 481, 687
$PPN[FeCl_3(NO)]$ (**8**)	442, 472, 647 (acetone)	400, 486, 660
$[Fe(bpy)_3][FeCl_3(NO)]_2$ (**9**)	448, 584	306, 374, 492, 538, 667
$CV[FeCl_3(NO)]$ (**10**)	-	214, 249, 304, 395, 583, 650
$[Fe(cp)_2][FeCl_3(NO)]*$	340, 410, 500, 696	438, 602 (**)
$PPh_4[FeBr_3(NO)]$ (**11**)	331, 341, 466, 596	466, 597
$AsPh_4[FeBr_3(NO)]$ (**12**)	330, 341, 352, 466, 601	370, 482, 663
$PPN[FeBr_3(NO)]$ (**13**)	477, 597	390, 483, 660
$NBnMe_3[FeBr_3(NO)]$	479, 610, 702	no crystalline product
$NBu_4[FeBr_3(NO)]$	476, 603	no crystalline product

* educt: $FeCl_3$, ** no crystal structure analysis available, CV[+]: crystal violet cation

Table 2.5: (continued).

Compound	λ/nm (MeOH)	λ/nm (crys)	$\tilde{\nu}$(N–O)$_{(MeOH)}$/cm^{-1}
NMe$_4$[FeCl$_2$(NO)$_2$] (**14a**)	510, 702	400, 514, 600, 703	1785, 1717
NMe$_4$[FeCl$_2$(NO)$_2$] (**14b**)	508, 696	401, 516, 696	1786, 1692
NEt$_3$[FeCl$_2$(NO)$_2$]*	501, 700	no crystalline product	1786, 1714
NBnMe$_3$[FeCl$_2$(NO)$_2$]*	505, 691	no crystalline product	1777, 1707
NBu$_4$[FeCl$_2$(NO)$_2$]*	511, 695	no crystalline product	1770, 1702
PPh$_4$[FeCl$_2$(NO)$_2$]	510, 700	no crystalline product	1784, 1715
PPN[FeCl$_2$(NO)$_2$] (**14c**)	-	234, 267, 334, 399, 429, 515, 693	1775, 1696
PPN[FeBr$_2$(NO)$_2$] (**15a**)	516, 691	-	1777, 1710
PPh$_4$[FeBr$_2$(NO)$_2$]	447, 518, 700	no crystalline product	

 * educt: FeCl$_3$

2.10 Crystal and molecular structures of tetracoordinated quartet-{FeNO}[7] compounds

The structures of mononitrosyl {FeNO}[7] ($S = 3/2$) iron complexes (**1**−**13**) with various cations are shown in this chapter. The [FeCl$_3$(NO)]$^-$ anion crystallized with small cations such as NMe$_4^+$ (**1a** and **1b**) and NEt$_4^+$ (**2a** and **2b**) in the orthorhombic space group *Pca*2$_1$. Voluminous cations such as NBnMe$_3^+$ (**3**) formed salts which crystallized in the triclinic space group $P\overline{1}$. [Co(cp)$_2$]$_2$[FeCl$_3$(NO)]$_2$ (**4**) crystallized in *Pca*2$_1$, PPh$_4$[FeCl$_3$(NO)] (**6**) crystallized in $P\overline{4}$, AsPh$_4$[FeCl$_3$(NO)] (**7**) crystallized in *P*2$_1$/*n*. When [Fe(bpy)$_3$]$^{2+}$ (**9**) was the counterion, the space group *P*2$_1$/*c* was adopted, whereas PPN[FeCl$_3$(NO)] (**8**) crystallized in the space group *C*2/*c*. The list of products (**1**−**19**) with their corresponding space groups is shown in Table 2.4.

The [FeCl$_3$(NO)]$^-$ ions had almost perfect *T*-4 configuration. The Fe–Cl bond lengths with an average distance about 2.23 Å lay in the range between this distance in [Fe^{II}Cl$_4$]$^-$ and [Fe^{III}Cl$_4$]$^-$ ions. The Fe1–N1 and N1–O1 bond lengths were found with an average distance of about 1.73 Å and 1.15 Å, respectively. The Fe1–N1–O1 fragments were nearly linear with the bond angle between 170–177°. The thermal ellipsoids of all atoms in the molecules were small. Especially the N and O atoms in the NO moiety were smaller than those in other {FeNO}[7] ($S = 3/2$) compounds with aminecarboxylato ligands.

The crystal structures of A[FeCl$_3$(NO)] where A is the counter ion are shown in Figure 2.10–Figure 2.22. The 'corrected' term in crystal structure annotation means that these structure analyses revealed positional disorder between Cl and NO (all values are less than 15% of Cl) which was successfully corrected in the course of the structure refinement (Table 2.6). The stated 'uncorrected' values are shown as well for the sake of comparison. These positional disorders were found in **1b**, **2b**, **9** and **10**.

Table 2.6: Comparison of structural parameters in NMe$_4$[FeCl$_3$(NO)] and NEt$_4$[FeCl$_3$(NO)] from FeCl$_2$ and FeCl$_3$. Corrected: corrected crystal structure refinement.

	Starting salt	Cation	Space group	dFe–Cl/Å	dFe–N/Å	dN–O/Å	Fe–N–O/°	$\tilde{\nu}$(N–O)/cm^{-1}	Min. and Max. Resd. Dens. [e/Å^3]
1a	FeCl$_2$	NMe$_4^+$	*Pca*2$_1$	2.2370	1.710(7)	1.154(9)	175.2(6)	1806	−0.30, 0.37
1b	FeCl$_3$	NMe$_4^+$	*Pca*2$_1$	2.2395	1.789(2)	1.059(3)	174.6(2)	1810	−0.16, 0.29
		corrected		2.2394	1.729(7)	1.1452(12)	174.1(3)	1810	−0.16, 0.29
2a	FeCl$_2$	NEt$_4^+$	*Pca*2$_1$	2.2379	1.7677(16)	1.103(2)	172.62(16)	1780	−0.14, 0.26
2b	FeCl$_3$	NEt$_4^+$	*Pca*2$_1$	2.2318	1.813(3)	0.995(4)	173.3(3)	1776	−0.29, 0.22
		corrected		2.2305	1.728(7)	1.149(15)	173.1(3)	1776	−0.26, 0.21

2.10.1 Crystal structure of NMe$_4$[FeCl$_3$(NO)] (1a) from FeCl$_2$ (1a) and FeCl$_3$ (1b)

Green crystals of **1a** and **1b** formed at 5° C within 2–3 days. **1a** is well-ordered while **1b** shows partly positional disorder of about 9% Cl on the NO position.
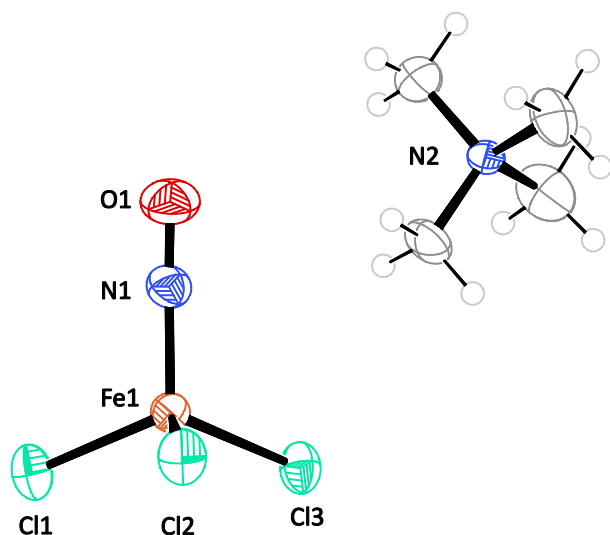
(Top, **1a**) (50% probability level at 293 K). Space group *Pca*2$_1$. Interatomic distances (Å) and angles (°) with the standard deviation of the last digit is given in parentheses: Fe1–Cl1 2.230(2), Fe1–Cl2 2.244(2), Fe1–Cl3 2.237(2), Fe1–N1 1.710(7), N1–O1 1.154(9), Fe1–N1–O1 175.2(6), Cl1–Fe1–N1 107.2(2), Cl2–Fe1–N1 109.8(2), Cl3–Fe1–N1 109.2(2), Cl1–Fe1–Cl2 111.10(8), Cl2–Fe1–Cl3 108.90(8), Cl3–Fe1–Cl1 110.59(8).
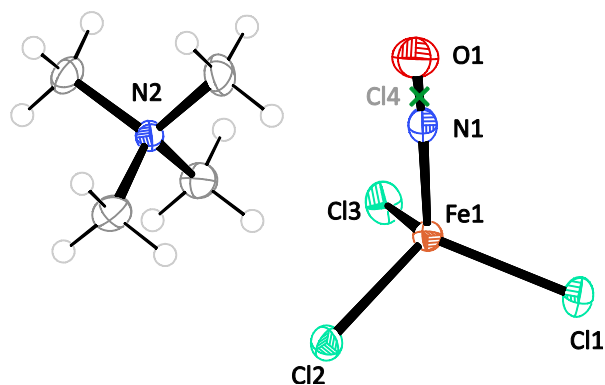
(Bottom, **1b**) (50% probability level at 173 K). Space group *Pca*2$_1$. Interatomic distances (Å) and angles (°) with the standard deviation of the last digit is given in parentheses: uncorrected: Fe1–Cl1 2.2394(6), Fe1–Cl2 2.2300(8), Fe1–Cl3 2.2490(6), Fe1–N1 1.789(2), N1–O1 1.059(3), Fe1–N1–O1 174.6(2), Cl1–Fe1–N1 109.53(7), Cl2–Fe1–N1 107.10(8), Cl3–Fe1–N1 110.15(6), Cl1–Fe1–Cl2 110.49(3), Cl2–Fe1–Cl3 111.02(3), Cl3–Fe1–Cl1 108.55(2).

corrected: Fe1–Cl1 2.2395(5), Fe1–Cl2 2.2299(7), Fe1–Cl3 2.2489(6), Fe1–Cl4 2.160(3) (9%Cl, green cross, ×), Fe1–N1 1.729(7), N1–O1 1.1452(12), Fe1–N1–O1 174.1(3), Cl1–Fe1–N1 109.38(12), Cl2–Fe1–N1 107.40(13), Cl3–Fe1–N1 109.97(12), Cl1–Fe1–Cl2 110.50(3), Cl2–Fe1–Cl3 111.03(3), Cl3–Fe1–Cl1 108.55(2).

Figure 2.10: ORTEP plot of ion pair in crystals of NMe$_4$[FeCl$_3$(NO)] (**1a**) and (**1b**).

2.10.2 Crystal structure of NEt₄[FeCl₃(NO)] from FeCl₂ (2a) and FeCl₃ (2b)

(Top, **2a**) (50% probability level at 103 K). Space group *Pca*2₁. Interatomic distances (Å) and angles (°) with the standard deviation of the last digit is given in parentheses: Fe1–Cl 1 2.2431(5), Fe1–Cl2 2.2389(6), Fe1–Cl3 2.2318(5), Fe1-N1 1.7677(16), N1–O1 1.103(2), Fe1–N1–O1 172.62(16), Cl1–Fe1–N1 110.20(6), Cl1–Fe1–Cl2 108.83(2), Cl1–Fe1–Cl3 112.08(2), Cl3–Fe1–N1 105.95(6), Cl2–Fe1–Cl3 109.52(2), Cl2–Fe1–N1 110.25(6).

(Bottom, **2b**) (50% probability level at 173 K). Space group *Pca*2₁. Interatomic distances (Å) and angles (°) with the standard deviation of the last digit is given in parentheses: uncorrected: Fe1–Cl1 2.2369(9), Fe1–Cl2 2.2320(9), Fe1–Cl3 2.2266(9), Fe1–N1 1.813(3), N1–O1 0.995(4), Fe1–N1–O1 173.3(3), Cl1–Fe1–N1 110.26(10), Cl1–Fe1–Cl2 108.79(4), Cl1–Fe1–Cl3 112.10(4), Cl3–Fe1–N1 106.16(9), Cl2–Fe1–Cl3109.58(3), Cl2–Fe1–N1 109.92(9).

Corrected: Fe1–Cl1 2.2365(9), Fe1–Cl2 2.2321(9), Fe1–Cl3 2.2263(9), Fe1–Cl4 2.227(13) (14%Cl, green cross, ×), Fe1–N1 1.728(7), N1–O1 1.149(15), Fe1–N1–O1 173.1(3), Cl1–Fe1–N1 109.63(13), Cl1–Fe1–Cl2 108.78(4), Cl1–Fe1–Cl3 112.11(3), Cl3–Fe1–N1 106.39(13), Cl2–Fe1–Cl3 109.57(4), Cl2–Fe1–N1 110.34(14).

Figure 2.11: ORTEP plot of ion pairs in crystals of NEt₄[FeCl₃(NO)] (**2a**) and (**2b**).

The synthesis of the [FeCl₃(NO)]⁻ anion with NEt₄⁺ cation was complicated. The reaction with FeCl₃ as the starting salt succeeded and the product crystallized faster (within two weeks) than the compound from FeCl₂ (within a year). This was, supposedly, due to the occurrence of [FeCl₄]⁻ anions as intermediate species, forming a yellow precipitate in a mixture solution before NO treatment. The same experiment was repeated with about the ten-fold amount of solvent. No precipitate formed in this case. The reaction with gaseous NO succeeded, but the crystallization time was longer and resulted in a much lower yield.

Molecular structures of NEt₄[FeCl₃(NO)] (**2a** and **2b**) are shown in Figure 2.11. As one can see, the Fe–Cl distances in **2b** were fairly similar to those in **2a**, but the Fe1–N1 bond (1.813(3) Å) was longer and the N1–O1 bond (0.995(4) Å) was shorter. If one considers only their IR, UV/Vis spectra as well

as X-ray data with low rest electron density (see Table 2.4), it seems that the same compound was obtained. However, the corrected structure refinement showed that a small amount of $[FeCl_4]^{2-}$ co-crystallized with the product so that a chlorido ligand between the N1 and O1 bond (of about 14%) caused a longer Fe1–N1 distance and, vice versa, a shorter N1–O1 distance. The disorder of the chloride atom is omitted in Figure 2.11 for the sake of clarity. In conclusion, it was, again, possible to synthesize {FeNO}[7] compounds from $FeCl_3$.

2.10.3 Crystal structure of NBnMe₃[FeCl₃(NO)] (3)

Green crystals of compound **3** were obtained by storing the reaction solution at 5 °C for some weeks while diffusing diethyl ether as antisolvent. The structure solution succeeded in triclinic space group $P\bar{1}$ with two formula units in the primitive cell, with an Fe1–N1–O1 angle near to linearity at 173.5(4)°. The Fe–Cl bond length had an average distance of 2.230 Å. The ions pair in crystals of **3** is depicted in Figure 2.12.
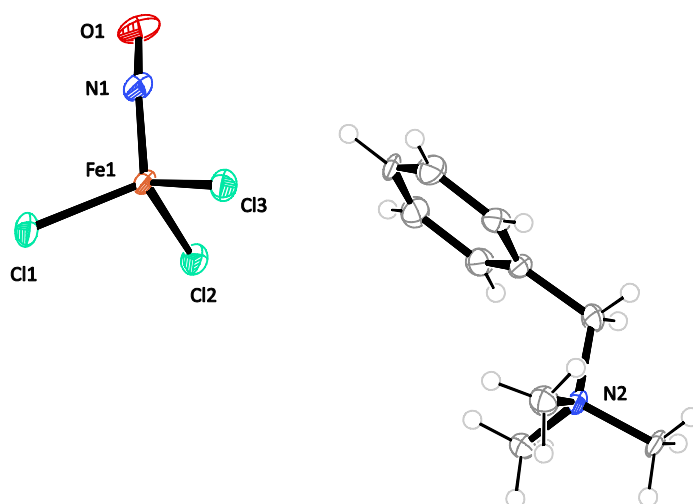
Figure 2.12: ORTEP plot of the ion pair in crystals of NBnMe₃[FeCl₃(NO)] (**3**) (50% probability level at 100 K). Space group $P\bar{1}$. Interatomic distances (Å) and angles (°) with the standard deviation of the last digit is given in parentheses: Fe1–Cl1 2.2368(15), Fe1–Cl2 2.2244(18), Fe1–Cl3 2.2276(19), Fe1–N1 1.732(4), N1–O1 1.134(5), Fe1–N1–O1 173.5(4), Cl1–Fe1–N1 112.13(12), Cl2–Fe1–N1 107.41(16), Cl3–Fe1–N1 111.35(17), Cl1–Fe1–Cl2 108.29(6), Cl2–Fe1–Cl3 109.07(6), Cl3–Fe1–Cl1 108.50(6).

2.10.4 Crystal structure of Mephaz[FeCl₃(NO)] (4)

Green crystals of **4** were obtained directly from the reaction solution by storing it at 5 °C for two weeks. They formed above the mother liquor. The structure solution succeeded in the monoclinic space group $P2_1/n$ with four formula units in the primitive cell. The structure of **4** is depicted in Figure 2.13 and examples of non-classical hydrogen bonds between hydrogen-bond donors to halogenido acceptors are illustrated in Figure 2.14.
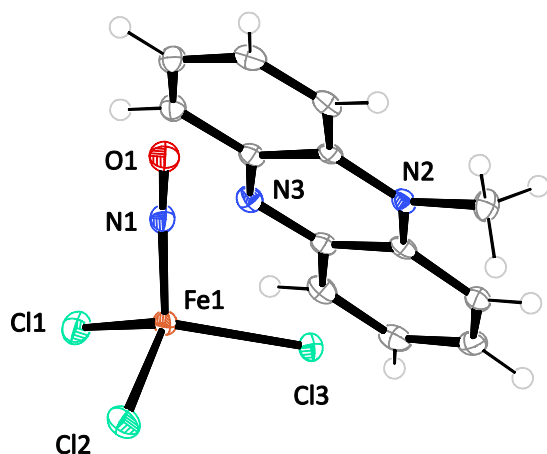
Figure 2.13: ORTEP plot of the ion pair in crystals of Mephaz[FeCl₃(NO)] (**4**) (50% probability level at 100 K). Space group $P2_1/n$. Interatomic distances (Å) and angles (°) with the standard deviation of the last digit is given in parentheses: Fe1–Cl1 2.2357(6), Fe1–Cl2 2.2290(7), Fe1–Cl3 2.2595(7), Fe1–N1 1.734(2), N1–O1 1.152(3), Fe1–N1–O1 170.12(17), Cl1–Fe1–Cl2 112.29(3), Cl1–Fe1–Cl3 111.16(2), Cl1–Fe1–N1 112.77(6), Cl2–Fe1–Cl3 109.06(2), Cl2–Fe1–N1 105.15(6), Cl3–Fe1–N1 106.05(6).
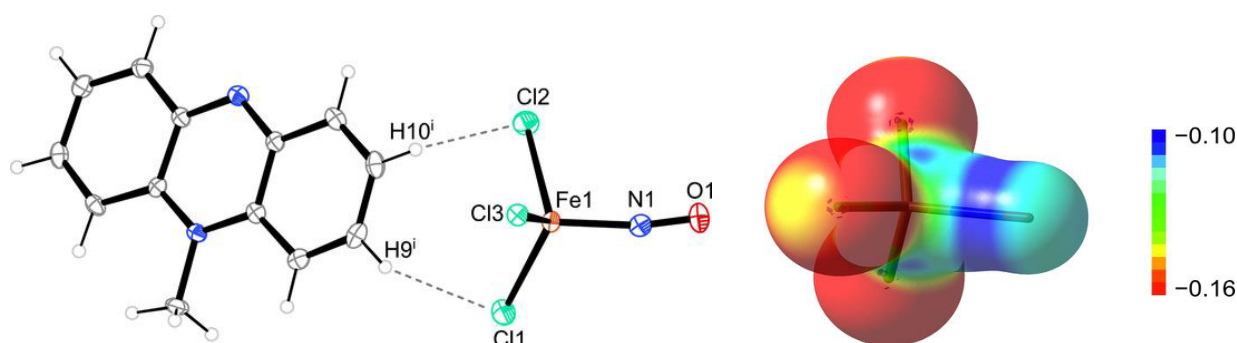
Figure 2.14: ORTEP plot of Mephaz[FeCl₃(NO)] (**4**) (50% probability level) depicting the shortest interatomic contact H10[i]···Cl2 with 2.782 Å and the second contact H9[i]···Cl1 with 2.969 Å. (ORTEP, 50 % ellipsoid probability). (Right) Note hydrogen bonding towards the region of highest charge lateral to the Fe−Cl bonds at the chlorine acceptor. The depicted hydrogen bond motif is repeated with Cl3 and Cl1 as a second acceptor couple. Symmetry code: [i] 5/2−*x*, *y*−1/2, 1/2−*z*. Interatomic distances in the anion (in Å): mean Cl–Fe–N 108.0, mean Cl–Fe–Cl 110.9. Right: The electrostatic potential (ESP) of the [FeCl₃(NO)]¯ ion (Cl left and backwards, NO right; atomic units), mapped on the 0.001 a.u. (ca. 0.0067 e Å⁻³) surface of the total electron density. The values were taken from a BP86/def2-TZVP calculation on the free [FeCl₃(NO)]¯ ion.[33]

2.10.5 Crystal structure of [Co(cp)$_2$][FeCl$_3$(NO)] (5) from FeCl$_3$

Compound **5** was prepared from FeCl$_3$ *via* the *in situ* reduction of FeCl$_3$ with cobaltocene and a subsequent reaction with gaseous NO. Green crystals crystallized at 5 °C above the mother liquor. Compound **5** crystallized in the orthorhombic space group *Pca*2$_1$ with two [FeCl$_3$(NO)]$^-$ ions and two [Co(cp)$_2$]$^+$ counter ions in the asymmetric unit. The complex anions have similar, almost linear Fe1–N1–O1 angles of about 176°. The ion pairs in crystals of **5** are depicted in Figure 2.15.
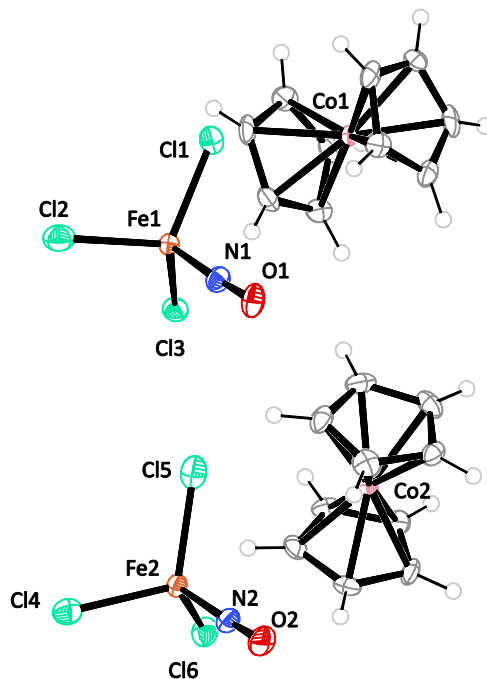
Figure 2.15: ORTEP plot of the ion pairs in crystals of [Co(cp)$_2$][FeCl$_3$(NO)] (**5**) (50% probability level at 173 K). Space group *Pca*2$_1$. Interatomic distances (Å) and angles (°) with the standard deviation of the last digit is given in parentheses: Fe1–Cl1 2.245(2), Fe1–Cl2 2.2541(19), Fe1–Cl3 2.241(2), Fe1–N1 1.715(6), N1–O1 1.161(9), Fe2–Cl4 2.2466(19), Fe2–Cl5 2.236(3), Fe2–Cl6 2.244(2), Fe2–N2 1.710(6), N2–O2 1.157(9), Fe1–N1–O1 176.3(6), Fe2–N2–O2 176.8(5), Cl2–Fe1–N1 109.0(2), Cl3–Fe1–N1 109.5(2), Cl2–Fe1–Cl3 109.51(9), Cl1–Fe1–Cl2 108.14(9), Cl1–Fe1–Cl3 111.66(9), Cl1–Fe1–N1 109.1(2), Cl4–Fe2–Cl6 109.77(9), Cl5–Fe2–Cl6 110.86(8), Cl4–Fe2–Cl5 107.40(9), Cl6–Fe2–N2 107.3(2), Cl5–Fe2–N2 112.0(2), Cl4–Fe2–N2 109.6(2).

In the same synthetic manner of **5**, [Fe(cp)$_2$][FeCl$_3$(NO)] was also successfully prepared but the crystallization was hampered. Its Fe–NO stretching band was found at 1771 cm^{-1}.

2.10.6 Crystal structure of PPh$_4$[FeCl$_3$(NO)] (6)

The green compound **6** was obtained immediately after the addition of gaseous NO to a methanolic solution of FeCl$_2$·4H$_2$O and PPh$_4$Cl salts. The structure solution succeeded in the tetragonal space group $P\overline{4}$. The primitive cell contained four formula units. The projection of the tetragonal space group $P\overline{4}$ along [001] as depicted in Figure 2.17 shows the cation and anion arrays. The PPh$_4^+$ ions occupy the special position with S_4 symmetry. The [FeCl$_3$(NO)]$^-$ anions lay between the PPh$_4^+$ ions.
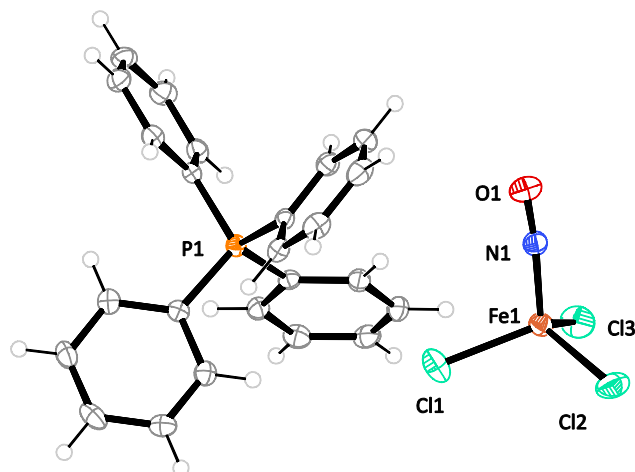
The NO ligands are well ordered. The asymmetric unit of **6** is depicted in Figure 2.16.

Figure 2.16. ORTEP plot of the ion pair in crystals of PPh$_4$[FeCl$_3$(NO)] (**6**) (50% probability level at 100 K). Space group $P\overline{4}$. Interatomic distances (Å) and angles (°) with the standard deviation of the last digit is given in parentheses: Fe1–Cl1 2.2302(12), Fe1–Cl2 2.2349(12), Fe1–Cl3 2.2336(12), Fe1–N1 1.724(3), N1–O1 1.158(4), Fe1–N1–O1 174.3(3), Cl1–Fe1–N1 105.22(10), Cl2–Fe1–N1 110.71(10), Cl3–Fe1–N1 109.39(10), Cl1–Fe1–Cl2 111.54(5), Cl2–Fe1–Cl3 109.35(5), Cl3–Fe1–Cl1 110.57(4).
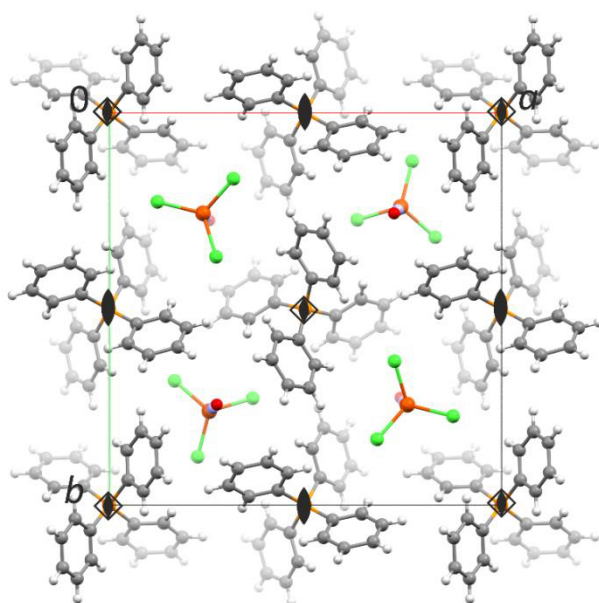
Figure 2.17: ORTEP plot of PPh$_4$[FeCl$_3$(NO)] (**6**) (50% probability level). Projection along [001] direction with PPh$_4^+$ ions occupy special positions with S_4 symmetry. Atoms: carbon (gray), hydrogen (white), chlorine (green), iron (orange), nitrogen (blue), oxygen (red).

2.10.7 Crystal structure of AsPh$_4$[FeCl$_3$(NO)] (7)

The green compound **7** was synthesized and analyzed in 1973 by Steimann *et al.*,[36] later by Wilfer[37]

using a modification of Kohlschütter's method[37] and recently was observed as cocrystallized in

Akutsu's AsPh$_4$[FeCl$_2$(NO)$_2$] compound.[38] As already mentioned in Chapter 1, the analyses of both

groups (Beck and Akutsu) were impaired by the NO/Cl disorder. In this thesis, compound **7** was

easily obtained by the reaction of FeCl$_2$·4H$_2$O and AsPh$_4$Cl. Green crystals crystallized immediately

upon exposure to NO (70% yield). The structure solution succeeded in the monoclinic space group

*P*2$_1$/*n* with four formula units in the primitive cell which supported Wilfer's result. By using the

synthesis developed in this thesis, the disorder problem was successfully overcome. The asymmetric

unit **7** is depicted in Figure 2.18.
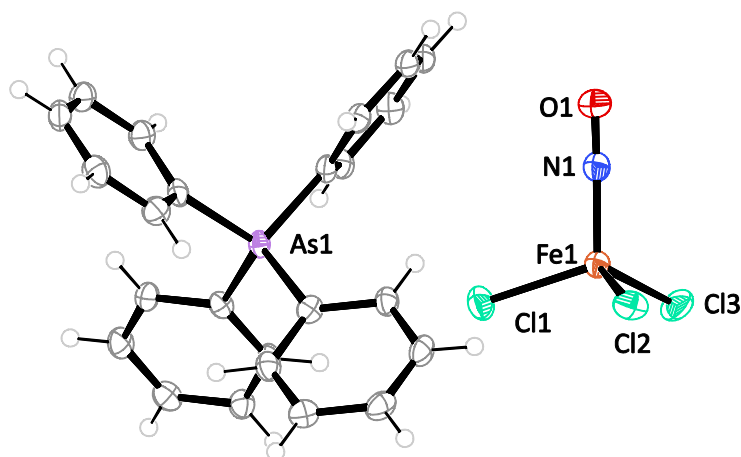
Figure 2.18: ORTEP plot of the ion pair in crystals of AsPh$_4$[FeCl$_3$(NO)] (**7**) (50% probability level at 100 K). Space group *P*2$_1$/*n*. Interatomic distances (Å) and angles (°) with the standard deviation of the last digit is given in parentheses: Fe1–Cl1 2.2388(8), Fe1–Cl2 2.2529(8), Fe1–Cl3 2.2454(9), Fe1–N1 1.734(3), N1–O1 1.150(3), Fe1–N1–O1 171.0(2), Cl1–Fe1–Cl2 110.69(3), Cl1–Fe1–Cl3 108.54(3), Cl2–Fe1–Cl3 112.12(3), Cl1–Fe1–N1 108.46(8), Cl2–Fe1–N1 104.57(9), Cl3–Fe1–N1 112.39(8).

2.10.8 Crystal structure of PPN[FeCl₃(NO)] (8)

Similar to **6** and **7**, the green compound **8** was obtained immediately after the reaction of gaseous NO with a methanolic solution of $FeCl_2 \cdot 4H_2O$ and PPNCl salt. The green compound **8** crystallized in the monoclinic space group $C2/c$ with eight formula units in the centered cell. This result was identical to Wolf's result.[41] The asymmetric unit of **8** is depicted in Figure 2.19.
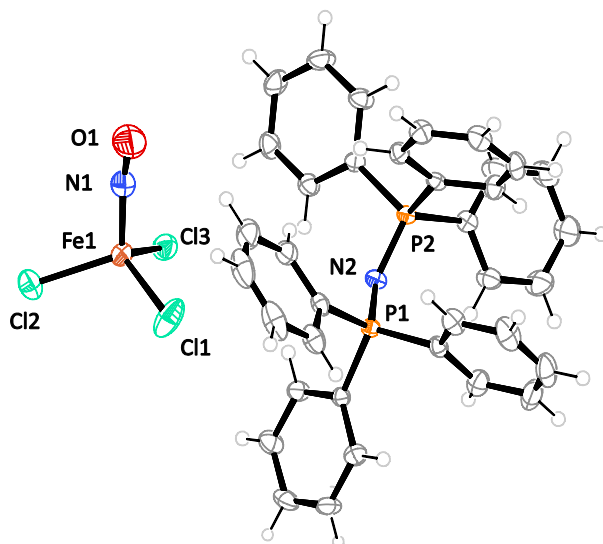
Figure 2.19: ORTEP plot of the ion pair in crystals of PPN[FeCl₃(NO)] (**8**) (50% probability level at 293 K). Space group $C2/c$. Interatomic distances (Å) and angles (°) with the standard deviation of the last digit is given in parentheses: Fe1–Cl1 2.2145(9), Fe1–Cl2 2.2337(8), Fe1–Cl3 2.2350(9), Fe1–N1 1.7407(19), N1–O1 1.133(3), Fe1–N1–O1 170.97(19), Cl1–Fe1–N1 105.20(7), Cl2–Fe1–N1 109.88(7), Cl3–Fe1–N1 110.25(8), Cl1–Fe1–Cl2 111.26(4), Cl2–Fe1–Cl3 108.87(3), Cl3–Fe1–Cl1 111.35(3).

2.10.9 Crystal structure of [Fe(bpy)₃][FeCl₃(NO)]₂ (9)

Compound **9** was prepared from the reaction of $FeCl_2 \cdot 4H_2O$, HCl (0.2 M) and bipyridine (bpy). It was first intended to prepare Hbpy[FeCl₃(NO)] but instead the dark red salt of [Fe(bpy)₃][FeCl₃(NO)]₂ was obtained. The structure solution succeeded in the monoclinic space group $P2_1/c$ and contained four formula units. There were four anions and two voluminous $[Fe(bpy)]^{2+}$ counterions. One of three of the [FeCl₃(NO)]⁻ anions had a Cl/NO disorder (30%). The other three [FeCl₃(NO)]⁻ were also involved with minor NO/Cl disorder. This disorder was caused by the intermediate species [FeCl₄]⁻ which was not completely substituted by the NO ligand to form the product. The IR and UV/Vis analyses (see Table 2.4 and Table 2.5) reflected the normal [FeCl₃(NO)]⁻ complex but, by considering the X-ray data, especially the Fe1–N1 bond lengths are, in fact, longer than those in the other [FeCl₃(NO)]⁻ compounds: Fe1–N1 1.835(6) Å, Fe2–N2 1.717(19) Å, Fe3–N3 1.760(6) Å, Fe4–N4 1.801(5) Å and *vice versa* N–O bond lengths are a little shorter: N1–O1 0.928(8) Å, N2–O2 1.150(3) Å, N3–O3 1.102(8) Å,

N4–O4 1.004(8) Å. An effort to place a chlorine atom between N1–O1 and N4–O4 failed. The asymmetric unit of **9** is depicted in Figure 2.20.
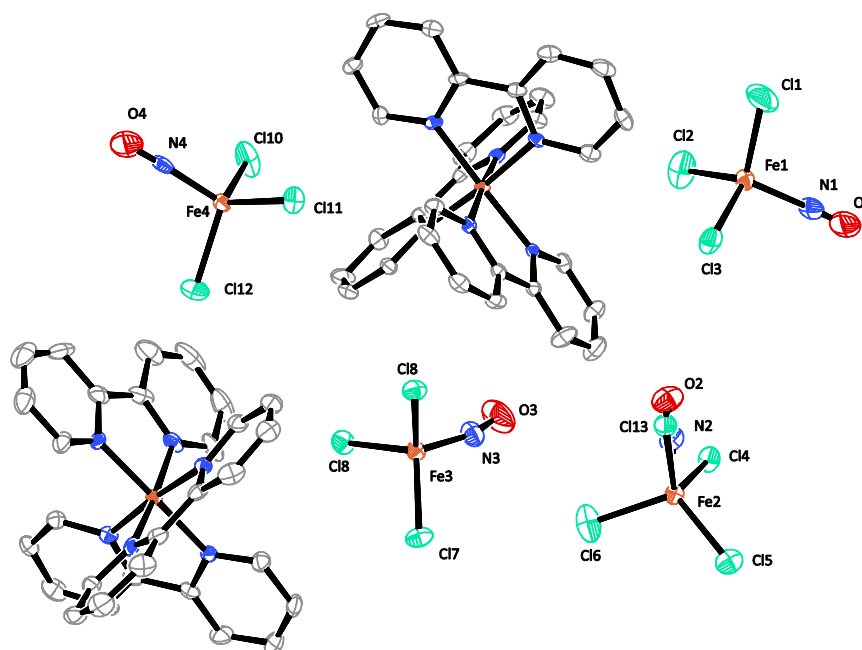
Figure 2.20: ORTEP plot of the asymmetric unit of [Fe(bpy)$_3$][FeCl$_3$(NO)]$_2$ (**9**) (50% probability level at 100 K). Space group *P*2$_1$/*c*. Hydrogen atoms were omitted for the sake of clarity. Interatomic distances (Å) and angles (°) with the standard deviation of the last digit is given in parentheses: Fe1–N1 1.835(6), Fe2–N2 1.717(19), Fe3–N3 1.760(6), Fe4–N4 1.801(5), N1–O1 0.928(8), N2–O2 1.150(3), N3–O3 1.102(8), N4–O4 1.004(8), Fe1–N1–O1 175.7(6), Fe2–N2–O2 173.3(9), Fe3–N3–O3 163.4(6), Fe4–N4–O4 173.4(6), Fe2–Cl5 2.2178(17), Fe2–Cl6 2.2143(18), Fe2–Cl13 2.226(11) (between N2–O2), Fe2–Cl4 2.2274(15), Fe1–Cl3 2.2426(15), Fe1–Cl1 2.2064(19), Fe1–Cl2 2.2228(19), Fe3–Cl8 2.2265(17), Fe3–Cl7 2.2404(14), Fe3–Cl9 2.2303(15), Fe4–Cl12 2.2098(18), Fe4–Cl10 2.2199(16), Fe4–Cl11 2.2281(17), Cl5–Fe2–Cl13 112.0(3), Cl5–Fe2–N2 111.7(3), Cl5–Fe2–Cl6 111.97(7), Cl6–Fe2–N2 108.4(4), Cl4–Fe2–Cl5 110.05(6), Cl6–Fe2–Cl13 104.8(3), Cl4–Fe2–Cl13 109.0(3), Cl4–Fe2–N2 105.7(3), Cl4–Fe2–Cl6 108.86(7), Cl3–Fe1–N1 106.87(17), Cl1–Fe1–Cl2 109.56(8), Cl2–Fe1–N1 113.27(17), Cl1–Fe1–Cl3 111.78(8), Cl2–Fe1–Cl3 107.50(7), Cl1–Fe1–N1 107.90(17), Cl8–Fe3–N3 102.57(19), Cl9–Fe3–N3 108.31(15), Cl7–Fe3–N3 114.46(17), Cl8–Fe3–Cl9 112.86(6), Cl7–Fe3–Cl9 108.35(5), Cl7–Fe3–Cl8 110.30(6), Cl10–Fe4–Cl12 114.80(7), Cl11–Fe4–Cl12 109.45(6), Cl10–Fe4–N4 104.05(18), Cl12–Fe4–N4 106.48(17), Cl11–Fe4–N4 113.63(17), Cl10–Fe4–Cl11 108.48(6).

2.10.10 Crystal structure of (C$_{25}$N$_3$H$_{30}$)[FeCl$_3$(NO)] (10)

The gold-green crystals of **10** were obtained after storing the NO mixture at room temperature for two weeks. The structure solution succeeded in the monoclinic space group *Pca*2$_1$ and contained four formula units in the primitive cell, consisting of two complex anions and two C$_{25}$N$_3$H$_{30}$$^+$ counterions. The cations C$_{25}$N$_3$H$_{30}$$^+$ had a propeller structure which could build intermolecular interactions between H and Cl atoms (Figure 2.22). The [FeCl$_3$(NO)]$^-$ anions had a NO/Cl disorder (18% Cl), which caused shorter Fe–N bond lengths and the Fe–N–O angles were smaller than in other

molecular structures of [FeCl$_3$(NO)]$^-$ compounds. An effort to place a chlorine atom between N1–O1 failed.
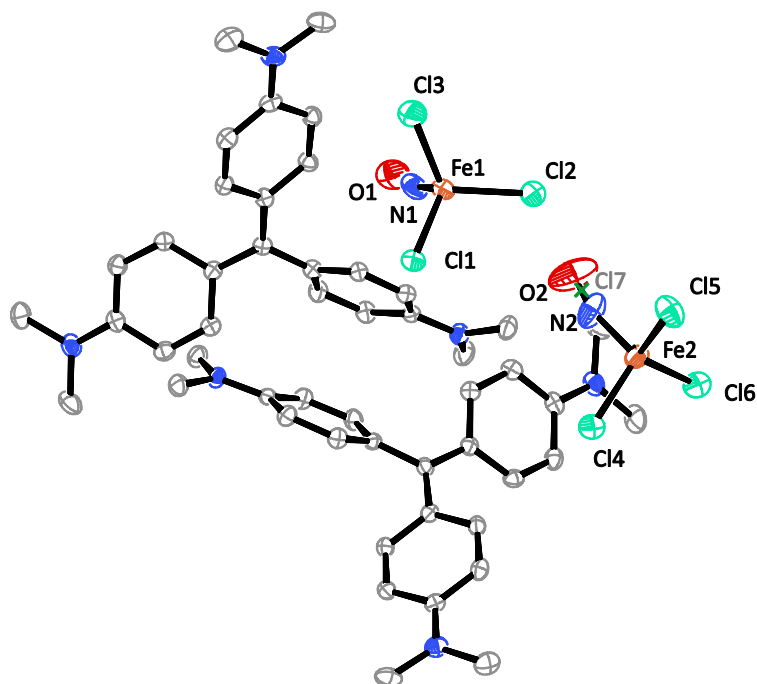
Figure 2.21: ORTEP plot of the ion pair in crystals of (C$_{25}$N$_3$H$_{30}$)[FeCl$_3$(NO)] (**10**) (50% probability level at 153 K). Space group *Pca*2$_1$. Hydrogen atoms are omitted for clarity. Interatomic distances (Å) and angles (°) with the standard deviation of the last digit is given in parentheses: Fe1–Cl1 2.2360(14), Fe1–Cl2 2.2541(18), Fe1–Cl3 2.2138(18), Fe1–N1 1.813(7), N1–O1 0.964(10), Fe1–N1–O1 160.2(8), Cl1–Fe1–Cl 108.50(6), Cl1–Fe1–Cl3 111.01(6), Cl3–Fe1–N1 101.5(2), Cl2–Fe1–Cl3 114.07(7), Cl2–Fe1–N1 110.38(18), Cl1–Fe1–N1 111.32(18), Fe2–Cl4 2.2877(19), Fe2–Cl5 2.2018(19), Fe2–Cl6 2.2484(17), Fe2–Cl7 2.335(12) (18%Cl disordered with NO, green cross ×), Fe2–N2 1.756(11), N2–O2 1.071(16), Fe2–N2–O2 163.1(12), Cl4–Fe2–Cl6 111.78(7), Cl4–Fe2–Cl7 129.0(4), Cl4–Fe2–N2 110.5(3), Cl5–Fe2–Cl6 115.83(7), Cl5–Fe2–Cl7 93.3(3), Cl5–Fe2–N2 102.7(3) , Cl6–Fe2–Cl7 101.8(3), Cl6–Fe2–N2 111.0(2), Cl4–Fe2–Cl5 104.52(7), Cl1–Fe1–Cl2 108.50(6).

Figure 2.22 depicts a MERCURY plot along [010] showing the zigzag channel of anions which are located between cations; one [FeCl$_3$(NO)]$^-$ ion contacts three adjacent cations. The propeller-like geometry of the crystal violet ion supports the intermolecular interaction. Hydrogen bonds and their distances are shown in Table 2.7.
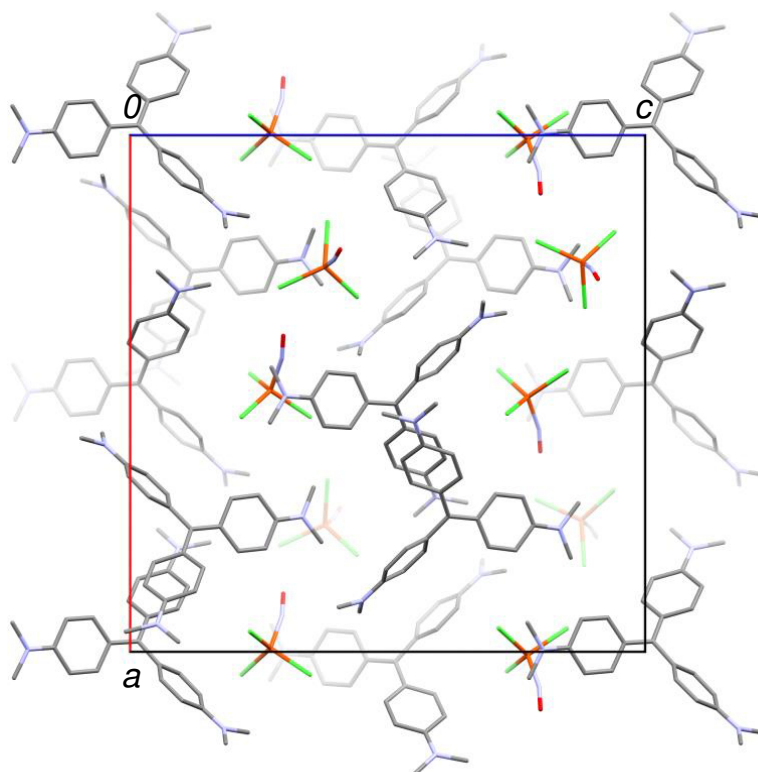
Figure 2.22: Mercury plot of the molecular structure of compound **10** (50% probability level) with projection along [010]. The anions locate between the cations like a zigzag channel, building intermolecular interactions between donors C–H⋯Cl acceptors.

Table 2.7: Hydrogen bonds in crystals of **10**.

Donor–Hydrogen⋯Acceptor	d(D–H)/Å	d(H⋯A)/Å	d(D⋯A) /Å	α(D–H⋯A)/°	Symmetry code
C19–H19⋯Cl6	0.950	2.848	3.611(4)	138.06	[i] −x+1, −y+1, z+1/2
C23–H23C⋯Cl6	0.980	2.906	3.668(6)	135.26	
C25–H25B⋯Cl2	0.980	2.812	3.744(5)	159.01	[ii] −x+1/2, y, z+1/2
C24–H24B⋯Cl7[i]	0.880	2.723	3.655(13)	159.01	
C32–H32B⋯Cl6	0.950	2.915	3.657(3)	135.81	[i] −x+1, −y+1, z+1/2
C38–H38⋯Cl1	0.950	2.893	3.621(4)	134.34	x, y+1, z
C47–H47C⋯Cl4	0.980	2.721	3.678(5)	165.23	
C51–H51C⋯Cl7[i]	0.980	2.988	3.962(14)	173.16	[ii] −x+1/2, y, z+1/2
C51–H51C⋯O2	0.980	2.422	3.381(17)	165.95	[ii] −x+1/2, y, z+1/2
C50–H50A⋯Cl4	0.980	2.906	3.397(6)	112.04	[i] −x+1, −y+1, z+1/2

2.10.11 Crystal structure of [FeBr$_3$(NO)]$^-$ compounds (11–13)

Mononitrosyl–A[FeBr$_3$(NO)] compounds had been previously prepared in our working group. Wilfer[37] synthesized a PPh$_4$[FeBr$_3$(NO)] salt by slowly adding gaseous NO to iron salt in HBr solution. X-ray analysis from these batches suffered from Br/NO disorder and a high residual electron density of $\approx$2e/ Å^3.[37] Böttcher also observed Br/NO disorder in such crystal structures from different preparations.[45] These included adding Br$_2$ to a solution of a salt of the [Fe(CO)$_3$(NO)]$^-$ ion. As described by Wolf[41], the reaction of Fe(OTf)$_2$ as the starting salt with one equivalent of HBr (40% wt. in H$_2$O) and PPNBr each, led to the formation of the PPN[FeBr$_3$(NO)] (**13b**)[41] after exposure to NO. The structure analysis by Wolf[41] succeeded in the monoclinic space group *C*2/*c* (**13b**) and resulted in a structure with minor disorder. In fact, a shorter N–O bond length of 1.085(4) Å and a longer Fe–N bond length of 1.760(3) Å indicated of Br/NO disorder to some extent. A corrected structure refinement was applied in this thesis and 5%Br was found at the NO position in **13b** (Table 2.8). The same synthetic route as Wolf was repeated and the same product in terms of net formula was obtained and assigned as **13a** (this work). The structure determination on crystals of **13a** succeeded in the triclinic space group *P*$\overline{1}$ resulting in a well-ordered structure of this new polymorph with reasonable Fe–N and N–O distances (see Table 2.8 for a comparison).

Further A[FeBr$_3$(NO)] salts (A: PPh$_4^+$ and AsPh$_4^+$) were prepared by preferably using iron(II) triflate over iron(II) bromide, due to the low solubility of the latter in methanol. Crystallization proceeded at room temperature, immediately upon the contact of gaseous NO with the solution of the iron salt and the bromide. The introduction of sterically demanding cations accelerated the formation of the desired products, allowing it to obtain them in good yields of about 70%. Besides this result, the use of Fe(OTf)$_2$ as the starting salt improved the quality of crystals by the suppression of co-crystallization of [FeBr$_4$]$^-$ ions, thus enabling the synthesis of well-ordered A[FeBr$_3$(NO)] compounds. The selected bond lengths and bond angles as well as IR data are shown in Table 2.8. The ion pairs in crystals of **11**−**13** are depicted in Figure 2.23–Figure 2.26.

In the compounds **11**−**13**, all [FeBr$_3$(NO)]$^-$ anions have *T*-4 configuration. The Fe–N–O moieties are nearly linear. The mean bond lengths are: 2.377 Å for Fe–Br, 1.728 Å for Fe–N and 1.14 Å for N–O. The N–O stretching vibration is found around 1800 cm^{-1}, similar to those of A[FeCl$_3$(NO)] compounds.

Table 2.8: Spectroscopic and structural parameters for A[FeBr$_3$(NO)] compounds; A: PPh$_4^+$, AsPh$_4^+$ and PPN$^+$.

Starting salt	Compound	Cation	Space group	dFe–Br/Å	dFe–N/Å	dN–O/Å	Fe–N–O/°	$\tilde{v}$(NO)$_{IR}$/cm^{-1}	Min, Max. Resd. Dens. [e/Å^3]
Fe(OTf)$_2$	**11**	PPh$_4^+$	$P\bar{4}$	2.3772	1.724(12)	1.158(15)	169.9(10)	1795	−1.17, 1.82
Fe(OTf)$_2$	**12**	AsPh$_4^+$	$P\bar{4}$	2.3771	1.732(5)	1.145(7)	173.5(5)	1794	−0.60, 0.44
FeBr$_2$	**13a**	PPN$^+$	$P\bar{1}$	2.3752	1.729(3)	1.150(4)	169.5(3)	1800	−0.79, 0.96
FeBr$_2$	**13b**[41] uncorrected	PPN$^+$	$C2/c$	2.362	1.760(3)	1.085(4)	170.5(3)	1772	−1.04, 0.90
	corrected	PPN$^+$	$C2/c$	2.362	1.725(5)	1.168(7)	171.2(5)	1772	−1.02, 0.84

Crystal structure of PPh4[FeBr3(NO)] (11) and AsPh4[FeBr3(NO)] (12)
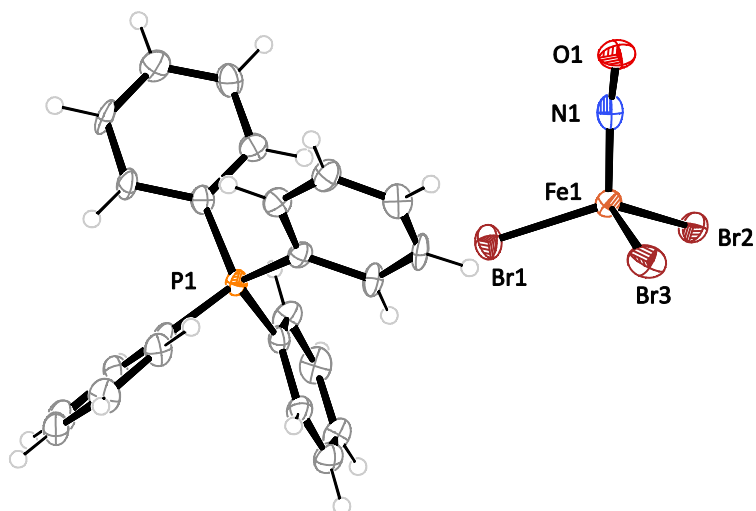
Figure 2.23: ORTEP plot of ion pair in crystals of PPh$_4$[FeBr$_3$(NO)] (**11**) (50% probability level at 100 K). Space group $P\bar{4}$. Interatomic distances (Å) and angles (°) with the standard deviation of the last digit is given in parentheses: Fe1–Br1 2.392(2), Fe1–Br2 2.373(2), Fe1–Br3 2.365(2), Fe1–N1 1.724(12), N1–O1 1.158(15), Fe1–N1–O1 169.9(10), Br2–Fe1–N1 110.7(4), Br3–Fe1–N1 102.7(4), Br1–Fe1–Br2 110.74(8), Br1–Fe1–Br3 110.93(8), Br1–Fe1–N1 111.6(4), Br2–Fe1–Br3 110.00(8).
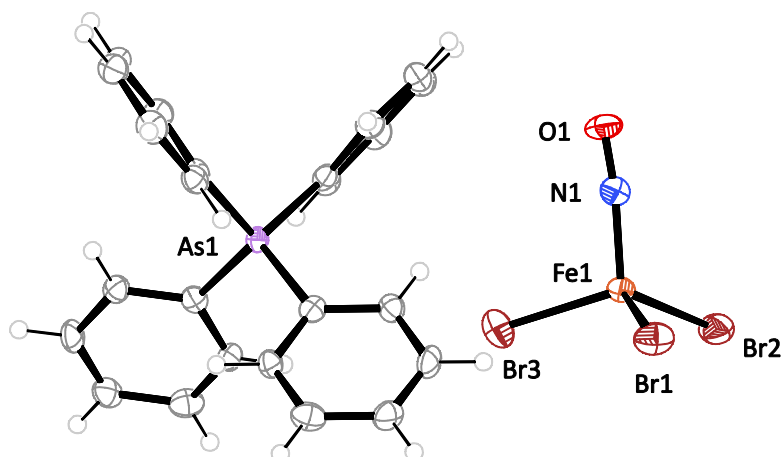
Figure 2.24: ORTEP plot of ion pair in crystals of AsPh$_4$[FeBr$_3$(NO)] (**12**) (50% probability level at 100 K). Space group $P\bar{4}$. Interatomic distances (Å) and angles (°) with the standard deviation of the last digit is given in parentheses: Fe1–Br1 2.3744(12), Fe1–Br2 2.3799(12), Fe1–Br3 2.3603(12), Fe1–N1 1.732(5), N1–O1 1.145(7), Fe1–N1–O1 173.5(5), Br2–Fe1–N1 111.60(19), Br3–Fe1–N1 104.34(19), Br1–Fe1–Br2 108.25(4), Br1–Fe1–Br3 111.91(4), Br1–Fe1–N1 108.99(19), Br2–Fe1–Br3 111.72(4).

Crystal structure of PPN[FeBr₃(NO)] (13a) and (13b)[41]
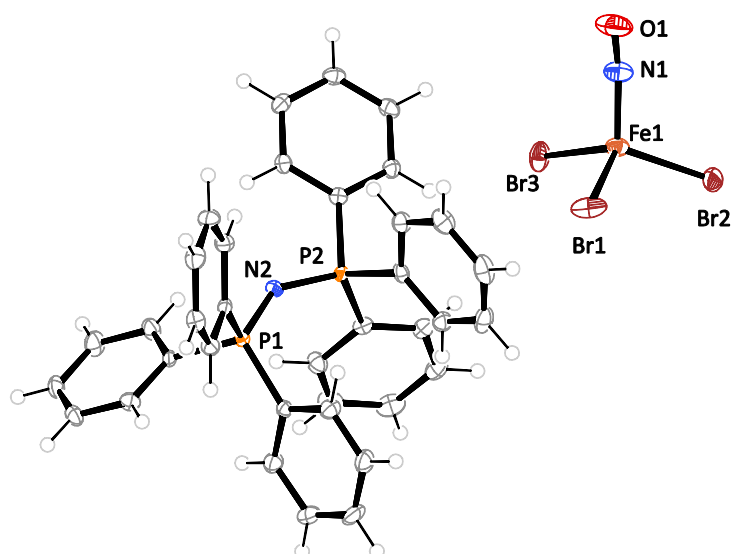
Figure 2.25: ORTEP plot of ion pair in crystals of PPN[FeBr$_3$(NO)] (**13a**) (50% probability level at 100 K). Space group $P\bar{1}$. Interatomic distances (Å) and angles (°) with the standard deviation of the last digit is given in parentheses: Fe1–Br1 2.3657(6), Fe1–Br2 2.3843(6), Fe1–Br3 2.3757(6), Fe1–N1 1.729(3), N1–O1 1.150(4), Fe1–N1–O1 169.5(3), Br3–Fe1–N1 109.35(10), Br2–Fe1–N1 113.63(11), Br1–Fe1–Br2 112.13(2), Br1–Fe1–Br3 108.83(2), Br1–Fe1–N1 104.73(11), Br2–Fe1–Br3 108.05(2).
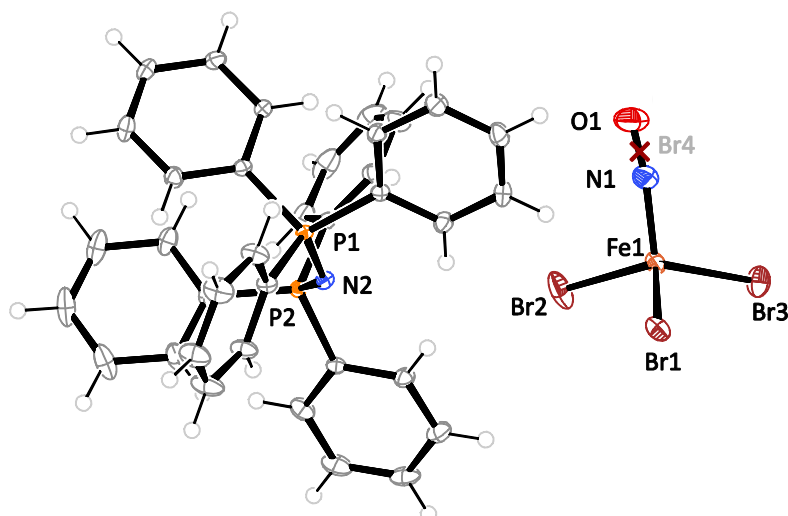
Figure 2.26: ORTEP plot of ion pair in crystals of PPN[FeBr$_3$(NO)] (**13b**)[41] (50% probability level at 173 K). Space group $C2/c$. Interatomic distances (Å) and angles (°) with the standard deviation of the last digit is given in parentheses: uncorrected: Fe1–Br1 2.3692(8), Fe1–Br2 2.3498(8), Fe1–Br3 2.3571(7), Fe1–N1 1.760(3), N1–O1 1.085(4), Fe1–N1–O1 170.5(3), Br3–Fe1–N1 110.25(10), Br2–Fe1–N1 103.79(11), Br1–Fe1–Br2 111.83(3), Br1–Fe1–Br3 107.99(2), Br1–Fe1–N1 111.64(11), Br2–Fe1–Br3 111.36(4). corrected: Fe1–Br1 2.3693(5), Fe1–Br2 2.3497(5), Fe1–Br3 2.3572(5), Fe1–Br4 2.37(2) (5%Br between N1–O1, red cross ×), Fe1–N1 1.725(5), N1–O1 1.168(7), Fe1–N1–O1 171.2(5), Br3–Fe1–N1 110.28(15), Br2–Fe1–N1 104.34(16), Br1–Fe1–Br2 111.83(2), Br1–Fe1–Br3 107.99(2), Br1–Fe1–N1 111.05(17), Br2–Fe1–Br3 111.36(2).

2.11 Crystal and molecular structures of tetra-coordinated doublet-{Fe(NO)$_2$}^{9} compounds (14–19)

2.11.1 Dichloridodinitrosylferrate (DNIC-Cl): Crystal structure of NMe$_4$[FeCl$_2$(NO)$_2$] from FeCl$_2$ (14a) and from FeCl$_3$ (14b) and PPN[FeCl$_2$(NO)$_2$] (14c)

NMe$_4$[FeCl$_2$(NO)$_2$] (**14a**−**14b**) were prepared from FeCl$_2$ or FeCl$_3$ and fluoride salt. This reaction was actually planned for the synthesis of A[FeF$_3$(NO)] complexes. Instead, DNIC-Cl was obtained. The reaction equation for the formation of **14a** and **14b** is shown in . The crystal structures of NMe$_4$[FeCl$_2$(NO)$_2$] (**14a**−**14b**) were solved in the orthorhombic space group *Pbcm* with four formula units in the primitive cell, whereby large dark red-brown crystals of **14c** were formed by the reaction of FeCl$_2$, PPN(OTf), NEt$_3$ and gaseous NO. The structure solution succeeded in the triclinic space group *P*$\bar{1}$ with two formula units in the primitive cell. PPN[FeCl$_2$(NO)$_2$] was already synthesized and obtained previously by Wolf (**14d**)[41] but from PPN[Fe(ONO)$_2$(NO)$_2$] as a precursor, requiring more synthetic steps.[41] It should be noted that whichever starting material was used, the [FeCl$_2$(NO)$_2$]$^-$ ions were free of disorder in the crystal structures (Figure 2.27–Figure 2.29). Table 2.9 shows a summary of structural parameters of **14a**–**14d**. In **14a**–**14d**, all [FeCl$_2$(NO)$_2$]$^-$ anions have a *T*-4 configuration. The Fe–N–O moieties are bent with the angle between 161°–166° with both Fe(NO) angles are in '*attracto*' position towards each other. The mean bond lengths are: 2.27 Å for Fe–Cl, 1.70 Å for Fe–N and 1.16 Å for N–O. The N–O stretching vibration bands are found around 1775$_{(sym)}$ and 1696$_{(asym)}$ cm^{-1}. DNIC-Cl is a {Fe(NO)$_2$}^{9} (*S* = 1/2) compound. The magnetism of **14c** was determined with a SQUID (PMS) measurement, with a μ_{eff} of 1.93 confirming one unpaired electron.

Table 2.9: Interatomic distances (Å) and angles (°) of NMe$_4$[FeCl$_2$(NO)$_2$] and PPN[FeCl$_2$(NO)$_2$].[33]

Starting salt		Cation	Space group	dFe–Cl/Å	dFe–N/Å	dN–O/Å	N–Fe–N/°	Fe–N–O/°	$\tilde{v}$(N–O)/cm^{-1}
FeCl$_2$	**14a**	NMe$_4$$^+$	*Pbcm*	2.2784(4) 2.2811(4)	1.7073(10)	1.1568(13)	108.09(7)	160.84(10)	1780, 1695
FeCl$_3$	**14b**	NMe$_4$$^+$	*Pbcm*	2.2797(8) 2.2751(7)	1.7088(18)	1.146(2)	108.30(11)	160.75(16)	1783, 1687
FeCl$_2$	**14c**	PPN$^+$	*P*$\bar{1}$	2.2772(5) 2.2714(5)	1.6986(17) 1.7121(16)	1.168(2) 1.147(2)	111.01(8)	165.64(15) 161.25(15)	1775, 1696
[Fe(ONO)$_2$(NO)$_2$]$^-$	**14d**[41]	PPN$^+$	*P*$\bar{1}$	2.2692(7) 2.2651(8)	1.696(2) 1.687(2)	1.161(3) 1.169(3)	110.71(10)	161.3(2) 165.7(2)	1773, 1697
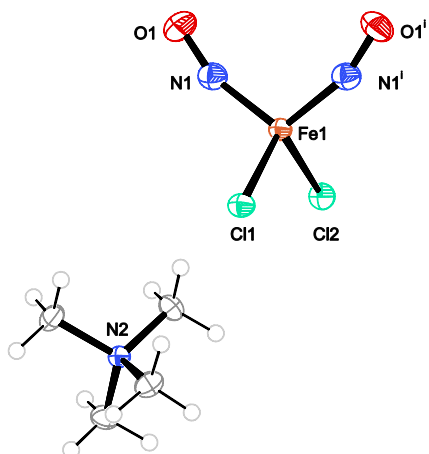
Figure 2.27: (Top) ORTEP plot of ion pair in crystals of $NMe_4[FeCl_2(NO)_2]$ (**14a**) (50% probability level at 100 K). Space group *Pbcm*. Interatomic distances (Å) and angles (°) with the standard deviation of the last digit is given in parentheses: Fe1–Cl1 2.2811(5), Fe1–Cl2 2.2784(5), Fe1–N1 1.7074(11), N1–O1 1.1567(14), Fe1–N1–O1 160.84(10, Cl1–Fe1–N1 110.14(3), Cl1–Fe1–Cl2 107.27(2), Cl2–Fe1–N1 110.61(3), N1–Fe1–N1^i 108.09(5).
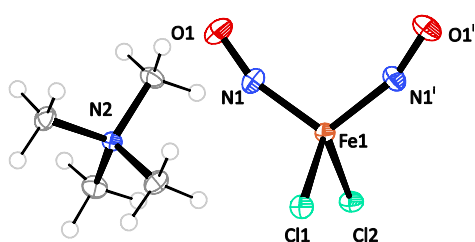
Figure 2.28: (Middle) ORTEP plot of ion pair in crystals of $NMe_4[FeCl_2(NO)_2]$ (**14b**) (50% probability level at 123 K). Space group *Pbcm*. Interatomic distances (Å) and angles (°) with the standard deviation of the last digit is given in parentheses: Fe1–Cl1 2.2797(8), Fe1–Cl2 2.2751(7), Fe1–N1 1.7088(18), N1–O1 1.146(2), Fe1–N1–O1 160.75(16), Cl1–Fe1–N1 110.07(6), Cl1–Fe1–Cl2 107.41(3), Cl2–Fe1–N1–110.50(6), N1–Fe1–N1^i 108.30(8).
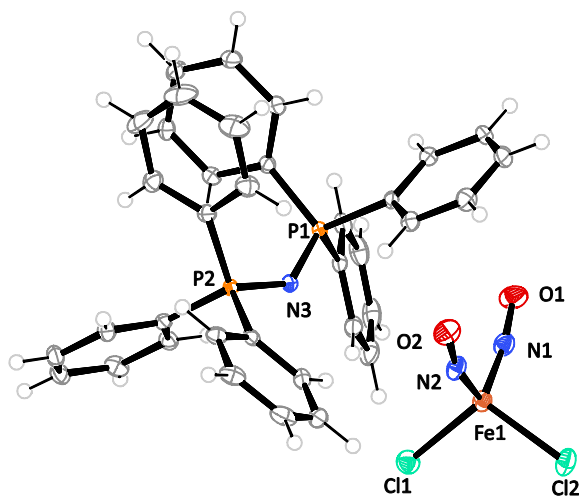
Figure 2.29: (Bottom) ORTEP plot of ion pair in crystals of $PPN[FeCl_2(NO)_2]$ (**14c**) (50% probability level at 100 K). Space group *P$\bar{1}$*. Interatomic distances (Å) and angles (°) with the standard deviation of the last digit is given in parentheses: Fe1–Cl1 2.2772(5), Fe1–Cl2 2.2714(5), Fe1–N1 1.6986(17), Fe1–N2 1.7121(16), N1–O1 1.168(2), N2–O2 1.147(2), Fe1–N1–O1 165.64(15), Fe1–N2–O2 161.25(16), Cl1–Fe1–N1 107.31(6), Cl1–Fe1–N2 113.00(6), Cl1–Fe1–Cl2 109.29(2), Cl2–Fe1–N1 111.02(6), Cl2–Fe1–N2 105.24(6), N1–Fe1–N2 111.01(8).

Non-classical hydrogen bonds were found in the molecular structure: one chlorido ligand contacted to four neighboring hydrogen atoms, resulting in a square planar network with C–H···Cl distances of about 2.878 Å and 3.3049 Å. Furthermore, two nitrosyl ligands between two neighboring $[FeCl_2(NO)_2]^-$ anions lay parallel apart from each other at a distance of about 3.061 Å. This kind of network was found only in **14a** and **14b**.
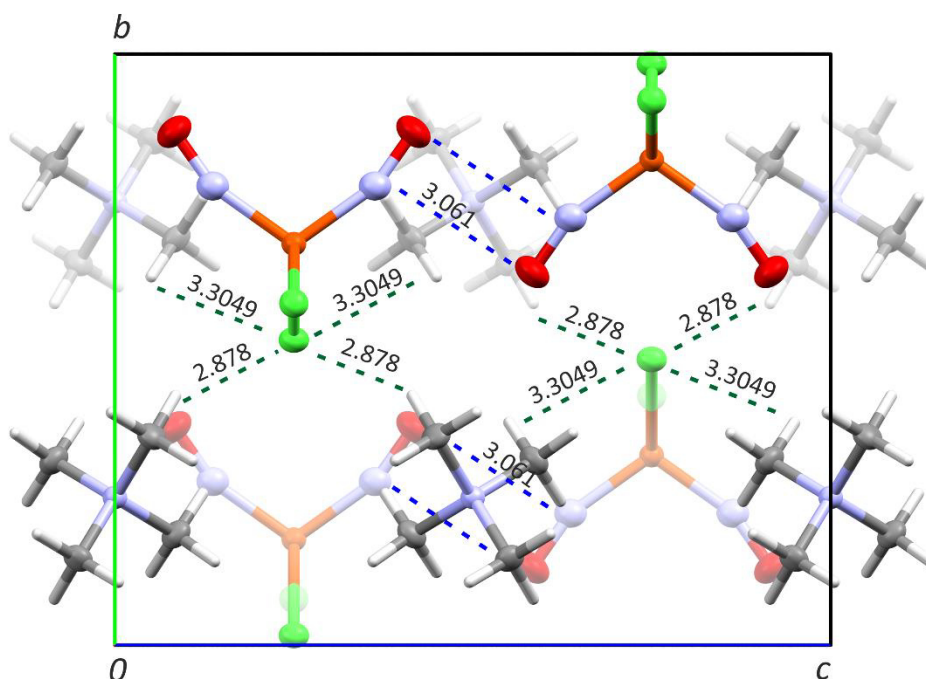
Figure 2.30: Non-classical hydrogen bonds in crystals of **14a** and **14b**. Atoms: carbon (gray), hydrogen (white), chlorine (green), iron (orange), nitrogen (blue), oxygen (red).

2.11.2 Dibromidodinitrosylferrate (DNIC-Br): Crystal structure of PPN[FeBr$_2$(NO)$_2$] (15a and 15b)

Similar to $[FeCl_2(NO)_2]^-$, solutions of $[FeBr_2(NO)_2]^-$ were successfully prepared and analyzed by IR and UV/Vis spectrometry. However, pure crystals of a bromido DNIC were not obtained as with the standard DNIC-Cl route. Compound **15a** was prepared by treating a solution of equimolar amounts of Fe(OTf)$_2$ and PPNBr with gaseous NO. For **15b** a solution of FeBr$_2$ and PPNBr (1:1) and some aqueous HBr (30 wt.%) was used as a starting solution. Both batches were intended to synthesize MNIC-Br. But in these dark green solutions, indicating the formation of MNIC-Br, two compounds were formed. Namely, green crystals of PPN[FeBr$_3$(NO)] (confirmed by X-ray diffraction) as the main product and red-brown crystals of PPN[FeBr$_2$(NO)$_2$] as a byproduct were obtained. When the usual stoichiometry of iron to bromide (1:3) was used, it led exclusively to the formation of PPN[FeBr$_3$(NO)] (**13**).

The formation of bromido DNICs points to a subsequent disproportionation of the MNIC species as the primary product according to Scheme 2.7.

$$2\,[FeBr_3(NO)]^- \rightarrow [FeBr_2(NO)_2]^- + [FeBr_4]^-$$

Scheme 2.7: Proposed formation of $[FeBr_2(NO)_2]^-$ via dismutation of PPN[FeBr$_3$(NO)].

The uncorrected as well as the corrected crystal structures of **15a** and **15b** are depicted in Figure 2.31–Figure 2.34.
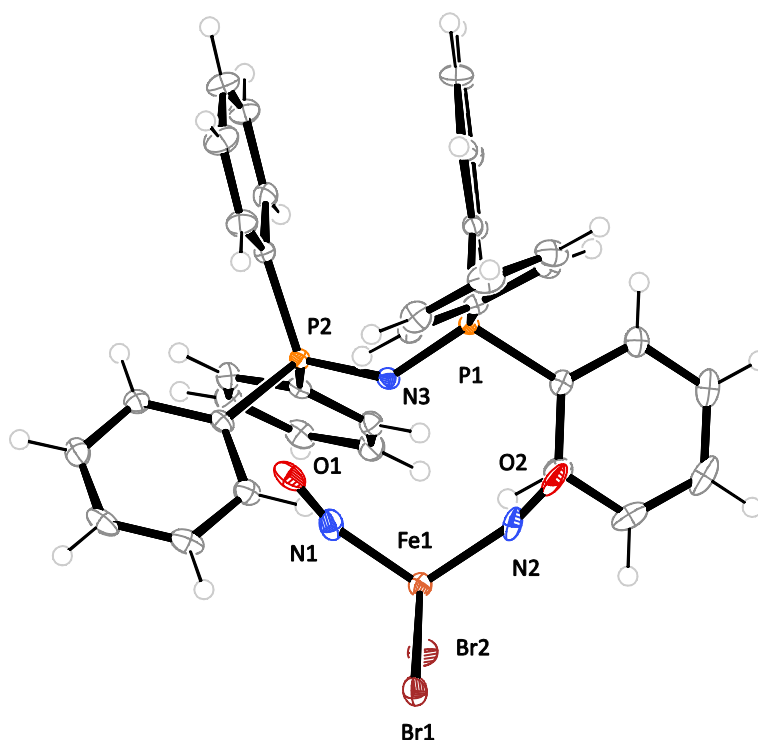
Figure 2.31: ORTEP plot of the ion pair in crystals of PPN[FeBr$_2$(NO)$_2$] (**15a**, uncorrected) (50% probability level at 100 K). Space group $P\bar{1}$. Interatomic distances (Å) and angles (°) with the standard deviation of the last digit is given in parentheses: Fe1–Br1 2.4063(4), Fe1–Br2 2.4131(4), Fe1–N1 1.730(2), Fe1–N2 1.770(2), N1–O1 1.068(3), N2–O2 0.969(3), Fe1–N1–O1 162.79(19), Fe1–N2–O2 167.0(2), N1–Fe1–N2 111.41(9), Br2–Fe1–N2 107.38(6), Br1–Fe1–Br2 109.14(1), Br1–Fe1–N1 104.55(7), Br1–Fe1–N2 111.03(6), Br2–Fe1–N1 113.34(7).

As is shown in Figure 2.31, the bond lengths of N1–O1 and N2–O2 are somehow shorter than the expected values. In fact, the molecular structure features a Br/NO disorder. Thus, 5% Br lay on the position between N1 and O1 and 8% Br between N2 and O2. The co-crystallization of $[FeBr_4]^-$ obviously affected the Fe–N as well as N1–O1 bond lengths, namely, which are longer or shorter, respectively, than their expected values (see Table 2.10). This aspect was successfully dealt with by the structure refinement. The molecular structures as well as its structural parameters are depicted

in Figure 2.32. These observations support the hypothesis of the disproportionation of the PPN[FeBr$_3$(NO)] as shown in Scheme 2.7.
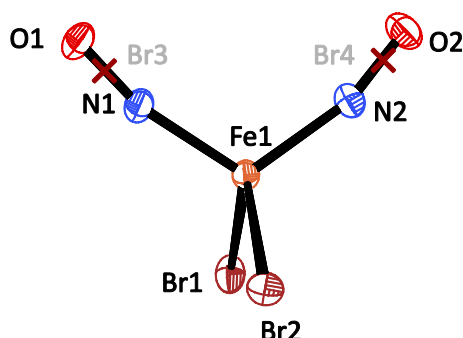
Figure 2.32: ORTEP plot of [FeBr$_2$(NO)$_2$]$^-$ anion (**15a** corrected) (50% probability level at 100 K). Space group $P\bar{1}$. Interatomic distances (Å) and angles (°) with the standard deviation of the last digit is given in parentheses: Fe1–Br1 2.4061(4), Fe1–Br2 2.4128(4), Fe1–Br3 2.322(5) (5% Br, red cross ×), Fe1–Br4 2.359(9) (8% Br, red cross ×), Fe1–N1 1.691(3), Fe1–N2 1.689(4), N1–O1 1.181(4), N2–O2 1.177(5), Fe1–N1–O1 163.4(3), Fe1–N2–O2 166.4(4), Br2–Fe1–Br4 120.2(2), Br2–Fe1–N1 112.91(9), Br2–Fe1–N2 107.11(10), Br2–Fe1–Br3 107.91(11), Br1–Fe1–Br4 103.4(2), Br1–Fe1–Br2 109.16(1), Br1–Fe1–Br3 113.45(12), Br1–Fe1–N1 104.64(10), Br1–Fe1–N2 110.71(12).

In Figure 2.33, the uncorrected structure of **15b** is shown. In terms of the N2–O2 distance, the analysis is affected by Br/NO disorder. It should be noted at this point that the admixture of even small amounts of Br caused a remarkable error due to the high electron number of Br. In fact, there were 3% Br partly disordered with the NO ligand, causing the bond length to be shorter than expected value. After correction of the crystal-structure refinement, the N2–O2 bond length was 1.182(5) Å (see Figure 2.34). Compounds **15a** and **15b** are the first examples of structurally resolved of [FeBr$_2$(NO)$_2$]$^-$ ions. However, details of the reaction still remain unclear, especially the reduction route of iron(III) in the bromide system.
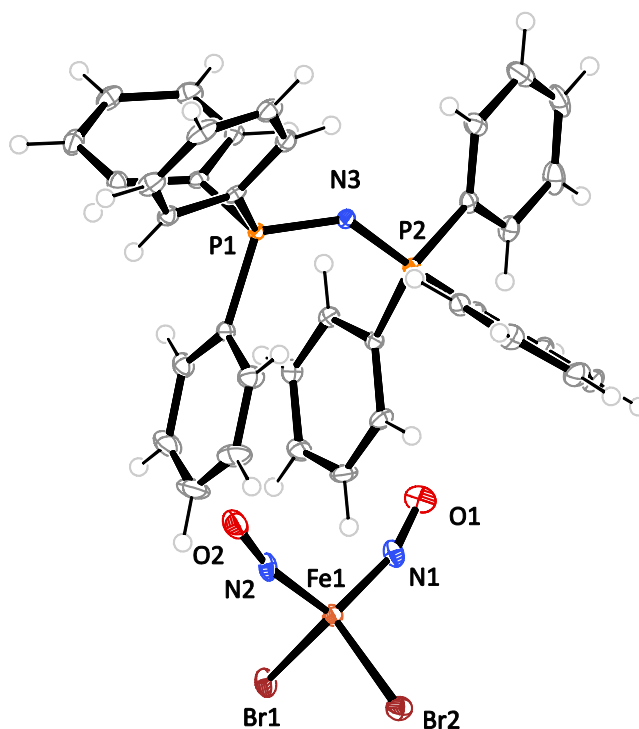
Figure 2.33: ORTEP plot of the ion pair in crystals of PPN[FeBr$_2$(NO)$_2$] (**15b**). (50% probability level at 100 K). Space group $P\overline{1}$. Interatomic distances (Å) and angles (°) with the standard deviation of the last digit is given in parentheses: Fe1–Br1 2.4108(4), Fe1–Br2 2.4173(4), Fe1–N1 1.7073(19), Fe1–N2 1.7229(19), N1–O1 1.145(2), N2–O2 1.099(3), Fe1–N1–O1 162.73(18), Fe1–N2–O2 166.34(18), N1–Fe1–N2 112.26(9), Br2–Fe1–N2 107.15(6), Br1–Fe1–Br2 109.12(1), Br1–Fe1 –N1 104.56(7), Br1–Fe1–N2 110.63(7), Br2–Fe1–N1 113.11(7).
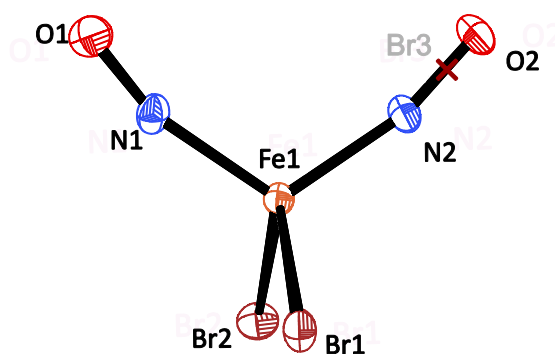
Figure 2.34: ORTEP plot of [FeBr$_2$(NO)$_2$]$^-$ anion (**15b**, corrected) (50% probability level at 100 K). Space group $P\overline{1}$. Interatomic distances (Å) and angles (°) with the standard deviation of the last digit is given in parentheses: Corrected Fe1–Br1 2.4108(4), Fe1–Br2 2.4173(4), Fe1–Br 2.313(14) (0.3%Br disordered, red cross ×), Fe1–N1 1.7077(19), Fe1–N2 1.686(4), N1–O1 1.144(2), N2–O2 1.182(5), Fe1–N1–O1 162.76(17), Fe1–N2–O2 166.1(4), N1–Fe1–N2 112.47(13), Br2–Fe1–N2 110.56(12), Br1–Fe1–Br2 109.13(1), Br1–Fe1–N1 104.58(6), Br1–Fe1–N2 110.63(7), Br2–Fe1–N1 113.13(6), Br3–Fe1–N1 109.3(3), Br1–Fe1–Br3 113.4(3), Br2–Fe1–Br3 107.5(3).

2.11.3 Diiodidodinitrosylferrate (DNIC-I): Crystal structure of PPN[FeI$_2$(NO)$_2$] (16), (PPN)$_2$[FeI$_2$(NO)$_2$]I$_3$ (17), AsPh$_4$[FeI$_2$(NO)$_2$] (18) and PPh$_4$[FeI$_2$(NO)$_2$] (19)

From the reaction mixture of Fe(OTf)$_2$, PPNI and gaseous NO at 50 °C, the compound **16** and **17** crystallized immediately. As mentioned earlier, A[FeI$_2$(NO)$_2$] salts crystallized mostly with an I$_3^-$ anion as a byproduct. The structure solution of **16** succeeded in the triclinic space group $P\overline{1}$ and contained two formula units in the primitive cell. Compound **16** was isotypic with the same salt obtained from a different synthetic route.[43]. Compound **17** has already been prepared and described by Wolf, but the crystal structure is of lower quality than the one presented here with a residual electron density of 1.176$_{max}$ and −0.895$_{min}$ e Å^{-3} compared to 5.629$_{max}$ and −6.843$_{min}$ e Å^{-3} in Wolf's case.[41] As with the PPN salts, **18** and **19** crystallized immediately upon exposure to NO. Their byproducts were AsPh$_4$I$_3$ and PPh$_4$I$_3$, respectively, both of which were pale brown. The crystal-structure solutions of both compounds **18** and **19** succeeded in the triclinic space group $P2/n$ with two formula units in the primitive cell. All [FeI$_2$(NO)$_2$]$^-$ anions had T-4 configuration. The Fe–N–O moieties were bent with the angle between 161° and 166° with both Fe(NO) groups are in '*attracto*' position towards each other. The mean bond lengths were: 2.59 Å for Fe–I, 1.69 Å for Fe–N and 1.18 Å for N–O. The N–O stretching vibrations were found at around 1757$_{(sym)}$ and 1707$_{(asym)}$ cm^{-1}. Table 2.10 shows the structural parameters of **16**–**19** as well as of **14** and **15** for comparison. In comparison to the other DNIC-Cl and DNIC-Br species with DNIC-I, they all had similar Fe–N and N–O bond lengths, as well as Fe–N–O angles. Only the Fe–X distances were different due to the radius of the halide atoms. The ion pair in crystals of **16**–**19** are depicted in Figure 2.35–Figure 2.38, respectively.

Table 2.10: Interatomic distances (Å) and angles (°) of [FeCl$_2$(NO)$_2$]$^-$ (**14**), [FeBr$_2$(NO)$_2$]$^-$ (**15**) and [FeI$_2$(NO)$_2$]$^-$ (**16–19**).

Compound	Cation		Space group	dFe–X/Å	dFe–N/Å	dN–O/Å	Fe–N–O/°	$\tilde{\nu}$(N–O)/cm^{-1}
14a	NMe$_4^+$	X=Cl	*Pbcm*	2.2784(4)	1.7073(10)	1.1568(13)	160.84(10)	1780, 1695
				2.2811(4)				
14c	PPN$^+$		*P$\bar{1}$*	2.2772(5)	1.6986(17)	1.168(2)	165.64(15)	1775, 1696
				2.2714(5)	1.7121(16)	1.147(2)	161.25(15)	
15a	PPN$^+$	X=Br		2.4063(4)	1.730(2)	1.068(3)	162.79(19)	1777, 1710
				2.4131(4)	1.770(2)	0.969(3)	167.0(2)	
15a*			*P$\bar{1}$*	2.4061(4)	1.691(3)	1.181(4)	163.4(3)	
				2.4128(4)	1.689(4)	1.177(5)	166.4(4)	
15b	PPN$^+$	X=Br	*P$\bar{1}$*	2.4108(4)	1.7073(19)	1.145(2)	162.73(18)	1776, 1709
				2.4173(4)	1.7229(19)	1.099(3)	166.34(18)	
15b*				2.4108(4)	1.7077(19)	1.144(2)	162.76(17)	
				2.4173(4)	1.686(4)	1.182(5)	166.1(4)	
16	PPN$^+$	X=I	*P$\bar{1}$*	2.5882(4)	1.686(2)	1.163(3)	164.75(19)	1758, 1709
				2.5982(4)	1.685(2)	1.165(3)	166.9(2)	
17	PPN$^+$		*Ibca*	2.5848(6)	1.693(2)	1.163(2)	166.7(2)	1760, 1711
18	AsPh$_4^+$		*P2/n*	2.5900(3)	1.6869(15)	1.172(2)	164.88(14)	1754, 1705
19	PPh$_4^+$		*P2/n*	2.5911(3)	1.6871(13)	1.1740(19)	165.24(14)	1753, 1704

* corrected crystal structure refinement.
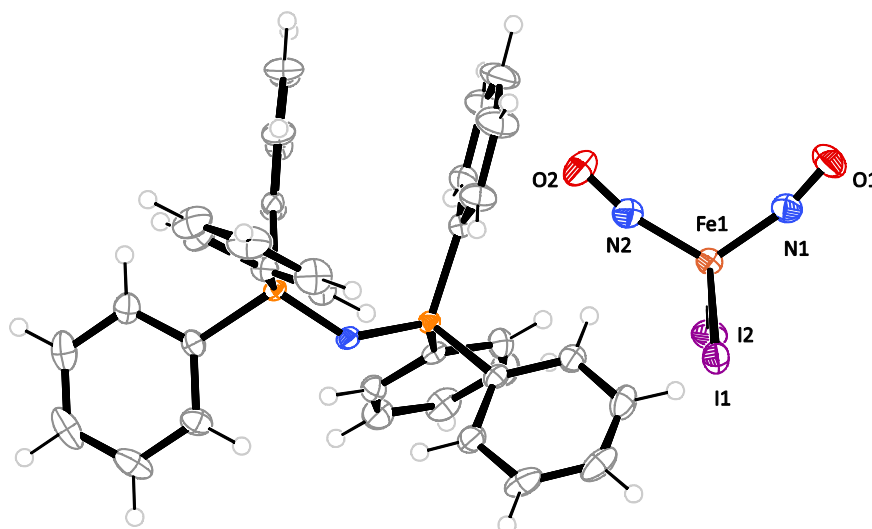
Figure 2.35: ORTEP plot of the ion pair in crystals of PPN[FeI$_2$(NO)$_2$] (**16**) (50% probability level at 173 K). Space group *P$\bar{1}$*. Interatomic distances (Å) and angles (°) with the standard deviation of the last digit is given in parentheses: Fe1–I1 2.5882(4), Fe1–I2 2.5982(4), Fe1–N1 1.686(2), Fe1–N2 1.685(2), N1–O1 1.163(3), N2–O2 1.165(3), Fe1–N1–O1 164.75(19), Fe1–N2–O2 166.9(2), I1–Fe1–I2 108.63(1), I1–Fe1–N2 110.20(8), I1–Fe1–N1 103.22(7), I2–Fe1–N1 113.61(7), I2–Fe1–N2 106.48(8), N1–Fe1–N2 114.61(10).
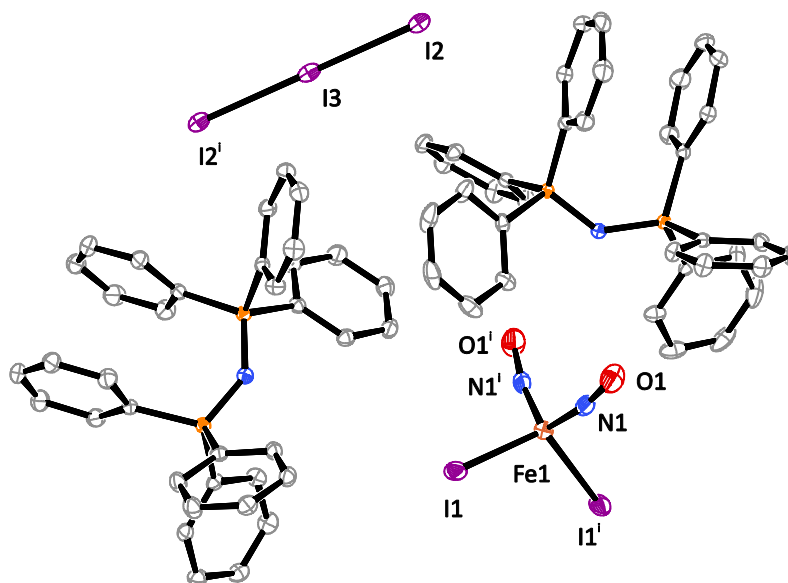
Figure 2.36: ORTEP plot of the ion pairs in crystals of (PPN)$_2$[FeI$_2$(NO)$_2$](I$_3$) (**17**) (50% probability level at 100 K). Space group *Ibca*. Hydrogen atoms were omitted for clarity. Interatomic distances (Å) and angles (°) with the standard deviation of the last digit is given in parentheses: Fe1–I1 2.5848(6), Fe1–N1 1.693(2), N1–O1 1.163(3), Fe1–N1–O1 166.7(2), I1–Fe1–I1^i 113.05(3), I1–Fe1–N1^i 108.00(7), I1–Fe1–N1 106.03(7), N1–Fe1–N1^i 115.94(10), I2–I3 2.908(6), I2–I3–I2^i 179.48(2). Symmetry code: ^{i} 1/2−*x*, +*y*, −*z*.
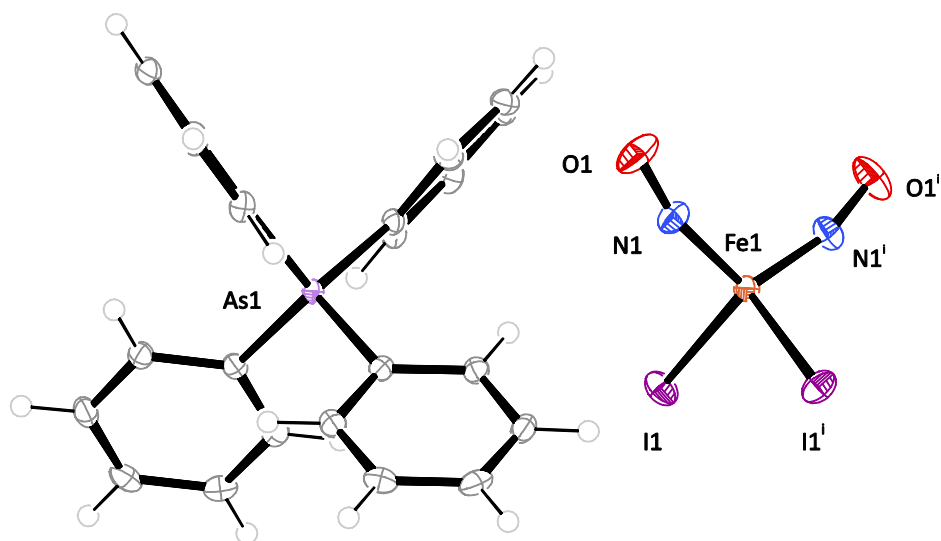
Figure 2.37: ORTEP plot of the ion pair in crystals of AsPh$_4$[FeI$_2$(NO)$_2$] (**18**) (50% probability level at 173 K). Space group *P*2/*n*. Interatomic distances (Å) and angles (°) with the standard deviation of the last digit is given in parentheses: Fe1–I1 2.5900(3), Fe1–N1 1.6869(15), N1–O1 1.172(2), Fe1–N1–O1 164.88(14), I1–Fe1–I1^i 111.90(1), I1–Fe–N1 110.66(5), I1^i–Fe1–N1 105.25(5), N1–Fe1–N1^i 113.28(7). Symmetry code: ^{i} 1/2−*x*, +*y*, 1/2−*z*.
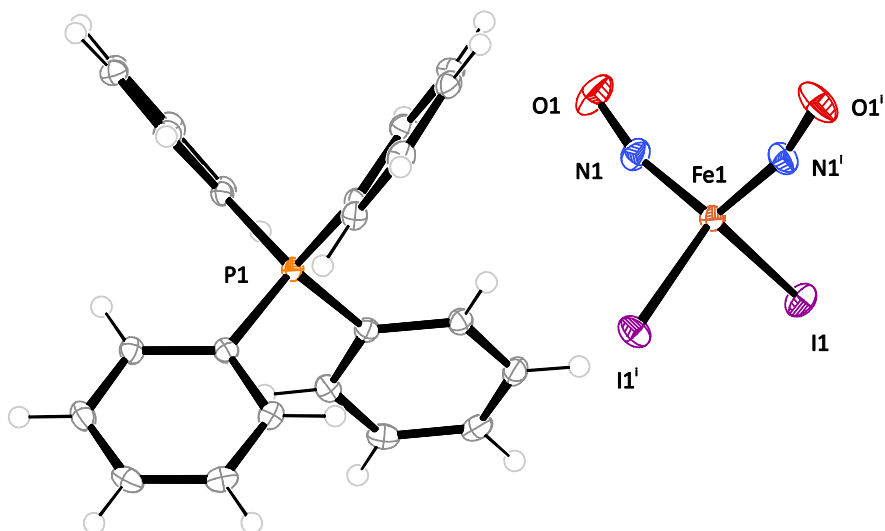
Figure 2.38: ORTEP plot of ion pair in crystals of PPh$_4$[FeI$_2$(NO)$_2$] (**19**) (50% probability level at 100 K). Space group *P*2*/n*. Interatomic distances (Å) and angles (°) with the standard deviation of the last digit is given in parentheses: Fe1–I1 2.5911(3), Fe1–N1 1.6871(13), N1–O1 1.1740(19), Fe1–N1–O1 165.24(14), I1–Fe1–I1^i 111.79(1), I1–Fe–N1 104.96(4), I1–Fe1–N1^i 110.81(4), N1–Fe1–N1^i 113.70(7). Symmetry code: ^{i} 3/2−*x*, +*y*, 1/2−*z*.

2.12 Synthesis of hexa-coordinated quartet-{FeNO}[7] and penta-coordinated doublet-{Fe(NO)₂}[9] compounds with bis(pyrazolyl)pyridine

This chapter deals with the synthesis and characterization of four new iron-nitrosyl coordination compounds bearing a bis(pyrazolyl)pyridine ligand.
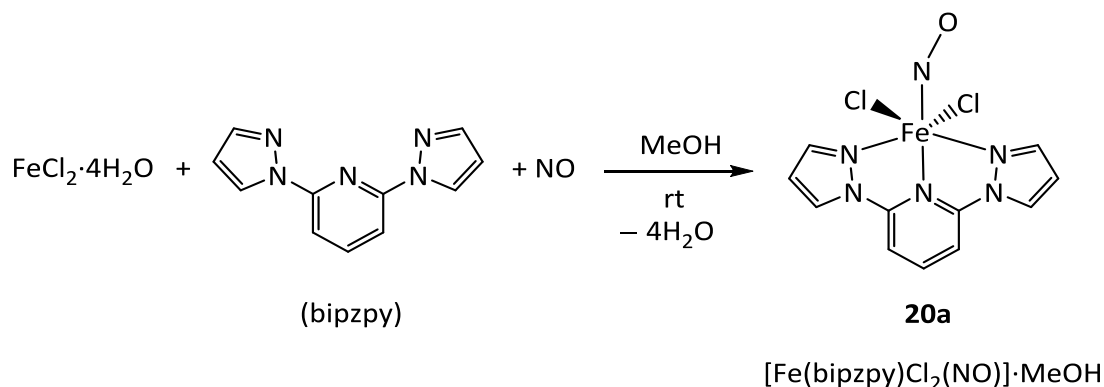
Scheme 2.8: Synthesis of **20a**.

Compound **20a** was prepared according to

Scheme **2.8**. FeCl₂ was mixed in a molar 1:1 ratio with bis(pyrazolyl)pyridine in methanol, resulting in a yellow solution and suspension. The mixture was treated with gaseous NO and a green solution formed. Green crystals were obtained after storing the solution at 5 °C, which were isolated and analyzed as [Fe(bipzpy)Cl₂(NO)]·MeOH (**20a**) (Figure 2.39). When the crystals were removed from the solvent, they exhibited a decent stability even without inert-gas or nitric-oxide atmosphere. However, when **20a** was dissolved in methanol, the solution lost its characteristic green color, indicating the loss of the nitrosyl ligand. By repeated treating the remaining yellow solution with NO, it turned green again and green crystals were obtained. After repeating the reaction with FeCl₃ (see Scheme 2.9), the same green-colored solution and crystals with the same habitus and color were obtained and analyzed as **20b** (Figure 2.40). Single-crystal X-ray analysis confirmed the same crystal structure as **20a**. In addition, some of the yellow suspension from the ferric route was stored at 5 °C, from which yellow crystals were obtained and analyzed by X-ray diffraction confirming the intermediate species as [Fe(bipzpy)Cl₃]·MeOH (**20c**, see Figure 2.41). By treating **20c** with NO, a nitrosyl group substituted the chlorido ligand *trans* to the *N*-pyridine fragment. The reductive nitrosylation of FeCl₃ was similar to the [FeCl₃(NO)]⁻ formation in which MeONO was observed (Scheme 2.9). In conclusion, compounds **20** were prepared from FeCl₂ and FeCl₃.
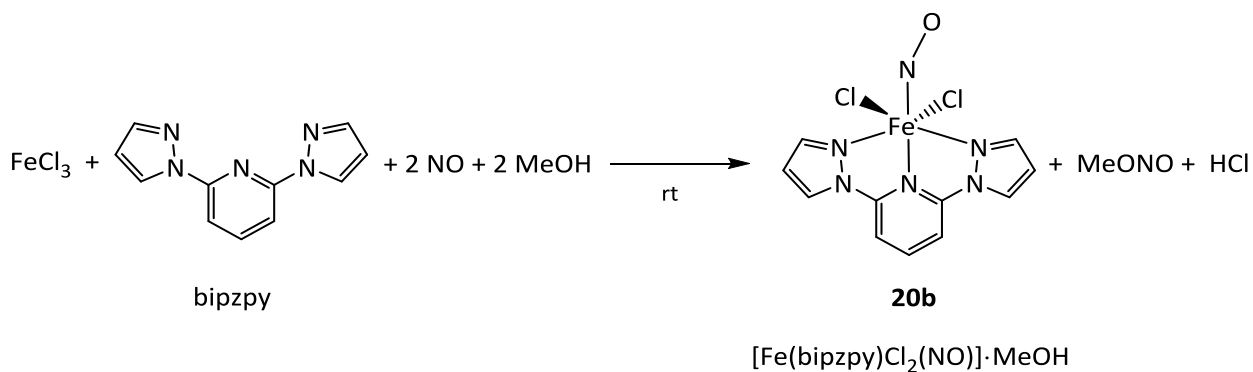
Scheme 2.9: Synthesis of **20b**.

*Crystal structure of [Fe(bipzpy)Cl$_2$(NO)]·MeOH (**20a**)*
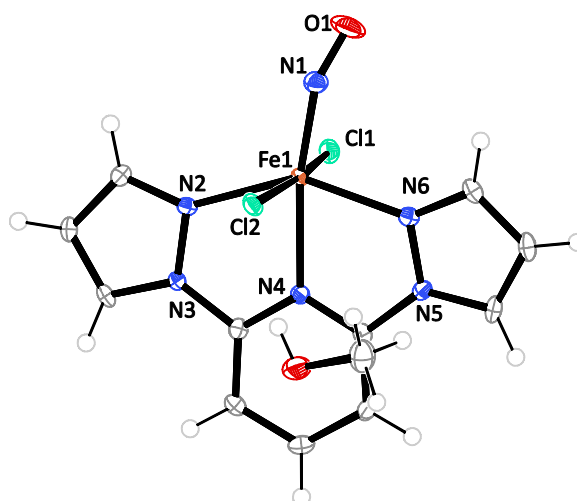
Figure 2.39: ORTEP plot of the molecular structure of [Fe(bipzpy)Cl$_2$(NO)]·MeOH (**20a**) (50% probability level at 100 K). Space group $P2_1/c$. Interatomic distances (Å) and angles (°) with the standard deviation of the last digit is given in parentheses: Fe1–Cl1 2.3748(7), Fe1–Cl2 2.4753(7), Fe1–N1 1.765(2), Fe1–N2 2.1967(19), Fe1–N4 2.1469(18), Fe1–N6 2.1390(18), N1–O1 1.153(3), Fe1–N1–O1 154.0(2), Cl1–Fe1–Cl2 173.08(3), Fe1–N6–N5 115.72(13), Cl1–Fe1–N1 88.52(8), Fe1–N6–C1 139.12(16), Cl1–Fe1–N2 87.67(6), Cl1–Fe1–N4 90.16(6), Cl1–Fe1–N6 94.14(6), Cl2–Fe1–N1 93.30(8), Cl2–Fe1–N2 85.54(6), Cl2–Fe1–N4 89.17(6), Cl2–Fe1–N6 92.26(6), N1–Fe1–N2 116.58(9), N1–Fe1–N4 170.18(9), N1–Fe1–N6 97.10(9), N2–Fe1–N4 73.07(7), N2–Fe1–N6 146.32(7), N4–Fe1–N6 73.29(7).

*Crystal structure of [Fe(bipzpy)Cl$_2$(NO)]·MeOH (**20b**)*
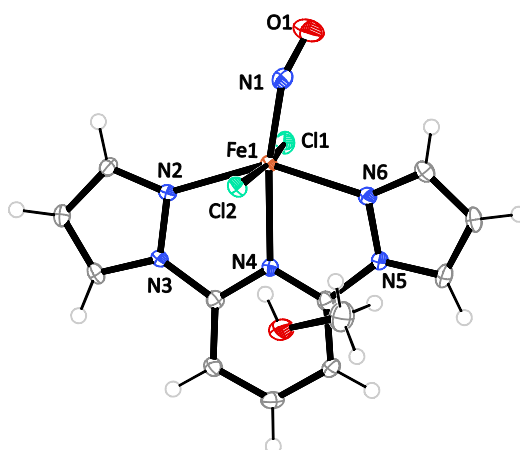
Figure 2.40: ORTEP plot of the molecular structure of [Fe(bipzpy)Cl$_2$(NO)]·MeOH (**20b**) (50% probability level at 100 K). Space group *P*2$_1$/*c*. Interatomic distances (Å) and angles (°) with the standard deviation of the last digit is given in parentheses: Fe1–Cl1 2.3737(7), Fe1–Cl2 2.4727(7), Fe1–N1 1.780(2), Fe1–N2 2.1998(19), Fe1–N4 2.1452(17), Fe1–N6 2.1398(18), N1–O1 1.128(3), Fe1–N1–O1 153.8(2), Cl1–Fe1–Cl2 172.87(3), Fe1–N6–N5 115.96(13), Cl1–Fe1–N1 88.71(7), Fe1–N6–C1 139.12(16), Cl1–Fe1–N2 87.56(6), Cl1–Fe1–N4 90.14(5), Cl1–Fe1–N6 94.14(6), Cl2–Fe1–N1 93.28(7), Cl2–Fe1–N2 85.43(6), Cl2–Fe1–N4 89.05(5), Cl2–Fe1–N6 92.40(6), N1–Fe1–N2 116.59(8), N1–Fe1–N4 170.23(8), N1–Fe1–N6 97.20(8), N2–Fe1–N4 73.03(7), N2–Fe1–N6 146.20(7), N4–Fe1–N6 73.21(7).

*Crystal structure of [Fe(bipzpy)Cl$_3$]·MeOH (**20c**)*
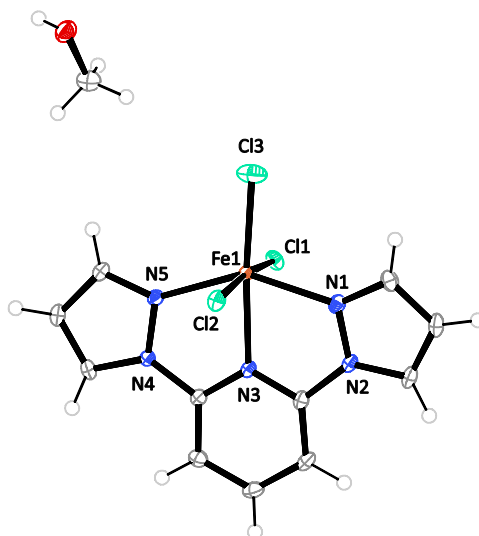
Figure 2.41: ORTEP plot of the molecular structure of [Fe(bipzpy)Cl$_3$]·MeOH (**20c**) (50% probability level at 100 K). Space group *P*2$_1$/*c*. Interatomic distances (Å) and angles (°) with the standard deviation of the last digit is given in parentheses : Fe1–Cl1 2.349(5), Fe1–Cl2 2.365(5), Fe1–Cl3 2.236(6), Fe1–N1 2.131(15), Fe1–N3 2.142(15), Fe1–N5 2.148(15), Cl1–Fe1–Cl2 172.25(2), Cl1–Fe1–Cl3 95.69(2), Cl1–Fe1–N1 88.67(4), Cl1–Fe1–N3 84.88(4), Cl1–Fe1–N5 88.96(4), Cl2–Fe1–Cl3 92.06(2), Cl2–Fe1–N1 89.60(4), Cl2–Fe1–N3 87.39(4), Cl2–Fe1–N5 88.34(4), Cl3–Fe1–N1 101.80(4), Cl3–Fe1–N3 175.08(4), Cl3–Fe1–N5 111.51(4), N1–Fe1–N3 73.31(5), N1–Fe1–N5 146.68(6), N3–Fe1–N5 73.37(5).

[Fe(bipzpy)Cl$_3$]·MeOH (**20a–b**) are neutral {FeNO}^{7}(S = 3/2) compounds, which are rarely seen in the literature. They have octahedral coordination geometry with three coordination sites occupied meridionally by the bipzpy ligand. The remaining sites are occupied by two Cl ligands in equatorial position and the NO ligand in axial position. The complex deviates from the ideal octahedral coordination. The bond lengths and angles are displayed in Table 2.11. The chlorido ligands are not equidistant to the iron center with bond lengths of 2.375 Å and 2.475 Å, respectively, and the Cl1–Fe1–Cl2 bond angle is about 173°. The bond lengths of the Fe1–N(L) are in the range from 2.139 Å to 2.199 Å, while the distance of Fe1–N(O) is 1.765(2) Å. The N–O bond length is 1.153(3) Å and the Fe–N–O bond angle is about 154°.

Table 2.11: Comparison of spectroscopic and structural parameters of **20a**, **20b**, **20c**, **21**, **22** and **23**.

	Code	Space group	dFe–Cl/Å	dFe–N$_L$/Å	dFe–NO/Å	dN–O/Å	Fe–N–O/°	$\tilde{\nu}$(N–O)/cm^{-1}	Min. and Max. Resd. Dens. [e/Å^3]
20a	uv573	$P2_1/c$	2.3748(7)	2.197(19)	1.765(2)	1.153(3)	154.0(2)	1781	−0.44, 0.38
			2.4753(7)	2.147(18)^{py}					
				2.139(18)					
20b	uv710	$P2_1/c$	2.3737(7)	2.199(19)	1.780(2)	1.128(3)	153.8(2)	1779	−0.32, 0.32
			2.4727(7)	2.145(17)^{py}					
				2.140(18)					
20c	uv678	$P2_1/c$	2.349(5)	2.131(15)					−0.43, 0.37
			2.365(5)	2.142(15)^{py}					
			2.236(6)	2.148(15)					
21	uv668	$P6_5$		2.167(4)	1.687(4)	1.176(6)	167.3(5)	1796, 1715	−0.38, 0.30
				2.113(5)^{py}	1.694(5)	1.180(7)	160.9(4)		
				2.147(4)					
22	vv115	$C2$		2.098(8)^{py}	1.704(8)	1.169(10)	164.6(7)	1801, 1716	−0.89, 0.84
				2.136(7)	1.698(7)	1.179(9)	167.3(7)		
				2.163(7)	1.704(7)	1.165(10)	168.3(7)		
				2.085(9)^{py}	1.704(7)	1.165(10)	168.3(7)		
				2.151(8)					
23	vv175	$I2/c$*	2.4545(10)	2.169(3)	1.809(3)	1.121(4)	148.8(3)	1765	−0.51, 0.57
				2.149(3)					
				2.122(3)					

py: N atom at pyridine in the bipzpy ligand, L: ligand (bipzpy), * non-standard setting (c$\bar{\text{b}}$a) of $I2/a$.

If $Fe(BF_4)_2 \cdot 6H_2O$ was used instead of $FeCl_2$ as the starting salt (Scheme 2.10), brown crystals of **21** were obtained by diffusion of diethyl ether into the NO mixture after two weeks. The synthesis was expected to obtain $[Fe(bipzpy)(H_2O)_2(NO)](BF_4)_2$ or $[Fe(bipzpy)F_2(NO)]$. It is known that F^- could be abstracted from BF_4^- and act as a ligand as is shown ,for example, in the synthesis of $[Fe(H_2L)_2F_2]BF_4$ from $Fe(BF_4)_2 \cdot 6H_2O$ and 2-amino-4-(2-pyridyl)thiazole as ligand.[60] However, the dinitrosyl-iron compound $[Fe(bipzpy)(NO)_2]BF_4$ (**21**) was obtained instead. The Fe–NO stretching vibrations of **21** were found at 1796 cm^{-1} and 1715 cm^{-1}.

Compound **21** is a representative of the rare class of cationic $\{Fe(NO)_2\}^9$ compounds. The crystal-structure solution succeeded in the hexagonal space group $P6_5$ with six formula units in the primitive cell. It consisted of the cation $[Fe(bipzpy)(NO)_2]^+$ and a BF_4^- anion. Five nitrogen atoms were coordinated to the iron center having trigonal-bipyramidal structure. The tridentate ligand bipzpy occupied a meridional site of the iron center, while the two remaining equatorial sites were occupied by nitrosyl ligands. This resulted in an unusual five-fold coordination of the iron center. Both Fe–N–O bond angles were fairly bent with an angle of 167.3(5)° for Fe1–N1–O1 and of 160.9(4)° for Fe1–N2–O2. These bond angles were similar to those in anionic DNIC compounds presented in this work. The average bond length of Fe–N(O) is about 1.69 Å and N–O is 1.18 Å. The molecular structure of **21** is depicted in Figure 2.42.
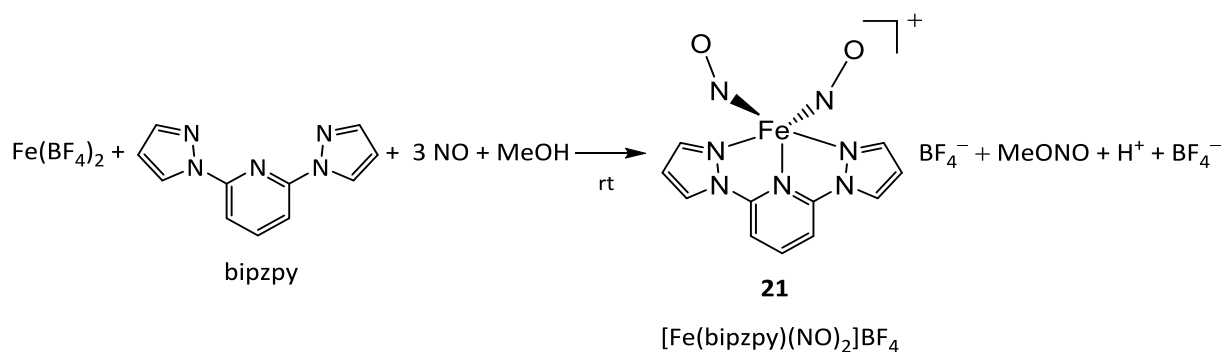
Scheme 2.10: Synthesis of **21**.
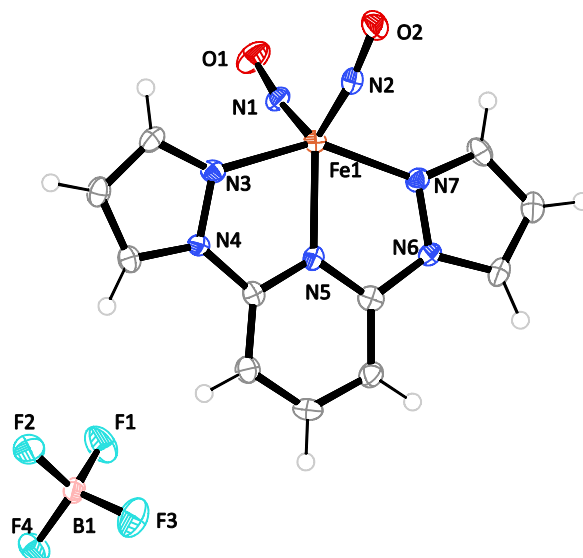
Figure 2.42: ORTEP plot of the molecular structure of [Fe(bipzpy)(NO)$_2$]BF$_4$ (**21**) (50% probability level at 100 K). Space group $P6_5$. Interatomic distances (Å) and angles (°) with the standard deviation of the last digit is given in parentheses: Fe1–N1 1.687(4), Fe1–N2 1.694(5), Fe1–N3 2.167(4), Fe1–N5 2.113(5), Fe1–N7 2.147(4), N1–O1 1.176(6), N2–O2 1.180(7), Fe1–N1–O1 167.3(5), Fe1–N2–O2 160.9(4), N1–Fe1–N2 112.1(2), N1–Fe1–N3 98.10(18), N1–Fe1–N5 120.1(2), N1–Fe1–N7 100.48(18), N2–Fe1–N3 101.39(18), N2–Fe1–N5 127.8(2), N2–Fe1–N7 96.99(18), N3–Fe1–N5 73.29(17), N3–Fe1–N7 146.60(19), N5–Fe1–N7 73.40(17), Fe1–N1–O1 167.3(5), Fe1–N2–O2 160.9(4), Fe1–N3–N4 114.6(3).

In further experiments, FeF$_3$ or FeF$_2$ were used as precursors in order to synthesize an iron-nitrosyl complex bearing fluorido ligands. For FeF$_3$ as reactant, the procedure of Scheme 2.11 was carried out: an 1:1 equimolar mixture of FeF$_3$ and bipzpy in methanol results in a light-green solution with some undissolved green FeF$_3$ (pH≈5 of the solution). The solution turned light brown upon exposure to NO, thereafter red-brown crystals formed above the mother liquid. The IR analysis showed the stretching vibration of N–O moieties at 1801 cm^{-1} and 1716 cm^{-1} for FeF$_3$ and at 1801 and 1706 cm^{-1} if the FeF$_2$ was used, indicating the formation of dinitrosyl-iron compounds. X-ray data of the product derived from FeF$_3$ confirmed compound **22** as [Fe(bipzpy)(NO)$_2$]$_2$(BF$_4$)(NO$_3$). For FeF$_2$, essentially the same crystalline product was obtained and analyzed but it revealed disorder in the crystal structure. The crystal structure solution of **22** succeeded in the monoclinic space group *C*2 with two formula units in the centered cell. Whereby atoms Fe2, N11 and B1 occupied the special positions, thus the asymmetric unit consists of one and half molecules of [Fe(bipzpy)(NO)$_2$]$_2^+$ ions, therefore **22** consisted of three [Fe(bipzpy)(NO)$_2$]$_2^+$ ions, one BF$_4^-$ and two NO$_3^-$ ions. The BF$_4^-$ ion could have originated from the side-reaction of the borosilicate glass with HF, while the NO$_3^-$ ion was formed during the reaction with gaseous NO. This side reaction involved the oxidation of NO to NO$_2^-$ and NO$_3^-$ and the simultaneous reduction of Fe^{III} to Fe^{II}. The oxidation is, however, still unexplained and has to be clarified. Nonetheless, the crystal structure of **22** had satisfying reliability values with *R*: 0.0506, *wR2*: 0.1205 and *S*: 1.16. The asymmetric unit of **22** is shown in Figure 2.43.
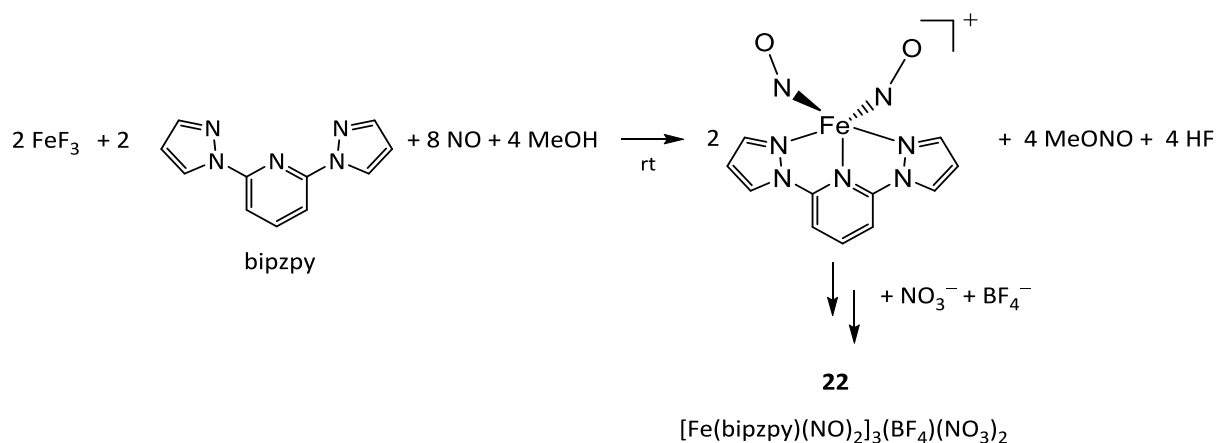
Scheme 2.11: Synthesis of **22**.
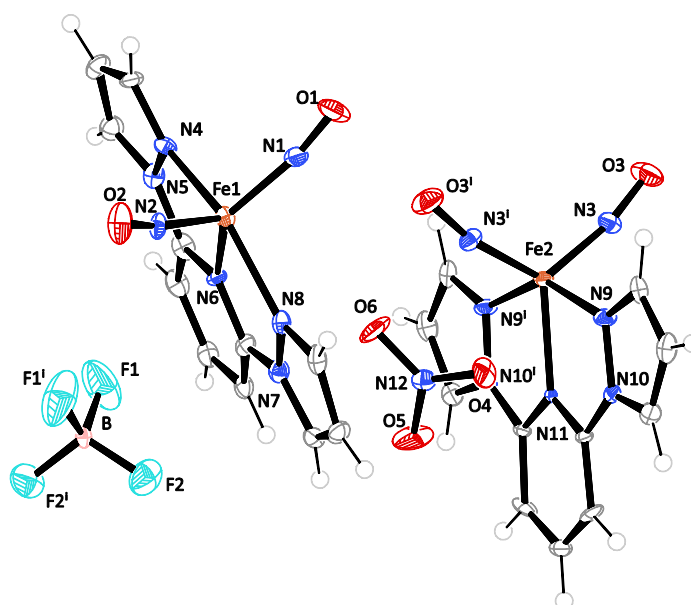
Figure 2.43: ORTEP plot of the extended asymmetric unit of $[Fe(bipzpy)(NO)_2]_3(BF_4)(NO_3)_2$ in crystals of **22** (50% probability level at 100 K). Space group $C2$. Interatomic distances (Å) and angles (°) with the standard deviation of the last digit is given in parentheses: Fe1–N1 1.704(8), Fe1–N2 1.698(7), Fe2–N3 1.704(7), N1–O1 1.169(10), N2–O2 1.179(9), N3–O3 1.165(10), Fe1–N1–O1 164.6(7), Fe1–N2–O2 167.3(7), Fe2–N3–O3 168.3(7), Fe1–N4 2.136(7), Fe1–N6 2.098(8), Fe1–N8 2.163(7), Fe2–N11 2.085(9), Fe2–N9 2.151(8), N1–Fe1–N2 115.6(4), N1–Fe1–N4 97.6(3), N1–Fe1–N6 124.0(3), N1–Fe1–N8 100.0(3), N2–Fe1–N4 98.7(3), N2–Fe1–N6 120.3(3), N2–Fe1–N8 97.9(3), N4–Fe1–N6 73.9(3), N4–Fe1–N8 147.8(3), N6–Fe1–N8 73.9(3), N3–Fe2–N9^i 97.1(3), N9–Fe2–N11 73.98(19), N9–Fe2–N11 73.98(19), N9–Fe2–N9^i 148.0(3), N3–Fe2–N9 99.0(3), N3–Fe2–N11 120.4(2), N3–Fe2–N3^i 119.2(3), N3–Fe2–N11 120.4(2), N9^i–Fe2–N11 73.98(19), N12–O4 1.268(10), N12–O5 1.235(11), N12–O6 1.255(10), O4–N12–O5 119.9(7), O4–N12–O6 120.0(7), O5–N12–O6 120.1(8), B1–F1 1.384(12), B1–F2 1.362(11), F1–B1–F2 110.3(4), F1–B1–F1^i 108.1(11), F1–B1–F2^i 107.7(4), F2–B1–F2^i 112.7(11), F1^i–B1–F2^i 110.3(5). Symmetry code: ^{i} 1–x, +y, 1–z. ^{ii} 1–x, +y,–z.

2.13 Synthesis of hexa-coordinated quartet-{FeNO}[7]-compounds with the 2-amino-4-(2-pyridyl)thiazole ligand

The ligand 2-amino-4-(2-pyridyl)thiazole (aptz) was prepared according to the literature.[60] The brown air-stable crystals of **23** were obtained immediately upon treatment of gaseous NO (see Scheme 2.12 and Experimental part). The structure solution succeeded in the monoclinic space group *I*2/*c* (non-standard setting (c$\bar{\text{b}}$a) of *I*2/*a*) and contained four formula units in the unit cell. The iron center was coordinated by two aptz ligands, one chlorido and one nitrosyl ligand. The nitrosyl ligand was *trans*-coordinated to the *N*-pyridine atom. The coordinated chlorine atoms Cl2, and Cl3 as a counterion are occupied 50% each, compensating the total charge of **23**. The complex deviated from the ideal octahedral coordination. This can be seen from the bond lengths and angles displayed in Figure 2.44. The nitrosyl group was tilted in the direction of the nitrogen atom N3 in the thiazole residue, while the nitrogen atom in the NO moieties was stabilized in the opposite direction by a hydrogen bond with D(N7–H)···N(O) acceptor at distance of about 2.477 Å (see Figure 2.45 and Table 2.12). The Fe1–Cl1 bond length was 2.4545(10) Å. The bond lengths of the Fe–N(L) were in the range from 2.122(3) Å to 2.199(3) Å, while Fe–N(O) is 1.809(3) Å. The N–O bond length is 1.121(4) Å and the Fe–N–O bond angle is 148.8(3)°. Compound **23** belonged to the class of cationic {FeNO}[7] (S = 3/2) compounds. The N–O stretching vibration was found at 1765 cm^{-1}.
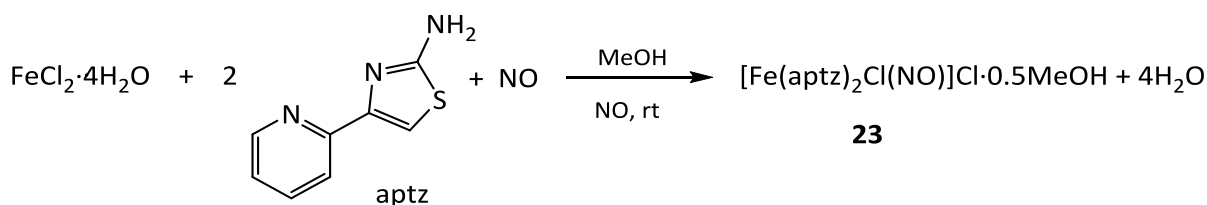
Scheme 2.12: Synthesis of **23**.
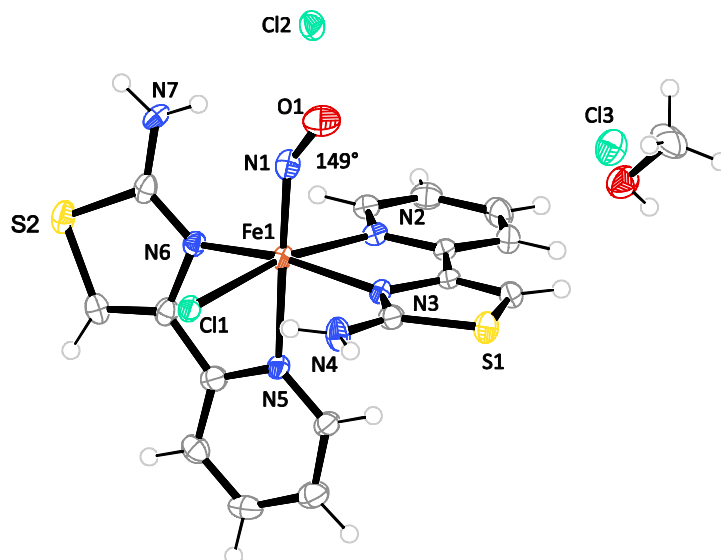
Figure 2.44: ORTEP plot of the molecular structure of [Fe(aptz)$_2$Cl(NO)]Cl·0.5MeOH (**23**) (50% probability level at 100 K). Space group *I*2/*c* (non-standard setting (c$\bar{b}$a) of *I*2/*a*). Interatomic distances (Å) and angles (°) with the standard deviation of the last digit is given in parentheses: Fe1–Cl 2.4545(10), Fe1–N1 1.809(3), Fe1–N2 2.169(3), Fe1–N3 2.149(3), Fe1–N4 2.199(3), Fe1–N5 2.122(3), N1–O1 1.121(4), Fe1–N1–O1 148.8(3), Cl1–Fe1–N1 96.30(9), Cl1–Fe1–N2 168.70(8), Cl1–Fe1–N3 96.50(8), Cl1–Fe1–N4 88.28(8), Cl1–Fe1–N5 87.03(8), N1–Fe1–N2 92.39(12), N1–Fe1–N3 90.35(12), N1–Fe1–N4 101.79(12), N1–Fe1–N5 176.18(12), N2–Fe1–N3 76.18(11), N2–Fe1–N4 97.03(11), N2–Fe1–N5 84.55(11), N3–Fe1–N4 166.42(11), N3–Fe1–N5 91.14(11), N4–Fe1–N5 76.37(11). (Cl3 is disordered with MeOH by each 50% occupying).
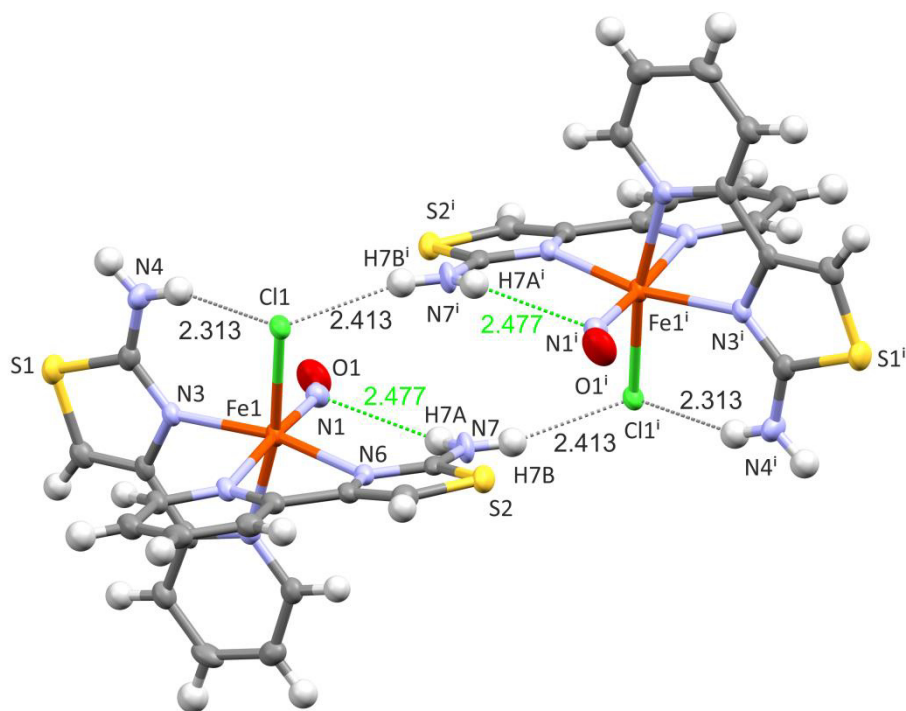
Figure 2.45: MERCURY plot of **23** shows the shortest intermolecular contact N7H7B···Cl1[i] with 2.413 Å (black dot) and shortest intramolecular contact N4H4A···Cl1 with 2.313 Å the second contact N7H7A···N1 with 2.477 Å (green dot). The Fe1–N3 is 3.214 Å. Symmetry code: [i] 3/2–*x*, 1/2–*y*, 3/2–*z*.

Table 2.12: Distances [Å] and angles [°] of hydrogen bonds in **23**, the standard deviation of the last decimal place is given in parentheses.

Donor–Hydrogen⋯Acceptor	d(D–H)/Å	d(H⋯A)/Å	d(D⋯A)/Å	α(D–H⋯A)/°
N7–H7A⋯N1	0.88	2.48	3.171(4)	136.2°
N4^{i}–H4A^{i}⋯Cl1^{i}	0.88	2.31	3.138(3)	156.2°
N7^{i}–H7B^{i}⋯Cl1^{i}	0.88	2.41	3.275(3)	166.3

Symmetry code: ^{i} 3/2−x, 1/2−y, 3/2−z.

2.14 Magnetic susceptibility measurement (SQUID/ PPMS)

SQUID (Superconducting Quantum Interference Device) magnetometry is an effective measurement method to determine the spin state of the $\{FeNO\}^7$ and $\{Fe(NO)_2\}^9$ compounds. High-purity crystalline products of $PPh_4[FeCl_3(NO)]$ (**6**), $AsPh_4[FeCl_3(NO)]$ (**7**), $PPN[FeCl_3(NO)]$ (**8**) and $PPN[FeCl_2(NO)_2]$ (**14c**) from different starting materials (Fe^{II} or Fe^{III} salts) were tested at the working groups of Prof. Birgit Weber (University Bayreuth) and Prof. Dirk Johrendt (Ludwig-Maximiliens-University) and calculated for magnetic susceptibility. By using Equation 3 the effective magnetic moment μ_{eff} was calculated from $\chi_M T$ which was determined by SQUID measurement. The spin-only equation (Equation 1 and Table 2.13) was used to compare the obtained experimental values. Figure 2.46–Figure 2.47 show the result of SQUID measurements on complexes **6**, **7**, **8** and **14c**.

$$\mu_{eff} = \sqrt{4S(S+1)} \cdot \mu_B \qquad (1)$$

$$\mu_{eff} = \sqrt{\frac{3k_B}{N_A \mu_B^2}} \cdot \sqrt{\chi_M T} \cdot \mu_B \qquad (2)$$

$$\mu_{eff} = 2.828 \sqrt{\chi_M T} \qquad (3)$$

μ_B: Bohr magneton

k_B: Boltzmann constant

N_A: Avogadro's number

S: total spin

χ_M: molar magnetic susceptibility

T: absolute temperature in Kelvin

Table 2.13: Calculated spin-only expected values: total spin (S), spin-only magnetic moment ($\mu_{S.O.}$) and the molar magnetic susceptibility ($\chi_M T$)

S	$\mu_{S.O.}$ [cm^3·mol^{-1}]	$\chi_M T$ [cm^3·K·mol^{-1}]
1/2	1.73	0.37
2/2	2.83	1.00
3/2	3.87	1.87
4/2	4.90	3.00
5/2	5.92	4.37

The summary of the magnetic properties of $PPN[FeCl_3(NO)]$ (**8**) and $PPN[FeCl_2(NO)_2]$ (**14c**) is shown in Table 2.14.

Table 2.14: Magnetic property of PPN[FeCl$_3$NO] (**8**) and PPN[FeCl$_2$(NO)$_2$] (**14c**).[33]

Starting salt	Product	μ_{eff}	$\chi_M T$/cm$^3\cdot$K$\cdot$mol^{-1}
FeCl$_2$	PPN[FeCl$_3$NO] (**8**)	4.20	2.20
FeCl$_3$	PPN[FeCl$_3$NO]	5.29	3.50
FeCl$_3$ diluted	PPN[FeCl$_3$NO]	4.20	2.20
$\mu_{eff\,(s.o.)}$ S = 3/2		3.87	1.87
FeCl$_2$	PPN[FeCl$_2$(NO)$_2$] (**14c**)	1.92	0.46
$\mu_{eff\,(s.o.)}$ S = 1/2		1.73	0.37

Figure 2.46 shows that both products **7** and **8** were paramagnetic with $\chi_M T$ values of about 2.0 cm^3 K mol^{-1} corresponding to three unpaired electrons in the respective formula unit, which resembled the {FeNO}^{7}(S = 3/2) formulation. According to Equation 3, both compounds had an effective magnetic susceptibility μ_{eff} = 4.20.

By comparing these results with the magnetic measurement of the corresponding compounds prepared from FeCl$_3$ as a starting material, a higher value of $\chi_M T$ (approximately 3.5 cm$^3\cdot$K$\cdot$mol^{-1} for both complexes) was observed (see Figure 2.47). This can be explained by the formation of PPN[FeCl$_4$] as an intermediate species which co-crystallized with the attempted product. A reason for the formation of PPN[FeCl$_4$] could be that there was not enough solvent used and/or the reaction time with NO(g) was too short to complete the reaction of the desired iron-nitrosyl product.
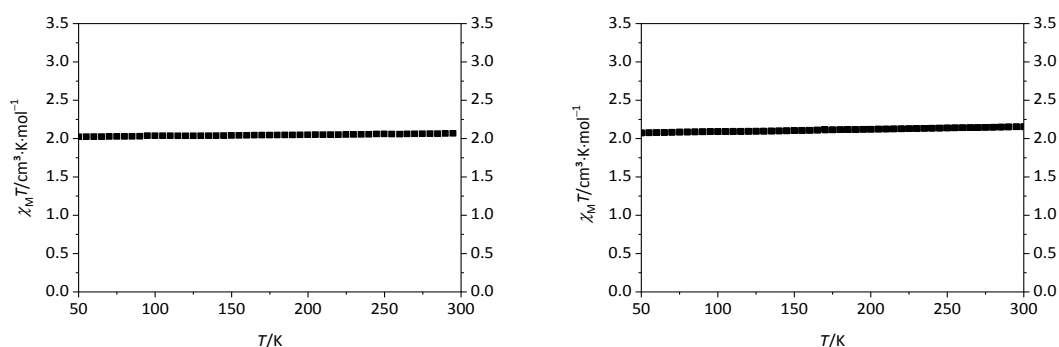
Figure 2.46: $\chi_M T$ vs. T plots of AsPh$_4$[FeCl$_3$(NO)] (**7**) (left) and PPN[FeCl$_3$(NO)] (**8**) (right) which were prepared from FeCl$_2$.
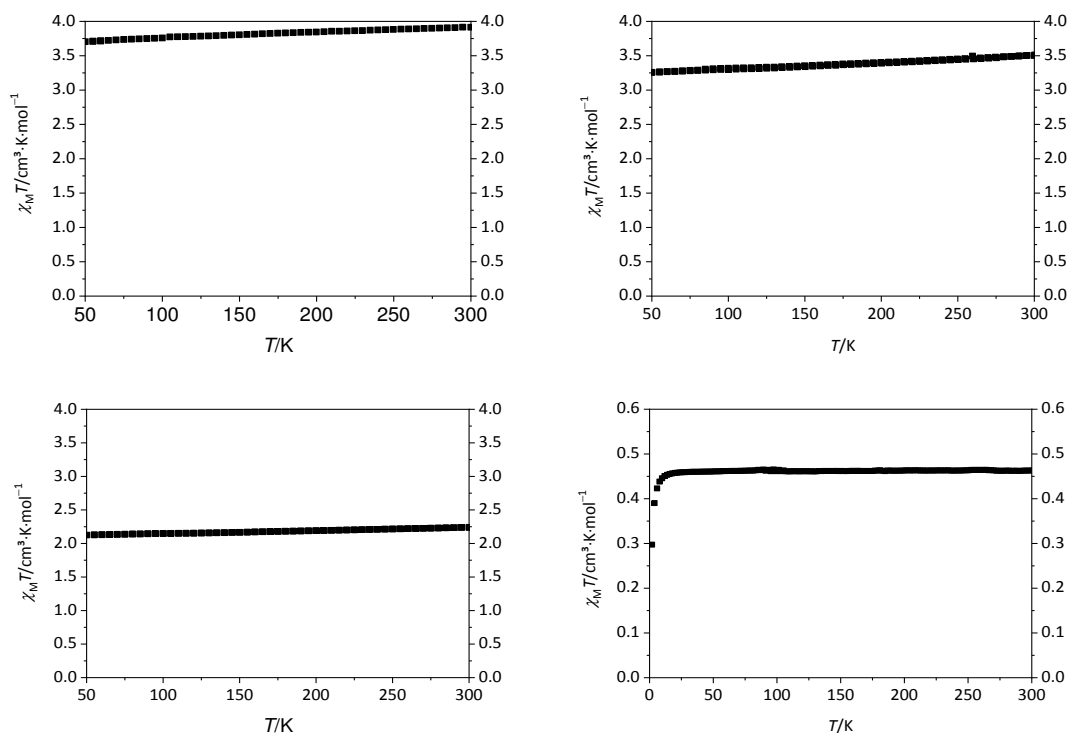
Figure 2.47: $\chi_M T$ vs. *T* plots of of AsPh$_4$[FeCl$_3$(NO)] (**7**) (top left) and PPN[FeCl$_3$(NO)] (**8**) (top, right) which were prepared from FeCl$_3$ and ten-fold diluted FeCl$_3$ (bottom left) and PPN[FeCl$_2$(NO)$_2$] (**14c**) (bottom right).

To check the reaction using FeCl$_3$ as a starting salt, the same experiment was repeated with the ten-fold amount of solvent, thus repressing the precipitation of solid [FeCl$_4$]$^-$ salt. Afterwards, the obtained product, PPN[FeCl$_3$(NO)], was tested again by the SQUID magnetometry. As is shown in Figure 2.47 (bottom left), the values measured for $\chi_M T$ and $\mu_{eff} = 4.20$ were in the expected range of an $S = 3/2$ compound, confirming that the same [FeCl$_3$(NO)]$^-$ product was obtained from both the FeCl$_2$ and FeCl$_3$ routes.

Besides the {FeNO}^{7} ($S = 3/2$) complexes, the magnetic property of PPN[FeCl$_2$(NO)$_2$] (**14c**) was determined using a VSM (Vibrating-sample magnetometer, at working group of Prof. Dirk Johrendt (LMU)). For this measurement, a single crystal of **14c** with an approximate size of 2×2 mm was mounted on a quartz glass and then measured. Figure 2.47 (bottom right) shows the VSM result of this compound, with the $\chi_M T$ value of 0.46 and $\mu_{eff} = 1.92$, which resembled one unpaired electron per formula unit

2.15 PLI measurements

After the successful syntheses of purely crystalline $\{FeNO\}^7$ and $\{Fe(NO)_2\}^9$ compounds, the study of photo-induced linkage isomerism (PLI) was done at the Schaniel working group (University of Lorraine, France) as part of a collaboration. Since the $PPN[FeCl_3(NO)]$ was one of the first $\{FeNO\}^7$ ($S = 3/2$) compounds that showed a photo-oxidized state in the PLI measurement, research on other analogous compounds were performed. In the present thesis the PLI experiments were done at 9 K with different irradiation wavelengths between 340–735 nm with complexes **1a**, **4**–**7**, **11**, **14a**, **14c**, **17**, **19** and **20a**. The results are summarized in Table 2.18. In contrast to the $PPN[FeCl_3(NO)]$, all of the tested $\{FeNO\}^7$ compounds showed the MS1-PLI state (Table 2.18). The MS1 had its O–N bond stretching vibration, shifted to a lower frequency (-200 to $-250\ cm^{-1}$) compared to the GS. Figure 2.51–Figure 2.54 show the PLI experiment results. Although the new absorption bands were detected, they were not intensive and the relaxation times were low, within 2–15 minutes. An extraordinary result was observed with the $Mephaz[FeCl_3(NO)]$ salt, namely, this compound showed the MS1 as well as the photo-oxidized state, both red and blue shifts were coincidentally observed, and a new small band at $\approx 1795\ cm^{-1}$ was detected (Figure 2.52, j, k). The result of $Mephaz[FeCl_3(NO)]$ (**5**) confirmed the results from the aforementioned $PPN[FeCl_3(NO)]$ salt. Furthermore, Figure 2.48 shows the calculated differential energies which were obtained from DFT calculations (BP86/def2-TZVP, d3 dispersion correction during changing of an angle of Fe–N1–O1 from 0°–180°). It indicated that a local minimum of a metastable MS2 state did not exist, therefore its NO stretching vibration band cannot be calculated (Table 2.15). Thus, in fact, it was not detected experimentally.

Analogous experiments were done with the DNIC compounds which showed similar results. New IR bands were detected at lower frequencies, namely at $1777\ cm^{-1}$ and approximately at $1400\ cm^{-1}$. Attempts to match these values with the DFT results (BP86/def2-TZVP) proved that the local minima were achieved by three steps. First, switching one of the Fe–N–O bonds to an Fe–O–N bond, subsequently bending another Fe–N–O moiety towards the other and finally, the Fe–O–N bond was then bent away to achieve the local minima. The optimized structure of the $[FeCl_2(NO)_2]^-$ ion for the PLI result is depicted in Figure 2.50 and was assigned as a 'bent MS1' state. DNIC-$[FeI_2(NO)_2]^-$ (**19**) showed similar results as with the $[FeCl_2(NO)_2]^-$ complex. The PLI results of DNIC-Cl are shown in Table 2.17 and Table 2.18 summarizes all PLI results.

Table 2.15: DFT calculations of linkage isomers of the [FeCl$_3$NO]$^-$ anion and their IR$_{(N-O)}$ frequencies. GS: ground state, MS1: isonitrosyl, MS2: side-on nitrosyl (BP86, def2-TZVP, d3).

State	$\tilde{v}$(N–O)/cm^{-1}
GS	1788
MS1: isonitrosyl	1598
MS2: side-on	-: no local minimum
[FeCl$_3$NO]$^{2-}$	1625
[FeCl$_3$NO]	1871
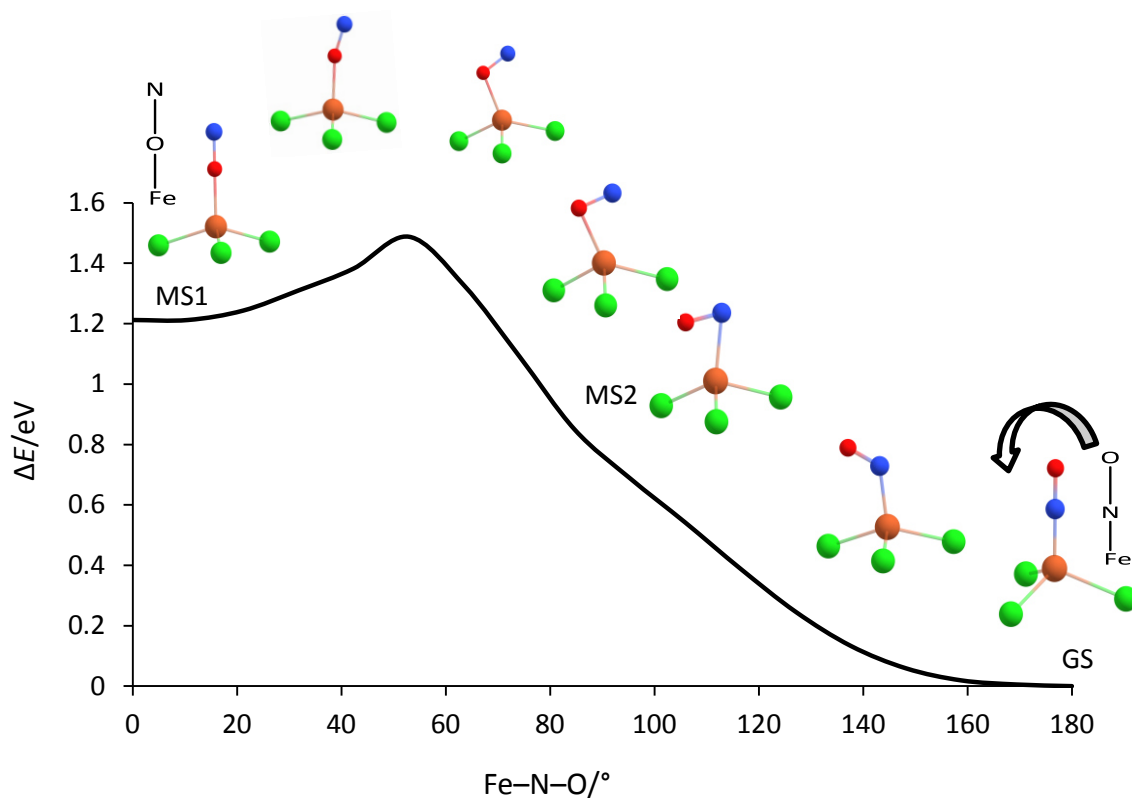
Figure 2.48: Relaxed surface scan for Fe–N1–O1 bond angles from 0°–180° (BP86/def2-TZVP, d3). CHEMCRAFT plot of bending potential of [FeCl$_3$(NO)]$^-$ anion against the Fe–N1–O1 angles. Atoms: chlorine (green), iron (orange), nitrogen (blue) and oxygen (red).

Table 2.16: DFT calculations of linkage isomers of [Fe(bipzpy)Cl$_2$(NO)] and the respective IR$_{(N-O)}$ frequencies. GS: ground state, MS1: isonitrosyl, MS2: side-on nitrosyl, (BP86, def2-TZVP, d3).

State	$\tilde{v}$(N–O)/cm^{-1}
GS, high-spin (S = 3/2)	1760
MS1: isonitrosyl	1587
MS2: side-on	-: no local minimum
GS, low-spin (S = 1/2)	1784
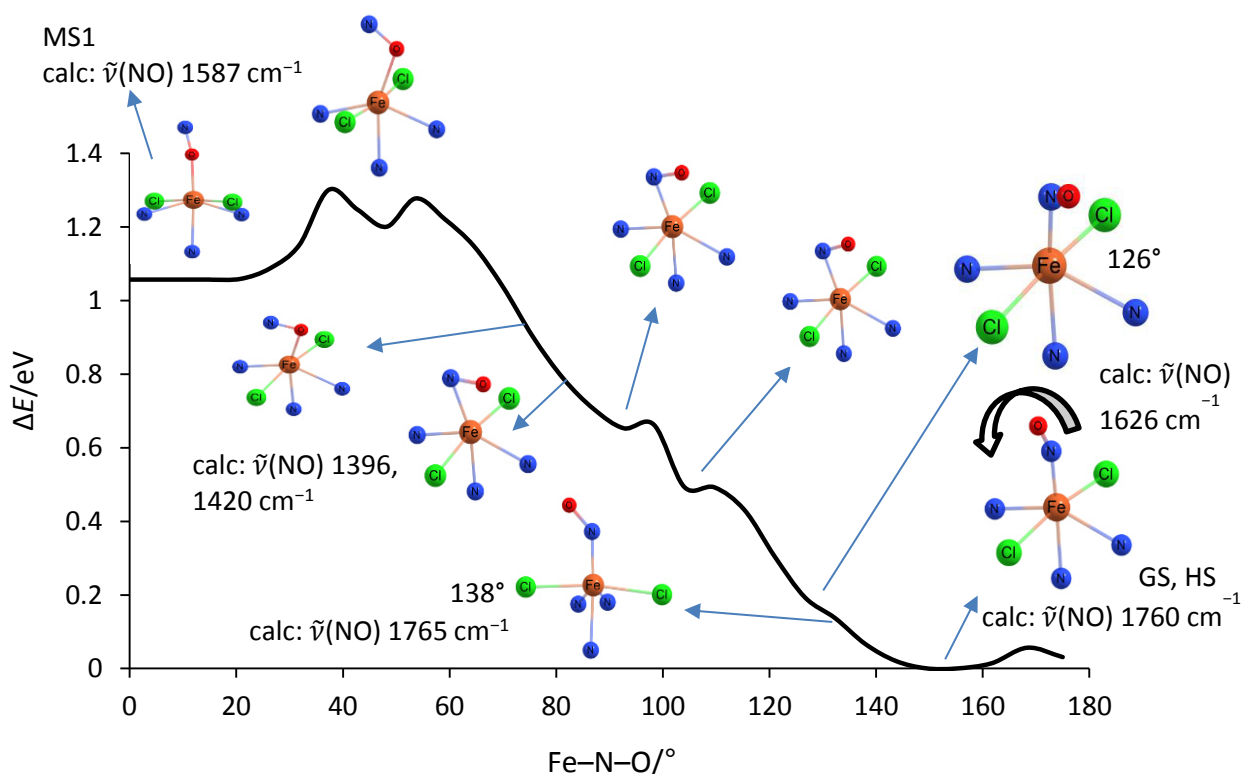
Figure 2.49: Relaxed surface scan of **20a** for Fe–N1–O1 bond angles from 0°–175°, (BP86/def2-TZVP, d3). CHEMCRAFT plot of bending potential of against the of Fe–N1–O1 angles of [Fe(bipzpy)Cl$_2$(NO)]. Atoms: chlorine (green), iron (orange), nitrogen (blue) and oxygen (red). The ligand bipzpy is not fully shown for the sake of clarity.

Upon cooling a sample of **21a** to 10 K, the NO band (GS) split into two peaks at $\tilde{v}$(NO) of 1780 cm^{-1} and 1810 cm^{-1} while the IR band at around 600 cm^{-1} rose as well as the broad band at around 1733 cm^{-1}, some depopulation was found also at around 1600 cm^{-1}. By irradiation, solids of **20a** at wavelengths of between 405–940 nm, one of the NO peaks (at 1810 cm^{-1}) reduced its absorption intensity and the IR peak at 1733 cm^{-1} increased (Figure 2.55, r). The relaxed surface scan of the Fe–N–O bond angles (Figure 2.49) showed that the GS state has its Fe–N–O bond angle of 149° with

the NO fragment tilted towards the chlorido ligand. Upon rotating the NO fragment, it tilted more to the chlorido ligand down to an angle of around 126°, then tilted away from Cl atom and lay between Cl and the N atom of the bipzpy ligand. At an angle of about 100°, the NO fragment lay in the middle of two Cl atoms, subsequently at the angles of between 70–75°, the Fe–N–O bond turned to be a Fe–O–N bond, at which no local minimum energy is observed. The bent Fe–O–N angle increased until it reached the MS1 state, where, again, the NO fragment tilted towards the Cl atom. The relaxed surface scans (Figure 2.49) and the relevant calculated IR values were not responsible for the new IR peak at 1733 cm^{-1}. It should be noted that no species was unraveled in the course of the irradiation, which showed an IR absorption close to 1733 cm^{-1}.

Table 2.17: PLI results of **14a** and **14b** with the calculated values (BP86/def2-TZVP).[33]

Compound	$\tilde{\nu}$(Fe–O–N)/cm^{-1}	$\tilde{\nu}$(N–O)/cm^{-1}
NMe$_4$[FeCl$_2$(NO)$_2$] (**14a**)	1398	1775
PPN[FeCl$_2$(NO)$_2$] (**14c**)	1406	1755
Calculated	1409	1738
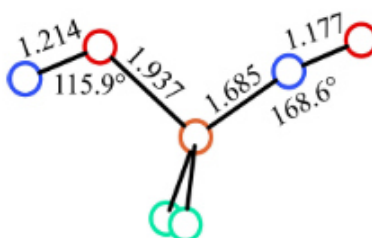
Figure 2.50: Optimized local minimum structure of the bent MS1 and its bonding parameters of [FeCl$_2$(NO)$_2$].[33]

Table 2.18: Summary of the PLI experiments of halogenidonitrosylferrates {FeNO}[7] and {Fe(NO)$_2$}[9]. GS: ground state. MS1: isonitrosyl, MS2: side-on nitrosyl and Ox: photo-oxidized.

Compound	PLI	$\tilde{\nu}_{GS, 9\,K}(NO)/cm^{-1}$	$\tilde{\nu}_{PLI}(N\text{–}O)/cm^{-1}$	Relaxation time/min
1. NMe$_4$[FeCl$_3$(NO)] (**1a**)	MS1	1843	1635,1627 ($\Delta = -216/208$)	4
2. NBnMe$_3$[FeCl$_3$(NO)] (**3**)	MS1	1803	1550 ($\Delta = -253$)	2
3. Mephaz[FeCl$_3$ (NO)] (**4**)	MS1, Ox	1807/1795,	1575 ($\Delta = -233$), 1861 ($\Delta = +51$)	-
4. [Co(cp)$_2$][FeCl$_3$(NO)] (**5**)	MS1	1809/1818	1572 ($\Delta = -237/246$)	4
5. PPh$_4$[FeCl$_3$(NO)] (**6**)	MS1	1812	1571 ($\Delta = -241$)	15
6. AsPh$_4$[FeCl$_3$ (NO)] (**7**)	MS1	1810/1820	1580 ($\Delta = -230$)	5
7. PPN[FeCl$_3$(NO)][41]	Ox	1809	1868 ($\Delta = +59$)	30
8. PPh$_4$[FeBr$_3$(NO)] (**11**)	MS1		1576 ($\Delta = -219$)	4
9. NMe$_4$[FeCl$_2$(NO)$_2$] (**14a**)	MS1	1783, 1687	1775 ($\Delta = -8$), 1398 ($\Delta = -289$)	2
10. PPN[FeCl$_2$(NO)$_2$] (**14c**)	MS1	1775, 1696	1755 ($\Delta = -20$), 1406 ($\Delta = -290$)	2
11. (PPN)$_2$[FeI$_2$(NO)$_2$]I$_3$ (**17**)	No	-	-	-
12. PPh$_4$[FeI$_2$(NO)$_2$] (**19**)	MS1	1765, 1721	1752 ($\Delta = -44$), 1430 $\Delta = -291$)	4
13. [Fe(bipzpy)Cl$_2$(NO)]·MeOH (**20a**)	*	1781, 1810,	1733 ($\Delta = -73$)	-

*: has to be clarified in future work
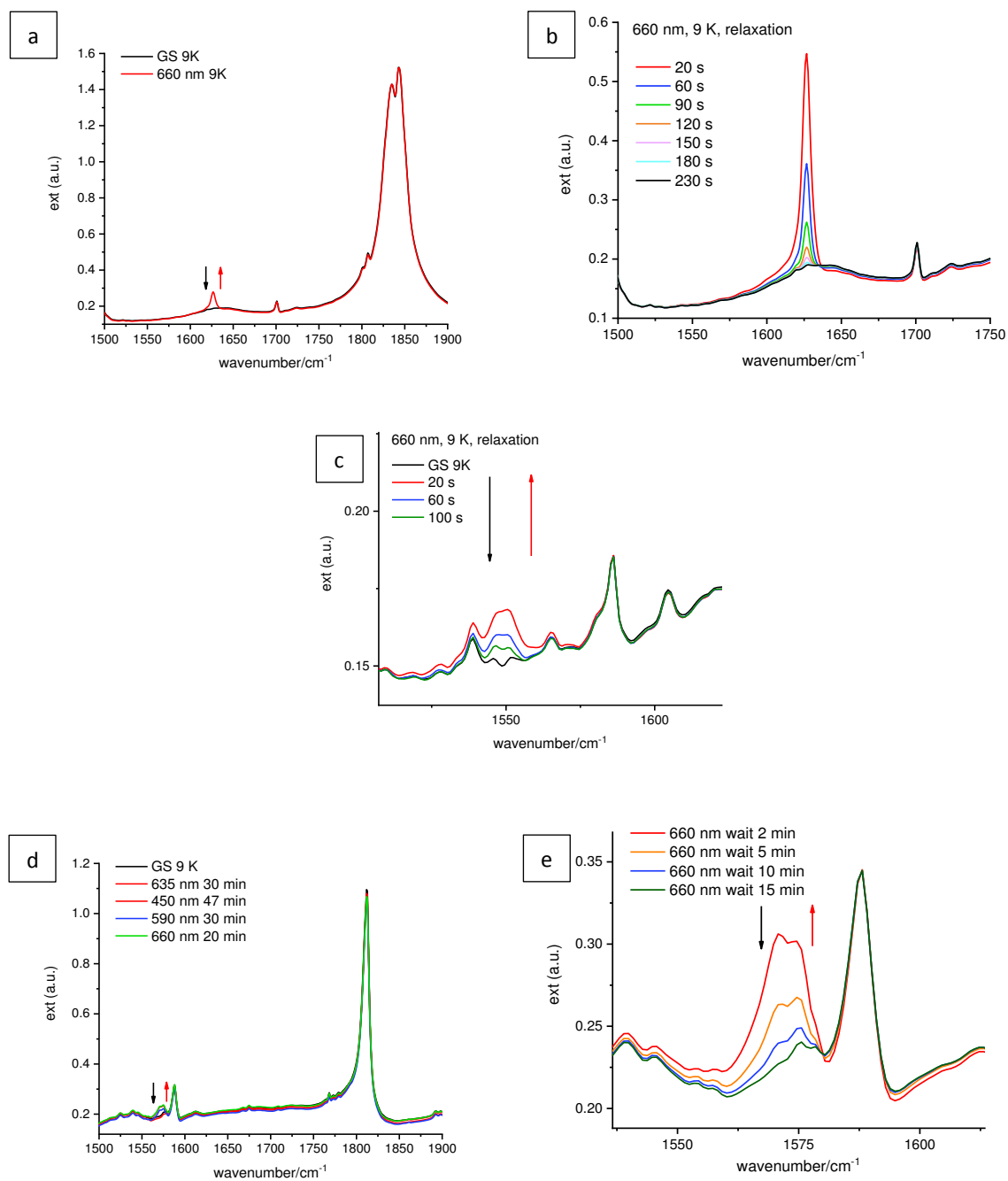
Figure 2.51: PLI results and relaxation time of **1a** (a, b), PLI results of **3** (c), PLI result and relaxation time of **6** (d, e).
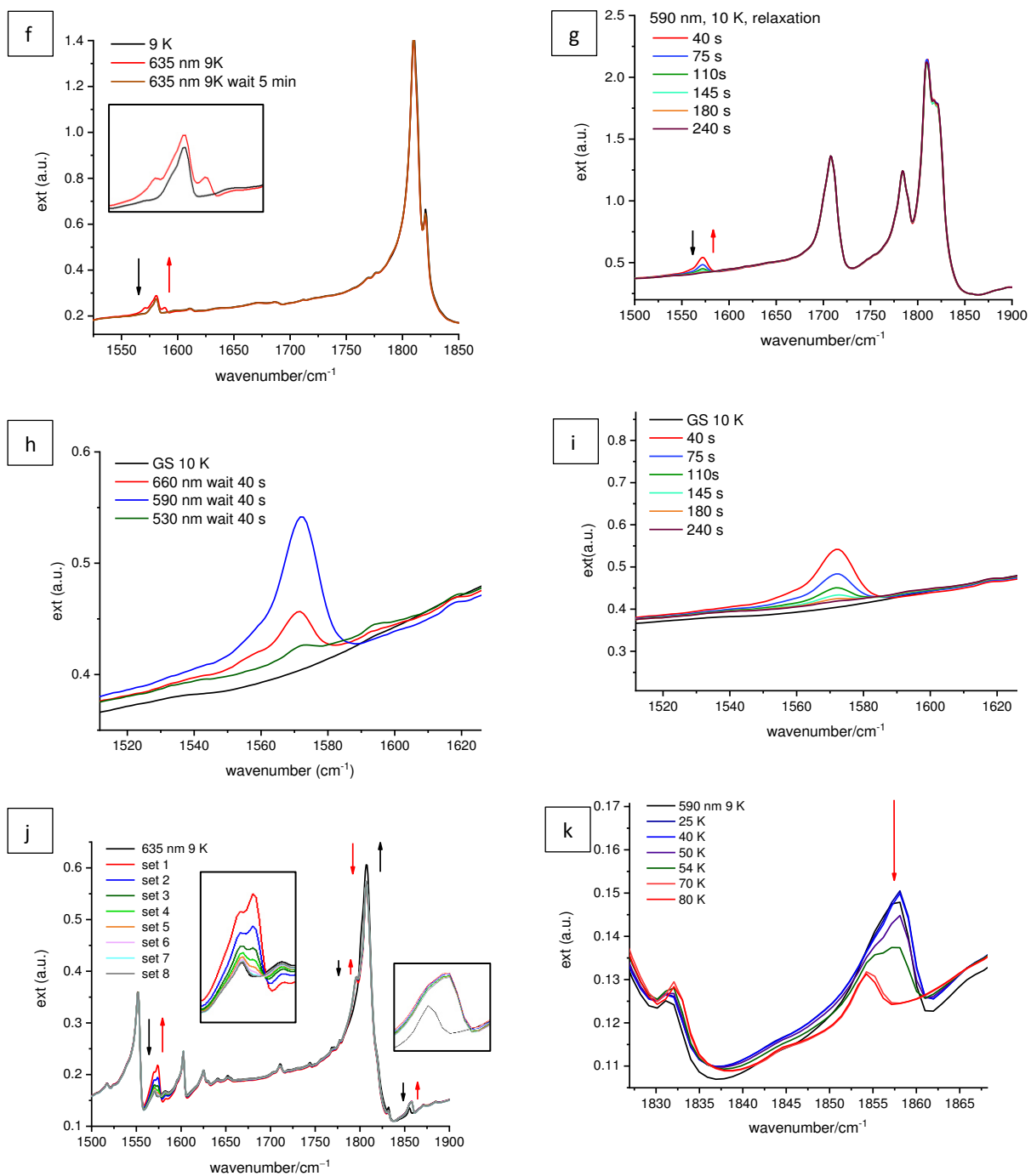
Figure 2.52: PLI results of **7** (f), PLI results and relaxation time of **4** (g, h, at 590 nm (i)), PLI results and relaxation of **5** (j, k).
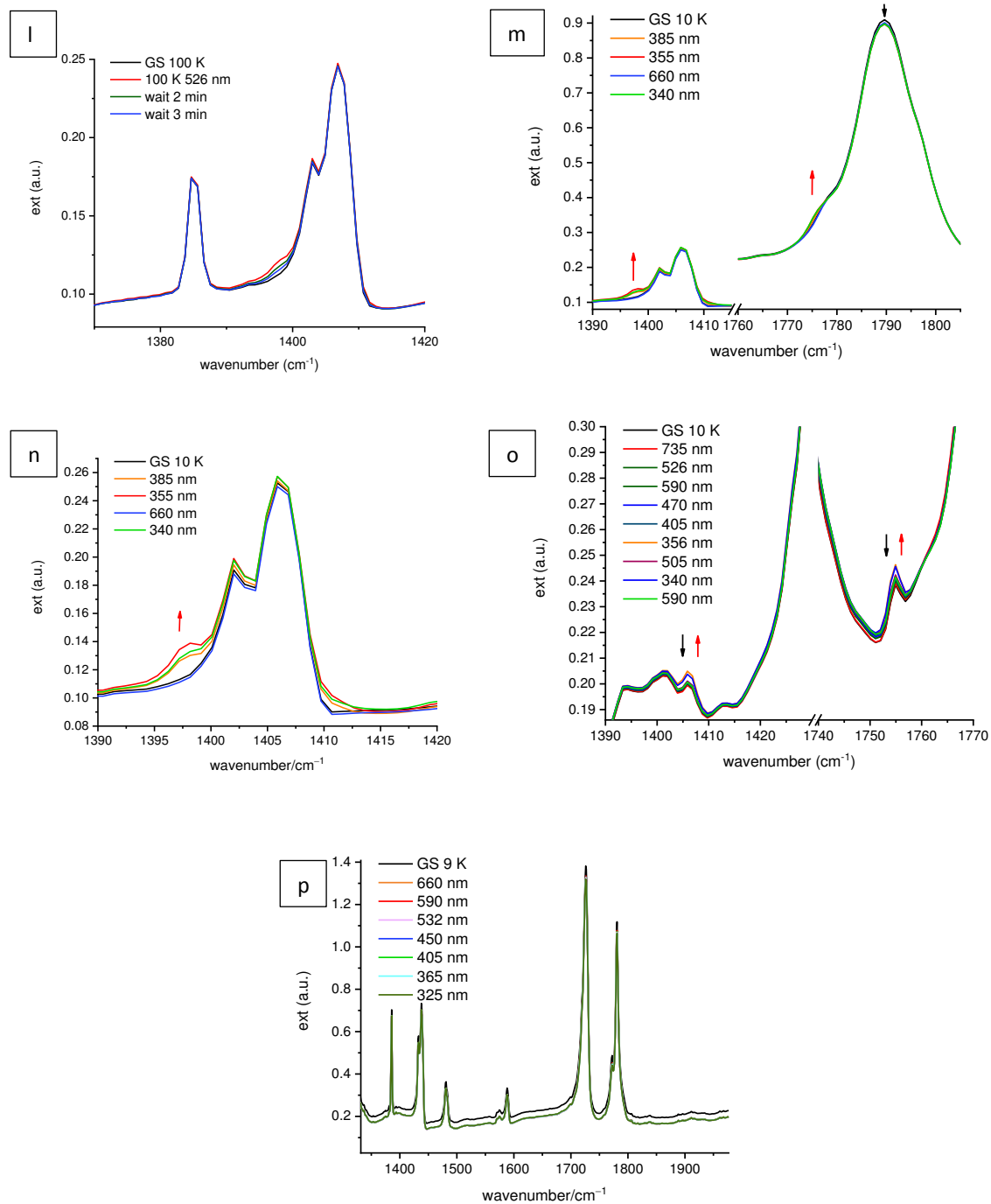
Figure 2.53: PLI results of **14a** (l, m n), PLI results of **14c** (o), PLI results of of **17** (p).
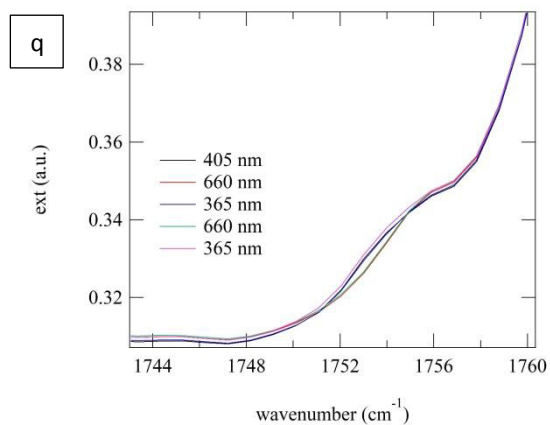
Figure 2.54: PLI results of **19** (q).
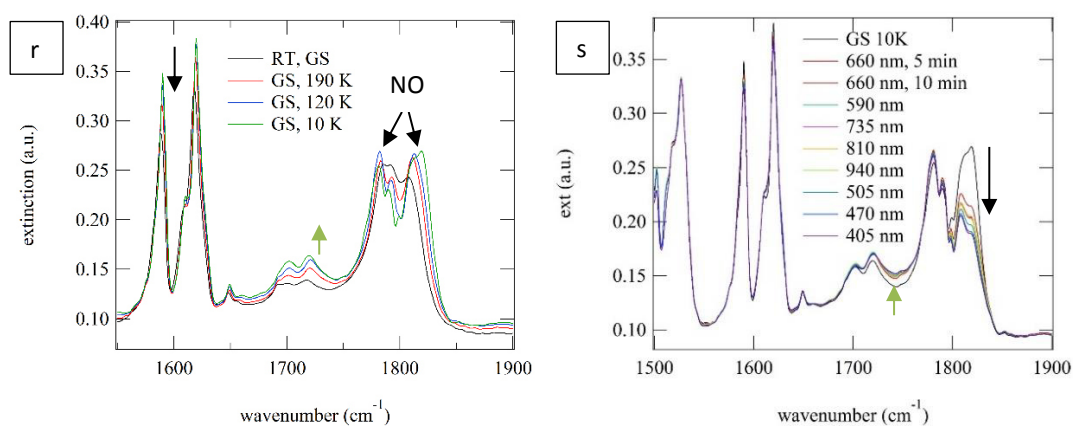
Figure 2.55: (Left) IR spectra of **20a** upon cooling the sample from RT, GS (room temperature, ground state) to 10 K. (right) Irradiation at 10 K with ƛ= 405−940 nm.

2.16 DFT calculations: broken symmetry, structural optimization, IR frequencies and UV/Vis absorptions

Quantum-chemical calculations, performed by ORCA (version 4.0.1), were used to gain a more detailed picture of the electronic structure of the $\{FeNO\}^7$ and $\{Fe(NO)_2\}^9$ complexes. The optimizations were accomplished with starting geometries derived from the experimental single-crystal-structural parameters. The calculations were performed using spin-unrestricted open-shell systems with a quartet spin state for the $\{FeNO\}^7$ compound and with a doublet spin state for the $\{Fe(NO)_2\}^9$ compounds. A satisfying geometry optimization was obtained by using the pure density functional BP86 with the def2-TZVP basis set level. Hence, all DFT calculations were executed on this level. In addition, Grimme's D3 dispersion correction[61] was applied to consider *van-der-Waals* interactions, and the CPCM model was applied for solvent correction. Time-dependent DFT (TD-DFT) calculations were applied to assign the electronic transitions and their corresponding orbital contributions to the UV/Vis spectroscopic data. The similar level BP86/def2-TZVP, d3 and cpcm(MeOH) was applied. Furthermore, the wave-function-based method CASSCF was, finally, applied in order to approve the data from the DFT calculations.

Table 2.19: DFT results on $[FeCl_3(NO)]^-$ and $[FeBr_3(NO)]^-$. Exp.: experimental data, calc.: calculated (BP86/def2-TZVP, d3, cpcm(MeOH)).

$[FeCl_3(NO)]^-$	Exp. **1a**	Calc.	$[FeBr_3(NO)]^-$	Exp. **12**	Calc.
Fe–Cl/Å	2.237*	2.248	Fe–Br/Å	2.371*	2.396
Fe–N1/Å	1.710(7)	1.703	Fe–N1/Å	1.732(5)	1.698
N–O1/Å	1.154(9)	1.166	N–O1/Å	1.145(7)	1.165
Fe–N–O/°	175.2(6)	179.1	Fe–N–O/°	173.5(3)	179.5
$\tilde{\nu}(N–O)/cm^{-1}$	1806	1789	$\tilde{\nu}(N–O)/cm^{-1}$	1794	1786

*mean value

Table 2.20: DFT results on $[FeCl_2(NO)_2]^-$, $[FeBr_2(NO)_2]^-$ and $[FeI_2(NO)_2]^-$. Exp.: experimental data, calc.: calculated (BP86/def2-TZVP, d3, cpcm(MeOH)).

d/Å	$[FeCl_2(NO)_2]^-$ Exp. *	Calc.	$[FeBr_2(NO)_2]^-$ Exp. **15b**	Calc.	$[FeI_2(NO)_2]^-$ Exp. **19**	Calc.
Fe–X1	2.275	2.286	2.4108(4)	2.435	2.5911(3)	2.611
Fe–X2	2.275	2.287	2.4173(4)	2.434	2.5911(3)	2.613
Fe–N1	1.702	1.665	1.7077(19)	1.662	1.687(13)	1.658
Fe–N2	1.158	1.665	1.7686(4)	1.663	1.687(13)	1.658
N1–O1	1.158	1.179	1.144(2)	1.177	1.1740(19)	1.177
N2–O2/	1.158	1.179	1.182(5)	1.177	1.1740(19)	1.177
Fe–N1–O1/°	162.6	161.9	166.1(4)	163.4	165.24(14)	166.0
Fe–N2–O2/°	162.6	161.8	162.76(17)	163.6	165.24(14)	166.5
$\tilde{v}$(N–O)/cm^{-1}	1695	1679	1709	1689	1704	1691
	1780	1766	1776	1768	1753	1759

*: mean of four X-ray experiments.

Table 2.21: DFT results on [Fe(bipzpy)Cl$_2$(NO)]·MeOH (**20a**) and [Fe(bipzpy)Cl$_3$]·MeOH (**20c**). Exp.: experimental data, calc.: calculated (BP86/def2-TZVP, d3, cpcm(MeOH)), calc.*: calculated (BP86/def2-TZVP without d3, cpcm(MeOH)).

d/Å	Exp. **20a**	Calc. d3	Calc. d3, cpcm(MeOH)	Calc.*	d/Å	Exp. **20c**	Calc.
Fe–Cl1	2.3748(7)	2.395	2.399	2.369	Fe–Cl1	2.349(5)	2.378
Fe–Cl2	2.4753(7)	2.337	2.478	2.370	Fe–Cl2	2.365(5)	2.375
Fe–N(O)	1.765(2)	1.728	1.726	1.723	Fe–Cl3	2.2236(6)	2.255
Fe–N1(L)	2.1967(19)	2.191	2.152	2.228	Fe–N1(L)	2.131(15)	2.150
Fe–N2(L)	2.1390(18)	2.193	2.153	2.229	Fe–N2(L)	2.148(15)	2.149
Fe–N3(L)	2.1469(18)	2.169	2.130	2.184	Fe–N3(L)	2.142(15)	2.178
trans to NO							
N–O1	1.153(3)	1.172	1.170	1.174			
Fe–N–O/°	154.0(2)	151.6	152.3	149.9			
$\tilde{v}$(N–O)/cm^{-1}	1781	1760	1735	1750			

Table 2.22: DFT results on [Fe(bipzpy)(NO)$_2$]BF$_4$ (**21**). Exp.: experimental data, calc.: calculated (BP86/def2-TZVP, d3, cpcm(MeOH)), calc.*: calculated (BP86/def2-TZVP without d3, cpcm(MeOH)).

d/Å	Exp. **21**	Calc. d3	Calc. d3 cpcm (MeOH)	d/Å	Exp. **23**	Calc. d3 cpcm (MeOH)	Calc. d3	Calc.*
Fe–N1	1.687(4)	1.680	1.676	Fe–Cl1	2.4545(10)	2.392	2.392	2.323
Fe–N2	1.694(5)	1.681	1.677	Fe–N1	1.809(3)	1.736	1.736	1.739
N1–O1	1.176(6)	1.165	1.170	N1–O1	1.121(4)	1.174	1.174	1.171
N2–O2	1.180(7)	1.165	1.170	Fe–N2	2.169(3)	2.221	2.221	2.260
Fe–N3(L)	2.133(5)	2.125	2.111	Fe–N5(L)	2.122(3)	2.190	2.190	2.227
trans to NO				*trans* to NO				
Fe–N4(L)	2.147(4)	2.164	2.154	Fe–N3(L)	2.149(3)	2.125	2.125	2.193
Fe–N5(L)	2.167(4)	2.166	2.156	Fe–N6(L)	2.199(3)	2.104	2.104	2.178
Fe–N1–O1/°	167.3(5)	163.0	160.8	Fe–N1–O1/°	148.8(3)	145.6	145.6	147.7
Fe–N2–O2/°	160.9(4)	162.9	160.3	$\tilde{v}$(N–O)/cm^{-1}	1765	1700	1733	1747
$\tilde{v}$(N–O)/cm^{-1}	1715	1800	1709					
	1796	1849	1797					

2.16.1 Broken-symmetry results

Broken-symmetry (BS) calculations were used to analyze spin-coupling parameters of the nitrosyl-iron compounds.[62,63] The Heisenberg exchange coupling constant J was calculated in order to quantify the strength of the antiferromagnetic spin coupling and the overlap integrals $S_{\alpha\beta}$ for estimating the covalent bonding character. The BS calculation started from a ferromagnetic coupled spin state (hs) and generated a broken-symmetry state by swapping the spins at the metal center with the smaller number of unpaired electrons. The coupling constant J determined the energetically arrangement of the spin states (Equation 4) and was calculated from the energy difference between the ferromagnetically coupled (E_{hs}) and the broken-symmetry state (E_{bs}) by Yamaguchi's expression (Equation 5).[64]

$$E\,(S) = \;\; -JS(S+1) \qquad\qquad (4)$$

$$J = \;\; -\frac{E_{hs}-E_{bs}}{<S^2>_{hs}-<S^2>_{bs}} \qquad\qquad (5)$$

All calculations in this chapter were performed using ORCA version 4.0.1. The geometries of all the models studied in this chapter were optimized in their respective high-spin states using the BP86/def2-TZVP, d3 dispersion correction and the continuum solvation CPCM method with MeOH as solvent.

Table 2.23: Results of the broken-symmetry calculation of $[FeCl_3(NO)]^-$ and $[FeBr_3(NO)]^-$. J: Heisenberg exchange coupling constants, $S_{\alpha\beta}$: overlap integral of the non-orthogonal single coupled orbital pair (HOMO−3) and (HOMO−4), S^2: broken-symmetry spin state.

	$[FeCl_3(NO)]^-$	$[FeBr_3(NO)]^-$
J/cm^{-1}	−2524	−2552
$S_{\alpha\beta}$ (HOMO−3)	0.92	0.93
$S_{\alpha\beta}$ (HOMO−4)	0.92	0.93
S^2	4.05	4.03

The calculated J values in the case of MNIC-Cl and MNIC-Br indicated a strong antiferromagnetic coupling between the iron center and the nitrosyl ligand. Furthermore, the $S_{\alpha\beta}$ of HOMO−3 and HOMO−4 were close to one and, therefore, consistent with an almost covalent bond in the nitrosyl-iron compound. Furthermore, the determined broken-symmetry spin states $<S^2>_{bs}$ of about 4.0 agreed with the real antiferromagnetic spin states $<S^2>_{af}$ of 3.75. These observations can be also

found from the broken-symmetry calculation results of the DNICs species (see Table 2.24). The average $S_{\alpha\beta}$ values of HOMO-1 to HOMO-4 were 0.98 for all $[FeCl_2(NO)_2]^-$, $[FeBr_2(NO)_2]^-$ and $[FeI_2(NO)_2]^-$ ions. These results supported the almost covalent bond in the Fe$-$N$-$O fragment. The determined broken-symmetry spin states $<S^2>_{bs}$ of about 0.92 agreed with the real antiferromagnetic spin states $<S^2>_{af}$ of 0.75.

Table 2.24: Results of the broken-symmetry calculation of $[FeCl_2(NO)_2]^-$, $[FeBr_2(NO)_2]^-$ and $[FeI_2(NO)_2]^-$. J: Heisenberg exchange coupling constants, $S_{\alpha\beta}$: overlap integral of the non-orthogonal single coupled orbital pair (HOMO-1) to (HOMO-4), S^2: broken-symmetry spin state.

	$[FeCl_2(NO)_2]^-$	$[FeBr_2(NO)_2]^-$	$[FeI_2(NO)_2]^-$
J/cm^{-1}	-2750	-2777	-2783
$S_{\alpha\beta}$ (HOMO-1)	0.97	0.97	0.98
$S_{\alpha\beta}$ (HOMO-2)	0.97	0.98	0.98
$S_{\alpha\beta}$ (HOMO-3)	0.97	0.98	0.98
$S_{\alpha\beta}$ (HOMO-4)	0.98	0.99	0.99
S^2	0.95	0.92	0.89

Table 2.25: Results of the broken-symmetry calculation of $[Fe(bipzpy)Cl_2(NO)]\cdot MeOH$ (**20a**) and $[Fe(bipzpy)(NO)_2](BF_4)$ (**21**) and $[Fe(aptz)_2Cl(NO)]Cl\cdot 0.5MeOH)$ (**23**). J: Heisenberg exchange coupling constants, $S_{\alpha\beta}$: overlap integral of the non-orthogonal single coupled orbital pair (HOMO-3) and (HOMO-4) for **20a**, (HOMO-1) to (HOMO-4) for **21**. S^2: broken-symmetry spin state.

	20a	23		21
J/cm^{-1}	-2539	-2401	J/cm^{-1}	-2880
$S_{\alpha\beta}$ (HOMO-3)	0.92	0.90	$S_{\alpha\beta}$ (HOMO-1)	0.97
$S_{\alpha\beta}$ (HOMO-4)	0.94	0.94	$S_{\alpha\beta}$ (HOMO-2)	0.97
S^2	4.03	4.07	$S_{\alpha\beta}$ (HOMO-3)	0.98
			$S_{\alpha\beta}$ (HOMO-4)	0.98
			S^2	0.95

The broken-symmetry calculation results from Table 2.25 showed that compound **20a** and **21** had a strong antiferromagnetic coupling between the iron center and the NO moieties, and the overlap integral values $S_{\alpha\beta}$ were consistent with an almost covalent bond in the Fe$-$N$-$O fragment. The determined broken-symmetry spin states $<S^2>_{bs}$ of about 4.03 in **20a** and 4.07 in **23** agreed with the real antiferromagnetic spin states $<S^2>_{af}$ of 3.75 and, and $<S^2>_{bs}$ of about 0.95 in **21** agreed with $<S^2>_{af}$ of 0.75.

2.16.2 Structure and bonding: the linear, high-spin, covalently π-bonded Fe–NO entity in {FeNO}^{7}(S = 3/2) species[33]

The wave-function theory (WFT), CASSCF calculations were done as part of the publication of the Reference [33] by Prof. Klüfers and are shown below for detail.

The use of density functional and wave function methods for high-spin {FeNO}^{7} species was described thoughtfully by Radoń *et al.*, including the well-known [Fe(H$_2$O)$_5$(NO)]$^{2+}$ ion.[65] Due to the small size of the [FeCl$_3$(NO)]$^-$ and [FeCl$_2$(NO)$_2$]$^-$ ions, a CASSCF(9,13) approach was possible, in which nine electrons were placed in the active space which included the lone pair at the N atom of a formal NO$^+$ donor ligand (3σ in a NO molecular-orbital scheme) and the seven 'Enemark-Feltham electrons'. In total, the active space was made up of the five Fe(3d) orbitals, five Fe(4d) 'second-shell' orbitals and three NO-based orbitals: the mentioned 3σ orbital and the two degenerate π* orbitals. Figure 2.56 shows the active space of nine electrons distributed in eight orbitals (second shell excluded).
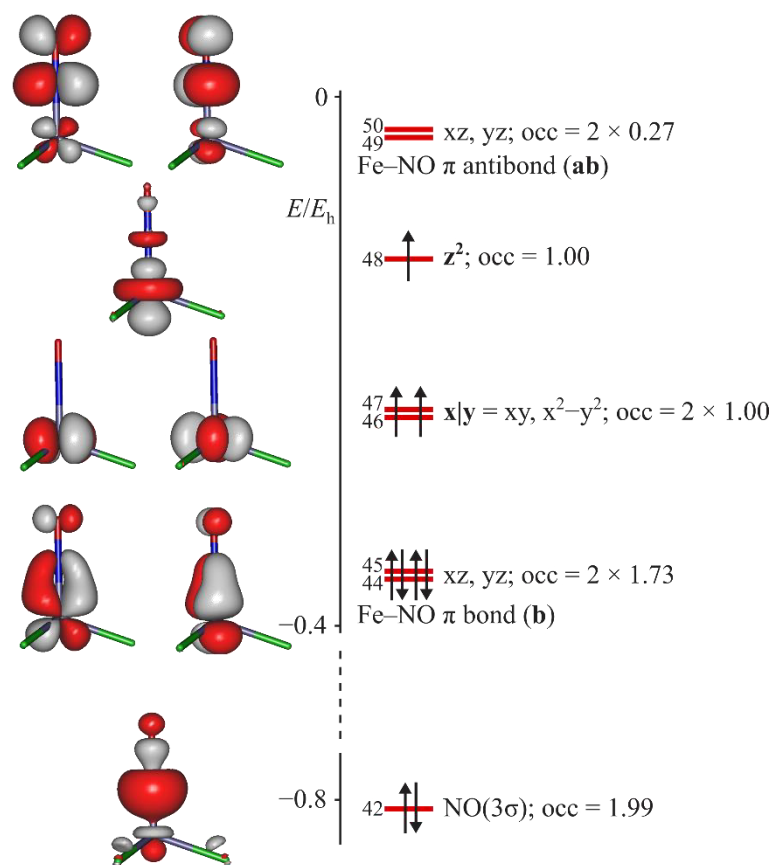
Figure 2.56: Frontier orbitals of the [FeCl$_3$(NO)]$^-$ ion [CASSCF(9,13)/def2-TZVP; isovalue 0.06 a.u.]. Orbital labels refer to Cartesian axes: *z* up, *y* to the right, *x* to the viewer; orbital numbering starts with "1" (= Orca numbering + 1). The 22211100 occupation-pattern indicated by the arrows refers to the ground state's leading configuration (65% contribution). Bold: the abbreviation of a level used in Table 2.29.[33]

The Fe–NO π bonds (MOs 44 and 45) were weakened with an occupation of 2x1.73, while the metal-centered MOs 46 and 46 were both occupied with one electron as well as in the HOMO (MO 48). The depopulation of the Fe–NO π bond corresponded to the population of the respective antibonds MO 49 and 50 of 2x0.27. The three unpaired electrons at the metal center pointed to the high-spin character of the $[FeCl_3(NO)]^-$ ion. In addition, the spin polarization along the Fe–NO fragment was investigated. The calculated Mulliken spin densities for $[FeCl_3(NO)]^-$ ion are: –0.50 on NO and 3.40 on the Fe atom[33] (see Table 2.27 for comparison) which was similar to the related $[Fe(H_2O)_5(NO)]^{2+}$ species of –0.49 on the NO ligand and 3.45 on the Fe atom.[65] The physical reason for the hindered overlap in the two Fe–NO π bonds between the Fe-d(xz and yz) pairs and two empty NO π* orbitals may be seen in Fe-d(xz, yz)–NO(π) Pauli repulsion. Furthermore, additional Pauli repulsion was caused from the nitrogen's lone pair which repelled the singly occupied Fe d_{z^2} orbital. To reduce the repulsion in the MO 48, the Fe–N–O bond angles were often found to be bent of about 150°–180°, as one also can see in **21a**, **21b** and **23** along with in other high–spin $S = 3/2$-{FeNO}^{7} compounds.[41,66] However, the bending of the Fe–N–O bond angles was missing in the $[FeCl_3(NO)]^-$ and $[FeBr_3(NO)]^-$ compounds. The reason for this phenomenon was that there was no ligand coordinating in *trans* position to the NO ligand in the tetrahedral species, therefore the antibonding character was reduced, by Fe(p$_z$) admixture to the Fe d_{z^2} orbital resulting in an almost linear Fe–NO fragment in the entities' compounds. If a broken-symmetry approach was chosen (Table 2.23) for the description of the Fe–NO π-bonds, antiferromagnetic coupling resulted. The calculated coupling constant J of −2524 cm^{-1} and the overlap integral $S_{\alpha\beta} = 0.97$(BP/def2-TZVP), ($S_{\alpha\beta} = 0.84$ on the TPSSh/def2-TZVP level)[33] indicated strong antiferromagnetic coupling, typical for a situation close to a covalent bond.

2.16.2.1 Structure and bonding: {Fe(NO)$_2$}^{9} (S = 1/2) species

A CASSCF(9,14) approach was used for the DNIC-Cl. The active space was made up by the five Fe-d orbitals, two pairs of NO-π* levels, and a second shell for Fe, summing up to 14 orbitals. The nine 'Enemark-Feltham' electrons were occupied in the MOs 41–45. The bonding situation is depicted in Figure 2.57. The calculation showed a close relationship of the DNIC and the respective MNIC. The four Fe–NO π bonds (MOs 41–44,) were weakened with an occupation of 1.77, 1.74, 1.72 and 1.73, respectively. It mirrored the similar occupation number as in the MNIC case (bonding: antibonding of 1.73: 0.27) and in the DNIC case (1.74: 0.26). The HOMO (MO 45) was occupied by a single electron. The depopulation of the Fe–NO π bond corresponded to the population of the respective antibonds MOs 46–48 each of about 0.26. Furthermore, the increase hindered overlap of those four Fe–NO π-bonds caused by the Pauli repulsion was higher than those in the MNIC-Cl species. Thus, these repulsions caused the bending of the Fe–N–O bond angles to approximately 160° (see Table 2.9).

Analogous to the MNIC, the strength of the antiferromagnetic couplings was investigated using

broken symmetry calculations which are presented in Table 2.24. The calculated coupling constant J of -2750 cm^{-1} and the overlap integral $S_{\alpha\beta} = 0.95$ indicated strong antiferromagnetic coupling, typical for a situation close to a covalent bond.
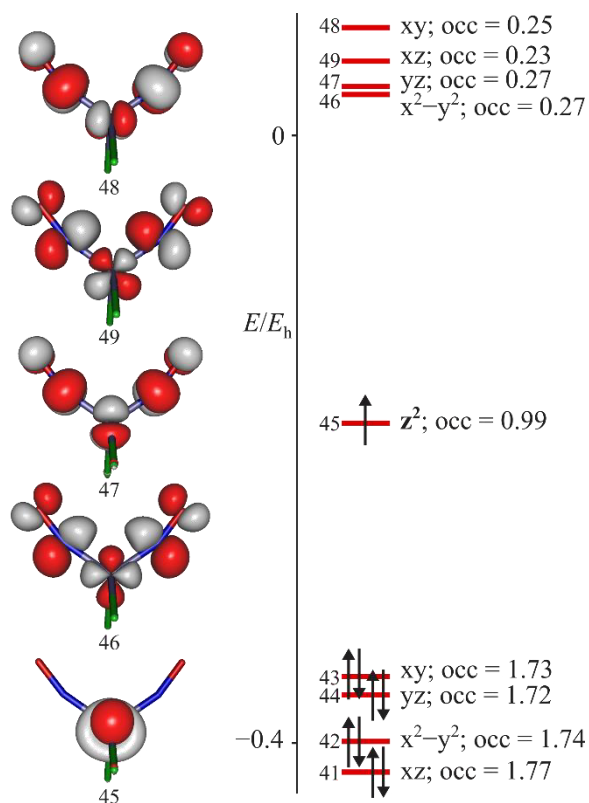
Figure 2.57. Frontier orbitals of the $[FeCl_2(NO)_2]^-$ ion [CASSCF(9,14)/def2-TZVP; isovalue 0.06 a.u.]. Orbital labels refer to Cartesian axes: z to the viewer, y up, x to the right, with a small tilt in favour of a better visualization; orbital numbering starts with "1" (= Orca numbering + 1). The 222210000 occupation pattern indicated by the arrows refers to the ground state's leading configuration (52% contribution). The metal contribution is used to specify an MO. The antibonding MOs are shown which highlight, due to their additional node, the contributing AOs. The bonding MOs ensue correspondingly.[33]

2.16.2.2 DFT calculation of the [FeCl$_3$(NO)]$^-$ ion for PLI investigations

In the PLI measurements which search for metastable states, the reliable assignment of the $\tilde{v}$(N–O)/cm^{-1} was important. Therefore, DFT calculations with different functionals were used and tested for comparison with the experimental data. In this survey, the hybrid functionals B3LYP and TPSSH resulted in too high $\tilde{v}$(N–O) values. A satisfying agreement was achieved with the BP86 functional. The calculated data are presented in the Table 2.26. It should be noted that part of calculations were performed by Prof. Klüfers and were published together in the Reference [33].

Table 2.26: Average distances, angles and $\tilde{v}$(N–O) of six reliably analyzed crystalline solids from the ferrous standard route, and the [FeCl$_3$(NO)]$^-$ ion in DFT calculations for the given method and the def2-TZVP basis set (Grimme's *van-der-Waals* correction; environment modelled by a COSMO [Orca3] or CPCM [Orca4] approach at practically infinite dielectric constant.[33]

	Fe–Cl/Å	Fe–N/Å	N–O/Å	Fe–N–O/°	Cl–Fe–Cl/°	$\tilde{v}$(N–O)/cm^{-1}
mean 6×Xray	2.236 ± 0.006[a]	1.726	1.149	173.5	110.1 ± 1.2[a]	1797
BP86	2.249	1.705	1.167	177.5	108.7	1786
BP86[b]	2.248	1.702	1.165	179.9	108.7	1791
TPSS[c]	2.251	1.712	1.163	176.9	109.2	1792
B97-D	2.275	1.745	1.161	178.3	109.4	1799
B97-D+zora	2.268	1.733	1.163	178.4	109.0	1794

[a] the given standard deviation of the mean exceeds the 10-fold of the mean standard deviation of the X-ray refinement, taken as indicating a 'soft' variable in a crystalline environment
[b] Orca4 with cpcm(water) instead of Orca3.03 with cosmo(water)
[c] the same values were obtained with the def2-aug-tzvpp basis set except 1790 cm^{-1} for the valence vibration

2.16.2.3 Charges

Mulliken population analyses were done for MNIC-Cl, DNIC-Cl, **20**, **21** and **23** and are shown in Table 2.27–Table **2.28**. Mulliken charges for the iron center were significantly method-dependent (Table 2.27). However, for the chlorido ligand, the values were similar and below a full negative charge. Thus, the Fe–Cl bonds appeared to be ionic with a covalent share. For the nitrosyl ligand, the sum of the Mulliken charges of N and O was close to zero. The QTAIM resulted in a slightly higher positive charge at the iron atom and a more negative charge at the nitrosyl ligand.[33]

Table 2.27: Population analyses of MNIC-Cl and DNIC-Cl. The first three entries refer to Mulliken charges for the respective method (def2-TZVP basis for all calculations). The fourth entry shows Mulliken spin densities (BP86/def2-TZVP). The bottom entry shows charges from a QTAIM analysis based on the BP86 calculation of the second entry.[33]

	$[FeCl_3NO]^-$				$[FeCl_2(NO)_2]^-$			
	Fe	N	O	Cl	Fe	N	O	Cl
Mulliken charge:								
CASSCF	1.05	0.25	−0.26	−0.68	0.96	0.08	−0.35	−0.71
BP86	0.47	0.11	−0.10	−0.50	0.38	0.02	−0.16	−0.55
TPSSh	0.57	0.15	−0.12	−0.54	0.44	0.05	−0.19	−0.59
Mulliken spin: BP86	3.11	−0.34	−0.30	0.17	1.80	−0.27	−0.22	0.09
QTAIM: BP86	1.26	0.08	−0.36	−0.66	1.16	0.32	−0.41	−0.71

Table 2.28: Population analyses of **20**, **21** and **23** (BP86/def2-TZVP, d3, cpcm(MeOH)).

			Fe	N	O	Cl
20	BP	charge	0.16	0.02	−0.14	−0.60
		spin	3.12	0.48	−0.26	0.20
	QTAIM (BP86)					−0.76
			1.36	0.10	−0.38	−0.70
21	BP	charge	0.15	0.05	−0.14	
		spin	1.73	−0.24	−0.20	
	QTAIM (BP86)		1.21	0.08	−0.38	
23	BP	charge	0.13	0.18	−0.09	
		spin	3.19	−0.29	−0.25	
	QTAIM (BP86)		1.36	0.09	−0.38	

2.16.3 Computational analysis of the $[FeCl_3(NO)]^-$ ion in terms of UV/Vis spectra

Figure 2.58 shows the typical UV/Vis spectrum of the $[FeCl_3(NO)]^-$ ion as solid (right) and a dissolution in acetone (left). Gauss deconvolution (performed by Prof. Klüfers) was used to assign the possible excitation states. Seven Gauss functions were applied for the solution spectrum where nine Gauss functions were used for the solid spectrum.
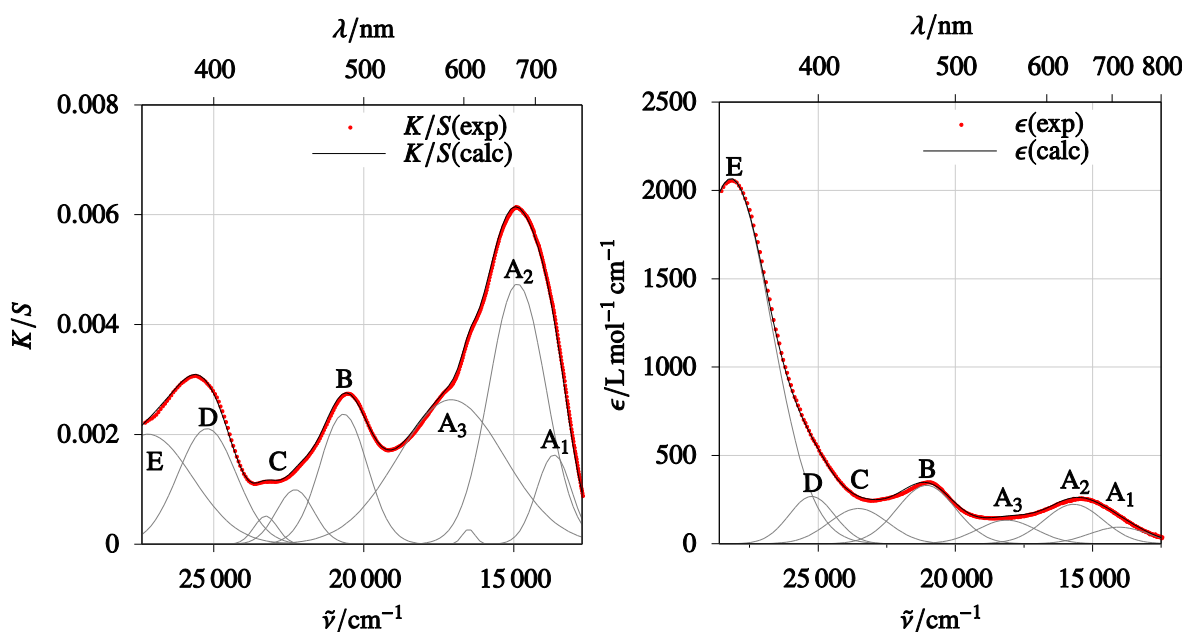
Figure 2.58: (Left) Gauss-deconvolved UV/Vis spectrum of **6** in acetone. Note that the sum (thin black line) of the individual Gauss curves (thin gray bell-shaped curves) coincides with the experimental points; $\varepsilon(\tilde{v})$ was fitted by seven Gauss functions; positions of the maxima (in cm^{-1}): 14030, 15683, 18125, 21054, 23531, 25233, 28183. (Right) Gauss-deconvolved reflectance spectrum of solid **2** diluted with BaSO$_4$. Note that the sum (thin black line) of the individual Gauss curves (thin gray bell-shaped curves) coincides with the experimental points. $K/S(\tilde{v})$ was fitted by nine Gauss functions; positions of the maxima (in cm^{-1}): 13663, 14884, 16507, 17087, 20674, 22288, 23266, 25220, 27185.[33]

TD-DFT and CASSCF(9,13) calculations (Table 2.29) allowed the interpretation of the transition states. As shown in Figure 2.58, three main excitation bands were expected in the α and β channel. The β-spin transitions could occur in three possible ways: (1) from the bonding Fe–NO (MOs 44 and 45) to the degenerate metal-centered MOs of d_{xy} plane (MOs 46 and 47) (label A), (2) to the metal Fe d_{z^2}-center (MO 48) (label B) and (3) to the degenerate antibonding Fe–NO orbitals (MOs 49 and 50) (label C). Three α-spin transitions could occur (1) from d_{z^2} (MO 48) (label D), (2) from degenerate d_{xy} plane (MOs 46 and 47) (label E) and (3) from bonding Fe–NO (MOs 44 and 45) into the degenerate antibonding Fe–NO orbitals (MOs 49 and 50) (label E). Weak excitations which were found only in solution and hardly mirror the calculations, were assigned by means of WFT as spin-forbidden quartet-to-sextet excitations.

Table 2.29: TD-DFT and WFT calculations of the possible transitions in [FeCl$_3$(NO)]$^-$ ion in $\tilde{\nu}$/cm^{-1} (in parentheses: oscillator frequency in atomic units). [a] b, ab and x|y as defined in Figure 2.56; ^{4}b and ^{6}ab refer to a spin-forbidden excitation from the quartet ground state to a sextet excited state. [b] Wave function theory (WFT): NEVPT2(9,13)/def2-TZVP, 15 quartet and 6 sextet state-averaged roots; CPCM ($\varepsilon=\infty$). [c] TD-DFT, f$_{osc}$ as before, TPSSh/def2-TZVP,CPCM ($\varepsilon=\infty$). [d] These columns refer to the experiments of Figure 2.58.[33]

Label	Transition[a]	WFT (f$_{osc}$/10^{-5})[b]	DFT (f$_{osc}$/10^{-5})[c]	Solution[d]	Solid[d]
To A	^{4}b$\rightarrow$^{6}ab	16010 (forb.) 16016 (forb.)	-	to A$_{1-3}$	
A$_{1-3}$	b$\xrightarrow{\beta}$x│y	16378 (0)	15405 (0)	14030	13663
		16692 (27)	15721 (13)	15683	14884
		16842 (68)	17086 (13)	18125	17087
		16886 (37)	17100 (13)		
B	b$\xrightarrow{\beta}$z^2	20424 (167)	22408 (19)	21054	20674
		20430 (167)	22437 (20)		
C	b$\xrightarrow{\beta}$ab	23106 (0)	20712 (2)	23531	22288
		23114 (6)	22776 (2)		23266
		23166 (0)	22756 (0)		
D	z^2$\xrightarrow{\alpha}$ab	25225 (135)	25493 (11)	25233	25220
		25231 (136)	25448 (9)		
E	x│y$\xrightarrow{\alpha}$ab	minor part in b$\xrightarrow{\alpha}$ab	25981 (78) 25977 (79 26533 (102) 26571 (105)	28183	27185
	b$\xrightarrow{\alpha}$ab	29855 (348)	27710 (96)		

As from TD-DFT and CASSCF calculations results, each transition will have weakened the Fe–NO bond, thus allowing change of the nitrosyl bonding situation, which could be achieved in PLI measurements by irradiation with an exemplary 660 nm laser source.

2.16.4 Computational analysis of the [FeCl$_2$(NO)$_2$]$^-$ ion in terms of UV/Vis spectra

Similar investigations were done with [FeCl$_2$(NO)$_2$]$^-$ complexes. The Gauss-deconvoluted UV/Vis spectra of a methanolic solution and solid NMe$_4$[FeCl$_2$(NO)$_2$] are shown in Figure 2.59. The MO scheme of the [FeCl$_2$(NO)$_2$]$^-$ ion in Figure 2.57 shows four classes of one-electron transitions expected in the α and β channel. The β-spin transitions could occur in two possible ways: from the bonding Fe–NO (MOs 41–44) to the (1) to the d$_{z^2}$ orbital (MOs 45) (label B) and (2) to the degenerate antibonding Fe–NO orbitals (MOs 46–48) (label C). Two α-spin transitions could occur from (1) from d$_{z^2}$ (MOs 45) (label D) and (2) from bonding Fe–NO (MOs 41–44) (label C) into the degenerate antibonding Fe–NO orbitals (MOs 46–48) (label D, E). When the TD-DFT and WFT calculations were done, however, the results did not give a clear explanation for the observed transitions. Due to many non-degenerate orbitals in the [FeCl$_2$(NO)$_2$]$^-$ ion, the spectra were broadened, and, thus, difficult to assign the transitions. However, the primary TD-DFT and WFT calculations should be used as a guideline.
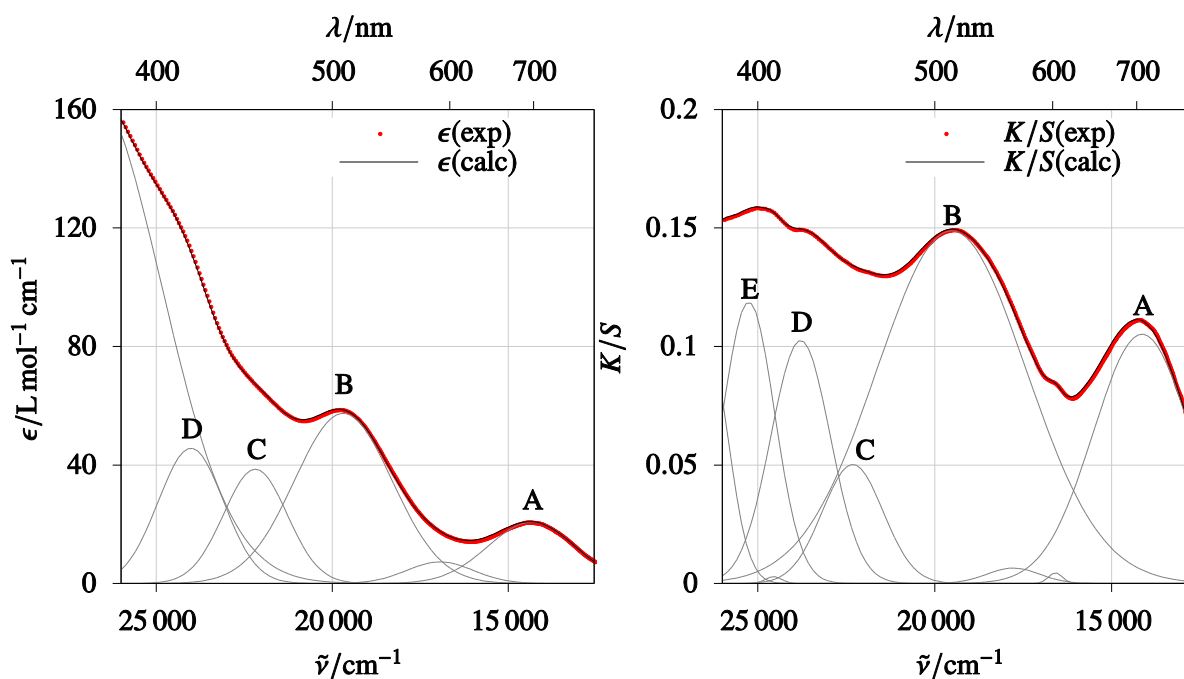
Figure 2.59: (Left) UV/Vis spectrum of NMe$_4$[FeCl$_2$(NO)$_2$] in methanol. The maxima of the visual range fit to 14343 (A), 19688 (B), 22186 (C) and 24016 cm^{-1} (D). (Right) UV/Vis spectrum of solid NMe$_4$[FeCl$_2$(NO)$_2$] diluted with BaSO4. The maxima of the visual range fit to 14139 (A), 19524 (B), 22317 (C), 23789 (D) and 25256 cm^{-1} (E).[33]

Table 2.30: TD-DFT and WFT calculations of the possible transitions in $[FeCl_2(NO)_2]^-$ compound. [a] b, ab and z^2 as defined in Figure 2.57; ^{2}b and ^{4}ab refer to a spin-forbidden excitation from the quartet ground state to a sextet excited state. [b] Wave function theory (WFT): $\tilde{\nu}/cm^{-1}$ (in parentheses: oscillator frequency in atomic units); NEVPT2(9,13)/def2-TZVP, 15 quartet and 6 sextet state-averaged roots; CPCM ($\varepsilon=\infty$). [c] TD-DFT, f_{osc} as before, TPSSh/def2-TZVP, CPCM ($\varepsilon=\infty$). [d] These columns refer to the experiments of Figure 2.59.[33]

Label	Transition[a]	WFT ($f_{osc}/10^{-5}$)[b]	DFT ($f_{osc}/10^{-5}$)[c]	Solution[d]	Solid[d]
A	$^2b\rightarrow{}^4ab$	11698 (forb.)		10905	14139
		13934 (forb.)		14343	
B	$b\xrightarrow{\beta}z^2$	16295(25)	16169(58)	19688	19524
		18880(307)	18208(260)		
		23035(67)			
	$b\xrightarrow{\beta}ab$	23846(56)			
C	$z^2\xrightarrow{\alpha}ab$	23363(103)	23917(603)	22186	22317
		24996 (22)			
D, E	$b\xrightarrow{\alpha}ab$	25324 (400)	26271 (640)	24016	23789
		25552 (40)	26650 (1481)		25256
		26769 (251)	28355 (30)		

3 Discussion

3.1 Synthesis of [FeCl$_3$(NO)]$^-$ ions from ferric route

The formation of methyl nitrite (MeONO) during the reaction of MeOH and NO in the presence of iron salt plays an important role. By treatment of the starting Fe^{III} salt with gaseous NO, the Fe^{III} ion was reduced *in situ* to Fe^{II} which reacted with further NO to form the {FeNO}^{7} ($S = 3/2$) species and methyl nitrite. This process is called reductive nitrosylation.[67,68] The formation of alkyl nitrites by treatment methanolic solution of FeCl$_2$ or CoCl$_2$ in the presence of base such as NEt$_3$ with gaseous NO is long known. It was observed as well, when NO$^+$ salts such as NOBF$_4$, NOPF$_6$ or (NO)HSO$_4$ were dissolved in alcoholic solvents (Scheme 3.1).[67,69] The latter solvolysis reactions can be accelerated when a base is present in the mixture solution (Scheme 3.1).[67,69]

$$NO^+ + ROH \rightleftharpoons RONO + H^+$$

Scheme 3.1: Solvolysis reaction of alkyl nitrite.[69]

An example for the formation of methyl nitrite was observed in the course of the synthesis of [Fe^{II}(TPP)(NO)], starting from [Fe^{III}(TPP)Cl] dissolved in toluene/methanol, and nitric oxide.[70] In this present work, when FeCl$_3$ plus additional Cl$^-$ or [FeCl$_4$]$^-$ was treated with gaseous NO, that NO first reduced Fe^{III} to Fe^{II} and turned itself to NO$^+$. Then, NO$^+$ reacted with MeOH to form MeONO and H$^+$, thus enhancing the acidity of the solution. The [FeCl$_4$]$^{2-}$ ion finally reacted with further NO to form [FeCl$_3$(NO)]$^-$. To sum up, the reaction mechanism of ferric precursor and gaseous NO in methanol can be described as shown in Scheme 3.2. In summary, the ferric precursor route requires two equivalents of gaseous nitric oxide to complete the formation of [FeCl$_3$(NO)]$^-$.

$$[Fe^{III}Cl_4]^- + NO + MeOH \rightleftharpoons [Fe^{II}Cl_4]^- + MeONO + H^+$$

$$[Fe^{II}Cl_4]^{2-} + NO \longrightarrow [FeCl_3(NO)]^- + Cl^-$$

$$\overline{[Fe^{III}Cl_4]^- + 2\,NO + MeOH \longrightarrow [FeCl_3(NO)]^- + MeONO + HCl}$$
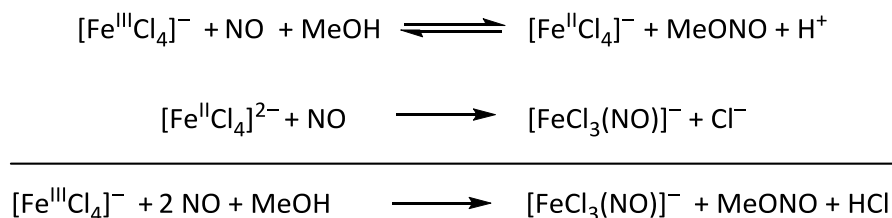
Scheme 3.2: Proposed mechanism of the synthesis of trichloridonitrosylferrates starting from [FeCl$_4$]$^-$ ion by formation of methyl nitrite.

In fact, MeONO was frequently observed in UV/Vis and IR spectra it was not quantitatively analyzed. If MeONO is present in the solution, a typical "five fingers" absorption spectrum with bands between

320–370 nm (Figure 2.5) is observed. Piper and Drago have studied the solubility of NO in different solvents and observed a similar five-finger pattern in MeOH as well as in CH_3CN and CCl_4.[71] The similar absorption pattern can be found also in aqueous HNO_2 but with a shift to longer wavelengths. To confirm the formation of MeONO via NO^+, $NOBF_4$ was dissolved in MeOH. Its absorption spectrum was compared to the one from the reaction of the $[FeCl_3(NO)]^-$ compound and confirmed the result. Recently, Speelman et al. detected gaseous MeONO by IR spectroscopy in the course of Fe^{III} reduction in MeOH and NO as a by-product in the DNICs $\{Fe(NO)_2\}^9$ synthesis.[72] That observation is analogous to the results in DNIC-Cl synthesis in which MeONO was detected by a UV/Vis analysis (see Figure 2.5, in Chapter 2).

Furthermore, the reductive nitrosylsation is not specific for $A[FeCl_3(NO)]$ but can also be applied for the synthesis of $[Fe(bipzpy)Cl_2(NO)]\cdot MeOH$ (**20b**) from the ferric route.

3.2 Consecutive MNIC-to-DNIC-transformation in the presence of base

The IR results in Section 2.7 showed that the synthesis of DNIC-Cl is a consecutive reaction and takes place via the formation of a green MNIC-$[FeCl_3(NO)]^-$ solution (see Equation 3). The reaction involved the formation of MeONO which was accelerated by the presence of base (here: fluoride). The water content of the starting iron salts or fluoride salts did not interfere with the reaction nor was a need to limit the NO dosage. Furthermore, the red-brown DNIC solutions are accessible more directly by using $(NMe_4)F$ (Equation 4). The summary of synthetic routes of DNIC-Cl is shown in Figure 3.1. Similar to these results, the formation of the anionic $[FeCl_2(NO)_2]^-$ in the presence of bases like NEt_3 has already been described by Gwost and Caulton (Equation 1–2) but at that time, no X-ray data was available.[67]

$$FeCl_2 + 3\ NO + MeOH + B \rightarrow [FeCl_2(NO)_2]^- + MeONO + BH^+ \tag{1}$$

$$FeCl_2 + 3\ NO + MeOH + NEt_3 \rightarrow NHEt_3[FeCl_2(NO)_2] + MeONO \tag{2}$$

$$[FeCl_3(NO)]^- + F^- + 2\ NO + MeOH \rightarrow [FeCl_2(NO)_2]^- + Cl^- + MeONO + H^+F^- \tag{3}$$

$$FeCl_2 + 2\ (NMe_4)F + 3\ NO + MeOH \rightarrow NMe_4[FeCl_2(NO)_2] + MeONO + NMe_4^+\ HF_2^- \tag{4}$$
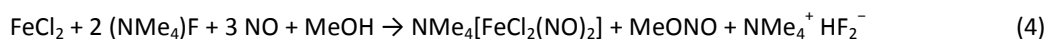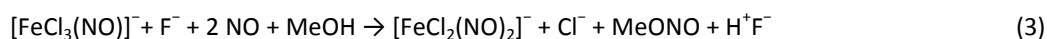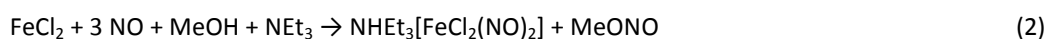
Scheme 3.3: Synthesis of dichloridodinitrosylferrate from $FeCl_3$ and $FeCl_2$ salt.[33]

FeCl$_2$·4H$_2$O
Fe(OTf)$_2$·4MeOH
Fe(OTs)$_2$·6H$_2$O

MNIC
[FeCl$_3$(NO)]$^-$

reductive nitrosylation

FeCl$_3$

base

[FeCl$_2$(NO)$_2$]$^-$

DNIC

base: (NMe$_4$)F, (NBnMe$_3$)F, (NBu$_4$)F, NEt$_3$
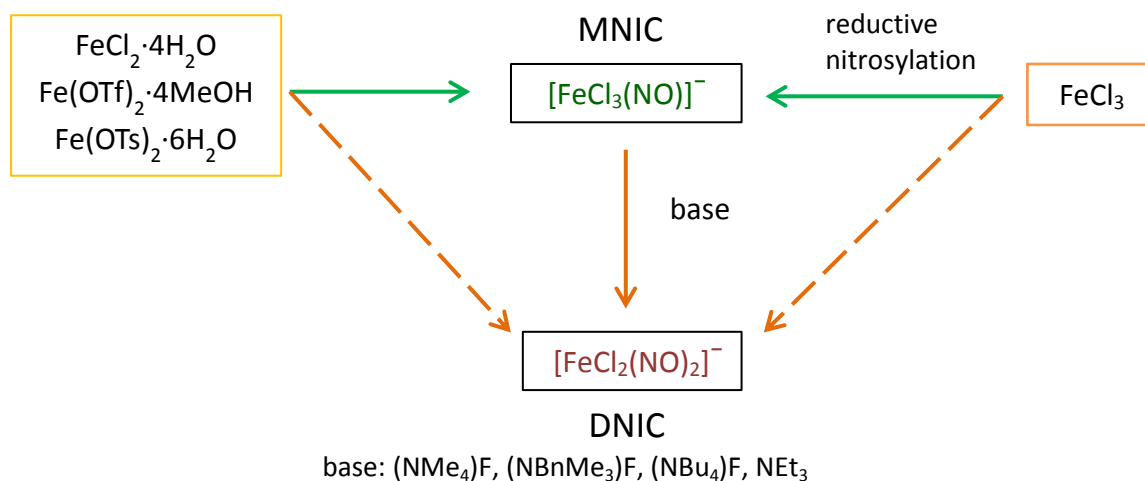
Figure 3.1: Synthesis of DNIC-[FeCl$_2$(NO)$_2$]$^-$ *via* formation of MNIC-[FeCl$_3$(NO)]$^-$ complex.

The stability of the MNIC and DNIC compounds

The methanolic solutions of halogenido-MNICs were stable under nitric oxide atmosphere for years, but they lose their green color at once on exposure to inert gas or air, which is caused by the loss of bonded NO. This reaction is reversible and reproducible (Scheme 3.4). In contrary, the halogenido-DNIC solutions are stable against air or inert gas and cannot be reversed to MNIC. In summary, MNIC-Cl is stable and may be captured in acidic media while DNIC-Cl is preferably formed in less acidic to basic solutions. Crystalline products of MNICs and DNICs compounds are air stable. However, when MNIC-Cl compounds are dissolved in methanol, they immediately lose NO ligand. Contrarily, on dissolution in acetone it is obviously stable. The instability of {FeNO}^{7} solutions against inert gas or air is known for stable aminocarboxylato {FeNO}^{7} compounds of limited stability.[27,41,57]

$$[FeCl_4]^{2-} + 2\,NO + MeOH \rightleftharpoons [FeCl_3(NO)]^- + MeONO + H^+ + Cl^-$$

H$^+$ $\quad$ + NO, base (B)

$$[FeCl_2(NO)_2]^- + Cl^- + BH^+ + MeONO$$
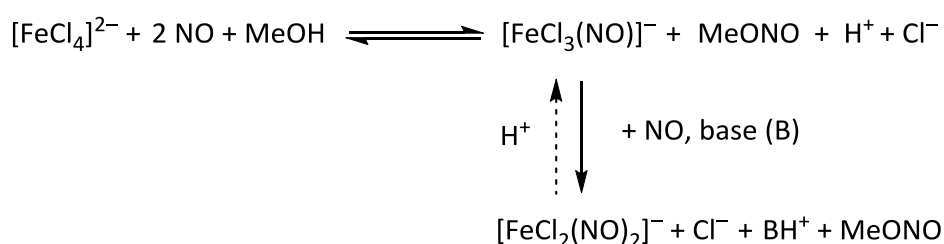
Scheme 3.4: Transformation of MNIC-[FeCl$_3$(NO)]$^-$ to DNIC-[FeCl$_2$(NO)$_2$]$^-$ in the presence of base.

3.3 Crystallography: crystal structures, crystal inconsistency and seeding

3.3.1 Crystal structures and spectroscopic data of the halogenidonitrosylferrates

During this thesis 19 halogenidonitrosylferrates were isolated in crystalline form and characterized by X-ray diffraction. The MNIC-X compounds (X = Cl, Br) feature an almost linear Fe–N–O fragment with an angle between 170–177°. The average bond lengths are: about 1.73 Å for Fe–N and 1.15 Å for N1–O1. The Fe–N–O stretches for all MNICs are found at around 1800 cm^{-1}. The UV/Vis spectra for all MNICs are found with λ_{max} at around 400 nm, 480 nm and 600 nm while for all DNICs are found at around 500 nm and 700 nm. All halogenidonitrosylferrates described in this thesis have tetrahedral coordination geometry. The structures of $[FeCl_3(NO)]^-$ and $[FeBr_3(NO)]^-$ in MNIC-X (**1**–**13**) are similar in geometry to those published in literature.[36,37,39–41] Most of the halogenido-nitrosylferrates presented in this thesis are novel and well-ordered. The structures of DNIC-X, (X = Cl, Br, I) (**14**–**19**) have slightly distorted tetrahedral coordination geometry. The Fe–N–O fragments are bent towards each other with an angle between 161° and 166°. The average Fe–N bond length is 1.70 Å and N–O bond length is 1.16 Å. The two NO stretches for all DNICs are found at around 1700$_{(asym)}$ and 1770$_{(sym)}$ cm^{-1}. The structures of $[FeCl_2(NO)_2]^-$ ion recently reported in literature is are disordered.[38,73] Hence, the DNIC-Cl compounds described in this work are the first well-ordered ever published (**14a**–**d**, CCDC database 1866200, 1867068, 1866202, 1867069). The structures of $[FeBr_2(NO)_2]^-$ ions reported herein are the first of this kind (**15a**–**b**, CCDC database, September 2019, 1866200 (**15b**).[33] However, the synthetic route for $[FeBr_2(NO)_2]^-$ ion has still to be improved. Finally, the structures of the $[FeI_2(NO)_2]^-$ ions in **16**–**19** are nearly identical to those published in literature.[43] Comparing all structures obtained in this work, it may be concluded that the counter ion have little influence on the geometry of the anions and the spectroscopic data.

3.3.2 Crystal pathology and seeding: a substitutional disorder

The crystalline halogenidonitrosylferrates exhibit a typical pathology that originates from the interchangeableness of the chlorido and nitrosyl moieties on the positions occupied by the ligands. The observed of disorder of chlorido and nitrosyl ligands usually resulted by substitution between $[FeCl_4]^-$, $[FeCl_3(NO)]^-$ and $[FeCl_2(NO)_2]^-$, when these ions are existed in the same mother liquor. Due to the instability of the $[FeCl_3(NO)]^-$ and $[FeBr_3(NO)]^-$ solutions, recrystallization was not available as a purification procedure. The substitional disorder is found, for example, in **2b**. The crystallization time of the product NEt$_4$[FeCl$_3$(NO)] (**2b**) derived from the FeCl$_3$ route was shorter than from the FeCl$_2$ route (two weeks compared to a year, respectively). After structure determination, the ferric-route batches revealed 15% of $[FeCl_4]^-$ co-crystallized in the **2b** salt. From this observation, it

concluded that the contaminant $NEt_4[FeCl_4]$ had served as a seed and enhanced the crystallization velocity, because of its low solubility in the mother liquor. The presence of a ferric contamination became obvious in the measurement of the magnetic properties of the samples (Figure 2.47). The results from the ferric-route samples showed higher values than the expected value for the $\{FeNO\}^7$ (S = 3/2) compound. These measured values were similar to those reported by Griffith *et al.* which describes products from the reaction of $FeCl_3$ and NO in ethanolic solution.[34] As already mentioned in Chapter 2, the sample with NMe_4^+ as a counter ion behaved similarly. Even small amount of the $[FeCl_4]^-$ contaminant can affect the atomic structural parameter seriously, especially the Fe–N and N–O bond lengths. Therefore, the DFT calculations of the optimized geometry were applied and used as a guideline for the expected experimental values. Table 3.1 shows the comparison of data derived from DFT results with the experimental data of the crystals derived from both $FeCl_2$ and $FeCl_3$ routes and theirs corresponding corrected values by the structural refinement process.

Table 3.1: Atomic distances from X-ray analyses on a crystal of pure (**1a**) (second row) and $[FeCl_4]^-$ contaminated $NMe_4[FeCl_3(NO)]$ (**1b**) (third and fourth row); 'uncorrected' refers to a nitrosyl position fully occupied by an NO group; 'corrected' includes splitting of the nitrosyl position which, after refinement, was occupied by 0.912(13) NO and 0.088 Cl with Fe–Cl 2.16(3) Å. (compare the typical Fe^{III}–Cl distance of 2.188 Å). b: Orca4 with CPCM(water).[33]

	Fe–N/Å	N–O/Å	$\Delta\rho/e\text{Å}^{-3}$	wR2
BP86[b]	1.702	1.165	-	-
$FeCl_2$ route (**1a**)	1.710(7)	1.154(8)	0.367	0.0875
$FeCl_3$ route (**1b**), corrected	1.729(7)	1.145(12)	0.311	0.0372
$FeCl_3$ route (**1b**), uncorrected	1.789(3)	1.059(3)	0.293	0.0378

As illustrated in Table 3.1, neither the *wR*2 value nor the residual electron density or the crystal structure parameters mirror the contamination of the $[FeCl_4]^-$ ion. However, the bond length of the Fe–N is longer and the N–O is shorter than the calculated values. Furthermore, the thermal ellipsoid of the nitrosyl group shows an unusual behavior: the nitrogen atom should not vibrate along the strong N–O bond but preferably perpendicular to it (Figure 3.2, left). After the structure correction (third row in Table 3.1) which assigned the occupation of the chloride atom of about 8.8% between the N–O bond (at green cross position, Figure 3.2 ,right), resulting both the N and O ellipsoids look reasonable.
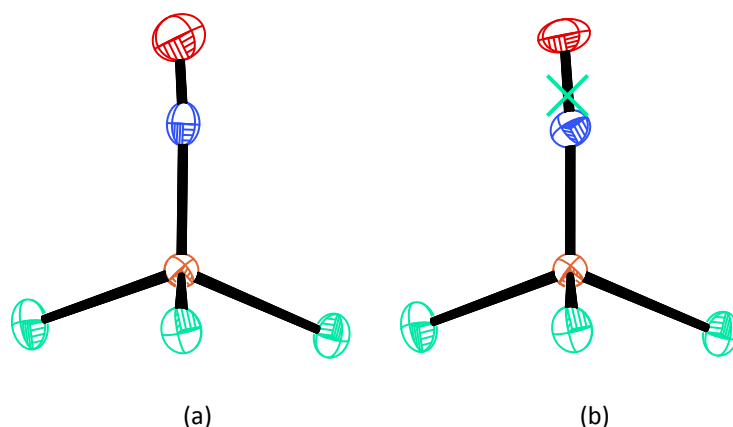
Figure 3.2: The molecular structure of the $[FeCl_3(NO)]^-$ ion in crystal of 1b (50% thermal ellipsoids) (a) the uncorrected X-ray analysis. (b) corrected structure after splitting of the NO position into the depicted N and O atoms with partial disorder of the fourth chloride atom (at the green cross, 0.088 occupancy of Cl and 0.912 occupancy of NO).[33]

As already mentioned in Section 2.4, a yellowish $A[FeCl_4]$ precipitate was frequently observed. Thus, the equation in Scheme 2.7 was reformulated as in the follows:

$$ACl + FeCl_3 + 2NO \rightleftharpoons A[FeCl_4] + 2NO + MeOH \rightleftharpoons A[FeCl_3(NO)] + MeONO + HCl$$

Scheme 3.5: Synthesis of trichloridonitrosylferrates from $FeCl_3$. A: cation.

The preparation of $PPN[FeCl_3(NO)]$ from $FeCl_3$ was investigated by preventing the precipitation of $A[FeCl_4]$ by using a ten-fold dilution of the reaction mixture. The crystallization time now was much longer than usual. However, pure crystalline $PPN[FeCl_3(NO)]$ salt was obtained in similar quality as from the $FeCl_2$ route including a SQUID measurement which revealed μ_{eff} = 4.20, identical to the value from the standard $FeCl_2$ route (see Table 2.14).

3.3.3   Oxidation state of Fe and NO in $[FeCl_3(NO)]^-$ and $[FeCl_2(NO)_2]^-$ complexes.

The bonding situations of the $\{FeNO\}^7$ compounds are discussed and published frequently.[27,33,65,66,74–81] In the past, a typical description was assigned as $Fe^I(S = 3/2)$–$(NO^+)(S = 0)]$.[82] More recently, formulation such as $Fe^{III}(S = 5/2)$–$(NO^-)(S = 1/2)]$[25,83,84] or $Fe^{II}(S = 2)$–$(NO^0)(S = 1)]$[85,86] were reported, with antiferromagnetic coupling of the spins. Besides that, some publications state the oxidation lays in between Fe^{II}–NO^0 and Fe^{III}–NO^-.[79,87] For the $\{Fe(NO)_2\}^9$ DNIC-Cl compounds, different assignments in literatures are found such as $[Fe^I(S = 3/2)$–$(NO^0)_2(S = 1)]$,[88,89] $[Fe^-(S = 1/2)$–$(NO^+)_2(S = 0)]$,[43] $[Fe^{III}(S = 5/2)$–$(NO^-)_2(S = 2)]$[90,91] and $[Fe^{II}(S = 2)$–$(NO^-)_2(S = 3/2)]$.[92]

In the present investigation, the bonding description of the Fe–NO moiety in the MNIC-Cl and DNIC-Cl compounds derives from the DFT calculations concerning two or four Fe–NO π bonds for MNIC

and DNIC, respectively. If four electrons are shared in two bonds (d_{xz}, d_{yz}, and N–O-π*(x), N–O-π*(y) for MNIC (Figure 2.56) or eight electrons are shared in four bonds (d_{xz}, $d_{x^2-y^2}$, d_{yz}, d_{xy} and two sets of N–O-π*(x), N–O-π*(y)) for DNIC (Figure 2.57) at about equal coefficients between the Fe atom and the nitrosyl ligand, it may assign almost covalent bonds. Additionally support was the broken-symmetry calculations which showed kind of almost covalent character with the overlap integral $S_{\alpha\beta}$ = 0.92 and 0.97 for MNIC-Cl and DNIC-Cl, respectively (see Section 2.16.1). Further consideration is the Fe–Cl bond lengths, which experimentally obtained lay in average distances of 2.237 Å, 2.275 Å for MNIC and DNIC, respectively (Table 2.19–Table 2.20). That values range in between the Fe^{II}–Cl bond (2.317 Å) and the Fe^{III}–Cl bond (2.188 Å) compared to CCDC Data base; BERROF01, FIWGIB, GOXLUA, IFEGUY, TMAFEC for $[FeCl_4]^{2-}$ and FUGDER, KURPET, QUXFAR, MECXUO, SURRON for $[FeCl_4]^-$). The Mulliken charge analyses showed that the atomic charges of the iron center varied upon the method but the charges of the NO ligand are close to zero (Table 2.27). Altogether, the results point at an oxidation state of the iron central atom between +2 and +3, say 2.5 + x, which, in turn, possibly assigns a charge of −0.5 + x to the nitrosyl ligand. To sum up, it is concluded that there is a more or less covalent nitrosyl-iron interaction through two or four π bonds (for MNIC and DNIC, respectively).

3.3.4 Crystal structure of hexacoordinated cationic {FeNO}^{7} compounds (20 and 23) and penta-coordinated cationic {Fe(NO)$_2$}^{9} compounds (21 and 22)

The optimized geometries derived from the DFT calculations for the compounds **20a**, **21, 22** and **23** are in good agreement with the crystal structures. Likewise, the frequency analyses reflected good agreement with the experimental data (solid state). DFT calculations without solvation correction showed better IR values for the MNIC-**20a** and MNIC-**23**. However, it fitted better when a solvent correction (CPCM) was used for the DNIC-**21** and DNIC-**22** (Table 2.21 and Table 2.22). Both MNIC-**20a** and MNIC-**23** featured a bent Fe–N–O fragment with an angle of 154° (**20a**) and 148° (**23**), respectively, whereby the DNIC-**21, 22** had its Fe–N–O fragments with an angle of about 167° and 161°. The Fe–N(O) bonds ranged between 1.76 and 1.80 Å and the N–O bond was about 1.12–1.15 Å long. The Fe–N–O stretches for MNICs are found at 1781 cm^{-1} (**21**) and 1765 (**23**) cm^{-1}. That structural parameters as well as spectroscopic data are consistent with other hexacoordinated {FeNO}^{7} (S = 3/2) compounds.[66,81] Cationic DNIC-**21** is a new penta-coordinated {Fe(NO)$_2$}^{9} which is rarely found in the literature, in contrast to the tetra-coordinated anionic, neutral and cationic DNICs with S-, N-, P-, C-, O-donor ligands.[72,93] However, the Fe–N and N–O bond lengths in DNIC-**21** and DNIC-**22** were similar to those of tetra-coordinated compounds published in literature with values of about 1.69 Å and 1.17 Å, respectively.

*Bonding situation in **21**−**23***

The electronic configurations of MNIC-**20a** and MNIC-**23** were investigated and confirmed the quartet spin state. Fe–coligand-bonds measured in crystals of [Fe(bipzpy)Cl$_2$(NO)]·MeOH (**20a**) were longer than in crystals of the ferric precursor [Fe(bipzpy)Cl$_3$]·MeOH (**20c**). For example, the Fe–Cl bond lengths were 2.3748(7) Å and 2.4753(7) Å in **20a** and 2.349(5) Å, 2.365(5) Å and 2.2236(6) Å in **20c** (Table 2.21), indicating that the iron center probably had an oxidation state between II and III. The N–O1 bond length was 1.153(3) Å and $\tilde{\nu}$(N–O) at 1781 cm^{-1}, which can be described as NO^0. Furthermore, the broken symmetry calculations for **20a** and **23** indicated an almost covalent bond between the Fe–NO bonds with the overlapping integral $S_{\alpha\beta}$ of about = 0.92. Additionally, the Mulliken population analyses in these two compounds assigned a nearly neutral charge to the nitrosyl ligand (Table 2.28). The spin densities at the iron center were about 3.10 and 3.19 for **20** and **23**, respectively. To summarize, all computational results as well as the experimental data herein pointed to a bonding situation in **20a** and **23** that should be described intermediated between Fe^{III}–NO$^-$ and Fe^{II}–NO^0 as the dominating oxidation states.

*Bending of the Fe–NO fragments in the MNIC-**20a** and MNIC-**23** compounds*

The Fe–N–O moieties in these crystal structures were bent ($\approx$150°) which the NO fragment tilted towards the chlorine atoms in crystals of **20a**, or towards the nitrogen atom of the thiazole moiety in crystals of **23**. The bending of the Fe–N–O moieties is similar to those in other hexa-coordinated {FeNO}^{7} (S = 3/2) compounds.[66,81] The tilt of NO towards the chlorine atom—or to another electronegative atom—can also be found in the structure of [Fe(edda)(H$_2$O)(NO)].[66] This structural feature is caused by an attractive interaction of the chloride atom and the oxygen atom of the NO fragment. However, bonding overlap in the β-HOMO orbital is responsible for the tilt of the NO fragment. This statement is supported by the DFT calculations shown in Figure 3.3. For **23**, the contrary was found: the Fe–N–O fragment does not tilt to the chlorine atom but towards the nitrogen atom of the thiazole moiety. The DFT calculation supported this statement in which the β-HOMO orbital shows the tilting direction and the β-HOMO−1 orbital shows an additional antibonding interaction between the NO fragment and chlorine atom, as is shown in Figure 3.3.
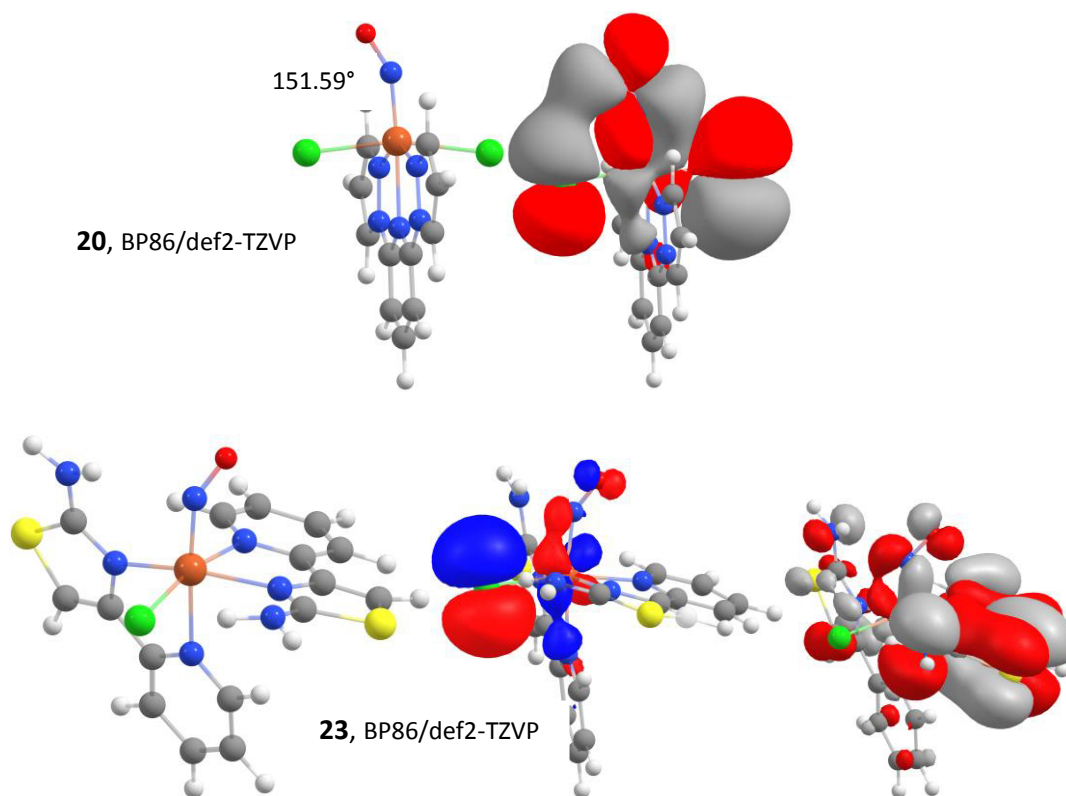
Figure 3.3: (Top left) CHEMCRAFT plot of BP/def2-TZVP, d3-optimized structure of **20a** and (right) β-HOMO of **20a** (BP/def2-TZVP, d3, cpcm(MeOH), isovalue 0.02). (Bottom left) CHEMCRAFT plot of BP/def2-TZVP, d3-optimized structure of **23**, (middle) and (right) β-HOMO−1 and β-HOMO of **20a**, respectively (BP/def2-TZVP, d3, isovalue 0.02).

3.4 PLI investigations in solids of [FeCl$_3$(NO)]$^-$ and [FeCl$_2$(NO)$_2$]$^-$ complexes

3.4.1 Photo-induced isonitrosyl (MS1) isomer[33]

The UV/Vis analyses (Section 2.16.3 and 2.16.4) as well as the TD-DFT and WFT calculations were performed (Section 2.16.2) as a prerequisite for the photophysical investigation. The UV/Vis analyses showed that the Cl$^-$ ligands did not contribute to the absorption in the visible range. Instead, the absorptions were related to transitions of alpha or beta electrons from the Fe–NO π bond into empty/singly occupied metal orbitals or into the Fe–NO antibonding orbitals. Hence, each of the transitions weakened the Fe–NO bonds, thus allowing the rearrangement of the Fe–NO fragment (GS) to an Fe–ON fragment (MS1). The PLI experiments confirmed the calculated of $\tilde{\nu}$(Fe–ON). In comparison, the MS1 and MS2 isomers of [Fe(CN)$_5$(NO)]$^{2-}$ complex lay approximately 2 eV and 1.5 eV above the GS, respectively, and the activation energy from MS to GS relaxation was found as almost 1 eV.[94] For [FeCl$_3$(NO)]$^-$, the MS1 lay approximately 1.2 eV above the GS. A local energy minimum of MS2 was absent. Thus, irradiation with wavelengths between 350–760 nm as used in the PLI experiments would easily overcome the energy barrier. Besides that, the activation barrier from MS1 to GS was only 0.3 eV (Figure 2.48) which was much lower than in the [Fe(CN)$_5$(NO)]$^{2-}$

complex. Thus, the relaxation times of the PLI event in the $[FeCl_3(NO)]^-$ complexes were expected to be short. Furthermore, the local energy MS2 minimum was also absent for the $[FeCl_2(NO)_2]^-$ species and, therefore, neither for $[FeCl_3(NO)]^-$ or for $[FeCl_2(NO)_2]^-$ could an MS2 be detected or stabilized in the PLI experiments.

3.4.2 Photo-induced one-electron anion-to-cation transfer[33]

Upon irradiation, Mephaz$[FeCl_3(NO)]$ (**4**) showed an MS1 as well as a photo-induced charge-transfer state which was indicated by a new IR band at higher energy. This new IR band indicated a strengthening of the Fe–NO bond wherein the electron density in the π-Fe–NO bond was reduced. Since in Mephaz$[FeCl_3(NO)]$ no solvent molecules or co-crystallized species were presented, the photo-induced oxidation should transfer one electron of $[FeCl_3(NO)]^-$ to the Mephaz$^+$ counter ion. The photo-induced oxidation product of the parent $\{FeNO\}^7$-$[FeCl_3(NO)]^-$ was thus $\{FeNO\}^6$-$[FeCl_3(NO)]$. The removal of one electron should occur in two possible ways, resulting in triplet or quintet-$\{FeNO\}^6$. The triplet state involved the withdrawal of the α spin electron from the d_{z^2} orbital (metal centered oxidation) and the quintet state involved the withdrawal of a β spin electron from an Fe–NO π bond (ligand centered oxidation). Both calculated N–O stretches (Table 2.15) matched with the experimental IR values: $1884\,cm^{-1}$ and $1866\,cm^{-1}$ for the triplet and the quintet, respectively. However, the triplet state was approximately $20\,kJ\,mol^{-1}$ stable more than the quintet. In conclusion, the oxidized product could probably be described as a triplet state. A similar decision between triplet and quintet states was recently published by the Lehnert group.[72] The photo-induced electron transfer of **4** confirmed the PLI result of the PPN$[FeCl_3(NO)]$[41] salt. Irritatingly, the $[Co(cp)_2][FeCl_3(NO)]$ (**5**) salt seemed to be a particularly well-suited compound in terms of cation-reducibility but only an MS1 was observed.

3.4.3 Photo-induced bent isonitrosyl (MS1) isomer in $[FeCl_2(NO)_2]^-$ complex

14a and **14c** showed preliminary PLI results in terms of a bent isonitrosyl state. The calculations matched the PLI experiments. However, the new bent isonitrosyl states were poorly populated. Future investigations are expected to clarify the difference between MNIC and DNIC PLI. Moreover, searching for further DNIC compounds which are PLI-active and feature high populations in the metastable states would be desirable.

Thermally induced spin change in [Fe(bipzpy)Cl$_2$(NO)]·MeOH (20a)

Upon cooling the sample [Fe(bipzpy)Cl$_2$(NO)]·MeOH (**20a**) to 10 K, the NO band (GS) split into two peaks at $\tilde{v}$(NO) of 1780 cm^{-1} and 1810 cm^{-1} while the IR band at around 600 cm^{-1} rose as well as the broad band at around 1733 cm^{-1}. Some depopulation was found also at around 1600 cm^{-1}. By irradiating the sample at 10 K with Λ = 405–940 nm, the NO peak at 1810 cm^{-1} significantly decreased and the band at 1733 cm^{-1} rose a little more.
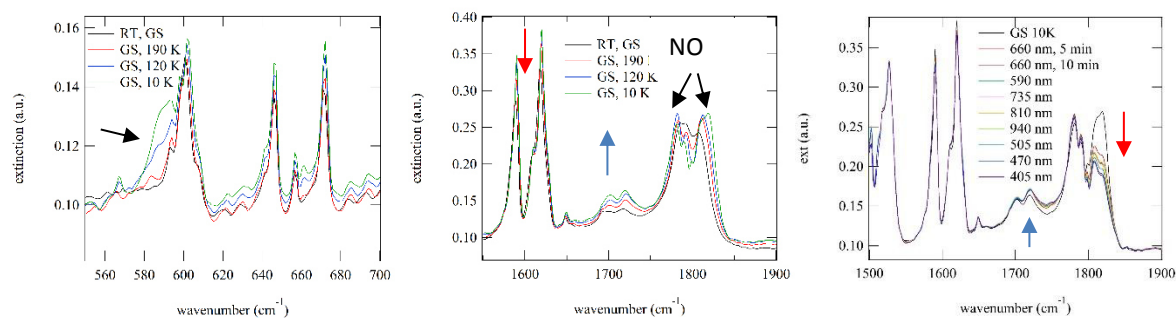
Figure 3.4: (Left, middle) IR spectra of **20a** upon cooling the sample from RT (ground state) to 10 K. (right) Irradiation at 10 K with Λ= 405−940 nm.

The reason for the splitting of the NO might be a thermally induced spin-flip (HS, S = 3/2 ↔ LS, S = 1/2) in the course of which one of the unpaired electrons from the HOMO turned briefly down and paired with the α electron in the lower-energy orbital. Correspondingly, the homoleptic analogue ligand, [Fe(bipzpy)$_2$]$^{2+}$ was described as a spin-crossover compound.[95–100]. X-Ray data at 298 K and 173 K showed that **21a** was an HS complex, which is supported by calculations and (Table 2.16, Table 3.2, Figure 3.5. The high-spin and low-spin states had an energy difference of only 4 kJ mol^{-1}. Moreover, the calculated values of $\tilde{v}$(NO), HS = 1760 cm^{-1} and LS = 1784 cm^{-1} lay close to the experimental value $\tilde{v}$(NO)$_{RT, solid}$ = 1781 cm^{-1}. The IR peak at around 600 cm^{-1} was assigned as the Fe–N(O) bond which was in LS shorter than in HS while the C=C bonds were responsible for the stretching at around 1600 cm^{-1} which was found to be shorter in the LS complex.

However, the calculation results did not explain the new IR band at $\tilde{v}$ 1733 cm^{-1}. Thus, in future work, further analytic methods such as SQUID, Mössbauer and EPR measurements as well as further DFT calculations will be required for clarify this phenomenon.
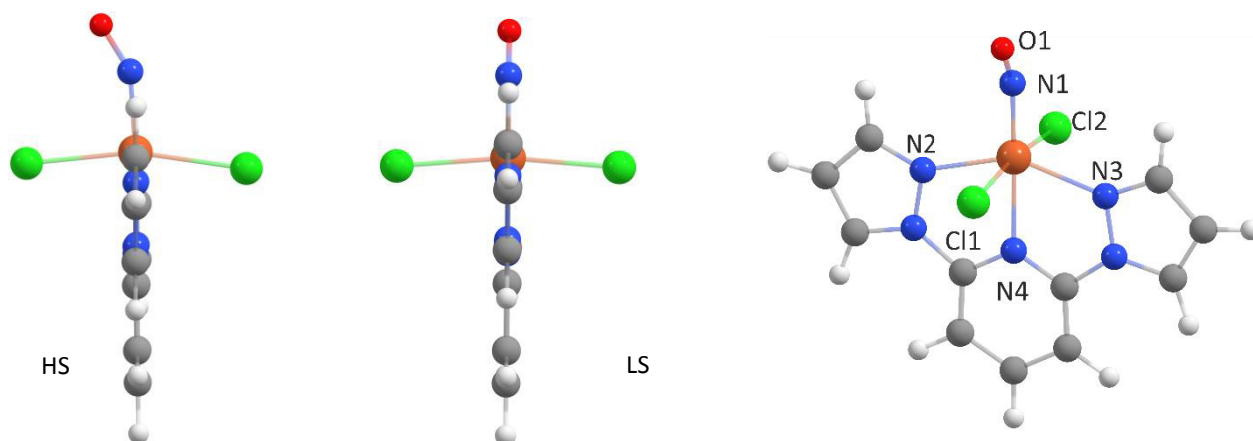
Figure 3.5: CHEMCRAFT plot of optimized geometries-BP/def2-TZVP, d3 for HS and LS in **20a**.

Table 3.2: Selected bond parameters of crystals in **21a**. Exp.: experimental data, calc.: calculated (BP/def2-TZVP, d3) for HS and LS.

	GS		HS	LS
d/Å	Exp. **20a***	Exp. **20a****	Calc. d3	
Fe–Cl1	2.3748(7)	2.3840(10)	2.395	2.29262
Fe–Cl2	2.4753(7)	2.4767(10)	2.337	2.29191
Fe–N(O)	1.765(2)	1.757(3)	1.728	1.65209
Fe–N1(L)	2.1967(19)	2.141(2)	2.191	2.34609
Fe–N2(L)	2.1390(18)	2.195(2)	2.193	1.99081
Fe–N3(L) *trans* to NO	2.1469(18)	2.152(2)	2.169	2.13752
N–O1	1.153(3)	1.113(5)	1.172	1.17301
Fe–N–O/°	154.0(2)	159.7(3)	151.6	160
$\tilde{\nu}$(N–O)/cm^{-1}	1781		1760	1784
			-3013.2738	-3013.2741

X-ray data at * 173 K, ** 298 K

4 Summary and outlook

This work is focused on the synthesis, crystallization, characterization and quantum-chemical analysis of quartet-$\{FeNO\}^7$ and doublet-$\{Fe(NO)_2\}^9$ compounds. A total of twenty-four novel nitrosyl-iron complexes were obtained of which sixteen were mononitrosyl-iron compounds of the $\{FeNO\}^7$ type and eight were dinitrosyl-iron compounds of the $\{Fe(NO)_2\}^9$ type. Pure crystalline samples were studied photophysically with photo-induced linkage isomers as the target species.

A standard ferrous route for the synthesis of MNICs-X, (X = Cl, Br) of the formula A[FeX$_3$(NO)] (**1–13**) (A = various cations) was developed, **1–13** were prepared by treating a methanolic solution of ferrous salts and the corresponding halide salt with purified gaseous nitric oxide. To synthesize A[FeCl$_3$(NO)] the molar ratio of ferrous chloride and chloride salt was 1:1, while to synthesize A[FeBr$_3$(NO)], a molar ratio of iron triflate and bromide salts of 1:3 was applied. A ferric route using ferric chloride and chloride salt (1:1) for A[FeCl$_3$(NO)] was developed as well. However, this route required more solvent in order to obtain well-ordered products. All MNICs-X solutions needed pH values lower than three to prevent the formation of dinitrosyl-iron compounds or a mixture of MNIC and DNIC. The tetrahedral [FeX$_3$(NO)]$^-$ ions featured almost linear Fe–N–O fragments with angles between 170° and 177° as are shown in Figure 4.1. The NO stretching vibrations were found at around 1800 cm^{-1} and the typical UV/Vis absorption bands were found at around 400 nm, 480 nm and 600 nm. SQUID measurements confirmed the quartet ground state in the $\{FeNO\}^7$ compounds. The counter ions in the MNICs-X molecules had no significant effect on structural parameters, IR or UV/Vis values but played a role concerning the PLI results (as described later).
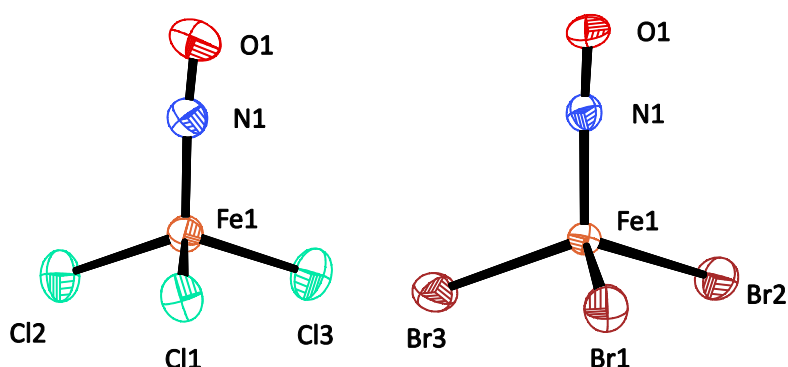
Figure 4.1: Ortep plot of [FeCl$_3$(NO)]$^-$ ion in crystals of **1a** and [FeBr$_3$(NO)]$^-$ ion in crystals of **12**.

The DNICs-X, (X = Cl, Br, I) **14–19** were obtained as crystalline solids. A[FeCl$_2$(NO)$_2$] (**14a–c**) were prepared by treatment of a methanolic solution of ferrous or ferric chloride and fluoride salts with gaseous nitric oxide. The solution had to keep its initial pH value of ≈3–4 before treatment with NO

otherwise, no reaction took place. The *in situ* IR analysis confirmed that the DNIC-Cl complexes formed *via* MNIC-Cl species, in a consecutive reaction, whereas fluoride salts reacted as a base. The DNICs-Br compounds (**15a–b**) were unexpectedly obtained as a byproduct from the MNIC-Br synthesis. They are the first-published structurally characterized compounds of that kind. However, the synthetic route has to be optimized in future work.[33] The DNICs-I (**16–19**) were formed along with the redox byproduct, triiodide salts. MNIC-I species have never been observed. All DNICs-X, $[FeX_2(NO)_2]^-$ complexes featured slightly bent Fe–N–O moieties with angles between 160 and 167°and in their tetrahedral structure (Figure 4.2). The N–O stretches were found at around $1775_{(sym)}$ cm^{-1} and $1696_{(asym)}$ cm^{-1} and their typical UV/Vis absorption bands were found at around 500 nm and 700 nm. The SQUID–determined value of μ_{eff} = 1.92 in crystals of **14c** confirmed the presence of one unpaired electron in the doublet-$\{Fe(NO)_2\}^9$ compounds.
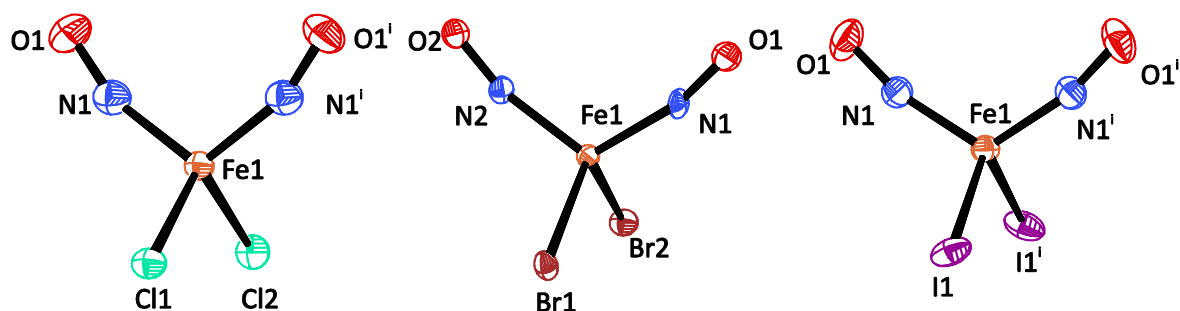
Figure 4.2: ORTEP plot of $[FeCl_2(NO)_2]^-$ ion in crystals of **14a**, $[FeBr_2(NO)_2]^-$ ion in crystals of **15a** and $[FeI_2(NO)_2]^-$ ion in crystals of **18**.

In addition, four new crystalline $\{FeNO\}^7$ (S = 3/2) and $\{Fe(NO)_2\}^9$ (S = 1/2) compounds bearing the tridentate ligand 2,6-di(1-pyrazolyl)pyridine (bipzpy) or the bidentate ligand 2-amino-4-(2-pyridyl)thiazole (aptz) were synthesized and analyzed by X-ray diffraction: the electroneutral-$\{FeNO\}^7$ compounds $[Fe(bipzpy)Cl_2(NO)]\cdot MeOH$ (**20a** and **20b**), the ionic-$\{FeNO\}^7$ compound $[Fe(aptz)_2Cl(NO)]Cl\cdot 0.5MeOH$ (**23**), and the ionic-$Fe(NO)_2\}^9$ compounds $[Fe(bipzpy)(NO)_2]BF_4$ (**21**) and $[Fe(bipzpy)(NO)_2]_2(BF_4)(NO_3)$ (**22**). All four solid compounds were stable against air but their NO-saturated solutions were not. They were prepared from ferrous (**20a**) or ferric chloride (**20b**) precursor with an equimolar ratio of iron salt and ligand. The products **20a** and **20b** from both routes are identical and have the same structural parameters as well as spectroscopic data. The Fe–N–O moieties were slightly bent with an angle of about 154° and were tilted towards one of the chlorine atoms. The bending of the Fe–N–O moieties is common and similar to those in other hexa-coordinated $\{FeNO\}^7$ (S = 3/2) compounds.[66,81] The origin of Fe–N–O bending seemed to be the decrease of the singly occupied Fe (d_{z^2}) orbital and the NO (3σ) lone pair.[27,33,78] The tilt of NO towards a chlorine atom or to another electron-rich atom was previously found also in the

[Fe(edda)(H_2O)(NO)] compound.[66] In a chlorine complex, this structural feature was caused by a bonding interaction of the chlorine atom and the oxygen atom of the NO fragment. The bonding overlaps in the β-HOMO and β-HOMO−2 orbitals were responsible for this tilting, which was supported by the DFT-optimized geometry as is shown in Figure 4.3.

[Fe(aptz)$_2$Cl(NO)]Cl·0.5MeOH (**23**) was an ionic-{FeNO}^{7} (S = 3/2) compound which was prepared from ferrous chloride and two equivalents of the aptz ligand. Again, the Fe–N–O moiety in this crystal was bent with an angle of 149° and the NO fragment tilted towards the nitrogen atom in the thiazole residue instead the chlorine atom (Figure 4.4).
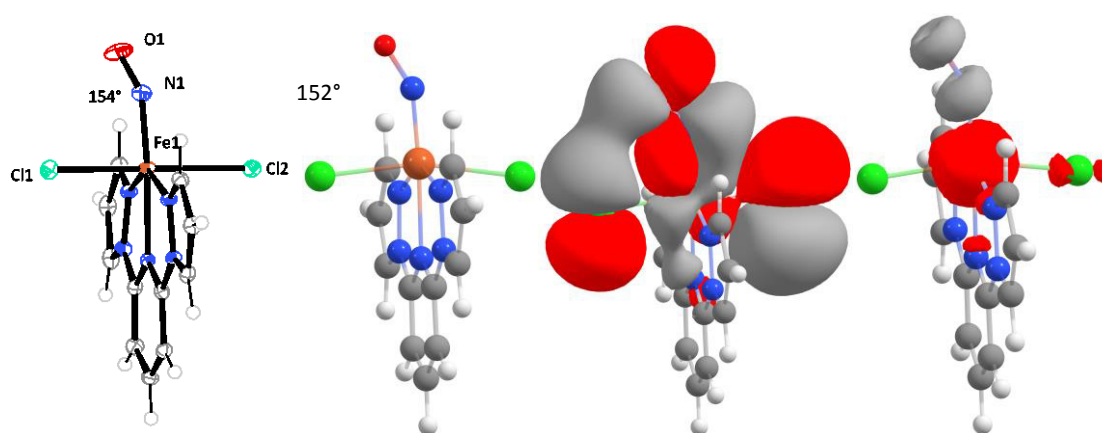
Figure 4.3: (Left) Ortep plot of [Fe(bipzpy)Cl$_2$(NO)]·MeOH in crystals of **20a**, MeOH is omitted for clarity (middle, left) the BP/def2-TZVP, d3-optimized structure of **20a**, (middle, right) β-HOMO of **20a** (BP/def2-TZVP, d3, isovalue 0.01) and (right) total spin density-(BP/def2-TZVP, d3, isovalue 0.01).
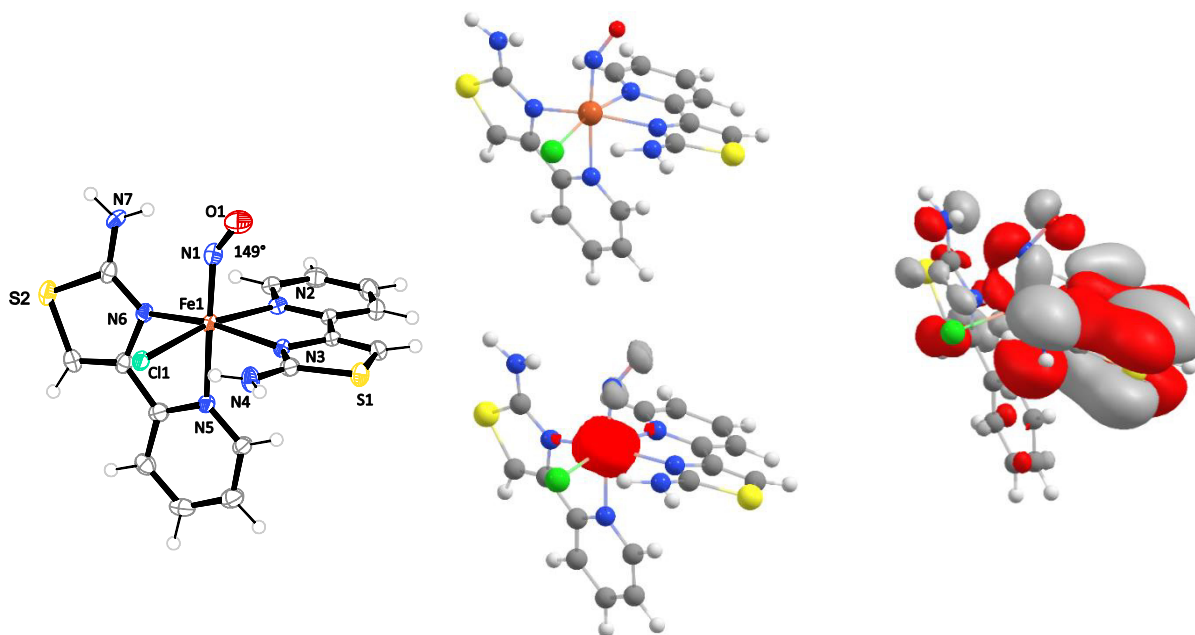
Figure 4.4: (Left) ORTEP plot of [Fe(aptz)Cl(NO)]⁺ in crystals of **23**, (middle, top) the BP/def2-TZVP, d3-optimized structure of **23**, (middle, bottom) the total α-β SCF density-(BP/def2-TZVP, d3, isovalue 0.02) of **23** and (right) β-HOMO−1 of **23** (BP/def2-TZVP, d3, isovalue 0.02), total spin density-(BP/def2-TZVP, d3, isovalue 0.02).

Further quantum-chemical calculations using DFT (in this thesis) together with CASSCF methods (Prof. Klüfers)[33] were performed to gain more details of Fe–N–O bonding. The optimized structure using BP/def2-TZVP, d3 and cpcm(MeOH) as well as frequency data were in line with the experimental data. Broken symmetry calculations, Mulliken charge analyze, IR analysis as well as bond lengths showed that the Fe–N–O moiety mainly as Fe^{II} antiferromagnetically coupled with NO^{0}. The broken symmetry results indicated a large covalent character in the Fe–N–O fragment ($S_{\alpha\beta}$ values close to one). Furthermore, the CASSCF methods complemented by TD-DFT results allowed the explanation of the electronic transitions of [FeCl$_3$(NO)]$^-$ and [FeCl$_2$(NO)$_2$]$^-$ ions. The relevant absorptions involved transitions of α or β spins from the Fe–NO π bonds into empty/singly occupied orbitals or into the antibonding orbitals. All relevant allowed electronic transitions in those samples weakened the Fe–NO bond. Thus, on irradiation into these transitions, new arrangements of the nitrosyl ligand in the sense of PLI isomers were observed. The metastable κO-bonding-state MS1 was detected in [FeCl$_3$(NO)]$^-$ ion with the following counterions: NMe$_4^+$, NBnMe$_3^+$, PPh$_4^+$, AsPh$_4^+$, [Co(cp)$_2$]$^+$, Mephaz$^+$, and in [FeBr$_3$(NO)]$^-$ with the PPh$_4^+$ ion. The metastable state *bent*-MS1 was detected in the [FeCl$_2$(NO)$_2$]$^-$ ion with NMe$_4^+$ and PPN$^+$ counterions, and in [FeI$_2$(NO)$_2$]$^-$ with the PPh$_4^+$ ion. A new metastable photo-induced-charge transfer state (Ox) was detected in the Mephaz[FeCl$_3$(NO)] salt in which one electron from the [FeCl$_3$(NO)]$^-$ ion was shortly transferred to

the Mephaz$^+$ counter ion, resulting in Mephaz$^-$[FeCl$_3$(NO)] which is of a triplet-{FeNO}^{6} type. This result confirmed a similar detection in the PPN[FeCl$_3$(NO)] salt.[41]

Further PLI results in crystals of [Fe(bipzpy)Cl$_2$(NO)]·MeOH (**20a**) raised a new possibility for the spin crossover of paramagnetic nitrosyl-iron compounds: upon cooling the sample, the NO band split into two peaks at $\tilde{\nu}$(NO) of 1780 cm^{-1} and 1810 cm^{-1}, assumed to be high-spin and low-spin, respectively. After irradiation with light between 405 and 940 nm at 10 K, the NO peak at 1806 cm^{-1} significantly decreased and a peak around 1733 cm^{-1} rose. A relaxed surface scan of the Fe–N–O angle and its stepwise-calculated IR values did not match the PLI result (Figure 2.49). Thus, the MS1 or MS2 states were most likely not responsible for this observation. The increase of the peak at 1733 cm^{-1} could thus not be explained at this time.

In conclusion, in this work appropriate standard synthetic routes of the MNICs-X and DNICs-X (X =Cl, Br, I) were developed, along with nitrosyl-iron compounds bearing multidentate ligands. The crystalline products showed photo-induced linkage isomers or photo-induced charge transfer. These results provide evidence for PLI in the rare case of paramagnetic nitrosyl-metal compounds.

Additionally, the red compound [Fe(CH$_3$OH)(NO)(μ_4-SO$_4$)]$_{n/n}$ (**A**) was successfully characterized and analyzed as a {FeNO}^{7} (S = 3/2)-type. Compound **A** and (H$_3$O)[{Fe(NO)(μ_4-SO$_4$)(μ_2-SO$_4$)$_{0.5}$}$_{n/n}$][32] have similar crystal habitus and color as described by Manchot. Thus it is assumed that (H$_3$O)[{Fe(NO)(μ_4-SO$_4$)(μ_2-SO$_4$)$_{0.5}$}$_{n/n}$][32] is identical to the product described by Manchot and **A** is a derivate of it, bearing the same 2D-assembly of nitrosyl- iron centers bridging μ_4-SO$_4$-ligand. **A** is related the "brown-ring" [Fe(H$_2$O)$_5$(NO)]$^{2+}$ complex, where both coincidently appear in the nitrate test. The characterization of **A** could support the better understanding of that test in the undergraduate course.

The present work supports the DFG priority program SPP1740, which is dedicated to the study of the influence of local transport processes in bubble flows, such as a reaction of a single bubble of gaseous NO and an aqueous solution of ferrous sulfate.[101,102] The consecutive synthesis and *in situ* characterization of mono- und dinitrosyl-iron complexes which have been demonstrated in this thesis (Section 3.2) is currently the basis of further investigations in the area of engineering science.

5 Experimental Part

5.1 Common working techniques

All reactions involving iron compounds, if not explicitly described otherwise, were carried out under argon atmosphere using standard Schlenk techniques. Schlenk flasks were evacuated and flushed with argon three times to remove the oxygen from air, air moisture from the atmosphere in the flask. Equipment such as pipettes, syringes and cannulas were purged with argon three times prior to use. All solvents were used as obtained from distributors and were deoxygenated before use. Figure 5.1 shows the NO setup apparatus, a 30 L NO-gas bottle was utilized. The NO-gas bottle, the impingers, the Woulff bottles and the Schlenk flask or Schlenk tube were connected by rubber hoses with hose clamps. Nitric oxide was purified by bubbling through an aqueous sodium hydroxide solution (4 M) to remove unwanted NO_x-gas. Excess nitric oxide was destroyed by bubbling through an aqueous sulfamic acid solution (2 M). Before and after the NO-gas introduction into the flask, the apparatus was flushed 10 minutes with argon, respectively.
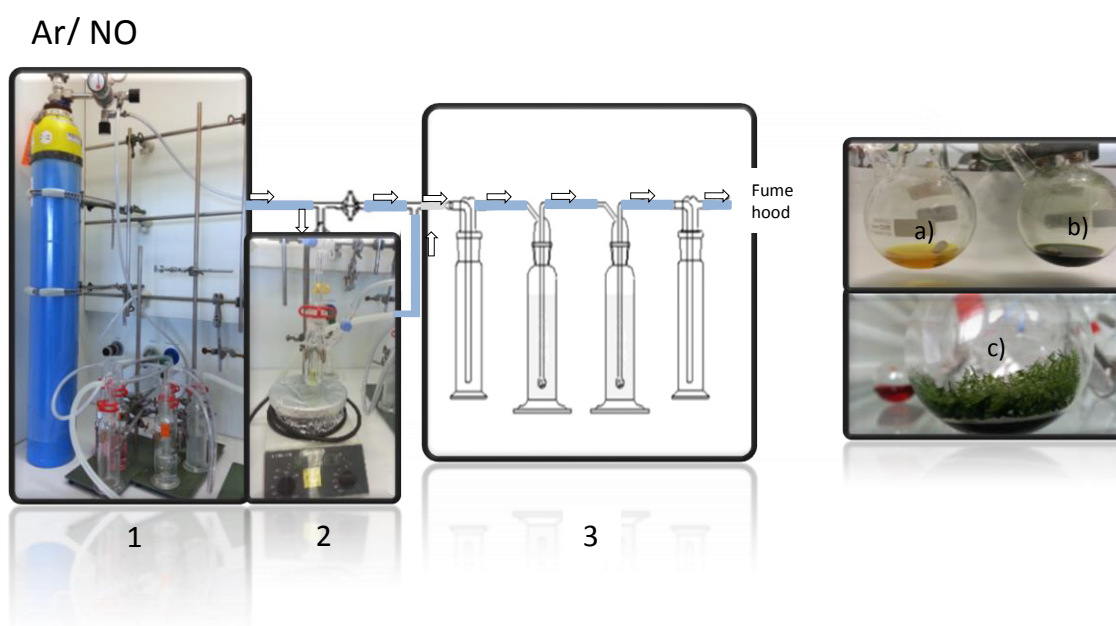
Figure 5.1: (Left) Experimental setup of the NO apparatus with the NO-gas stream direction (arrows): The NO gas from the bottle (blue) passes through three Woulff bottles, one impinger filled with a sodium hydroxide solution (4 M) (impinger 1), a reaction Schlenk fask (impinger 2) and two impingers filled with sulfamic acid solution (impinger 3). (Right) A methanolic solution of chlorido ferrate before treatment with gaseous NO (a), after treatment with gaseous NO (b) and typical green crystals of trichloridonitrosylferrate (c).

5.2 Analytical methods

5.2.1 Elemental analysis

CHN analyses were performed on an *Elementar vario EL* (C, H, N content), *Metrohm 888 Titrando* (F, Cl, Br, I content) and *Varian* Vista RL CCD simultaneous ICP-AES (Fe, Co content).

5.2.2 IR spectroscopy

IR spectra were recorded on a *JASCO FT/IR-4100typeA* spectrometer with a resolution of 4 cm^{-1} and an accumulation of either 16 or 32. Solid samples were measured using an ATR diamond plate. The measuring range (wavenumber) was set from 650 to 4000 cm^{-1}. All spectra were interpreted using the software *Spectra Manager II*.

5.2.3 NMR spectroscopy

NMR spectra were recorded on spectrometers of the type *Bruker 400 TR*, *Bruker 400*, *Jeol 270*, and *Jeol 400*. The chemical shift (δ) is given in ppm and refers to the solvent peak of the deuterated solvent. Software *MestReNova* were used for interpreting the spectra.

5.2.4 Mass spectrometry

Mass spectra were recorded on spectrometers of *Jeol JMS 700*, *Thermo Finnigan MAT 95* and *FAB*. FAB samples were ionized in a nitrobenzyl alcohol or glycerine matrix, using 8 kV fast argon atom.

5.2.5 Magnetic susceptibilities

Magnetic susceptibilities data were recorded with a Quantum Design *MPMS XL-5 SQUID* magnetometer over 10–300 K in the sweep mode. The author would like to thank Prof. Birgit Weber (University of Bayreuth) and Prof. Dirk Jorendt (LMU Munich) for the magnetic susceptibility measurements.

5.2.6 Raman spectroscopy

Raman spectra were recorded on spectrometers of the type *Bruker MultiRamII*. This was controlled by the software OPUS 6.5. Nd:YAG was used as laser source with a laser power of 50–1000 mW and wavelength of 1064 nm. The data was recorded with 50–100 scans. The author would like to thank the working group of Prof. Kornath (LMU) for the Raman measurements.

5.2.7 UV/Vis spectroscopy

For liquid UV-Vis spectroscopy, the *Cary 50* UV-Vis Spectrophotometer with a 190 to 1100 nm wavelength range was utilized. The background measurement was carried out with methanol, using a quartz cuvette with a thickness of 1 cm. The wavelength range was set from 200 to 800 nm. The

Cary 50 UV-Vis spectrometer was controlled by the software *Cary WinUV*. Solid samples were measured on a *Carry 500 Scan UV-Vis-NIR Spectrophotometer* with *Lapsphere DRA-CA-5500* photometer sphere. The diffused reflection was measured and converted using the *Kubelka-Munk* function comparable to the experimental value.

$$\frac{K}{S} = \frac{(1-R)^2}{2R} \qquad (1)$$

K: absorption coefficient; R: remission; S: scattering coefficient

5.2.8 PLI measurements

The author would like to thank Prof. Dominik Schaniel from the University of Lorraine (Institut Jean Barriol) for the PLI measurements. In the course of the PLI experiments, infrared spectra were collected on a Nicolet 5700 FTIR spectrometer in the range 4000–360 cm^{-1} with a resolution of 2 cm^{-1}. The sample was mixed with KBr (spectroscopy grade), finely ground, and pressed into pellets. The pellets were glued with silver paste to a copper sample holder on the cold finger of an Oxford Optistat V01, allowing temperature regulation in the range 9–300 K. KBr windows allowed for *in situ* irradiation of the sample in the ultraviolet, visible and near infrared spectral range.

5.2.9 X-Ray diffraction

Crystalline products were selected using a *Leica MZ6* polarization microscope. Single crystals were measured on a single diffractometer of the type *Oxford XCalibur 3*, *Bruker D8 Venture* and *Bruker D8 Quest* using MoK$_\alpha$ irradiation. The structure solutions were carried out by a direct method using program *SHELXS-2014*, *ShelXle* and *ShelXT*. All non-hydrogen atoms were refined anisotropically using a full-matrix, least-squares technique on F^2. The program *Platon* was used to calculate bond distances and angles. The crystal structure was edited and visualized by the program *ORTEP*, *Mercury* version 3.7 and *CorelDRAW* Graphics Suite x7.

5.2.10 Computational methods

All quantum-chemical calculations at the DFT level were done with the program system ORCA 4.0.1.[103] Initial geometries were taken from crystal-structure analyses. Wave functions were calculated at the multipole-accelerated RI-DFT level[104,105] using TZVP[106] and def2-TZVP basis sets[107] and the functional BP86[108,109] and TPSSh.[110–112] The CPCM solvation model[113] and dispersion correction was applied, using Grimme's DFT-D3[114] with BJ-damping[61]. Frequency analyses were done numerically. QTAIM analyses were performed with the program system MULTIWFN.[115]

5.3 Reagents and solvents

Table 5.1: Manufacturer and percentage purity of the solvents and reagents.

Chemical formula	Manufacturer (purity)	CAS-number
2-acetylpyridine	Sigma-Aldrich (≥ 99.0%)	1122-62-9
4-(pyridin-2-yl)-1,3-thiazol-2-amine	[116]	30235-28-0
ammonium chloride	Sigma-Aldrich (≥ 99.0%)	12125-02-9
benzyltrimethylammonium fluoride hydrate	Sigma-Aldrich (97%)	329-97-5
benzyltrimethylammonium chloride	Fluka	56-93-9
2,2'-bipyridyl	Alfa Aesar (99%)	366-18-7
bis(triphenylphosphane)iminium chloride	ABCR (97%)	21050-13-5
bromine	Acros (≥ 99%)	7726-95-6
caesium chloride	Acros Organics (≥ 99.0%)	7647-17-8
citric acid monohydrate	Sigma-Aldrich (≥ 99%)	5949-29-1
cobaltocene	Acros Organics (98%)	1277-43-6
crystal violet	Sigma-Aldrich (≥ 90%)	548-62-9
dichloromethane	Brenntag (99.9%)	75-09-2
diethyl ether	VWR (99.9%)	60-29-7
2,6-di(1-pyrazolyl)pyridine	[117]	123640-38-0
ethanol	Sigma-Aldrich (abs.)	64-17-5
hydrobromic acid	VWR (48%)	10035-10-6
hydrobromic acid in acetic acid (33 wt.%)	Alfa Aesar	10035-10-6
iron(II) triflate tetramethanol	[118]	59163-91-6
iron(II) chloride tetrahydrate	ABCR (99%)	59163-91-6
iron(II) fluoride	ABCR (99%)	7789-28-8
iron(II) perchlorate monohydrate	Aldrich (97%)	335159-18-7
iron(II) tosylate hexahydrate	[119]	59163-91-6
iron(III) chloride	Aldrich (97%)	7705-08-0
iron(III) fluoride	Acros Organics (99.8%)	7783-50-8
magnesium sulfate heptahydrate	Sigma-Aldrich (≥ 99%)	10034-99-8

Chemical formula	Manufacturer (purity)	CAS-number
methanol	Acros Organics (99.8%)	67-56-1
methyl *tert*-butyl ether	Sigma-Aldrich (95%)	1634-04-4
nitric oxide	Air Liquide	10102-43-9
nitrosonium tetrafluoroborate	Sigma-Aldrich (95%)	14635-75-7
phenazine ethosulfate	Sigma-Aldrich (≥95%)	10510-77-7
phenazine methosulfate	Sigma-Aldrich (≥90%)	299-11-6
potassium bromide	Fluka (≥99.5%)	7758-02-3
potassium cyanide	Alfa Aesar (≥97%)	151-50-8
potassium iodide	Grüssing (98%)	7681-11-0
silver(I) fluoride	Acros (≥99%)	7775-41-9
sodium hydroxide	Grüssing (puriss.)	1310-73-2
sodium nitrite	Grüssing (puriss)	7632-00-0
tetrabutylammonium chloride	Aldrich (≥ 97.0%)	1112-67-0
tetrabutylammonium fluoride	Aldrich (≥ 99.0%)	87749-50-6
tetraethylammonium chloride	Aldrich (≥ 99.0%)	56-34-8
tetramethylammonium chloride	Aldrich (97%)	75-57-0
tetramethylammonium fluoride	Sigma-Aldrich (97%)	373-68-2
tetraphenylarsonium chloride	Sigma-Aldrich (97%)	507-28-8
tetraphenylphosphonium bromide	Sigma-Aldrich (97%)	2751-90-8
tetraphenylphosphonium chloride	Aldrich (98%)	2001-45-8
thiourea	ABCR (99%)	62-56-6
trifluoromethanesulfonic acid	ABCR (99%)	1493-13-6
water (deionized)	House-installation	7732-18-5

5.4 Synthesis of PPN$^+$, PPh$_4$$^+$ and AsPh$_4$$^+$ salts

5.4.1 Bis(triphenylphosphane)iminium bromide, (PPN)Br
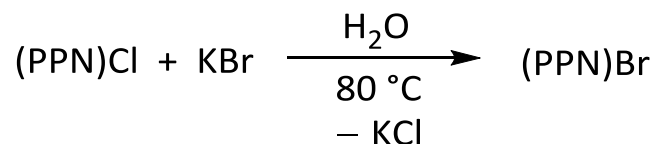
$$(PPN)Cl \ + \ KBr \ \xrightarrow[\substack{80\,°C \\ -\ KCl}]{H_2O} \ (PPN)Br$$

Literature: A. Martinsen, J. Songstad, *Acta Chem. Scand.* **1977**, *A 31*, 645–650.

Starting material: Potassium bromide, bis(triphenylphosphane)iminium chloride, acetonitrile, diethyl ether, water.

Procedure: PPNCl (1.0 g, 1.7 mmol, 1 eq.) was dissolved in 80 mL of water at 80 °C. Potassium bromide (5.0 g, 42 mmol, 24 eq.) was dissolved in 8 mL of water at 80 °C and added under constant stirring to the hot (PPN)Cl solution. Immediately, a colorless precipitate formed. The suspension was kept at 4 °C overnight, then filtered and washed with cold water. The colorless residue was dried under reduced pressure and recrystallized from acetonitrile/diethyl ether. (PPN)Br was obtained as a colorless powder.

Yield: 0.69 g, 1.1 mmol, 65% based on (PPN)Cl.

Empirical formula: $C_{36}H_{30}BrNP_2$, M = 618.49 gmol^{-1}.

MS (FAB$^-$): m/z (%) = 78.9 (81.1) [Br]$^-$, calcd. 78.9, 80.92.

MS (FAB$^+$): m/z (%) = 538.2 [M − Br]$^+$, calcd. 538.5.

Elemental analysis: Calcd. (%): N 2.26, C: 69.91, H: 4.89.

Found (%): N: 2.07, C: 68.85, H: 5.52.

5.4.2 Bis(triphenylphosphane)iminium fluoride, (PPN)F

$$\text{(PPN)Cl} + \text{AgF} \xrightarrow[\substack{50\,°C \\ -\,\text{AgCl}}]{\text{MeOH}} \text{(PPN)F}$$
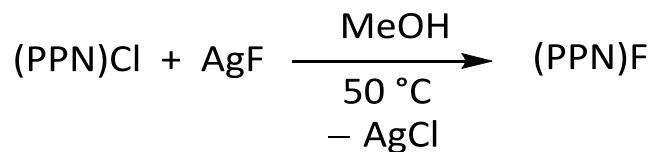
Literature: A. Martinsen, J. Songstad, *Acta Chem. Scand*. **1977**, *A 31*, 645–650.

Starting material: Silver fluoride, bis(triphenylphosphane)iminium chloride, acetone, diethyl ether, water.

Procedure: Under low-light conditions PPNCl (1.0 g, 1.7 mmol, 1 eq.) and silver fluoride (0.22 g, 1.7 mmol, 1 eq.) were dissolved in 50 mL of deoxygenated methanol at 50 °C for 2 hours. The colorless suspension turned gray. The gray precipitate was removed via syringe. To the clear solution, silver fluoride (0.050 g, 0.39 mmol, 0.23 eq.) was added and stirred. Afterwards the solvent was removed at 40 °C *in vacuo*. To the precipitate, 10 mL of methanol was added, stirred and then removed at 40 °C *in vacuo.* This process was repeated 4 times until the precipitate turned colorless. The colorless residue was dried under reduced pressure and recrystallized from acetone/diethyl ether. (PPN)F was obtained as a colorless powder.

Yield: 0.672 g, 1.21 mmol, 69% based on (PPN)Cl.

Empirical formula: $C_{36}H_{30}FNP_2$, M = 557.39 g mol^{-1}.

MS (FAB$^-$): m/z (%) = 19.1 [F]$^-$, calcd. 19.0.

MS (FAB$^+$): m/z (%) = 538.3 [M − F]$^+$, calcd. 538.5.

Elemental analysis: Calcd. (%): N: 2.51, C: 77.55, H: 5.42.

Found (%): N: 2.11, C: 66.29, H: 6.07 = ((PPN)F·5.2 H_2O).

5.4.3 Bis(triphenylphosphane)iminium iodide, (PPN)I
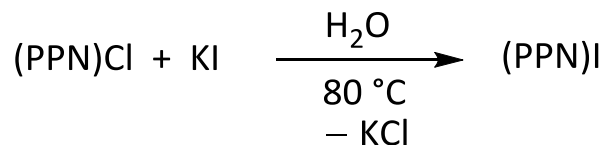
$$(PPN)Cl\ +\ KI\ \xrightarrow[\substack{80\ °C \\ -\ KCl}]{H_2O}\ (PPN)I$$

Literature: A. Martinsen, J. Songstad, *Acta Chem. Scand.* **1977**, *A 31*, 645–650.

Starting material: Potassium iodide, bis(triphenylphosphane)iminium chloride, acetonitrile, diethyl ether, water.

Procedure: PPNCl (1.0 g, 1.7 mmol, 1 eq.) was dissolved in 80 mL of water at 80 °C. Potassium iodide (5.0 g, 30 mmol, 17 eq.) was dissolved in 8 mL of water at 80 °C and added under constant stirring to the hot (PPN)Cl solution. Immediately, a white precipitate formed. The suspension was kept at 4 °C overnight, then filtered and washed with cold water. The colorless residue was dried under reduced pressure and recrystallized from acetonitrile/diethyl ether. (PPN)I was obtained as a colorless powder.

Yield: 1.1 g, 1.6 mmol, 90% based on (PPN)Cl.

Empirical formula: $C_{36}H_{30}INP_2$, M = 665.48 g mol^{-1}.

MS (FAB$^-$): m/z (%) = 127.0 [I]$^-$, calcd. 126.9.

MS (FAB$^+$): m/z (%) = 538.4 [M − I]$^+$, calcd. 538.5.

Elemental analysis: Calcd. (%): N: 2.10, C: 64.97, H: 4.54, I: 19.07.

Found (%): N: 2.07, C: 64.91, H: 4.53, I: 19.17.

5.4.4 Tetraphenylphosphonium iodide, (PPh$_4$)I
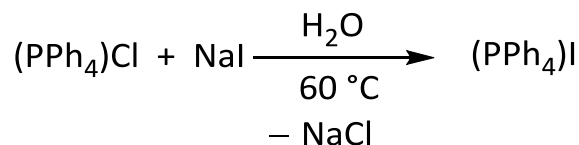
$$(PPh_4)Cl \ + \ NaI \ \xrightarrow[\substack{60\,°C \\ -\ NaCl}]{H_2O} \ (PPh_4)I$$

Analogous to Literature: A. Martinsen, J. Songstad, *Acta Chem. Scand*. **1977**, *A 31*, 645–650.

Starting material: Sodium iodide, tetraphenylphosphonium chloride, acetonitrile, diethyl ether, water.

Procedure: PPh$_4$Cl (1.0 g, 2.7 mmol, 1 eq.) was dissolved in 20 mL of water at 60 °C. Sodium iodide (5.0 g, 33 mmol, 12 eq.) was dissolved in 8 mL of water at 60 °C and added under constant stirring to the hot PPh$_4$Cl solution. Immediately, a colorless precipitate formed. The suspension was kept at 4 °C overnight, then filtered and washed with cold water. The colorless residue was dried under reduced pressure and recrystallized from acetonitrile/diethyl ether. PPh$_4$I was obtained as a colorless powder.

Yield: 1.0 g, 2.2 mmol, 80%.

Empirical formula: C$_{24}$H$_{20}$IP, M = 466.03 g mol^{-1}.

MS (FAB$^-$): m/z (%) = 127.0 [I]$^-$, calcd. 126.9.

MS (FAB$^+$): m/z (%) = 339.4 [M – I]$^+$, calcd. 339.4.

Elemental analysis: Calcd. (%): C: 61.82; H: 4.32; I: 27.22

Found (%): C: 61.77, H: 4.28, I: 26.41.

5.4.5   Tetraphenylarsonium bromide, (AsPh$_4$)Br
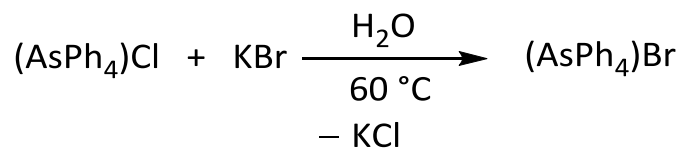
$$(AsPh_4)Cl \ + \ KBr \ \xrightarrow[\substack{60\ °C \\ -\ KCl}]{H_2O} \ (AsPh_4)Br$$

Analogous to Literature: A. Martinsen, J. Songstad, *Acta Chem. Scand*. **1977**, *A 31*, 645–650.

Starting material: Potassium bromide, tetraphenylarsonium chloride, acetonitrile, diethyl ether, water.

Procedure: AsPh$_4$Cl (1.0 g, 2.5 mmol, 1 eq.) was dissolved in 20 mL of water at 60 °C. Potassium bromide (5.0 g, 42 mmol, 17 eq.) was dissolved in 8 mL of water at 60 °C and added under constant stirring to the hot (AsPh$_4$)Cl solution. Immediately, a colorless precipitate formed. The suspension was kept at 4 °C overnight, then filtered and washed with cold water. The colorless residue was dried under reduced pressure and recrystallized from acetonitrile/diethyl ether. (AsPh$_4$)Br was obtained as a colorless powder.

Yield: 1.0 g, 2.2 mmol, 88% based on (AsPh$_4$)Cl.

Empirical formula: C$_{24}$H$_{20}$BrAs, M = 462.0 g mol^{-1}.

MS (FAB$^-$): m/z (%) = 79.1, 81.1 [Br]$^-$, calcd. 78.9, 80.92.

MS (FAB$^+$): m/z (%) = 383.3 [M − Br]$^+$, calcd. 383.3.

5.4.6 Tetraphenylarsonium iodide, (AsPh₄)I
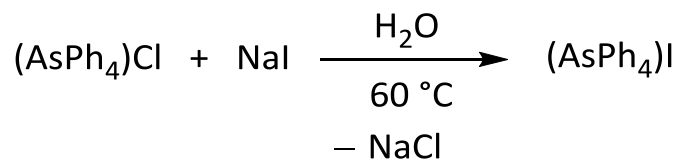
$$(AsPh_4)Cl \;+\; NaI \quad \xrightarrow[\substack{60\,°C \\ -\,NaCl}]{H_2O} \quad (AsPh_4)I$$

Analogous to Literature: A. Martinsen, J. Songstad, *Acta Chem. Scand.* **1977**, *A 31*, 645–650.

Starting material: Sodium iodide, tetraphenylarsonium chloride, acetonitrile, diethyl ether, water.

Procedure: AsPh₄Cl (1.06 g, 2.53 mmol, 1 eq.) was dissolved in 20 mL of water at 60 °C. Sodium iodide (5.03 g, 33.5 mmol, 13 eq.) was dissolved in 8 mL of water at 60 °C and added under constant stirring to the hot (AsPh₄)Cl solution. Immediately, a colorless precipitate formed. The suspension was kept at 4 °C overnight, then filtered and washed with cold water. The colorless residue was dried under reduced pressure and recrystallized from acetonitrile/diethyl ether. (AsPh₄)I was obtained as a colorless powder.

Yield: 1.25 g, 2.45 mmol, 97% based on (AsPh₄)Cl.

Empirical formula: $C_{24}H_{20}IAs$, M = 509.98 g mol^{-1}.

MS (FAB⁻): m/z (%) = 127.0 [I]⁻, calcd. 126.9.

MS (FAB⁺): m/z (%) = 383.3 [M − I]⁺, calcd. 383.3.

5.5 Synthesis of iron(II) triflate

$$Fe + 2\ CF_3SO_3H + 4\ MeOH \xrightarrow[\text{2) refluxed 60 °C, 1 h}]{\text{1) 0 °C, stirred 1.5 h}} Fe(OTf)_2 \cdot 4MeOH$$
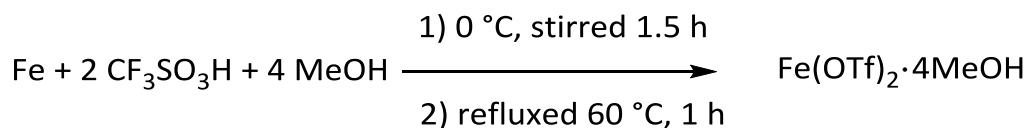
Analogous to Literature [118]: K. S. Hagen, *Inorganic Chemistry* **2000**, *39*, 5867–5869.

Starting material: iron powder, trifluoromethanesulfonic acid, methanol, water.

Procedure: Under an argon atmosphere, iron powder (5.6 g, 0.10 mol) was added to 100 mL of methanol in a three necks round flask. CF_3SO_3H (19 mL, 0.21 mol) was slowly added to the suspension via a dropping funnel at 0 °C and stirred for 1.5 h. Afterwards the solution was refluxed at 60 °C for 1 h, the rest of the unreacted iron powder was filtered and separated. The nearly colorless solution was concentrated under high pressure until the solution had half of its initial volume, then it was accumulated and kept at −27 °C for three days. The product was washed with diethyl ether and dried under high pressure. $Fe(OTf)_2 \cdot 4MeOH$ was obtained as a colorless powder.

Yield: 18 g, 37 mmol, 37% based on iron powder.

Empirical formula: $C_6H_{16}F_6FeO_{10}S_2$, M = 482.14 g mol^{-1}.

IR spectroscopy (RT, solid), (intensity): $\tilde{v}$ = 3463 (m, OH), 1228, 1184, 1030 (s, SO).

Elemental analysis: Calcd. (%): C: 14.95, H: 3.35, S: 13.30.

Found (%): C: 13.08, H: 3.03, S: 13.87.

5.6 Synthesis of tetra-coordinated {FeNO}[7] and {Fe(NO)$_2$}[9] complexes

5.6.1 Tetramethylammonium trichloridonitrosylferrate (1a)
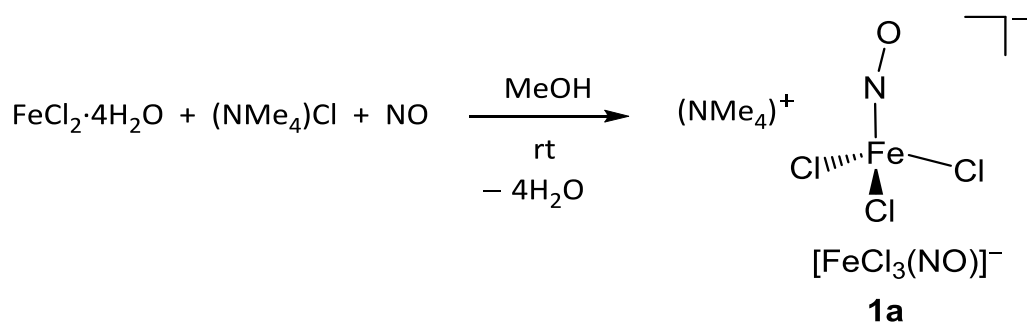
$$FeCl_2 \cdot 4H_2O + (NMe_4)Cl + NO \xrightarrow[\substack{rt \\ -4H_2O}]{MeOH} (NMe_4)^+$$

[FeCl$_3$(NO)]$^-$

1a

Starting material: Iron(II) chloride tetrahydrate, tetramethylammonium chloride, methanol, nitric oxide.

Procedure: In a Schlenk flask a mixture of FeCl$_2$·4H$_2$O (81 mg, 0.50 mmol, 1 eq.) and tetramethylammonium chloride (55 mg, 0.50 mmol, 1 eq.) was dissolved in deoxygenated methanol (3 mL) which resulted in a clear yellow solution. Afterwards the solution was treated with gaseous NO at room temperature for 10 minutes. The yellow solution turned dark green. After being kept at 5 °C for about 2 weeks, small green crystals were formed and collected by filtration and washed with diethyl ether. The green crystals were stable in air.

Yield: 70 mg, 0.26 mmol, 52% based on FeCl$_2$·4H$_2$O.

Empirical formula: C$_4$H$_{12}$Cl$_3$FeN$_2$O, M = 266.36 g mol^{-1}.

IR spectroscopy (RT, solid), (intensity): $\tilde{\nu}$ = 1806 (s, NO) cm^{-1}.

IR spectroscopy (RT, MeOH), (intensity): $\tilde{\nu}$ = 1800 (s, NO) cm^{-1}.

UV/VIS (MeOH): λ = 472, 604 nm.

UV/VIS (solid): λ = 399, 476, 711 nm.

X-ray structure analysis: tq006.

5.6.2   Tetramethylammonium trichloridonitrosylferrate (1b)
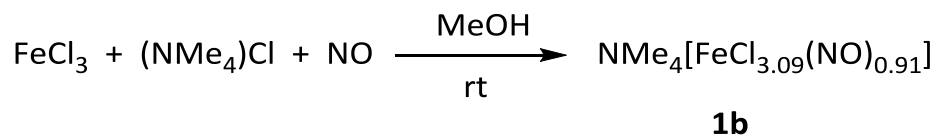
$$FeCl_3 + (NMe_4)Cl + NO \xrightarrow[\text{rt}]{\text{MeOH}} NMe_4[FeCl_{3.09}(NO)_{0.91}]$$

1b

Starting material: Iron(III) chloride, tetramethylammonium chloride, methanol, nitric oxide.

Procedure: In a Schlenk flask a mixture of $FeCl_3$ (99 mg, 0.50 mmol, 1 eq.) and tetramethylammonium chloride (55 mg, 0.50 mmol, 1 eq.) was dissolved in deoxygenated methanol (3 mL), resulting in a clear yellow solution. Afterwards the solution was treated with gaseous NO at room temperature for 10 minutes. Small green crystals above the solvent were observed during the treatment with NO. After being kept at 5 °C for about 2 weeks, small green crystals were collected by decantation and washed with diethyl ether. The green crystals were stable in air.

Yield: 60 mg, 0.23 mmol, 45% based on $FeCl_3$.

Empirical formula: $C_4H_{12}Cl_{3.09}FeN_{1.91}O_{0.91}$, M = 266.81 g mol^{-1}.

IR spectroscopy (RT, solid), (intensity): $\tilde{\nu}$ = 1808 (s, NO) cm^{-1}.

IR spectroscopy (RT, MeOH), (intensity): $\tilde{\nu}$ = 1803 (w, NO) cm^{-1}.

UV/VIS (MeOH): λ = 475, 604 nm.

UV/VIS (solid, $BaSO_4$): λ = 322, 381, 472, 726 nm.

X-ray structure analysis: tv242.

5.6.3 Tetraethylammonium trichloridonitrosylferrate (2a)

$$\text{FeCl}_2 \cdot 4\text{H}_2\text{O} + (\text{NEt}_4)\text{Cl} + \text{NO} \xrightarrow[\text{rt}]{\text{MeOH}} \text{NEt}_4[\text{FeCl}_3(\text{NO})]$$

$$- 4\text{H}_2\text{O} \qquad \textbf{2a}$$
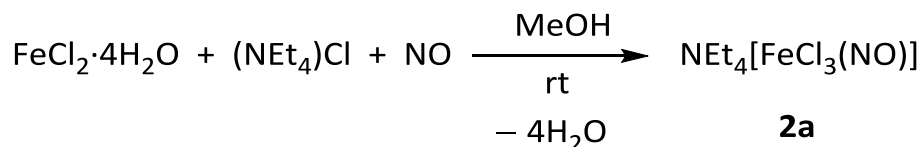
Starting material: Iron(II) chloride tetrahydrate, tetraethylammonium chloride, methanol, nitric oxide.

Procedure: In a Schlenk flask a mixture of $\text{FeCl}_2 \cdot 4\text{H}_2\text{O}$ (39.8 mg, 0.2 mmol, 1 eq.) and tetraethylammonium chloride (36.7 mg, 0.2 mmol, 1 eq.) was dissolved in deoxygenated methanol (3 mL), resulting in a clear yellow solution and yellowish precipitate. Afterwards the solution was treated with gaseous NO at room temperature for 10 minutes. After being kept at 5 °C for about 4 weeks, small green crystals were collected by removing the mother liquor.

Yield: low yield.

Empirical formula: $C_8H_{20}Cl_3FeN_2O$, M = 322.46 g mol^{-1}.

IR spectroscopy (RT, solid), (intensity): $\tilde{\nu}$ = 1780 (vs, NO) cm^{-1}.

IR spectroscopy (RT, MeOH), (intensity): $\tilde{\nu}$ = 1796 (s, NO) cm^{-1}.

UV/VIS (solid, BaSO$_4$): λ = 246, 317, 390, 486, 569, 609, 668 nm.

X-ray structure analysis: vv686.

5.6.4 Tetraethylammonium trichloridonitrosylferrate (2b)

$$FeCl_3 + (NEt_4)Cl + NO \xrightarrow[\text{rt}]{\text{MeOH}} NEt_4[FeCl_{3.16}(NO)_{0.84}]$$

2b
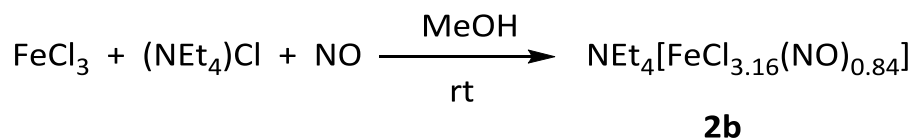
Starting material: Iron(III) chloride, tetraethylammonium chloride, methanol, nitric oxide.

Procedure: In a Schlenk flask a mixture of $FeCl_3$ (99.4 mg, 0.50 mmol, 1 eq.) and tetraethylammonium chloride (82.0 mg, 0.50 mmol, 1 eq.) was dissolved in deoxygenated methanol (3 mL), resulting in a clear yellow solution and yellowish precipitate. Afterwards the solution was treated with gaseous NO at room temperature for 10 minutes. After being kept at 5 °C for about 4 weeks, small green crystals were collected by removing the mother liquor, washed with diethyl ether, dried and stable under inert atmosphere.

Yield: 15.1 mg, 0.046 mmol, 9.2% based on $FeCl_3$.

Empirical formula: $C_8H_{20}Cl_{3.16}FeN_{1.84}O_{0.84}$, M = 323.35 g mol^{-1}.

IR spectroscopy (RT, solid), (intensity): $\tilde{\nu}$ = 1776 (s, NO) cm^{-1}.

UV/VIS (MeOH): λ = 475, 604 nm.

X-ray structure analysis: uo104.

5.6.5 Benzyltrimethylammonium trichloridonitrosylferrate (3)

$$\text{FeCl}_2 \cdot 4\text{H}_2\text{O} + (\text{NBnMe}_3)\text{Cl} + \text{NO} \xrightarrow[\substack{\text{rt} \\ -\,4\text{H}_2\text{O}}]{\text{MeOH}} \text{NBnMe}_3[\text{FeCl}_3(\text{NO})]$$
$$\textbf{3}$$
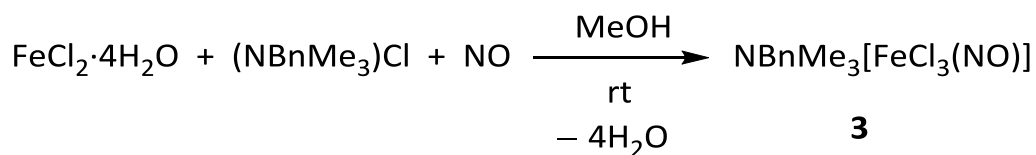
Starting material: Iron(II) chloride tetrahydrate, benzyltrimethylammonium chloride, methanol, nitric oxide.

Procedure: In a Schlenk flask a mixture of $\text{FeCl}_2 \cdot 4\text{H}_2\text{O}$ (99.4 mg, 0.50 mmol, 1 eq.) and benzyltrimethylammonium chloride (92.9 mg, 0.50 mmol, 1 eq.) was dissolved in deoxygenated methanol (3 mL), resulting in a clear yellow solution. Afterwards the solution was treated with gaseous NO at room temperature for 10 minutes. Green crystals were obtained after adding diethyl ether (3 mL) to the solution and keeping at 5 °C for about 4 weeks. The solvent was then removed by pipette and green crystals were washed with diethyl ether and dried under inert atmosphere. They were stable under inert atmosphere.

Yield: 92 mg, 0.27 mmol, 54% based on $\text{FeCl}_2 \cdot 4\text{H}_2\text{O}$.

Empirical formula: $C_{10}H_{16}Cl_3FeN_2O$, M = 342.45 g mol^{-1}.

IR spectroscopy (rt, solid), (intensity): $\tilde{\nu}$ = 1805 (s, NO) cm^{-1}.

UV/VIS (MeOH): λ = 461, 601 nm.

X-ray structure analysis: tv136.

5.6.6 Methyphenazinium trichloridonitrosylferrate (4)

Starting material: Iron(II) chloride tetrahydrate, phenazine methosulfate, methanol, nitric oxide.

Procedure: In a Schlenk flask a mixture of FeCl$_2$·4H$_2$O (99 mg, 0.50 mmol, 1 eq.) and phenazine methosulfate (0.15 g, 0.50 mmol, 1 eq.) was dissolved in deoxygenated methanol (3 mL), resulting in a bright yellow solution with light green-yellow precipitate. Afterwards the solution was treated with gaseous NO at room temperature for 10 minutes. The solution and precipitate turned green. Green crystals crystallized in the mother liquor immediately. The solvent was then removed by pipette and green crystals were washed with diethyl ether and dried under inert atmosphere. They were stable under inert atmosphere.

Yield: 0.10 g, 0.26 mmol, 52% based on FeCl$_2$·4H$_2$O.

Empirical formula: C$_{13}$H$_{11}$Cl$_3$FeN$_3$O, M = 387.45 g mol^{-1}.

IR spectroscopy (rt, solid), (intensity): $\tilde{\nu}$ = 1792 (s, NO) cm^{-1}.

UV/VIS (MeOH): λ = 425, 460, 604nm.

Elemental analysis: Calcd. (%): C: 40.30, H: 2.86, N: 10.85, Cl: 27.45.

Found (%): C: 39.11, H: 3.13, N: 9.29, Cl: 24.61.

X-ray structure analysis: vv064.

5.6.7 Cobaltocenium trichloridonitrosylferrate (5)

$$FeCl_3 + Co(cp)_2 + NO \xrightarrow[\text{rt}]{\text{MeOH}} [Co(cp)_2][FeCl_3(NO)]$$

5
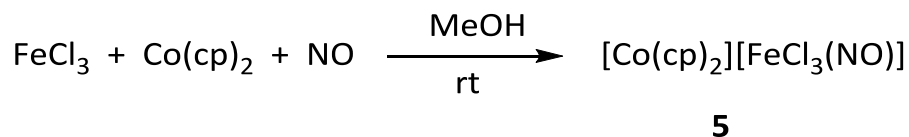
Starting material: Iron(III) chloride, cobaltocene, methanol, nitric oxide.

Procedure: In a Schlenk flask a mixture of $FeCl_3$ (17.0 mg, 0.10 mmol, 1 eq.) and cobaltocene (20.0 mg, 0.10 mmol, 1 eq.) was dissolved in deoxygenated methanol (3 mL), resulting in a brown solution. Afterwards the solution was treated with gaseous NO at room temperature for 10 minutes, which turned deep brown. Dark green crystals were obtained after keeping the solution at 5 °C for about 1 week. The solvent was then removed by pipette and green crystals were washed with diethyl ether and dried under inert atmosphere. Green crystals were stable under inert atmosphere.

Yield: 15 mg, 0.04 mmol, 40% based on $FeCl_3$.

Empirical formula: $C_{10}H_{10}CoFeNOCl_3$, M = 381.32 g mol^{-1}.

IR spectroscopy (RT, solid), (intensity): $\tilde{v}$ = 1793 (s, NO) cm^{-1}.

UV/VIS (MeOH): λ = 340, 352, 417, 600, 687 nm.

UV/VIS (solid): λ = 269, 322, 396, 472, 689 nm.

MS (FAB⁻): m/z (%) = 160.9 [M−NO]⁻, calcd. 160.84.

MS (FAB⁺): m/z (%) = 339.4 [Co(Cp)$_2$]⁺, calcd. 189.0.

Elemental analysis: Calcd. (%): C: 31.50, H: 2.64, N: 3.67, Cl: 27.89.

Found (%): C: 30.39, H: 3.06, N: 2.72, Cl: 21.25.

ICP analysis: Calcd (%): Co 15.45, Fe 14.65.

Found (%): Co 15.35, Fe 13.41.

X-ray structure analysis: tv206.

5.6.8 Tetraphenylphosphonium trichloridonitrosylferrate (6)

$$FeCl_2 \cdot 4H_2O + (PPh_4)Cl + NO \xrightarrow[-4H_2O]{\substack{MeOH \\ rt}} PPh_4[FeCl_3NO]$$

6
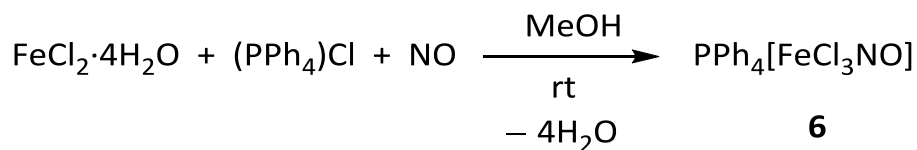
Starting material: Iron(II) chloride tetrahydrate, tetraphenylphosphonium chloride, methanol, nitric oxide.

Procedure: In a Schlenk flask a mixture of $FeCl_2 \cdot 4H_2O$ (99 mg, 0.50 mmol, 1 eq.) and tetraphenylphosphonium chloride (187 mg, 0.50 mmol, 1 eq.) was dissolved in deoxygenated methanol (3 mL), resulting in a bright yellow solution. Afterwards the solution was treated with gaseous NO at room temperature for 10 minutes, small green crystals were obtained during the treatment with NO. The green crystals were collected by filtration, washed with diethyl ether, dried under inert atmosphere and were stable in air.

Yield: 194 mg, 0.36 mmol, 73% based on $FeCl_2 \cdot 4H_2O$.

Empirical formula: $C_{24}H_{20}Cl_3FeNOP$, M = 531.58 g mol^{-1}.

IR spectroscopy (RT, solid), (intensity): $\tilde{\nu}$ = 1797 (s, NO) cm^{-1}.

UV/VIS (acetone): λ = 327, 358, 476, 646 nm.

UV/VIS (solid): λ = 231, 273, 293, 305, 322, 399, 480, 684 nm.

Elemental analysis: Calcd. (%): C: 54.22, H: 3.79, N: 2.63, Cl: 20.01.

Found (%): C: 54.39, H: 3.06, N: 2.60, Cl: 19.15

X-ray structure analysis: tv135.

5.6.9 Tetraphenyl arsonium trichloridonitrosylferrate (7)

$$FeCl_2 \cdot 4H_2O \; + \; (AsPh_4)Cl \; + \; NO \; \xrightarrow[\substack{rt \\ -\,4H_2O}]{MeOH} \; AsPh_4[FeCl_3(NO)]$$

7
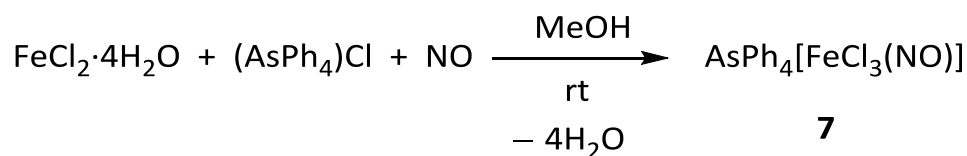
Starting material: Iron(II) chloride tetrahydrate, tetraphenylarsonium chloride, methanol, nitric oxide.

Procedure: In a Schlenk flask a mixture of $FeCl_2 \cdot 4H_2O$ (99 mg, 0.50 mmol, 1 eq.) and tetraphenylarsonium chloride (209 mg, 0.50 mmol, 1 eq.) was dissolved in deoxygenated methanol (3 mL), resulting in a bright yellow solution. Afterwards the solution was treated with gaseous NO at room temperature for 10 minutes, small green crystals were obtained during the treatment with NO. The green crystals were collected by filtration, washed with diethyl ether, dried under inert atmosphere and were stable in air but it had to be kept under inert atmosphere.

Yield: 0.20 g, 0.35 mmol, 70% based on $FeCl_2 \cdot 4H_2O$.

Empirical formula: $C_{24}H_{20}Cl_3AsFeNO$, M = 575.53 g mol^{-1}.

IR spectroscopy (RT, solid), (intensity): $\tilde{v}$ = 1797 (s, NO) cm^{-1}.

UV/VIS (solid): λ = 395, 481, 687 nm.

Elemental analysis: Calcd. (%): C: 50.08, H: 3.50, N: 2.43.

Found (%): C: 50.08, H: 3.54, N: 2.35.

X-ray structure analysis: vv505.

5.6.10 Bis(triphenylphosphane)iminium trichloridonitrosylferrate (8)
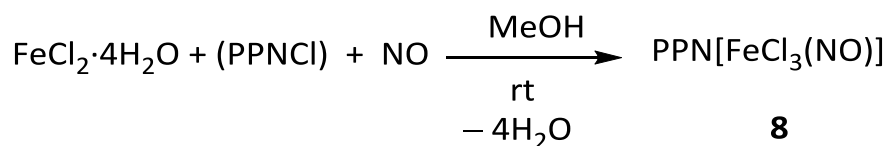
$$FeCl_2 \cdot 4H_2O + (PPNCl) \ + \ NO \ \xrightarrow[\substack{rt \\ -\,4H_2O}]{MeOH} \ PPN[FeCl_3(NO)]$$

$$\mathbf{8}$$

Starting material: Iron(II) chloride tetrahydrate, bis(triphenylphosphane)iminium chloride, methanol, nitric oxide.

Procedure: In a Schlenk flask a mixture of $FeCl_2 \cdot 4H_2O$ (99.4 mg, 0.50 mmol, 1 eq.) and bis(triphenylphosphane)iminium chloride (287 mg, 0.50 mmol, 1 eq.) was dissolved in deoxygenated methanol (3 mL), resulting in a bright yellow solution. Afterwards the solution was treated with gaseous NO at room temperature for 10 minutes, small green crystals were obtained during the treatment with NO. The green crystals were collected by filtration, washed with diethyl ether, dried under inert atmosphere and were very stable in air.

Yield: 0.33 g, 0.45 mol, 90% based on $FeCl_2 \cdot 4H_2O$.

Empirical formula: $C_{36}H_{30}Cl_3FeN_2OP_2$, M = 730.76 g mol^{-1}.

IR spectroscopy (rt, solid), (intensity): $\tilde{\nu}$ = 1791 (s, NO) cm^{-1}.

Raman spectroscopy (rt, solid, 50 Watt, 1064 nm): $\tilde{\nu}$= 1791 cm^{-1} (w, NO), 500 cm^{-1} (w, Fe–N)

UV/VIS (solid): λ = 400, 486, 660 nm.

Elemental analysis: Calcd. (%): C: 59.17, H: 4.14, N: 3.83, Cl: 14.55.

Found (%): C: 58.91, H: 4.11; N: 3.61, Cl: 13.76.

X-ray structure analysis: tq012.

5.6.11 Tris(2,2'-bipyridine)iron(II) trichloridonitrosylferrate (9)

$$3 \ FeCl_2 \cdot 4H_2O \ + 3 \ (2,2'\text{-bipyridine}) \ + \ HCl \ + 2 \ NO \ \xrightarrow[\ -\ HCl, \ -\ 4H_2O\ ]{\overset{MeOH}{rt}} \ \{Fe(bpy)_3\}[FeCl_3(NO)]_2$$

9
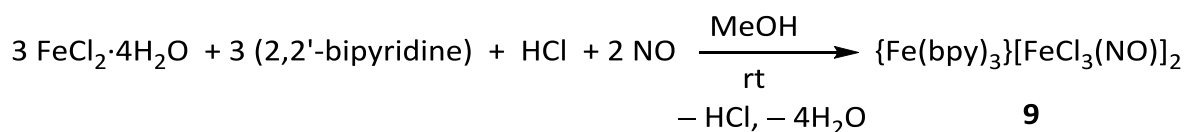
Starting material: Iron(II) chloride tetrahydrate, 2,2'-bipyridine, methanol, nitric oxide.

Procedure: In a Schlenk flask a mixture of 2,2'-bipyridine (32 mg, 0.20 mmol, 1 eq.) and hydrochloric acid (0.2 M, 23 µL, 0.20 mmol, 1 eq.) was dissolved in deoxygenated methanol (3 mL), then $FeCl_2 \cdot 4H_2O$ (40 mg, 0.20 mmol, 1 eq.) was added, resulting in a red solution. The solution was later treated with gaseous NO at room temperature for 10 minutes. Dark red crystals were obtained during the treatment with NO, which were collected by filtration after 4 days and were stable in air.

Yield: 15 mg, 8 µmol, 4% based on $FeCl_2 \cdot 4H_2O$.

Empirical formula: $C_{60}H_{48}Cl_{12.30}Fe_6N_{15.70}O_{3.70}$, M = 1819.26 g mol^{-1}.

IR spectroscopy (rt, solid), (intensity): $\tilde{\nu}$ = 1777 (s, NO) cm^{-1}.

UV/VIS (solid): λ = 306, 374, 492, 538, 667

X-ray structure analysis: tv406.

5.6.12 [4-[4,4'-bis(dimethylamino)benzhydrylidene]cyclohexa-2,5-dien-1-ylidene] dimethylammonium trichloridonitrosylferrate (10)
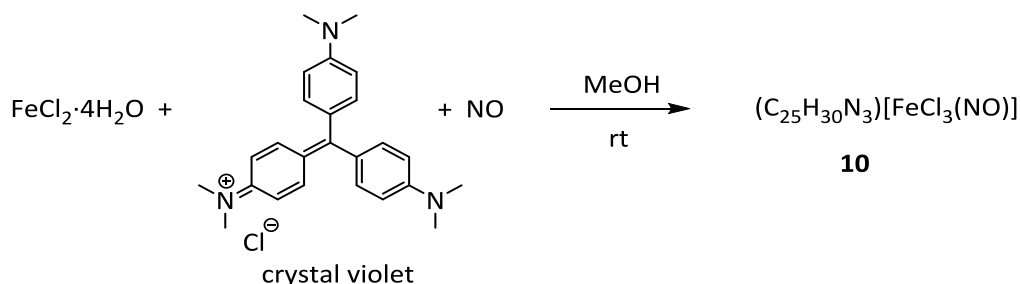
Starting material: Iron(II) chloride tetrahydrate, [4-[4,4'-bis(dimethylamino)benzhydrylidene]-cyclohexa-2,5-dien-1-ylidene]dimethylammonium chloride (crystal violet), methanol, nitric oxide.

Procedure: In a Schlenk flask a mixture of $FeCl_2 \cdot 4H_2O$ (40 mg, 0.20 mmol, 1 eq.) and crystal violet (82 mg, 0.20 mmol, 1 eq.) was dissolved in deoxygenated methanol (6 mL), resulting in a violet solution. Afterwards the solution was treated with gaseous NO at room temperature for 10 minutes. Small gold-green crystals were obtained after leaving the mixture at room temperature for about 2 weeks. The gold-green crystals were collected by filtration.

Yield: 12 mg, 0.021 mmol, 11% based on $FeCl_2 \cdot 4H_2O$.

Empirical formula $C_{25}H_{30}Cl_3FeN_4O$, M = 564.74 g mol^{-1}.

IR spectroscopy (rt, solid), (intensity): $\tilde{\nu}$ = 1771 (s, NO) cm^{-1}.

UV/VIS (solid): λ = 214, 249, 304, 395, 583, 650 nm.

Elemental analysis: Calcd. (%): C: 53.17, H: 5.35, N: 9.92.

Found (%): C: 52.06, H: 5.35, N: 8.82.

X-ray structure analysis: uv295.

5.6.13 Tetraphenylphosphonium tribromidonitrosylferrate (11)

$$\text{Fe(OTf)}_2 \ + \ 3 \ \text{(PPh}_4\text{)Br} \ + \ \text{NO} \ \xrightarrow[\begin{subarray}{c} \text{rt} \\ - \ 2 \ \text{(PPh}_4\text{)(OTf)} \end{subarray}]{\text{MeOH}} \ \text{PPh}_4\text{[FeBr}_3\text{(NO)]}$$

11
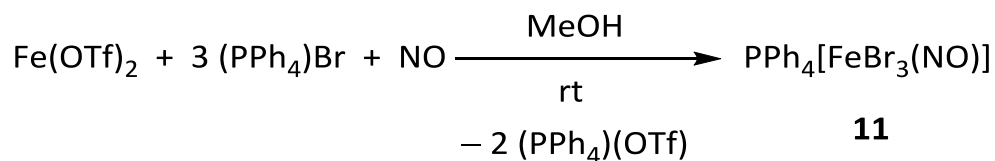
Starting material: Iron(II) triflate, tetraphenyl phosphonium bromide, methanol, nitric oxide.

Procedure: In a Schlenk flask a mixture of Fe(OTf)_2 (77.2 mg, 0.20 mmol, 1 eq.) and tetraphenylphosphonium bromide (252 mg, 0.60 mmol, 3 eq.) was dissolved in deoxygenated methanol (6 mL), resulting in a bright yellow-orange solution. Afterwards the solution was treated with gaseous NO at room temperature for 10 minutes and turned green-brown. The green-brown crystals crystallized in the mother liquor after being kept under 5 °C for several days.

Yield: 10 mg, 0.015 mmol, 7% based on Fe(OTf)_2.

Empirical formula: $C_{24}H_{20}Br_3FeNOP$, M = 664.96 g mol^{-1}.

IR spectroscopy (rt, solid), (intensity): $\tilde{\nu}$ = 1797 (s, NO) cm^{-1}.

UV/VIS (MeOH): λ = 331, 341, 466, 596 nm.

X-ray structure analysis: uv505.

5.6.14 Tetraphenylarsonium tribromidonitrosylferrate (12)

$$Fe(OTf)_2 + 3\ (AsPh_4)Br\ +\ NO\ \xrightarrow[\ -\ 2\ (AsPh_4)(OTf)]{\overset{MeOH}{rt}}\ AsPh_4[FeBr_3(NO)]$$

$$\textbf{12}$$
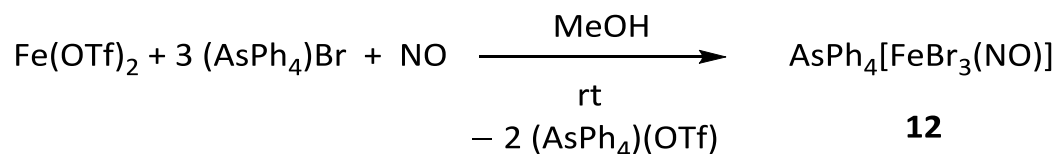
Starting material: Iron(II) triflate, tetraphenylarsonium bromide, methanol, nitric oxide.

Procedure: In a Schlenk flask a mixture of $Fe(OTf)_2$ (38.6 mg, 0.10 mmol, 1 eq.) and tetraphenylarsonium bromide (139 mg, 0.30 mmol, 3 eq.) was dissolved in deoxygenated methanol (3 mL), resulting in a bright yellow-orange solution. Afterwards the solution was treated with gaseous NO at room temperature for 10 minutes and turned green-brown. The green-brown crystals crystallized in the mother liquor after being kept under 5 °C for several days.

Yield: 0.02 g, 0.02 mmol, 21% based on $Fe(OTf)_2$.

Empirical formula: $C_{24}H_{20}AsBr_3FeNO$, M = 708.91 g mol^{-1}.

IR spectroscopy (rt, solid), (intensity): $\tilde{\nu}$ = 1794 (s, NO) cm^{-1}.

UV/VIS (MeOH): λ = 330, 341, 352, 466, 601 nm.

UV/VIS (solid): λ = 370, 482, 663 nm.

X-ray structure analysis: uv591.

5.6.15 Bis(triphenylphosphane)iminium tribromidonitrosylferrate (13)

$$\text{Fe(OTf)}_2\cdot4\text{MeOH} + 3\ (\text{PPN})\text{Br} + \text{NO} \xrightarrow[\substack{\text{rt} \\ -\ 2\ (\text{PPN})(\text{OTf}) \\ -\ 4\ \text{MeOH}}]{\text{MeOH}} \text{PPN[FeBr}_3(\text{NO})]$$

13
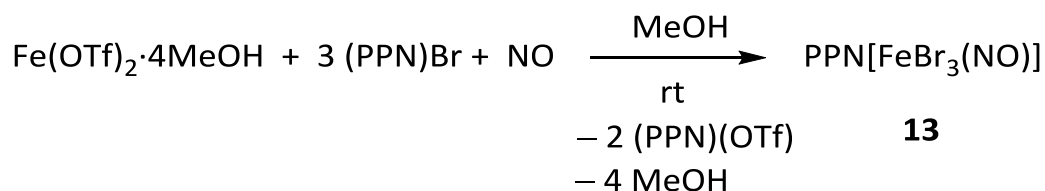
Starting material: Iron(II) triflate tetramethanol, bis(triphenylphosphane)iminium bromide, methanol, nitric oxide.

Procedure: In a Schlenk flask a mixture of iron(II) triflate tetramethanol (193 mg, 0.50 mmol, 1 eq.) and bis(triphenylphosphane)iminium bromide (928 mg, 1.50 mmol, 3 eq.) was dissolved in deoxygenated methanol (3 mL), resulting in a bright yellow solution. Afterwards the solution was treated with gaseous NO at room temperature for 10 minutes, small green crystals were obtained during the treatment with NO. The green crystals were collected by filtration and were stable in air.

Yield: 0.30 g, 0.35 mmol, 69% based on Fe(OTf)$_2\cdot$4MeOH.

Empirical formula: C$_{36}$H$_{30}$Br$_3$FeN$_2$OP$_2$, M = 864.14 g mol^{-1}.

IR spectroscopy (rt, solid), (intensity): $\tilde{\nu}$ = 1774 (m, NO) cm^{-1}.

UV/VIS (MeOH): λ = 477, 597 nm.

UV/VIS (solid): λ = 390, 483, 660 nm.

Elemental analysis: Calcd. (%): C: 50.04, H: 3.50, N: 3.24, Br: 27.74.

Found (%): C: 57.35, H: 4.03, N: 2.54, Br: 12.73.

5.6.16 Bis(triphenylphosphane)iminium tribromidonitrosylferrate (13a)
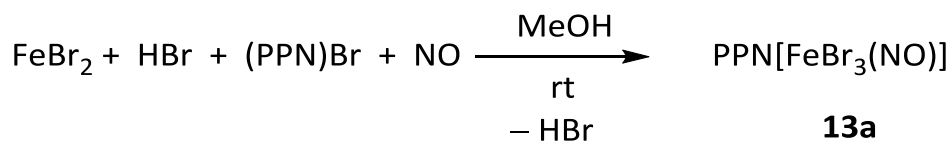
$$FeBr_2 + HBr + (PPN)Br + NO \xrightarrow[\substack{rt \\ -HBr}]{MeOH} PPN[FeBr_3(NO)]$$

13a

Starting material: Iron(II) bromide, bis(triphenylphosphane)iminium bromide, methanol, H_2O, hydrobromic acid, nitric oxide.

Procedure: In a Schlenk flask a mixture of iron(II) bromide (22 mg, 0.10 mmol, 1 eq.) and bis(triphenylphosphane)iminium bromide (62 mg, 0.10 mmol, 1 eq.) was dissolved in deoxygenated methanol (3 mL), then HBr (40%, 0.1 mL, 0.6 mmol) and deoxygenated H_2O 0.25 mL were added. The solution was then treated with gaseous NO at room temperature for 10 minutes. Green crystals (**13a**) formed in the mother liquor along with small brown-red crystals (**15b**) were obtained after allowing to store at 5 °C for some weeks.

Yield: low yield.

Empirical formula: $C_{36}H_{30}Br_3FeN_2OP_2$, M = 864.14 g mol^{-1}.

IR spectroscopy (rt, solid), (intensity): $\tilde{\nu}$ = 1800 (s, NO) cm^{-1}.

X-ray structure analysis: wv365.

5.6.17 Tetramethylammonium dichloridodinitrosylferrate (14a)
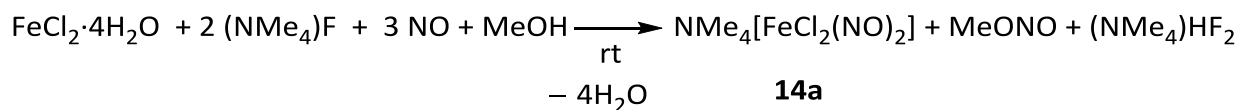
$$FeCl_2 \cdot 4H_2O + 2 (NMe_4)F + 3 NO + MeOH \xrightarrow[- 4H_2O]{rt} NMe_4[FeCl_2(NO)_2] + MeONO + (NMe_4)HF_2$$

14a

Starting material: Iron(II) chloride tetrahydrate, tetramethylammonium chloride, methanol, nitric oxide.

Procedure: In a Schlenk flask a mixture of $FeCl_2 \cdot 4H_2O$ (0.12 g, 0.60 mmol, 1 eq.) and tetramethylammonium fluoride (0.11 g, 1.2 mmol, 2 eq.) was dissolved in deoxygenated methanol (3 mL), resulting in a light yellow solution with pH value $\approx$3-4 (in MeOH). Afterwards the solution was treated with gaseous NO at room temperature for 2 minutes and turned immediately brown. The brown-red crystals crystallized above the mother liquor and were stable in air once dried.

Yield: 47 mg, 0.18 mmol, 30% based on $FeCl_2 \cdot 4H_2O$.

Empirical formula: $C_4H_{12}Cl_2FeN_3O_2$, M = 260.92 g mol^{-1}.

IR spectroscopy (rt, solid), (intensity): $\tilde{v}$ = 1779 (m, NO), 1695 (s, NO) cm^{-1}.

IR spectroscopy (rt, MeOH), (intensity): $\tilde{v}$ = 1785 (w, NO), 1717 (s, NO) cm^{-1}.

UV/VIS (MeOH): λ = 510, 702 nm.

UV/VIS (solid): λ = 400, 514, 600, 703 nm.

X-ray structure analysis: vv661.

5.6.18 Tetramethylammonium dichloridodinitrosylferrate (14b)

$$FeCl_3 + 3\ (NMe_4)F + 4\ NO + 2\ MeOH \xrightarrow{rt} NMe_4[FeCl_2(NO)_2] + (NMe_4)Cl + 2\ MeONO$$

$$\textbf{14b} \qquad + (NMe_4)HF_2 + HF$$

Starting material: Iron(III) chloride, tetramethylammonium chloride, methanol, nitric oxide.

Procedure: In a Schlenk flask a mixture of iron(III) chloride (28 mg, 0.16 mmol, 1 eq.) and tetramethylammonium fluoride (46 mg, 0.50 mmol, 3.1 eq.) was dissolved in deoxygenated methanol (3 mL), resulting in a light yellow solution. Afterwards the solution was treated with gaseous NO at room temperature for 10 minutes. After allowing the mixture solution stand at room temperature or at 5 °C this green solution turned brown. Brown crystals crystallized above the mother liquor and were collected by removing the mother liquor and were stable in air once dried.

Yield: 10 mg, 38 µmol, 24% based on $FeCl_3$.

Empirical formula: $C_4H_{12}Cl_2FeN_3O_2$, M = 260.92 g mol^{-1}.

IR spectroscopy (rt, solid), (intensity): $\tilde{\nu}$ = 1783 (w, NO), 1687 (s, NO) cm^{-1}.

IR spectroscopy (rt, MeOH, (intensity): $\tilde{\nu}$ = 1786 (w, NO), 1692 (s, NO) cm^{-1}.

UV/VIS (MeOH): λ = 508, 696 nm.

X-ray structure analysis: uo024.

5.6.19 Bis(triphenylphosphane)iminium dichloridodinitrosylferrate (14c)
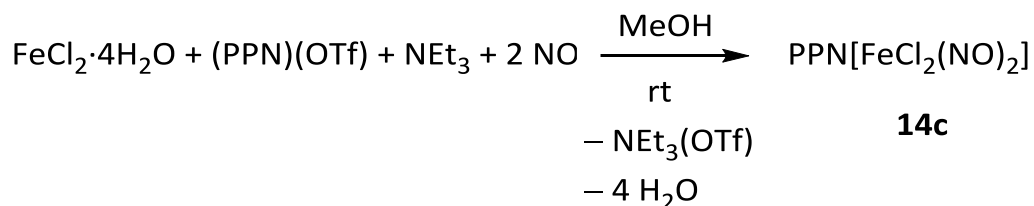
$$\text{FeCl}_2\cdot 4\text{H}_2\text{O} + \text{(PPN)(OTf)} + \text{NEt}_3 + 2\ \text{NO} \xrightarrow[\text{rt}]{\text{MeOH}} \text{PPN[FeCl}_2\text{(NO)}_2]$$

$$-\ \text{NEt}_3\text{(OTf)} \qquad \textbf{14c}$$
$$-\ 4\ \text{H}_2\text{O}$$

Starting material: Iron(II) chloride tetrahydrate, bis(triphenylphosphane)iminium triflate, triethylamine, methanol, nitric oxide.

Procedure: In a Schlenk flask a mixture of iron(II) chloride tetrahydrate (40 mg, 0.20 mmol, 1 eq.) and bis(triphenylphosphane)iminium triflate (0.14 g, 0.20 mmol, 3.1 eq.) was dissolved in deoxygenated methanol (3 mL), resulting in a light yellow solution with pH value of 2-3 (in MeOH). Then triethylamine (0.03 mL, 0.2 mmol, 1 eq.) was added, pH value was ~3-4(in MeOH), the solution was light green and the suspension was observed. MeOH (1 mL) was added before the solution was treated with gaseous NO at room temperature for 2 minutes. The mixture turned brown with a yellow suspension. Large brown crystals were obtained after the solution was kept at 5 °C overnight. Brown crystals were isolated by removing the mother liquor and dried under inert atmosphere which were stable in air.

Yield: >0.14 g, 0.19 mmol, >90% based on $\text{FeCl}_2\cdot 4\text{H}_2\text{O}$.

Empirical formula: $C_{36}H_{30}Cl_2FeN_3O_2P_2$, M = 725.32 g mol^{-1}.

IR spectroscopy (rt, solid), (intensity): $\tilde{\nu}$ = 1775 (m, NO), 1696 (s, NO) cm^{-1}.

UV/VIS (solid, BaSO$_4$): λ = 234, 267, 334, 399, 429, 515, 693 nm.

X-ray structure analysis: vv643.

5.6.20 Bis(triphenylphosphane)iminium dibromidodinitrosylferrate (15a)

$$2.5 \ Fe(OTf)_2 + \ 5 \ (PPN)Br + 3 \ NO \xrightarrow[\substack{rt \\ -5 \ (PPN)(OTf)}]{MeOH} \ PPN[FeBr_2(NO)_2] + ... + PPN[FeBr_3(NO)]$$

15a
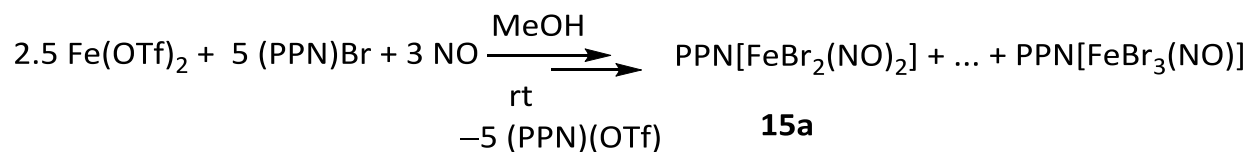
Starting material: Iron(II) triflate , bis(triphenylphosphane)iminium bromide, methanol, nitric oxide.

Procedure: In a Schlenk flask a mixture of iron(II) triflate (71 mg, 0.20 mmol, 1 eq.) and bis(triphenylphosphane)iminium bromide (0.12 g, 0.20 mmol, 1 eq.) was dissolved in deoxygenated methanol (3 mL). The solution was then treated with gaseous NO at room temperature for 2 minutes. In the green solution, the small brown-red crystals were obtained after allowed to store at 5 °C for two weeks. Besides these brown-red crystals, green crystals of PPN[FeBr$_3$(NO)] were observed as well as a main product in the Schlenk flask.

Yield: 4 mg, 5 μmol, 2.5%.

Empirical formula: $C_{36}H_{30}Br_2Fe \ N_3O_2P_2$, M = 814.24 g mol^{-1}.

IR spectroscopy (rt, solid), (intensity): $\tilde{\nu}$ = 1777 (w, NO), 1710 (m, NO) cm^{-1}.

UV/VIS (MeOH): λ = 516, 691 nm.

X-ray structure analysis: vv286.

5.6.21 Bis(triphenylphosphane)iminium dibromidodinitrosylferrate (15b)
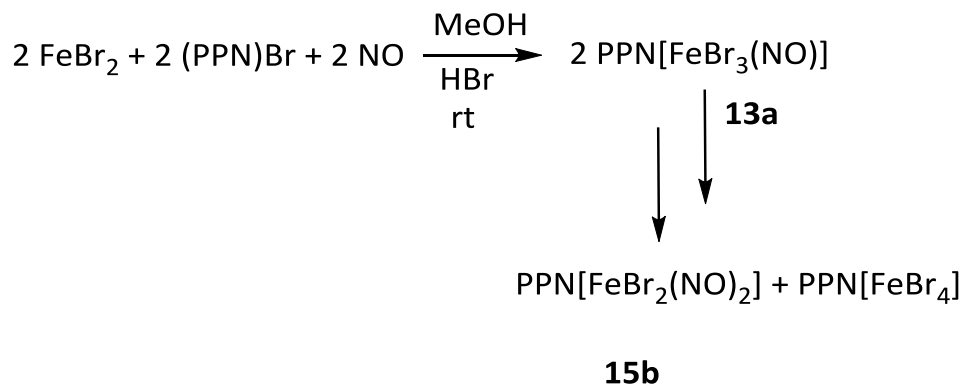
$$2 \text{ FeBr}_2 + 2 \text{ (PPN)Br} + 2 \text{ NO} \xrightarrow[\text{rt}]{\begin{array}{c}\text{MeOH}\\ \text{HBr}\end{array}} 2 \text{ PPN[FeBr}_3(\text{NO})]$$

13a

$$\text{PPN[FeBr}_2(\text{NO})_2] + \text{PPN[FeBr}_4]$$

15b

Starting material: Iron(II) bromide, bis(triphenylphosphane)iminium bromide, methanol, H_2O, hydrobromic acid, nitric oxide.

Procedure: In a Schlenk flask a mixture of iron(II) bromide (22 mg, 0.10 mmol, 1 eq.) and bis(triphenylphosphane)iminium bromide (62 mg, 0.10 mmol, 1 eq.) was dissolved in deoxygenated methanol (3 mL), then HBr (40%, 0.1 mL, 0.6 mmol) and deoxygenated H_2O 0.25 mL were added. The solution was then treated with gaseous NO at room temperature for 10 minutes. Small brown-red crystals were obtained after allowing to store at 5 °C for some weeks.

Yield: 5 mg, 6 µmol, 6% based on FeBr_2.

Empirical formula: $C_{36}H_{30}Br_2FeN_3O_2P_2$, M = 814.24 g mol^{-1}.

IR spectroscopy (rt, solid), (intensity): $\tilde{\nu}$ = 1776 (s, NO), 1709 (vs, NO) cm^{-1}.

X-ray structure analysis: tv280.

5.6.22 Bis(triphenylphosphane)iminium diiododinitrosylferrate (16) and di-bis(triphenylphosphane)iminium diiododinitrosylferrate triiodide (17)

$$2\ Fe(OTf)_2 \cdot 2MeOH + 7\ (PPN)I + 4\ NO \xrightarrow[\substack{50\ °C \\ -\ 4\ (PPN)(OTf) \\ -\ 4\ MeOH}]{MeOH} \underset{\textbf{16}}{PPN[FeI_2(NO)_2]} + \underset{\textbf{17}}{(PPN)_2[FeI_2(NO)_2](I_3)}$$
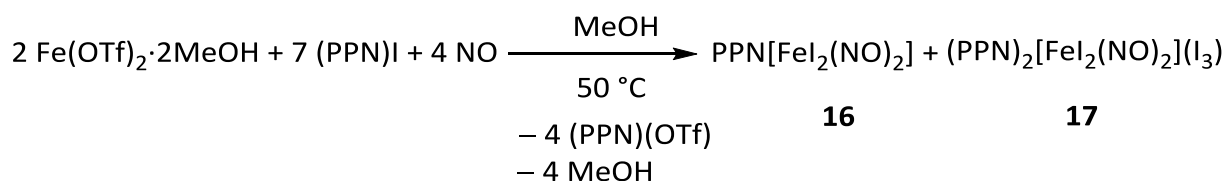
Starting material: Iron(II) triflate dimethanol, bis(triphenylphosphane)iminium iodide, methanol, nitric oxide.

Procedure: In a Schlenk flask a mixture of iron(II) triflate tetramethanol (44 mg, 0.10 mmol, 1eq.) and bis(triphenylphosphane)iminium iodide (0.20 g, 0.30 mmol, 3 eq.) was dissolved in deoxygenated methanol (3 mL). The solution was heated at 50 °C and treated with gaseous NO for 10 minutes. Brown-red crystals were obtained during suggestion of gaseous NO. The obtained crystals were filtered and then washed with diethyl ether and kept under argon atmosphere. The crystals were stable in air. Product **16** as a main product and **17** as a byproduct were obtained in the same reaction Schlenk tube.

Yield: 35 mg, 0.013 mmol, 13% (**16** and **17,** M_{total} = 2735.69 g mol^{-1}.) based on Fe(OTf)$_2$·2MeOH.

Empirical formula: $C_{36}H_{30}FeI_2N_3O_2P_2$ (**16**), M = 908.22 g mol^{-1}.

IR spectroscopy (rt, solid), (intensity): $\tilde{\nu}$ = 1758 (s, NO), 1709 (vs, NO) cm^{-1}.

X-ray structure analysis: tv038 (**16**).

Empirical formula: $C_{72}H_{60}FeI_5N_4O_2P_4$ (**17**), M = 1827.47 g mol^{-1}.

IR spectroscopy (rt, solid), (intensity): $\tilde{\nu}$ = 1760 (m, NO), 1711 (s, NO) cm^{-1}.

X-ray structure analysis: tv029 (**17**).

Elemental analysis: Calcd. (%): C: 47.61, H: 3.33, N: 4.63.

Found (%): C: 47.57, H: 3.35, N: 3.78. = PPN[FeI$_2$(NO)$_2$] ·0.45 (PPN)$_2$[FeI$_2$(NO)$_2$](I$_3$)

5.6.23 Tetraphenylarsonium diiododinitrosylferrate (18)

$$\text{Fe(OTf)}_2\cdot\text{2MeOH} + 3.5\ (\text{AsPh}_4)\text{I} + 2\ \text{NO} \xrightarrow[\text{rt}]{\text{MeOH}} \text{AsPh}_4[\text{FeI}_2(\text{NO})_2] + 0.5\ (\text{AsPh}_4)\text{I}_3$$
$$- 2\ (\text{AsPh}_4)(\text{OTf}) \qquad \mathbf{18}$$
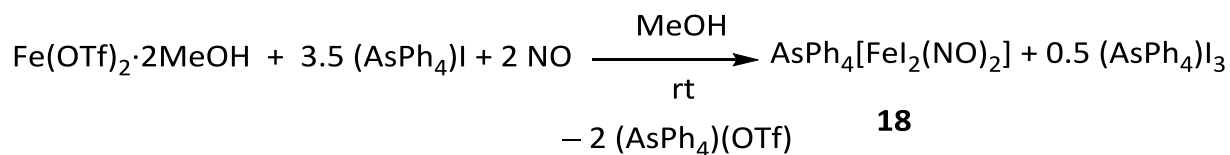
Starting material: Iron(II) triflate dimethanol, tetraphenylarsonium iodide, methanol, nitric oxide.

Procedure: In a Schlenk flask a mixture of iron(II) triflat dimethanol (44 mg, 0.10 mmol, 1 eq.) and tetraphenylarsonium iodide (0.15 g, 0.30 mmol, 3 eq.) was dissolved in deoxygenated methanol (3 mL). The solution was then treated with gaseous NO at room temperature for 10 minutes. The colorless solution turned deep green. The brown crystals crystallized immediately in the mother liquor. These crystals were collected by filtration, then washed with diethyl ether and dried under inert atmosphere. These brown crystals were stable in air.

Yield: 38 mg, 0.05 mmol, 50% based on Fe(OTf)$_2$·2MeOH.

Empirical formula: $C_{24}H_{20}AsFeI_2N_2O_2$, M = 752.99 g mol^{-1}.

IR spectroscopy (rt, solid), (intensity): $\tilde{v}$ = 1754 (m, NO), 1705 (s, NO) cm^{-1}.

X-ray structure analysis: uv122.

5.6.24 Tetraphenylphosphonium diiododinitrosylferrate (19)

$$\text{Fe(OTf)}_2\cdot 2\text{MeOH} + 3.5\ (\text{PPh}_4)\text{I} + 2\ \text{NO} \xrightarrow[\text{rt}]{\text{MeOH}} \text{PPh}_4[\text{FeI}_2(\text{NO})_2] + 0.5\ (\text{PPh}_4)\text{I}_3$$

$$-\ 2\ (\text{PPh}_4)(\text{OTf}) \qquad \textbf{19}$$
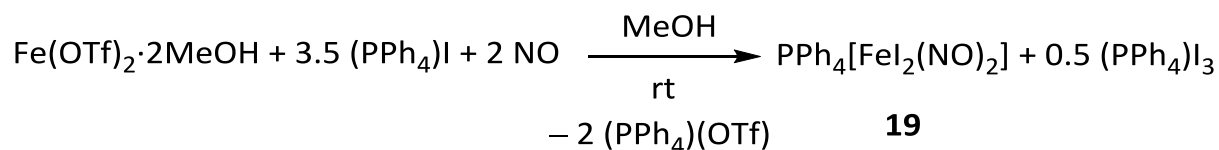
Starting material: Iron(II) triflate dimethanol, tetraphenylphosphonium iodide, methanol, nitric oxide.

Procedure: In a Schlenk flask a mixture of iron(II) triflate dimethanol (0.044 g, 0.10 mmol, 1 eq.) and tetraphenylphosphonium   iodide (0.14 mg, 0.30 mmol, 3 eq.) was dissolved in deoxygenated methanol (3 mL). The colorless solution was then treated with gaseous NO at room temperature for 10 minutes, resulting in a green solution. In this green solution, the small brown-red crystals were obtained during treatment with gaseous NO. These crystals were collected by filtration and washed with diethyl ether and dried under inert atmosphere. These brown crystals were stable in air.

Yield: 35 mg, 49 µmol, 49% based on Fe(OTf)$_2\cdot$2MeOH.

Empirical formula: C$_{24}$H$_{20}$FeI$_2$N$_2$O$_2$P, M = 709.04 g mol^{-1}.

IR spectroscopy (rt, solid), (intensity): $\tilde{\nu}$ = 1753 (m, NO), 1704 (s, NO) cm^{-1}.

X-ray structure analysis: uv222.

5.7 Synthesis of quartet {FeNO}[7] compounds with bis(pyrazoly)pyridine ligands

5.7.1   2,6-Di(1-pyrazolyl)pyridyl dichloridonitrosyliron methanol (20a-b)

(bipzpy)

20a

[Fe(bipzpy)Cl$_2$(NO)]·MeOH
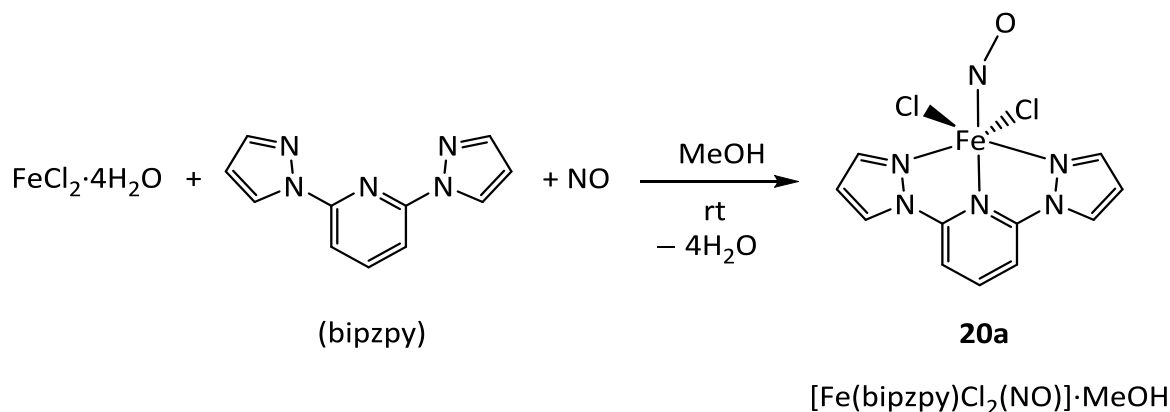
Starting material: Iron(II) chloride tetrahydrate, 2,6-di(1-pyrazolyl)pyridine (bipzpy), methanol, nitric oxide.

Procedure: In a Schlenk flask a mixture of iron(II) chloride tetrahydrate (20 mg, 0.10 mmol, 1 eq.) and 2,6-di(1-pyrazolyl)pyridine (bipzpy) (21 mg, 0.10 mmol, 1 eq.) was dissolved in deoxygenated methanol (3 mL), resulting in a bright yellow solution with yellowish precipitate. Afterwards the mixture solution was treated with gaseous NO at room temperature for ten minutes, the yellow solution turned green. The green-brown crystals crystallized above the mother liquor after being kept under 5 °C within 5 days. These green-brown crystals were stable in inert atmosphere.

Yield: 15 mg, 0.04 mmol, 40% based on FeCl$_2$·4H$_2$O.

Empirical formula: C$_{12}$H$_{13}$Cl$_2$FeN$_6$O$_2$, M = 400.03 g mol^{-1}.

IR spectroscopy (rt, solid), (intensity): $\tilde{\nu}$ = 1781 (s, NO) cm^{-1}.

UV/VIS (MeOH): λ = 446, 616 nm.

Elemental analysis: Calcd. (%): C: 36.03, H: 3.28, N: 21.01, Cl: 17.72.

Found (%): C: 37.86, H: 3.39, N: 20.58, Cl: 17.15.

X-ray structure analysis: uv573.

The product **21** was also prepared from $FeCl_3$ as starting material:

$[Fe(bipzpy)Cl_2(NO)]\cdot MeOH$
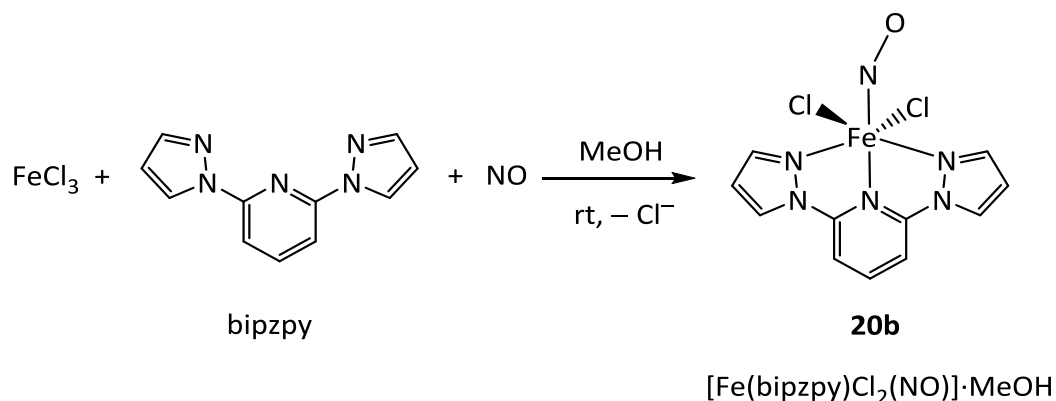
Starting material: Iron(III) chloride, 2,6-di(1-pyrazolyl)pyridine, methanol, nitric oxide.

Procedure: Analogous to product **20a** in a Schlenk flask a mixture of iron(III) chloride (16 mg, 0.10 mmol, 1 eq.) and 2,6-di(1-pyrazolyl)pyridine (bipzpy) (21 mg, 0.10 mmol, 1 eq.) was dissolved in deoxygenated methanol (3 mL), resulting in a bright yellow solution with yellowish precipitate. Afterwards the mixture solution was treated with gaseous NO at room temperature for 10 minutes, the yellow solution turned green. Green-brown crystals crystallized above the mother liquor after being kept under 5 °C within 5 days. These green-brown crystals were stable in inert atmosphere.

Yield: 10 mg, 25 µmol, 25% based on $FeCl_3$.

Empirical formula: $C_{12}H_{13}Cl_2FeN_6O_2$, M = 400.03 g mol^{-1}.

IR spectroscopy (rt, solid), (intensity): $\tilde{\nu}$ = 1779 (m, NO) cm^{-1}.

X-ray structure analysis: uv710.

5.7.2 2,6-Di(1-pyrazolyl)pyridyl dinitrosyliron tertrafluoroborate (21)

$[Fe(bipzpy)(NO)_2]BF_4$
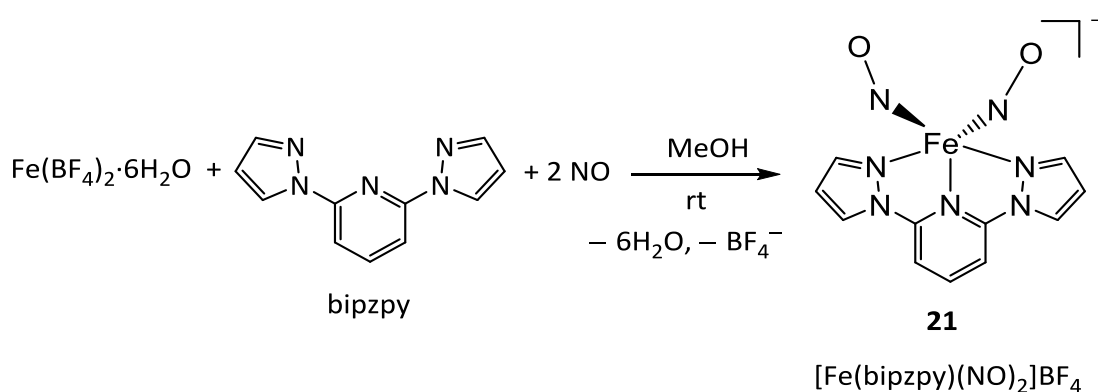
Starting material: Iron(II) tetrafluoroborate hexahydrate, 2,6-di(1-pyrazolyl)pyridine, methanol, nitric oxide.

Procedure: In a Schlenk flask a mixture iron(II) tetrafluoroborate hexahydrate (0.17 g, 0.50 mmol, 1 eq.) and 2,6-di(1-pyrazolyl)pyridine (0.11 g, 0.50 mmol, 1 eq.) was dissolved in deoxygenated methanol (3 mL), resulting in a bright yellow solution with a yellowish precipitate. The solution was separated from the precipitate and afterwards the mixture solution was treated with gaseous NO at room temperature for 10 minutes, the yellow solution turned dark green. Brown crystals crystallized in the mother liquor after slowly diffusion of *tert*-butyl methyl ether (3 mL) and were isolated. The brown crystals were stable in air.

Yield: 9 mg, 0.02 mmol, 4% based on $Fe(BF_4)_2 \cdot 6H_2O$.

Empirical formula: $C_{11}H_9BF_4FeN_7O_2$, M = 413.91 g mol^{-1}.

IR spectroscopy (rt, solid), (intensity): $\tilde{\nu}$ = 1796 (s, NO), 1715 (s, NO) cm^{-1}.

X-ray structure analysis: uv668.

5.8 Synthesis of quartet {FeNO}[7] compounds with 2-amino-4-(2-pyridyl)thiazole ligand

5.8.1 Synthesis of 2-amino-4-(2-pyridyl)thiazole ligand
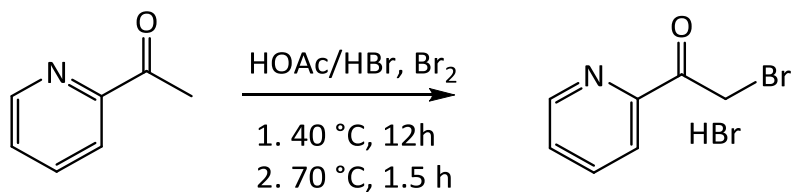
Literature[116]: Theses ligand was prepare according to Huxel *et al*. *via* two steps reaction.

Starting material: 2-(Acetyl)pyridine, Br_2, HOAc/HBr (33 wt%), Et_2O.

Step 1. Procedure: 2-(Acetyl)pyridine was distilled and 6.1 g (50 mmol) of the substance was dissolved in HOAc/HBr (190 mL, (33 wt%)). The light-yellow solution was cooled to 0 °C and 2.7 mL bromine was added *via* dropping funnel. The reaction mixture turned to a dark orange color after stirring over night at 40 °C. The mixture was then refluxed at 70 °C for 1.5 h, cooled to room temperature, and Et_2O was added to precipitate the product. The light-yellow substance was filtered of, washed with diethyl ether and acetone, and dried under reduced pressure.

Yield: 11.8 g, 42 mmol, 84% based on C_7H_7NO.

Empirical formula: C_7H_6BrNO, M = 200.04 g mol^{-1}.

^{1}**H-NMR** (DMSO, 400 MHz): δ [ppm] = 8.72 (dddd, *J*=7.6, 4.8, 1.7, 0.8, 1H), 8.68 (td, *J*=7.9, 1.6, 1H), 8.03-8.00 (m, 1H), 7.73 (ddd, *J*=7.6, 4.8, 1.3, 1H), 4.95 (s, 2H).

^{13}**C{^{1}H}-NMR** (DMSO, 100 MHz): δ [ppm] = 199.6, 149.2, 139.1, 128.8, 122.1, 95.5, 65.6.

IR (rt, solid), (intensity): $\tilde{v}$ = 3107 (w), 3077 (w), 2805 (br) 2332 (vw), 1865 (vw), 1725 (s), 1627 (w), 1604 (s), 1521 (s), 1453 (s), 1368 (m), 1316 (m), 1300 (m), 1219 (s), 1197 (s), 1156 (m), 1095 (m), 1038 (m), 1014 (s), 956 (m), 897 (m), 870 (w), 771 (s), 715 (m) cm^{-1}.
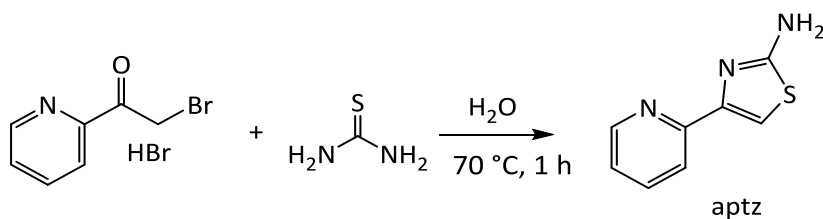
Starting material: 2-(Bromoacetyl)-pyridine hydrobromide, thiourea, NaOH, H_2O.

Step 2. Procedure: 2-(Bromoacetyl)-pyridine hydrobromide from step 1 (10 g, 35 mmol, 1 eq.), and thiourea (2.7 g, 35 mmol, 1 eq.) were dissolved in 50 mL and 20 mL H_2O, respectively and the combined solution was stirred for 1.5 h at room temperature. The acidic reaction mixture was then neutralized with NaOH until pH = 7 and the colorless precipitate was filtered of, washed with water and dried *in vacuo*.

Yield: 5.0 g, 28 mmol, 81% based on C_7H_6BrNO.

Empirical formula: $C_8H_7N_3S$, M = 177.23 g mol^{-1}.

Elemental analysis: Calcd. (%): C: 54.22, H: 3.98, N: 23.71, S: 18.09

Found (%): C: 54.22, H: 4.00, N: 23.73, S: 18.33

MS (FAB⁻): m/z (%) = 176[M−H]⁻, calcd. 176.0. No Br⁻

MS (FAB⁺): m/z (%) = 178.1 [M + H]⁺, calcd. 178.0.

5.8.2 Di-(2-amino-4-(2-pyridyl)thiazole) chlorido nitrosyl iron chloride methanol (23)
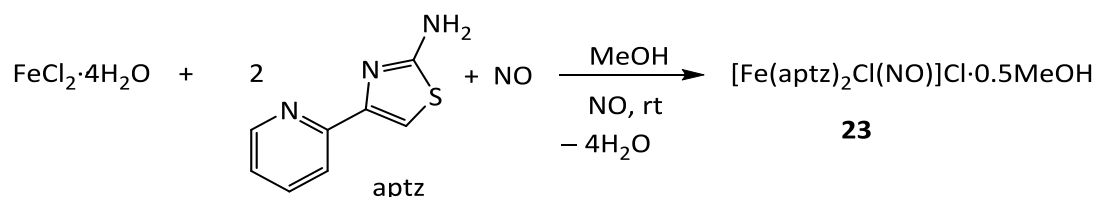
Starting material: Iron(II) chloride tetrahydrate, 2-amino-4-(2-pyridyl)thiazole (aptz), methanol, nitric oxide.

Procedure: In a Schlenk flask a mixture iron(II) chloride tetrahydrate (59.4 mg, 0.3 mmol, 1eq.) and 2-amino-4-(2-pyridyl)thiazole (aptz) (106 mg, 0.6 mmol, 2 eq.) was dissolved in deoxygenated methanol (3 mL), resulting in a bright yellow solution with yellow precipitate. One mL of the mixture solution was transferred to a new Schlenk flask and methanol (3 mL) was added, Afterwards the mixture solution was treated with gaseous NO at room temperature for 5 minutes, the yellow solution turned brown. The green-brown crystals crystallized immediately in the mother liquor. These brown crystals were stable in air.

Yield: 12 mg, 23 µmol, 8% based on $FeCl_2 \cdot 4H_2O$.

Empirical formula: $C_{16.49}H_{15.95}Cl_2FeN_7O_{1.49}S_2$, M = 526.83 g mol^{-1}.

IR spectroscopy (rt, solid), (intensity): $\tilde{v}$ = 1765 (m, NO) cm^{-1}.

X-ray structure analysis: vv175.

5.9 Synthesis of [Fe(CH₃OH)(NO)(μ₄-SO₄)]ₙ/ₙ (A)

$$5.9 \quad \textbf{Synthesis of } [\text{Fe(CH}_3\text{OH})(\text{NO})(\mu_4\text{-SO}_4)]_{n/n} \ (\textbf{A})$$

$$[\text{Fe(CH}_3\text{OH})(\text{NO})(\mu_4\text{-SO}_4)]_{n/n}$$
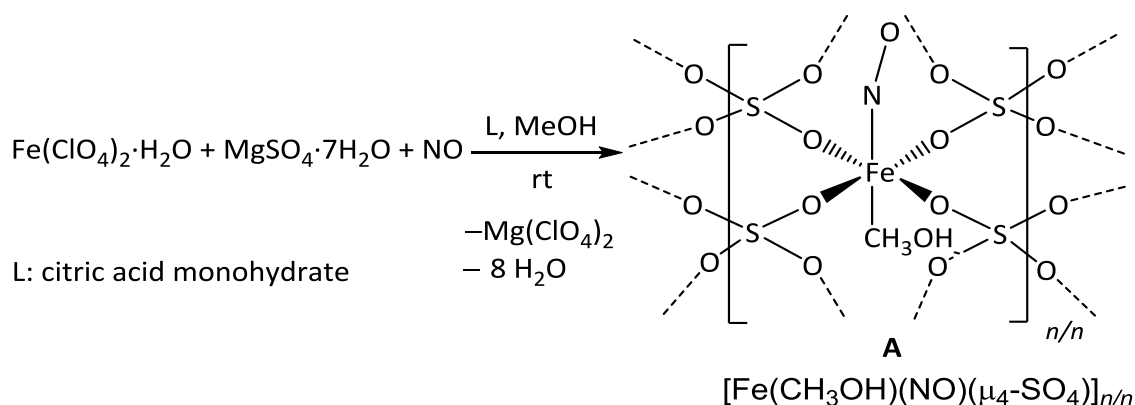
Starting material: Iron(II) perchlorate monohydrate, magnesium sulfate heptahydrate, citric acid monohydrate, methanol, nitric oxide.

Procedure: In a Schlenk flask with a dividing wall, a mixture of Fe(ClO₄)₂·H₂O (0.14 g, 0.50 mmol, 1 eq.), magnesium sulfate heptahydrate (0.12 g, 0.50 mmol, 1 eq.), citric acid monohydrate (0.21 g, 2.0 mmol, 2 eq.), was dissolved in deoxygenated methanol (3 mL) and water (0.05 mL), resulting in a clear yellow solution (pH~1). Another side of the Schlenk flask was filled with acetone (3 mL) as an antisolvent. Afterwards the solution was treated with gaseous NO at room temperature for 10 minutes. The solution turned dark green. After being kept at room temperature (25 °C) within one day, the small red crystals were formed. The red plate shape crystals were collected and washed with diethyl ether. Dried crystals were stable in air.

Yield: 0.23 g, 0.11 mmol, 21% based on Fe(ClO₄)₂·H₂O.

Empirical formula: CH₄FeNO₆S, M = 213.96 gmol⁻¹.

IR spectroscopy (rt, solid), (intensity): $\tilde{\nu}$ = 1837 (s, NO) cm⁻¹ or 1840 (s, NO) cm⁻¹ as an amorphous.

UV/VIS (MeOH): λ = 447, 583 nm.

UV/VIS (crystals): λ = 248, 342, 406, 479, 573 nm.

UV/VIS (solid): λ = 248, 342, 406, 479, 564 nm.

Elemental analysis: Calcd. (%): N: 5:78, C: 3:41, H: 1.15, S: 16:57.

Found (%): N: 5:03, C: 2:51, H: 1:57, S: 15:65→ [Fe(CH₃OH)₀.₅₅(NO)₀.₈(μ₄-SO₄)]

X-ray structure analysis: sv227, sv352, wv079, wv067
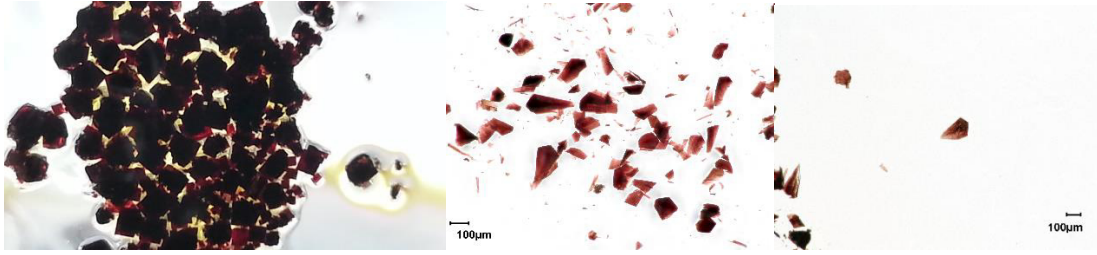
Figure 5.2: Images of the red crystals of **A**.
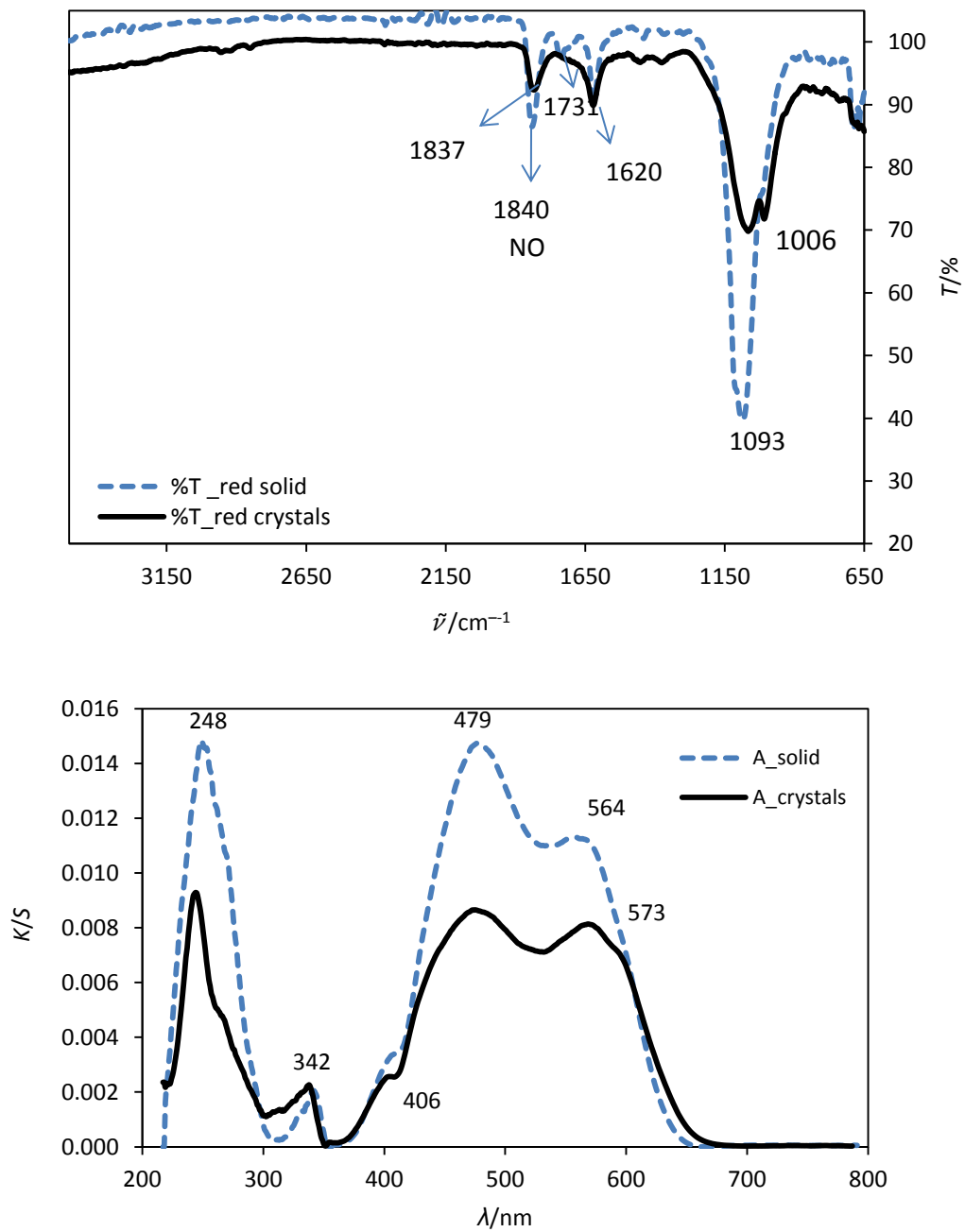
Figure 5.3: (Top) IR spectra of **A** and UV/Vis spectra of A (as amorphous (blue line) and as crystals (black line)).

6 Appendix

6.1 Packing diagrams of the crystal structures
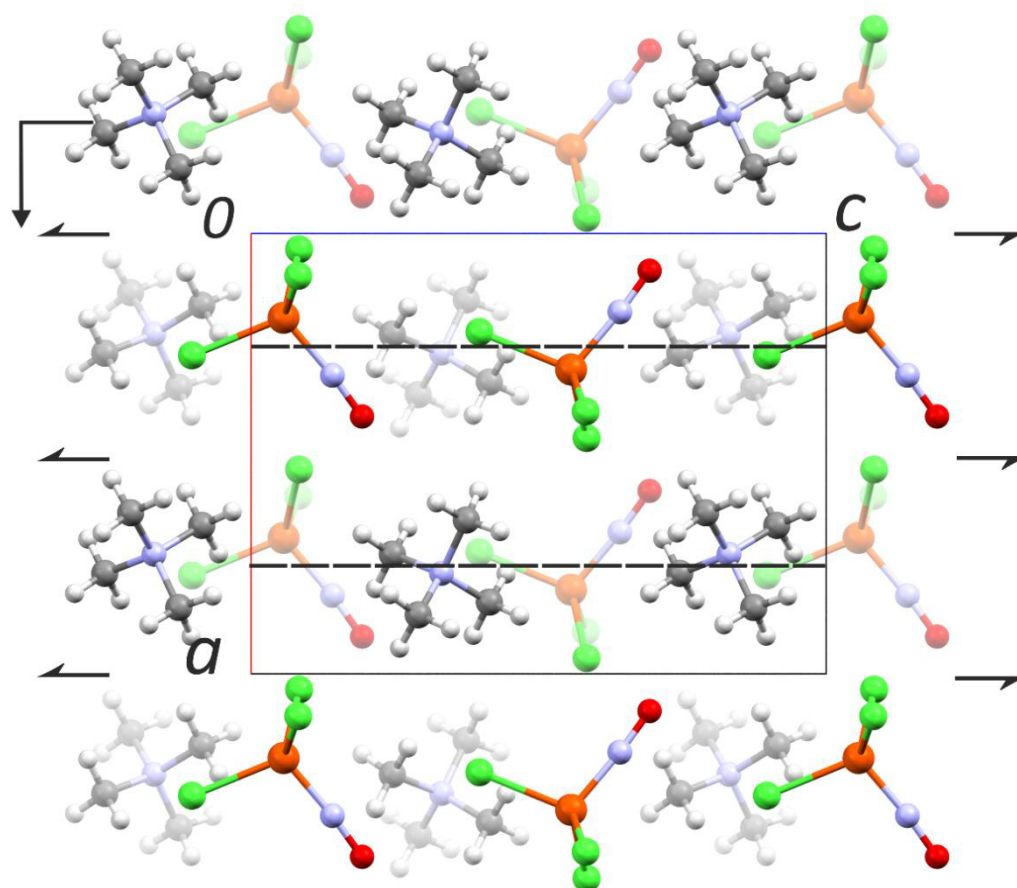
Figure 6.1: Packing diagram of **1a** in the orthorhombic space group *Pca*2$_1$ with view along [010]. The symmetry elements are overlaid. Atoms: carbon (gray), chlorine (green), hydrogen (white), iron (orange), nitrogen (blue), oxygen (red).
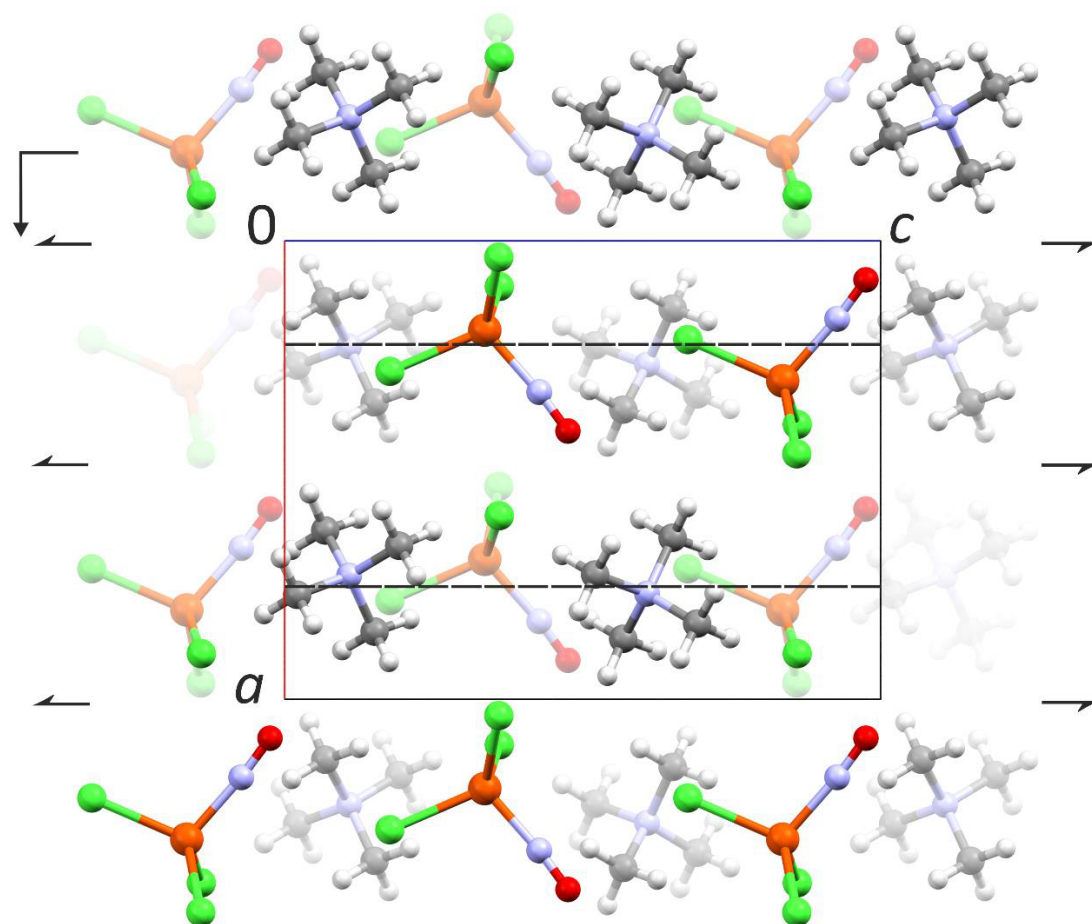
Figure 6.2: Packing diagram of **1b** in the orthorhombic space group *Pca*2$_1$ with view along [010]. The symmetry elements are overlaid. Atoms: carbon (gray), chlorine (green), hydrogen (white), iron (orange), nitrogen (blue), oxygen (red).
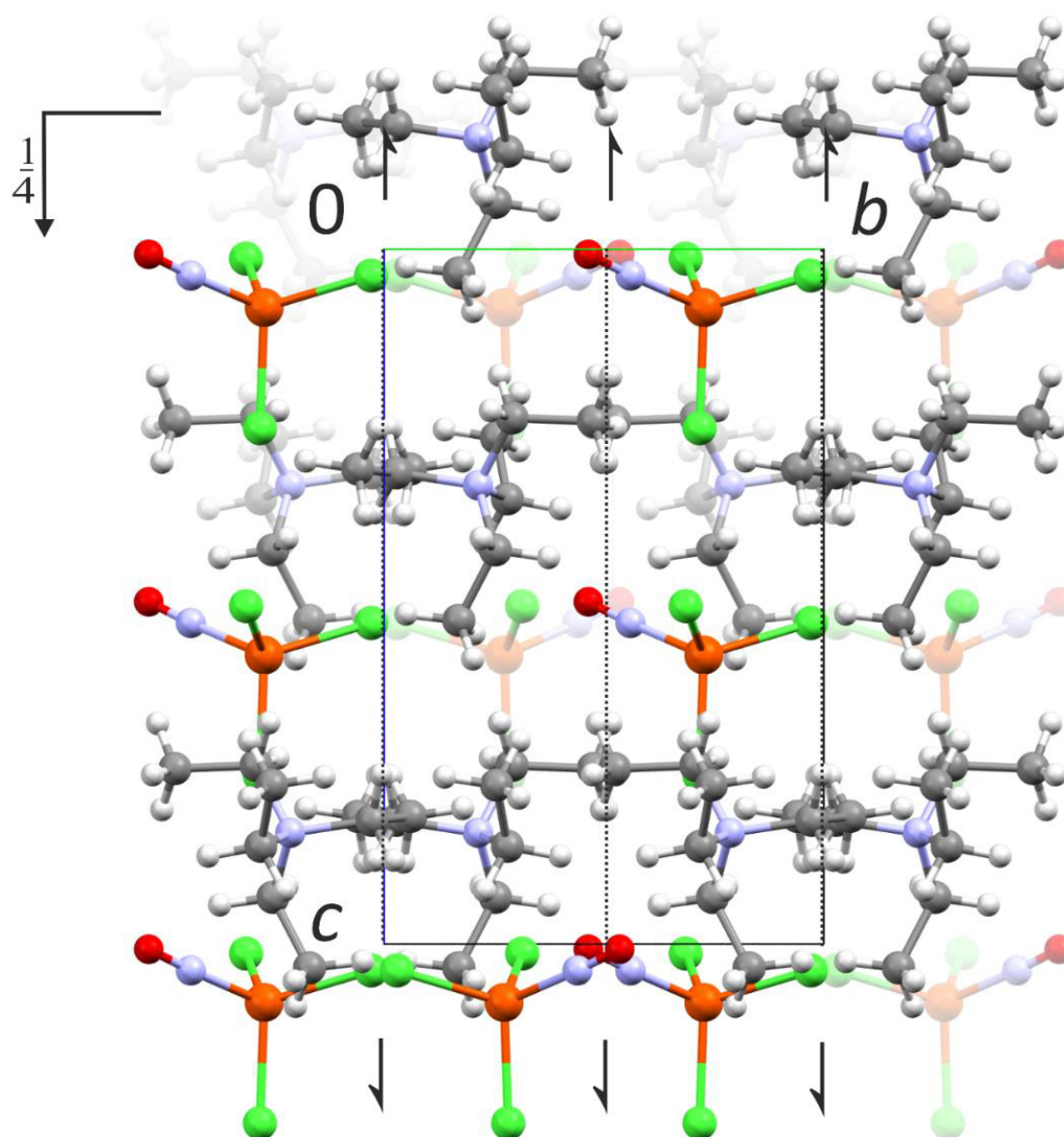
Figure 6.3: Packing diagram of **2a** in the orthorhombic space group *Pca*2₁ with view along [100]. The symmetry elements are overlaid. Atoms: carbon (gray), chlorine (green), hydrogen (white), iron (orange), nitrogen (blue), oxygen (red).
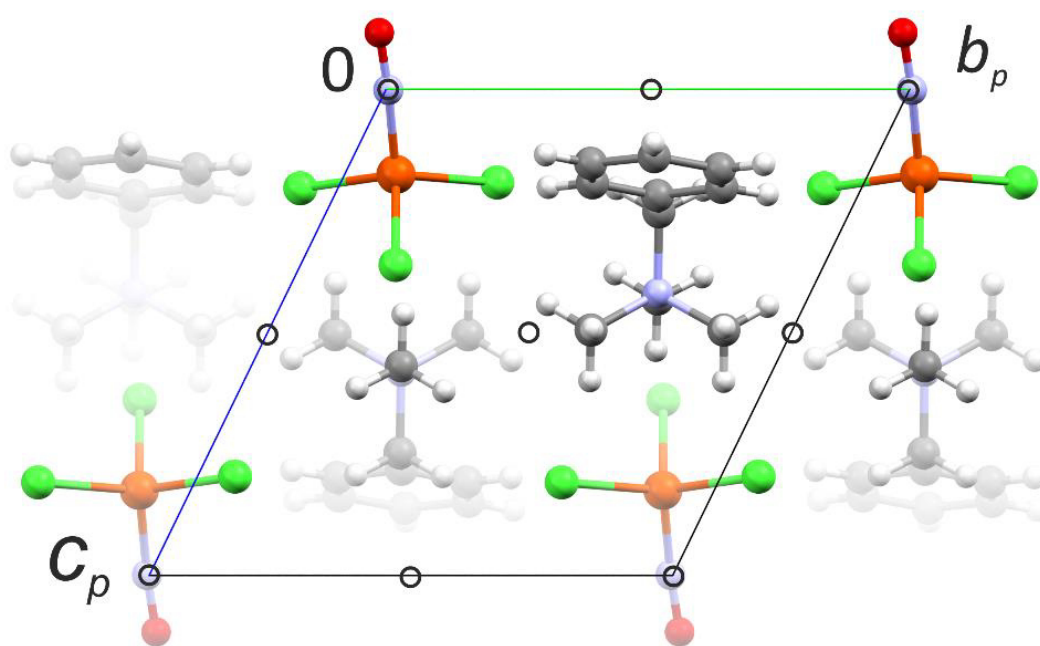
Figure 6.4: Packing diagram of **3** in the triclinic space group $P\bar{1}$ with view along [100]. The symmetry elements are overlaid. Atoms: carbon (gray), chlorine (green), hydrogen (white), iron (orange), nitrogen (blue), oxygen (red).
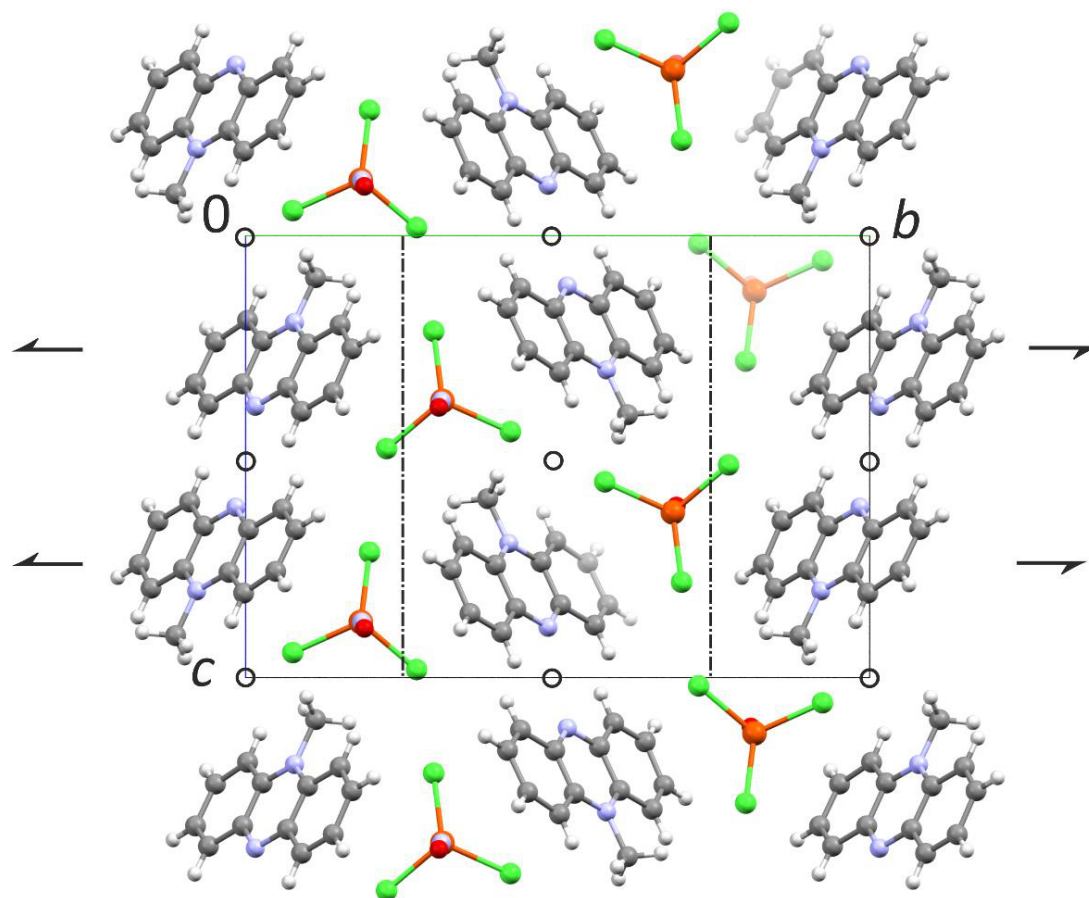
Figure 6.5: Packing diagram of **4** in the monoclinic space group $P2_1/n$ with view along [100] setting with unique axis *b*. The symmetry elements of the space group $P2_1/n$ are overlaid. Atoms: carbon (gray), chlorine (green), hydrogen (white), iron (orange), nitrogen (blue), oxygen (red).
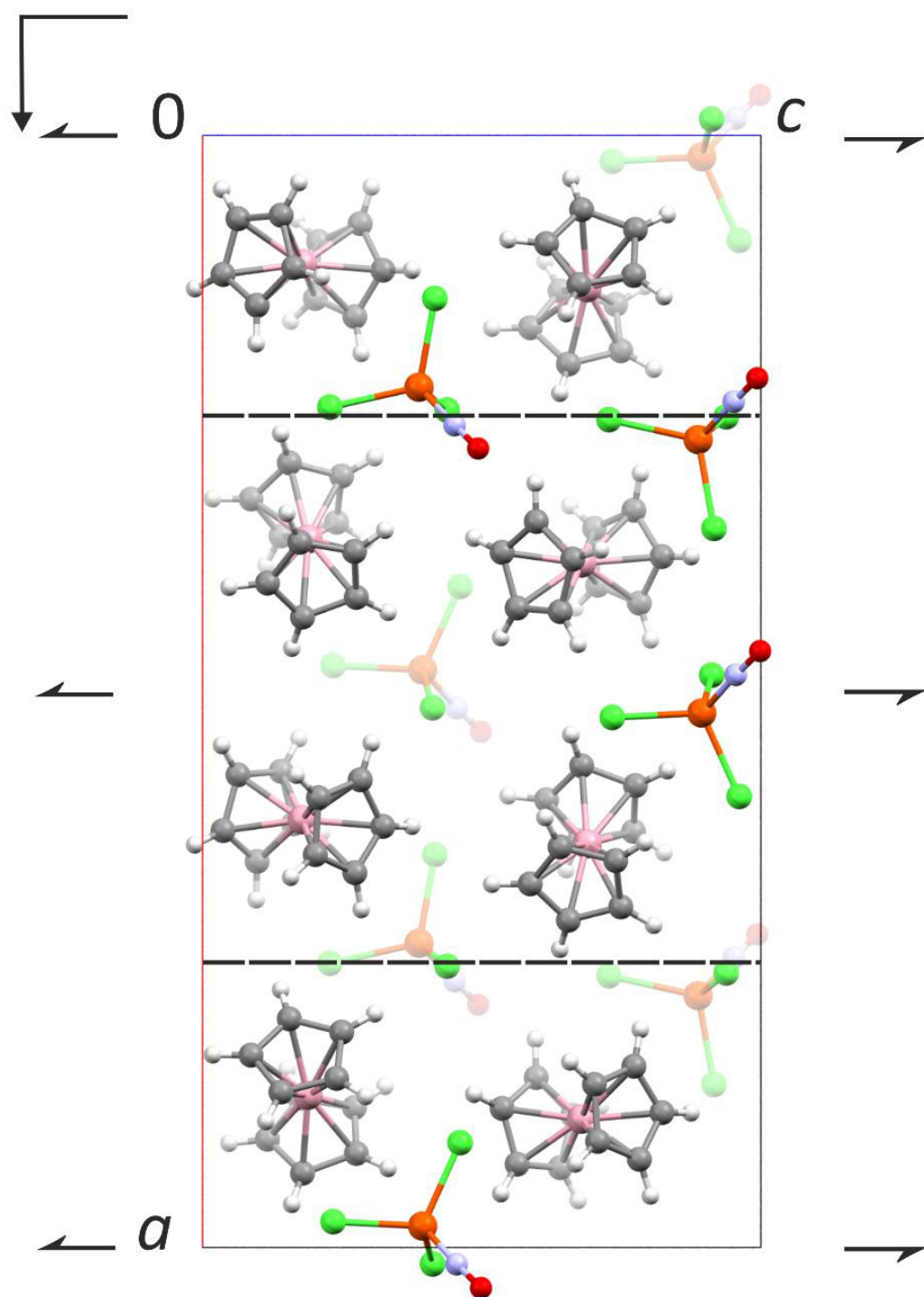
Figure 6.6: Packing diagram of **5** in the orthorhombic space group $Pca2_1$ with view along [010]. The symmetry elements are overlaid. Atoms: carbon (gray), cobalt (pink), chlorine (green), hydrogen (white), iron (orange), nitrogen (blue), oxygen (red).
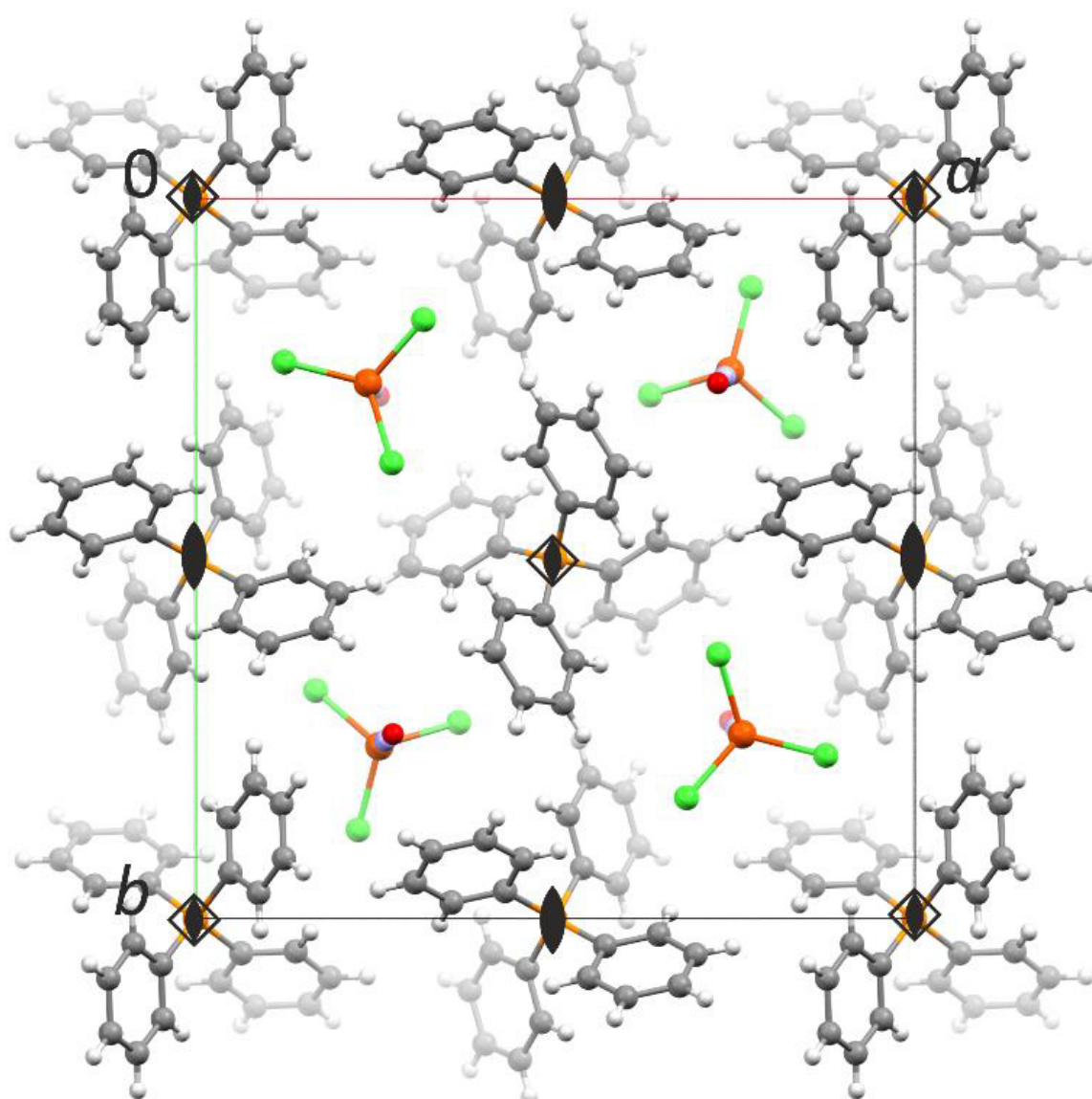
Figure 6.7: Packing diagram of **6** in the tetragonal space group $P\bar{4}$ with view along [001]. The symmetry elements are overlaid. Atoms: carbon (gray), chlorine (green), hydrogen (white), iron (orange), nitrogen (blue), oxygen (red), phosphorous (yellow). This packing diagram is similar to compounds **11** and **12**.
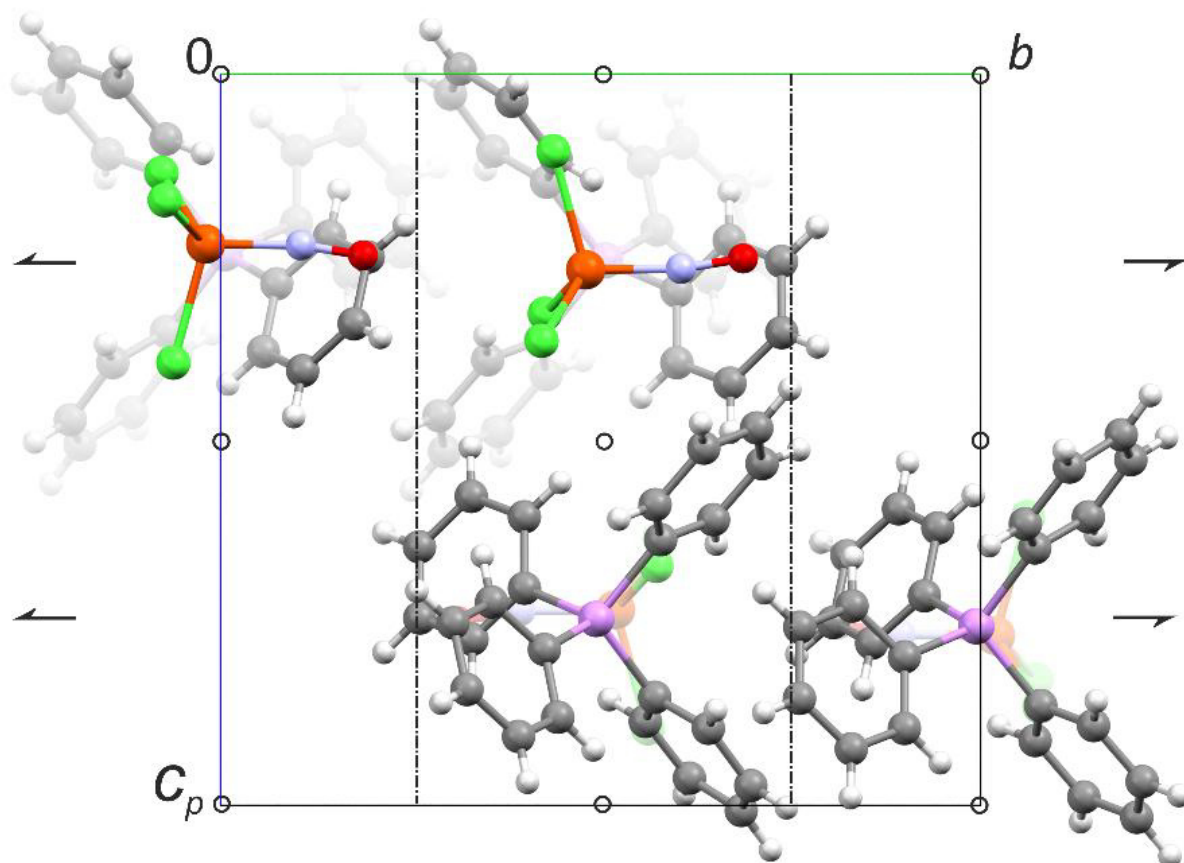
Figure 6.8: Packing diagram of **7** in the monoclinic space group $P2_1/n$ with view along [100] setting with unique axis *b*. The symmetry elements of the space group $P2_1/n$ are overlaid. Atoms: arsenic (purple), carbon (gray), hydrogen (white), chlorine (green), iron (orange), nitrogen (blue), oxygen (red).
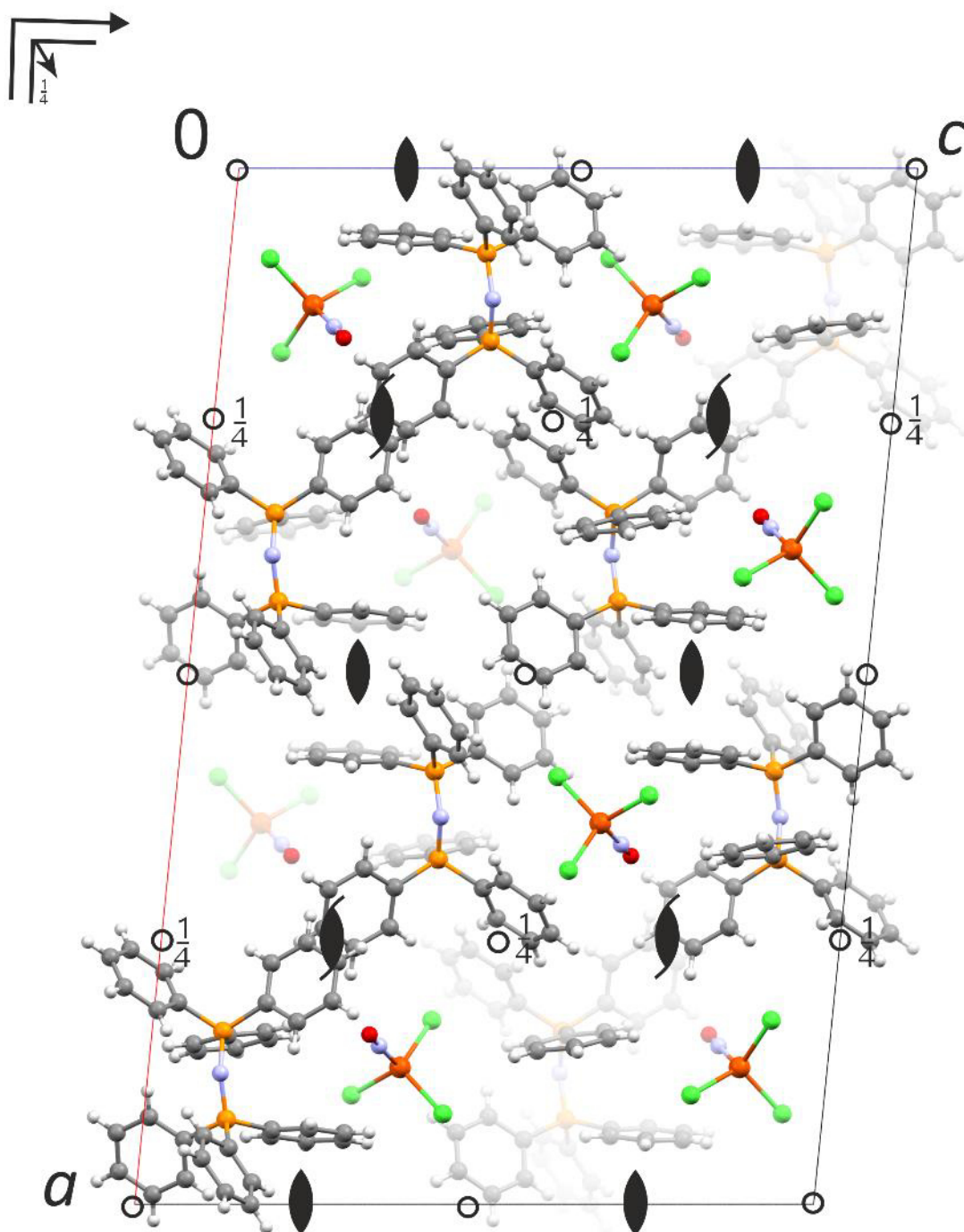
Figure 6.9: Packing diagram of **8** in the monoclinic space group *C*2*/c* with view along [010] setting with unique axis *b*. The symmetry elements of the space group *C*2*/c* are overlaid. Atoms: carbon (gray), hydrogen (white), chlorine (green), iron (orange), nitrogen (blue), oxygen (red), phosphorous (yellow).
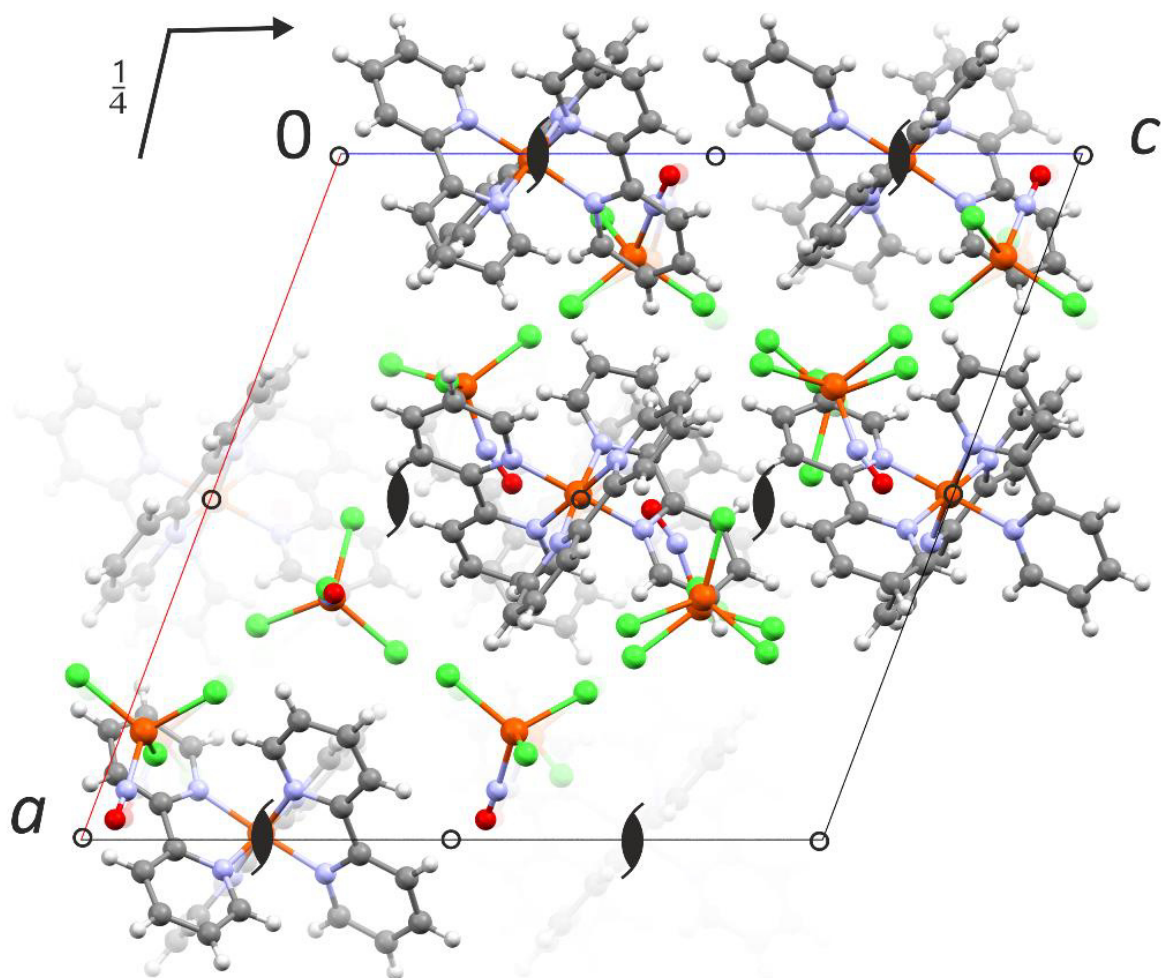
Figure 6.10: Packing diagram of **9** in the monoclinic space group $P2_1/c$ with view along [010], setting with unique axis *b*. The symmetry elements of the space group $P2_1/c$ are overlaid. Atoms: carbon (gray), hydrogen (white), chlorine (green), iron (orange), nitrogen (blue), oxygen (red).
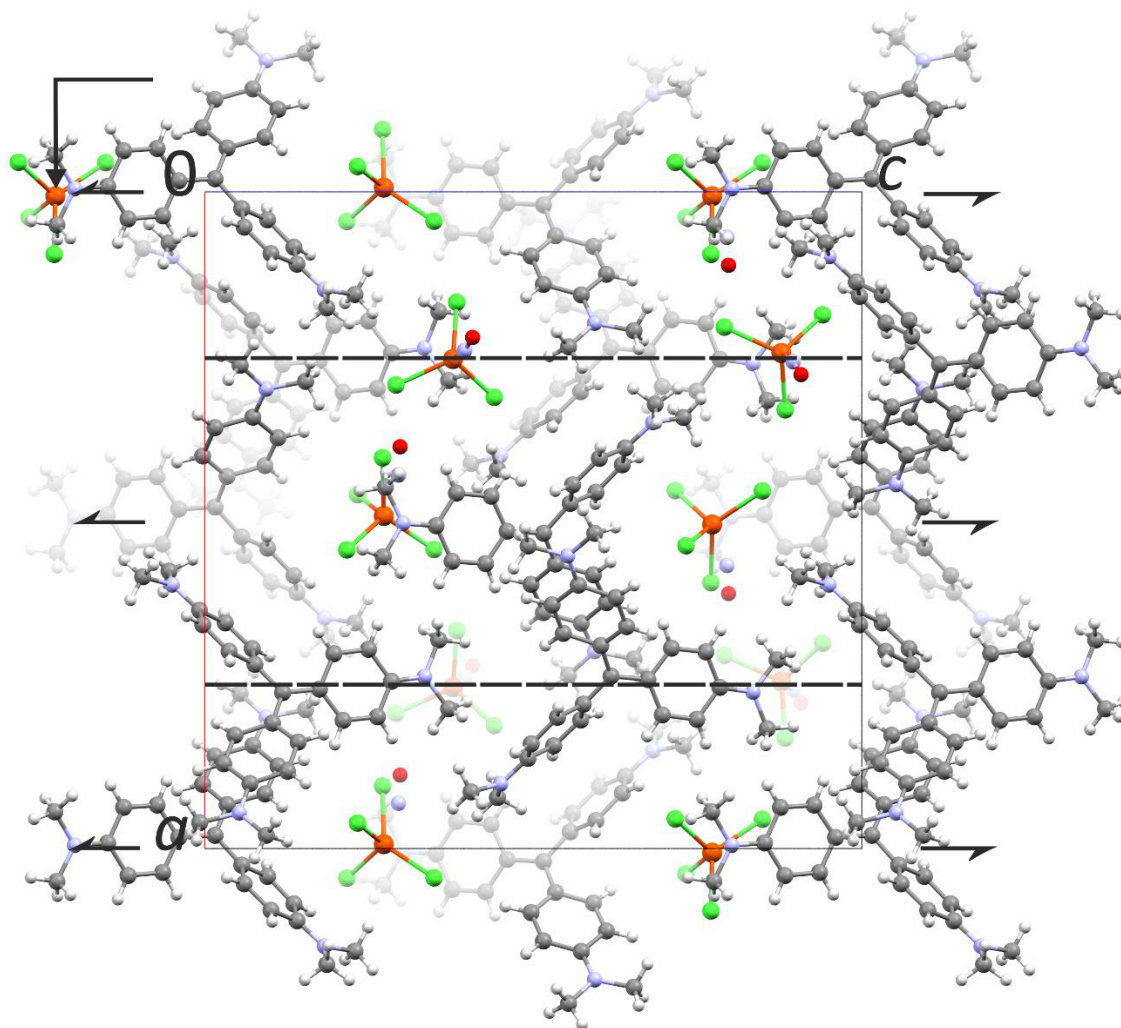
Figure 6.11: Packing diagram of **10** in the orthorhombic space group *Pca*2₁ with view along [010]. The symmetry elements are overlaid. Atoms: carbon (gray), cobalt (pink), chlorine (green), hydrogen (white), iron (orange), nitrogen (blue), oxygen (red).
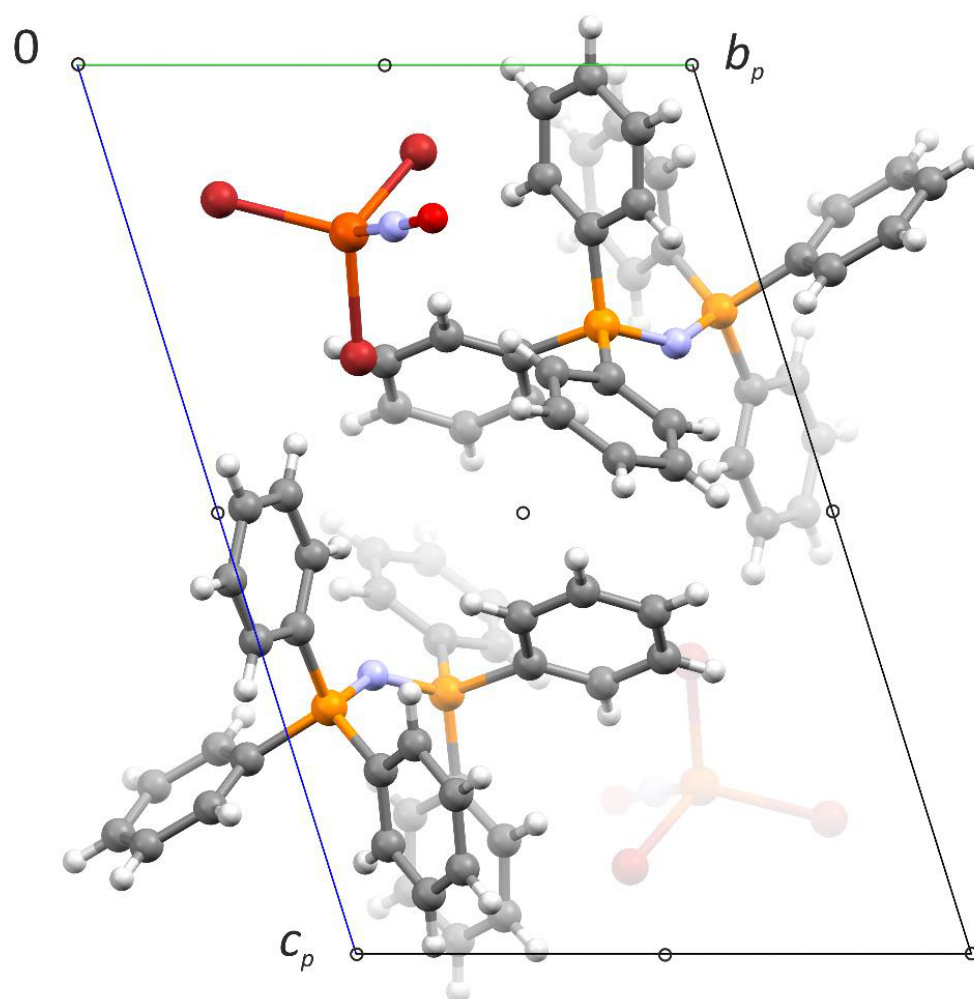
Figure 6.12: Packing diagram of **13** in the monoclinic space group $P\bar{1}$ with view along [100], setting with unique axis *b*. The symmetry elements of the space group $P\bar{1}$ are overlaid. Atoms: carbon (gray), hydrogen (white), bromine (red), iron (orange), nitrogen (blue), oxygen (red), phosphorous (yellow).
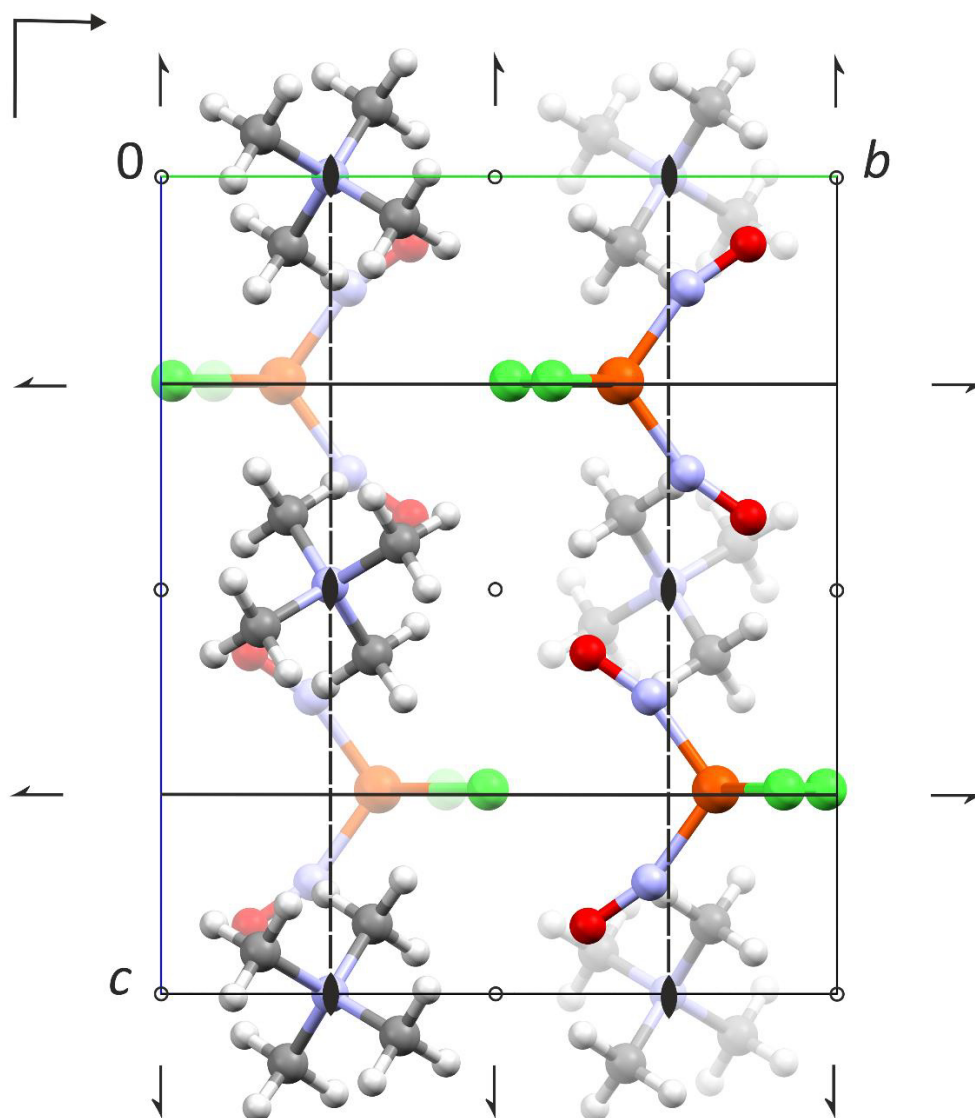
Figure 6.13: Packing diagram of **14a** in the orthorhombic space group *Pbcm* with view along [100], setting with unique axis *b*. The symmetry elements of the space group *Pbcm* are overlaid. Atoms: carbon (gray), chlorine (green), hydrogen (white), iron (orange), nitrogen (blue), oxygen (red).
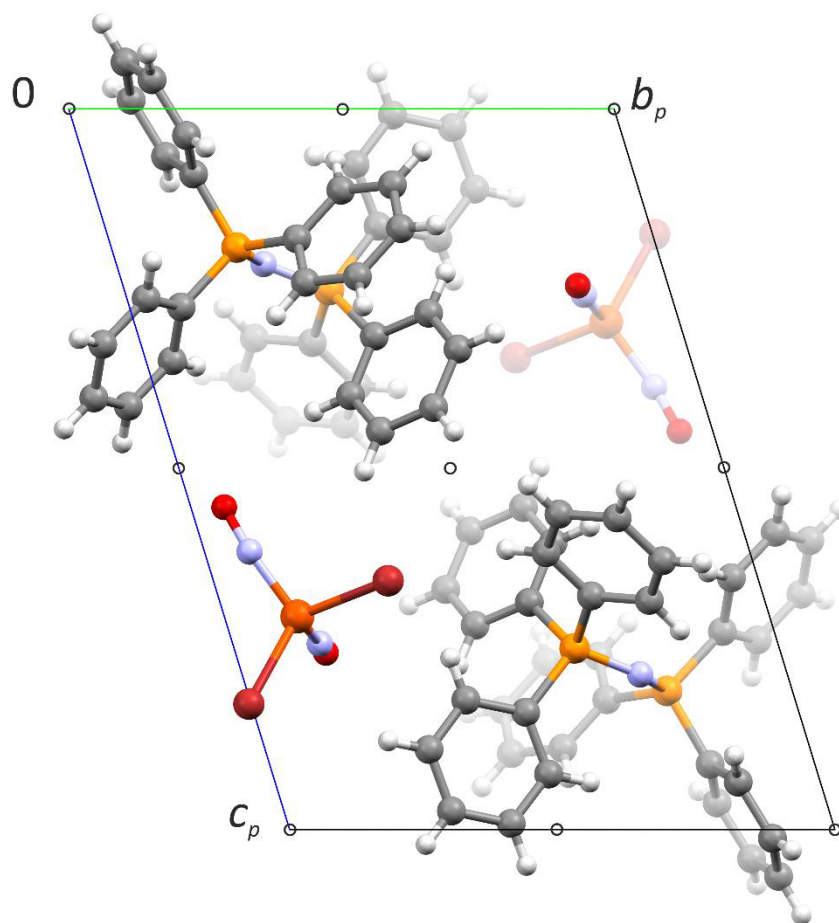
Figure 6.14: Packing diagram of **15b** in the triclinic space group $P\overline{1}$ with view along [100], setting with unique axis *b*. The symmetry elements of the space group $P\overline{1}$ are overlaid. Atoms: carbon (gray), hydrogen (white), bromine (red), iron (orange), nitrogen (blue), oxygen (red), phosphorous (yellow). This packing diagram is similar to compound **15a**.
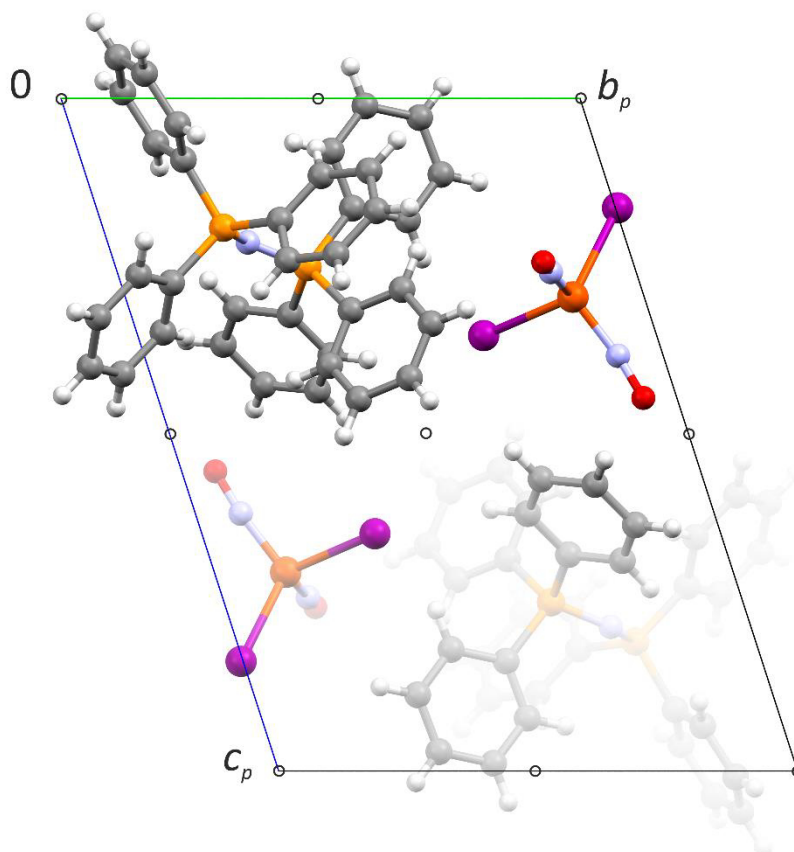
Figure 6.15: Packing diagram of **16** in the triclinic space group $P\bar{1}$ with view along [100], setting with unique axis *b*. The symmetry elements of the space group $P\bar{1}$ are overlaid. Atoms: carbon (gray), hydrogen (white), iodine (violet), iron (orange), nitrogen (blue), oxygen (red), phosphorous (yellow).
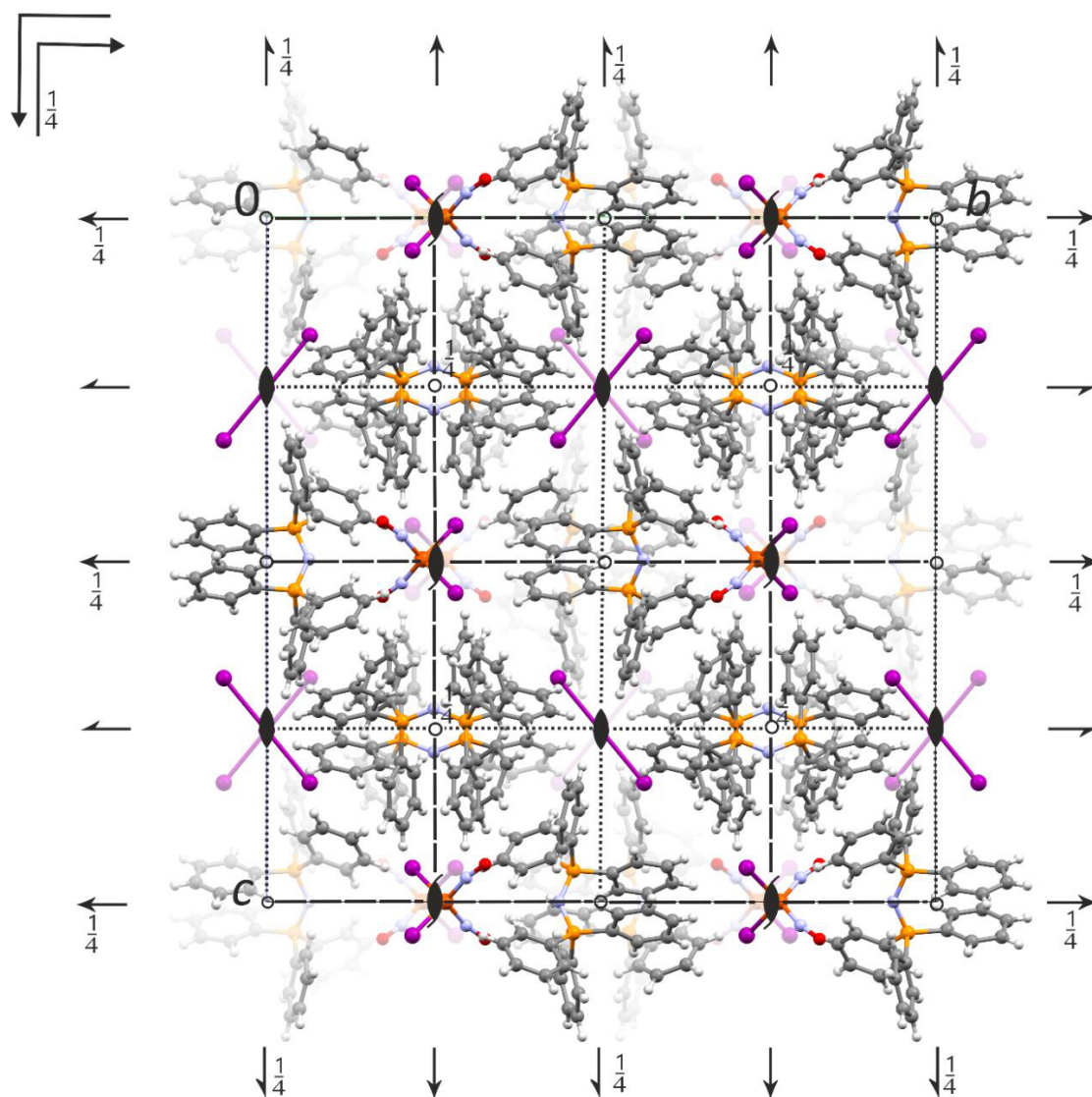
Figure 6.16: Packing diagram of **17** in the orthorhombic space group *Ibca* with view along [100], setting with unique axis *b*. The symmetry elements of the space group *Ibca* are overlaid. Atoms: carbon (gray), hydrogen (white), iodine (violet), iron (orange), nitrogen (blue), oxygen (red), phosphorous (yellow).
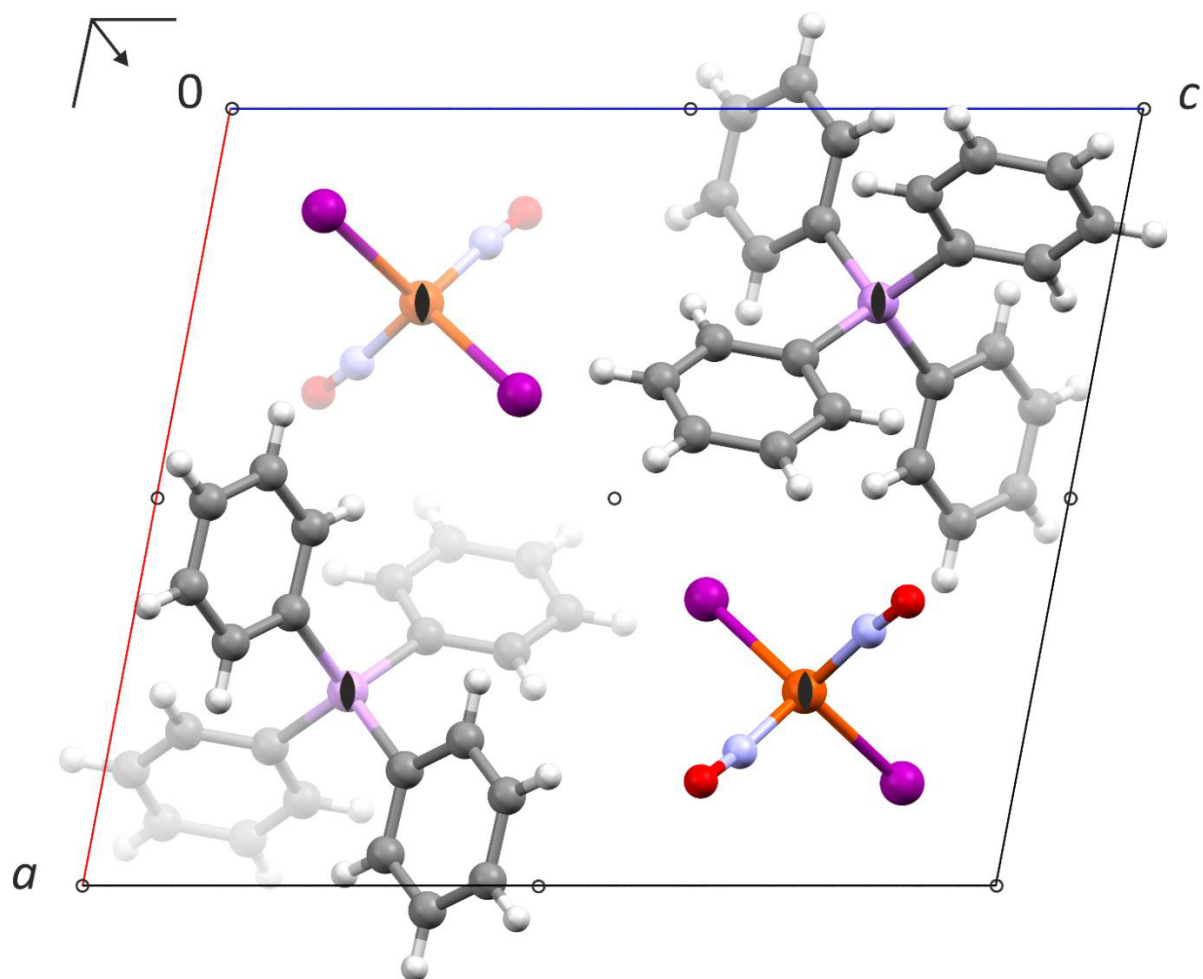
Figure 6.17: Packing diagram of **18** in the monoclinic space group *P*2*/n* with view along [010], setting with unique axis *b*. The symmetry elements of the space group *P*2*/n* are overlaid. Atoms: arsenic (light purple), carbon (gray), hydrogen (white), iodine (violet), iron (orange), nitrogen (blue), oxygen (red), phosphorous (yellow). This packing diagram is similar to compound **19**.
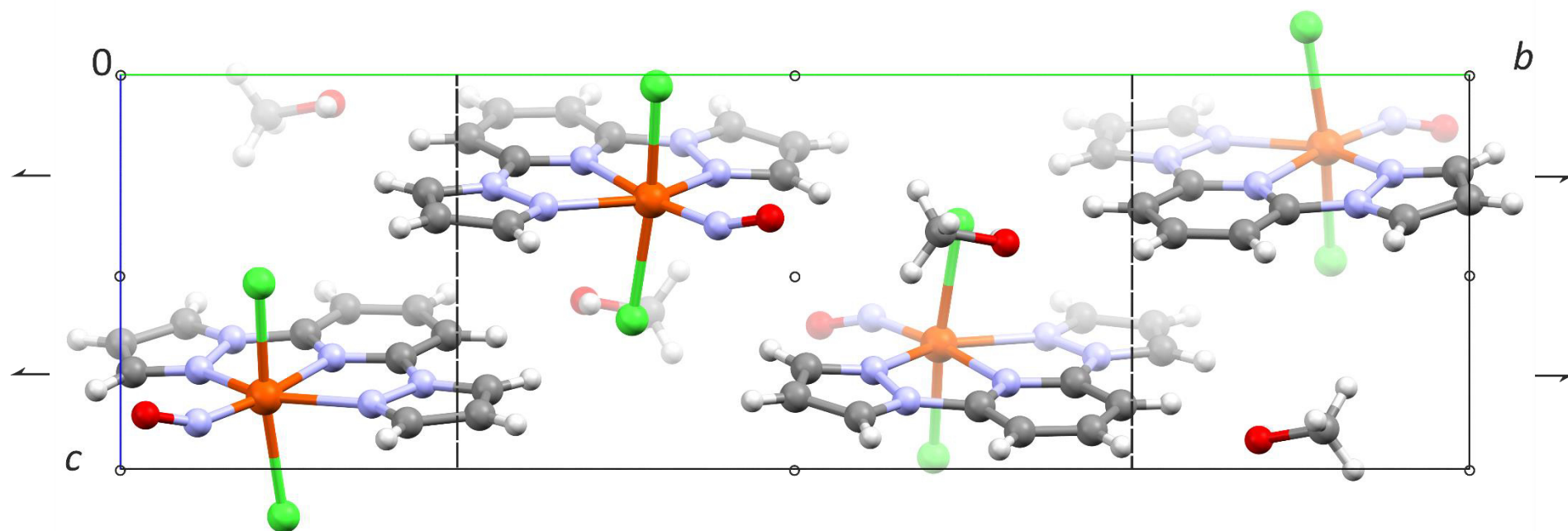
Figure 6.18: Packing diagram of **20a** in the monoclinic space group *P*2*/c* with view along [100], setting with unique axis *b*. The symmetry elements of the space group *P*2*/c* are overlaid. Atoms: carbon (gray), chlorine (green), hydrogen (white), iron (orange), nitrogen (blue), oxygen (red). This packing diagram is similar to compound **20b**.
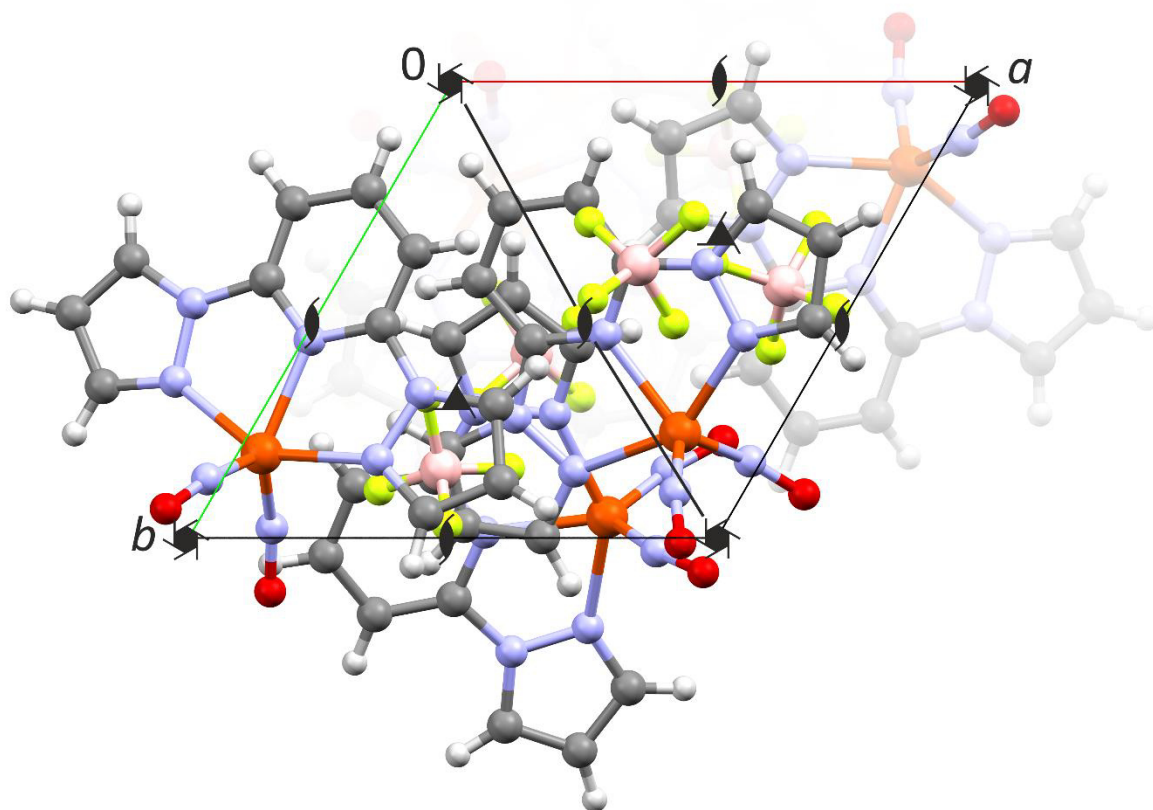
Figure 6.19: Packing diagram of **21** in the hexagonal space group $P6_5$ with view along [001], setting with unique axis *b*. The symmetry elements of the space group $P6_5$ are overlaid. Atoms: boron (pink), carbon (gray), fluorine (yellow), hydrogen (white), iron (orange), nitrogen (blue), oxygen (red).
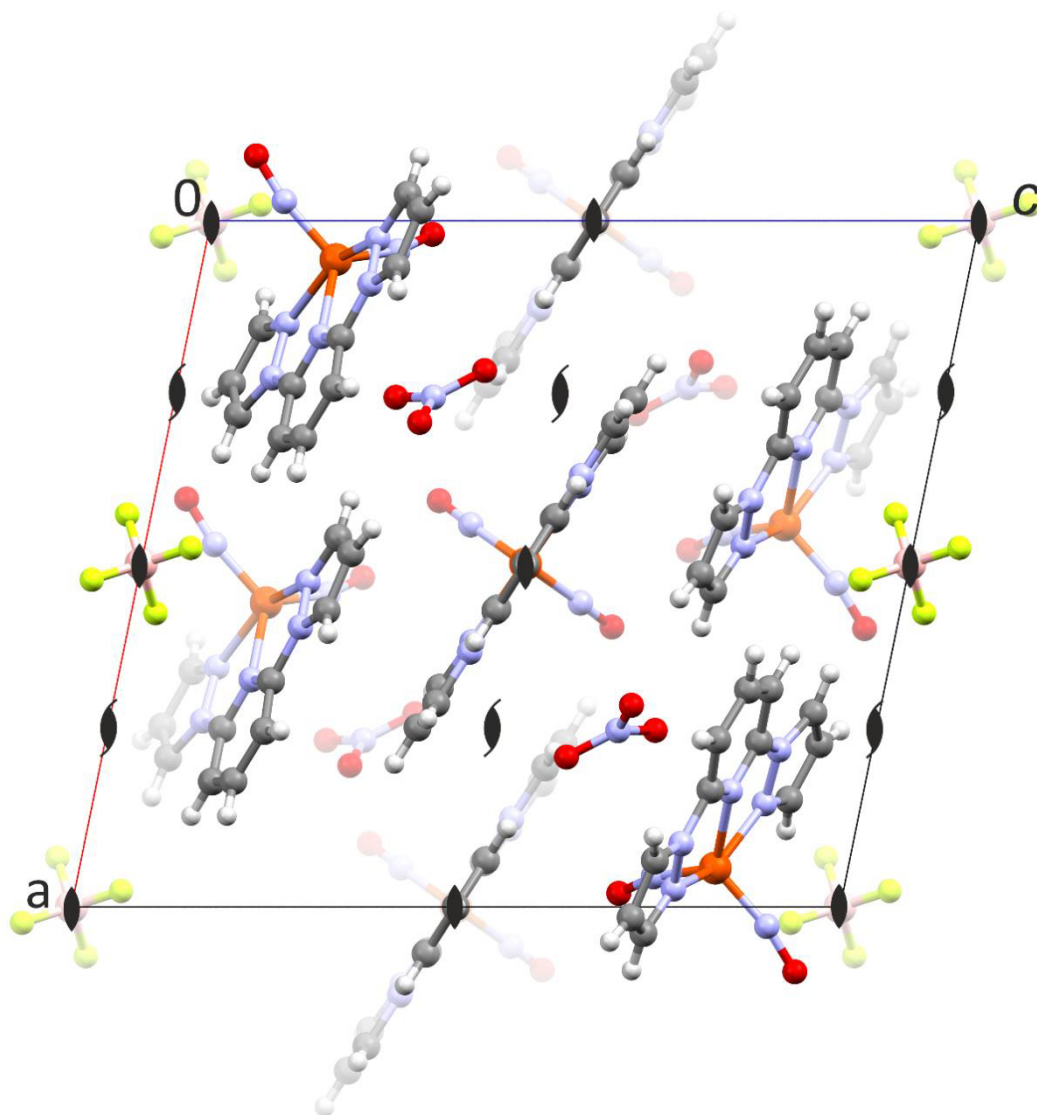
Figure 6.20: Packing diagram of **22** in the monoclinic space group *C*2 with view along [010], setting with unique axis *b*. The symmetry elements of the space group *C*2 are overlaid. Atoms: boron (pink), carbon (gray), fluorine (yellow), hydrogen (white), iron (orange), nitrogen (blue), oxygen (red).
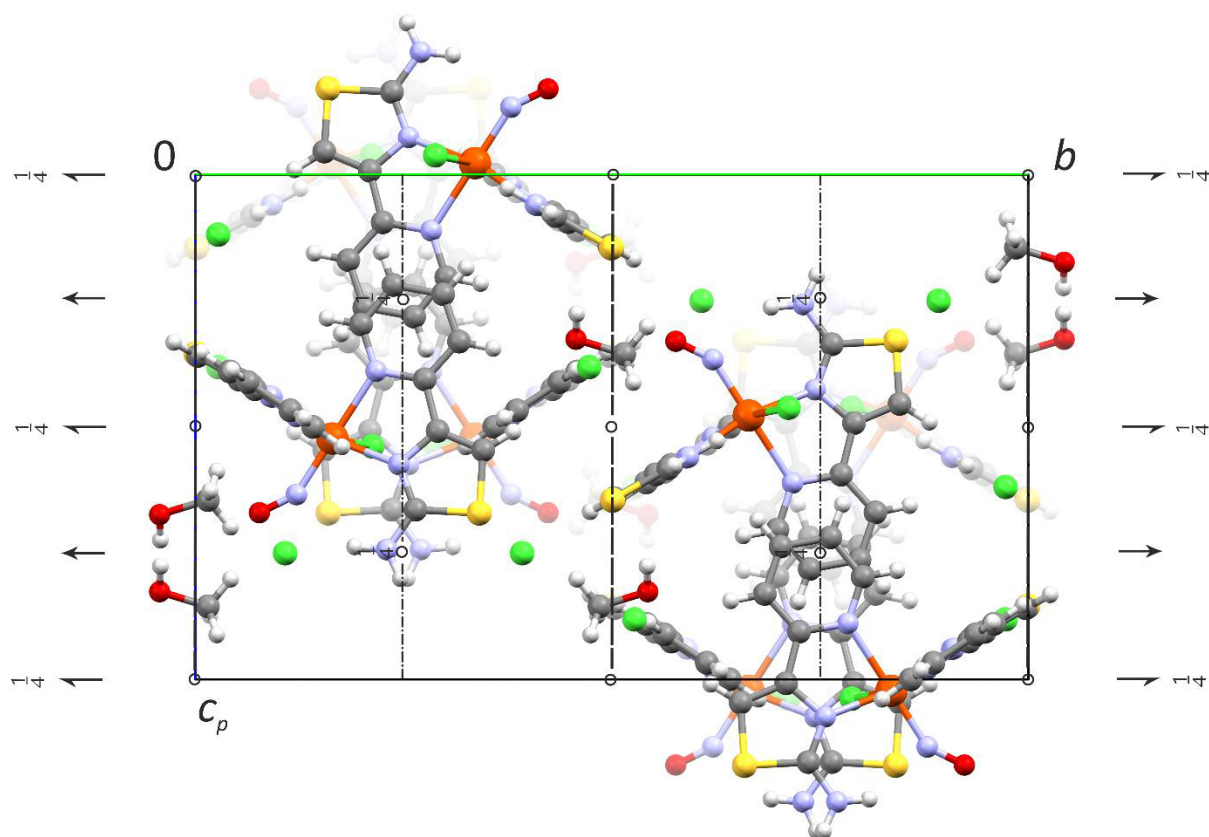
Figure 6.21: Packing diagram of **23** in the monoclinic space group *I*2/*c* (non-standard setting (cb̄a) of *I*2/*a*) with view along [100], setting with unique axis *b*. The symmetry elements of the space group *I*2/*c* (non-standard setting (cb̄a) of *I*2/*a*) are overlaid. Atoms: carbon (gray), chlorine (green), hydrogen (white), iron (orange), nitrogen (blue), oxygen (red), sulfur (yellow).

6.2   Crystallographic tables

Table 6.1: Crystallographic data of $NMe_4[FeCl_3(NO)]$ (**1a**), $NMe_4[FeCl_{3.09}(NO)_{0.91}]$ (**1b**), $NEt_4[FeCl_{3.16}(NO)_{0.84}]$ (**2a**).

Compound	1a	1b	2a
Formula	$C_4H_{12}Cl_3FeN_2O$	$C_4H_{12}Cl_{3.09}FeN_{1.91}O_{0.91}$	$C_8H_{20}Cl_{3.16}FeN_{1.84}O_{0.84}$
M_r/g mol^{-1}	266.36	266.81	323.35
Crystal system	Orthorhombic	Orthorhombic	Orthorhombic
Space group	$Pca2_1$	$Pca2_1$	$Pca2_1$
a/Å	9.8929(19)	9.8479(4)	13.9640(5)
b/Å	8.8888(16)	8.8473(4)	8.1062(3)
c/Å	12.912(2)	12.8148(6)	12.8198(4)
V/Å^3	1135.4(3)	1116.52(9)	1451.14(9)
Z	4	4	4
ρ/g cm^{-3}	1.558	1.587	1.480
μ/mm^{-1}	1.990	2.043	1.599
Crystal size/mm	0.100 × 0.080 × 0.020	0.100 × 0.050 × 0.020	0.367 × 0.276 × 0.226
Temperature/K	293(2)	173(2)	173(2)
Diffractometer	Bruker D8Quest	Bruker D8Venture	Oxford XCalibur
Radiation	MoKα	MoKα	MoKα
Rated input/kW	50	2.5	2.0
θ-range/°	2.291–25.16	3.095–26.43	4.167–27.483
Reflexes for metric	4002	8410	3785
Absorption correction	multi-scan	multi-scan	multi-scan
Transmissions factors	0.5454–0.7452	0.6668–0.7454	0.95907–1.0000
Reflexes measured	17782	12709	9123
Independent reflexes	2026	2153	3267
R_{int}	0.1034	0.0252	0.0247
Mean $\sigma(I)/I$	0.0600	0.0238	0.0281
Reflexes with $I \geq 2\sigma(I)$	1686	2085	3111
x, y (Weighting scheme)	0.0318, 0.9994	0.0156, 0.1548	0.0258
Hydrogen refinement	[a,b]	[a]	[a]
Flack-Parameter	0.07(4)	0.002(7)	−0.018(10)
Parameters	105	109	150
restraints	1	1	1
$R(F_{obs})$	0.0456	0.0164	0.0243
$R_w(F^2)$	0.0875	0.0372	0.0553
S	1.044	1.053	1.067
shift/error$_{max}$	0.001	0.001	0.001
max. electron density/e Å^{-3}	0.367	0.311	0.205
min. electron density /e Å^{-3}	−0.297	−0.139	−0.257
CCDC number	1866190	1866191	1866192

[a] All H atoms were calculated in idealized positions, riding on their parent atoms. U_{iso} was always coupled to the parent atom. [b] Refined as a 2-component inversion twin.

Table 6.2: Crystallographic data of NBnMe$_3$[FeCl$_3$(NO)] (**3**), Mephaz[FeCl$_3$(NO)] (**4**), [Co(cp)$_2$][FeCl$_3$(NO)] (**5**).

Compound	3	4	5
Formula	C$_{10}$H$_{16}$Cl$_3$FeN$_2$O	C$_{13}$H$_{11}$Cl$_3$FeN$_3$O	C$_{10}$H$_{10}$Cl$_3$CoFeNO
M_r/g mol^{-1}	342.45	387.45	381.32
Crystal system	Triclinic	Monoclinic	Orthorhombic
Space group	$P\bar{1}$	$P2_1/n$	$Pca2_1$
a/Å	8.711(3)	6.4605(3)	27.2879(10)
b/Å	9.635(4)	18.2602(6)	7.3133(3)
c/Å	9.962(3)	12.9496(5)	13.6797(6)
α/°	115.910(10)	90	90
β/°	93.359(9)	92.6670(10)	90
γ/°	90.711(11)	90	90
V/Å^3	750.1(5)	1526.01(10)	2729.98(19)
Z	2	4	8
ρ/g cm^{-3}	1.516	1.686	1.856
μ/mm^{-1}	1.525	1.513	2.845
Crystal size/mm	0.080 × 0.060 × 0.020	0.500 × 0.300 × 0.100	0.090 × 0.070 × 0.020
Temperature/K	100(2)	100(2)	173(2)
Diffractometer	Bruker D8Venture	Bruker D8Venture	Bruker D8Venture
Radiation	MoKα	MoKα	MoKα
Rated input/kW	2.5	2.5	2.5
ϑ-range/°	3.151–24.88	3.150–25.69	3.160–25.38
Reflexes for metric	3192	7476	5195
Absorption correction	multi-scan	multi-scan	multi-scan
Transmissions factors	0.5633–0.7451	0.6932–0.7453	0.6614–0.7452
Reflexes measured	8222	23479	28919
Independent reflexes	2510	2882	4979
R_{int}	0.0465	0.0380	0.0722
Mean $\sigma(I)/I$	0.0478	0.0292	0.0594
Reflexes with $I \geq 2\sigma$ (I)	2127	2493	4127
x, y (Weighting scheme)	0.0407, 1.0229	0.0184, 1.5050	0.0280, 2.0743
Hydrogen refinement	a,b	a	a
Flack-Parameter	–	–	0.02(2)
Parameters	158	191	308
restraints	0	0	1
$R(F_{obs})$	0.0389	0.0282	0.0381
$R_w(F^2)$	0.0994	0.0591	0.0716
S	1.092	1.050	1.022
shift/error$_{max}$	0.001	0.001	0.007
max. electron density/e Å^{-3}	0.611	0.350	0.746
min. electron density /e Å^{-3}	−0.414	−0.222	−0.559
CCDC number	1866193	1866194	1866195

[a] All H atoms were calculated in idealized positions, riding on their parent atoms. U_{iso} was always coupled to the parent atom. [b] Refined as a 2-component twin.

Table 6.3: Crystallographic data of PPh$_4$[FeCl$_3$(NO)] (**6**), AsPh$_4$[FeCl$_3$(NO)] (**7**), PPN[FeCl$_3$(NO)] (**8**).

Compound	6	7	8
Formula	C$_{24}$H$_{20}$Cl$_3$FeNOP	C$_{24}$H$_{20}$AsCl$_3$FeNO	C$_{36}$H$_{30}$Cl$_3$FeN$_2$OP$_2$
M_r/g mol^{-1}	531.58	575.53	730.76
Crystal system	Tetragonal	Monoclinic	Monoclinic
Space group	$P\bar{4}$	$P2_1/n$	$C2/c$
a/Å	17.9967(5)	12.9081(8)	34.4457(17)
b/Å	17.9967(5)	13.8437(8)	8.9899(4)
c/Å	7.2933(4)	13.3256(9)	22.4439(9)
β/°	90	90.610(2)	95.740(2)
V/Å^3	2362.16(18)	2381.1(3)	6915.2(5)
Z	4	4	8
ρ/g cm^{-3}	1.495	1.605	1.404
μ/mm^{-1}	1.063	2.366	0.792
Crystal size/mm	0.070 × 0.060 × 0.040	0.100 × 0.080 × 0.010	0.100 × 0.100 × 0.070
Temperature/K	100(2)	100(2)	293(2)
Diffractometer	Bruker D8Venture	Bruker D8Venture	Bruker D8Quest
Radiation	MoKα	MoKα	MoKα
Rated input/kW	2.5	2.5	50
ϑ-range/°	3.014–25.39	3.483–26.45	2.274–26.45
Reflexes for metric	7565	9886	9909
Absorption correction	multi-scan	multi-scan	multi-scan
Transmissions factors	0.6660–0.7452	0.6331–0.7454	0.6880–0.7454
Reflexes measured	40299	61082	51339
Independent reflexes	4343	4845	7086
R_{int}	0.0802	0.0625	0.0449
Mean $\sigma(I)/I$	0.0449	0.0341	0.0339
Reflexes with $I \geq 2\sigma(I)$	3604	3990	5568
x, y (Weighting scheme)	0.0293,	0.0335, 2.4899	0.0326, 9.8169
Hydrogen refinement	[a]	[a]	[a]
Flack-Parameter	−0.020(10)	–	–
Parameters	280	280	406
restraints	0	0	0
$R(F_{obs})$	0.0280	0.0320	0.0370
$R_w(F^2)$	0.0611	0.0801	0.0814
S	1.038	1.056	1.027
shift/error$_{max}$	0.001	0.001	0.002
max. electron density/e Å^{-3}	0.257	0.689	0.456
min. electron density /e Å^{-3}	−0.234	−0.582	−0.411
CCDC number	1866196	1866197	1866198

[a] All H atoms were calculated in idealized positions, riding on their parent atoms. U_{iso} was always coupled to the parent atom.

Table6.4: Crystallographic data of $[Fe(bpy)_3]_2[Fe_4Cl_{12.3}(NO)_{3.7}]$ (**9**), $(C_{25}H_{30}N_3)_2[Fe_2Cl_{6.18}(NO)_{1.82}]$ (**10**).

Compound	9	10
Formula	$C_{60}H_{48}Cl_{12.30}Fe_6N_{15.70}O_{3.70}$	$C_{50}H_{60}Cl_{6.18}Fe_2N_{7.82}O_{1.82}$
M_r/g mol^{-1}	1819.26	1130.83
Crystal system	Monoclinic	Orthorhombic
Space group	$P2_1/c$	$Pca2_1$
a/Å	18.8237(9)	23.5697(19)
b/Å	21.6294(10)	9.7244(8)
c/Å	19.0365(9)	23.570
β/°	110.7482(14)	90
V/Å^3	7248.0(6)	5402.2(6)
Z	4	4
ρ/g cm^{-3}	1.667	1.390
μ/mm^{-1}	1.679	0.888
Crystal size/mm	0.080 × 0.050 × 0.030	0.100 × 0.050 × 0.020
Temperature/K	100(2)	153(2)
Diffractometer	Bruker D8Venture	Bruker D8Venture
Radiation	MoKα	MoKα
Rated input/kW	2.5	2.5
ϑ-range/°	2.363–25.06	3.219–25.69
Reflexes for metric	9963	9347
Absorption correction	multi-scan	multi-scan
Transmissions factors	0.6564–0.7452	0.6496–0.7456
Reflexes measured	12483	145525
Independent reflexes	12481	7739
R_{int}	0.0676	0.0318
Mean $\sigma(I)/I$	0.0651	0.0318
Reflexes with $I \geq 2\sigma(I)$	9933	7448
x, y (Weighting scheme)	0.0157, 15.7257	0.0780, 0.9715
Hydrogen refinement	[a,b]	[a,b]
Flack-Parameter	–	0.137(19)
Parameters	889	636
restraints	0	2
$R(F_{obs})$	0.0542	0.0361
$R_w(F^2)$	0.0890	0.1028
S	1.091	1.035
shift/error$_{max}$	0.001	0.001
max. electron density/e Å^{-3}	0.555	0.557
min. electron density /e Å^{-3}	−0.871	−0.467
CCDC number	–	–

[a] All H atoms were calculated in idealized positions, riding on their parent atoms. [b] Refined as a 2-component twin. U_{iso} was always coupled to the parent atom.

Table6.5: Crystallographic data of PPh$_4$[FeBr$_3$(NO)] (**11**), AsPh$_4$[FeBr$_3$(NO)] (**12**), PPN[FeBr$_3$(NO)] (**13a**).

Compound	11	12	13a
Formula	C$_{24}$H$_{20}$Br$_3$FeNOP	C$_{24}$H$_{20}$AsBr$_3$FeNO	C$_{36}$H$_{30}$Br$_3$FeN$_2$OP$_2$
M_r/g mol^{-1}	664.96	708.91	864.14
Crystal system	Tetragonal	Tetragonal	Triclinic
Space group	$P\bar{4}$	$P\bar{4}$	$P\bar{1}$
a/Å	17.9982(8)	18.3082(2)	10.2775(9)
b/Å	17.9982(8)	18.3082(2)	10.9790(9)
c/Å	7.6499(9)	7.5039(2)	17.2470(17)
α/°	90	90	72.078(3)
β/°	90	90	72.078(3)
γ/°	90	90	85.652(3)
V/Å^3	2478.1(4)	2515.23(9)	1779.8(3)
Z	4	4	2
ρ/g cm^{-3}	1.782	1.872	1.613
μ/mm^{-1}	5.527	6.687	3.912
Crystal size/mm	0.100 × 0.030 × 0.020	0.100 × 0.050 × 0.020	0.090 × 0.080 × 0.080
Temperature/K	100(2)	100(2)	109(2)
Diffractometer	Bruker D8Venture	Bruker D8Venture	Bruker D8Venture
Radiation	MoKα	MoKα	MoKα
Rated input/kW	2.5	2.5	2.5
ϑ-range/°	3.396–26.57	2.934–26.38	3.566–26.42
Reflexes for metric	6920	9893	9985
Absorption correction	multi-scan	multi-scan	multi-scan
Transmissions factors	0.4549–0.7454	0.6275–0.7454	0.6910–0.7454
Reflexes measured	53559	56750	27034
Independent reflexes	4373	5154	6482
R_{int}	0.1237	0.0557	0.0387
Mean $\sigma(I)/I$	0.0664	0.0343	0.0499
Reflexes with $I \geq 2\sigma(I)$	3666	4607	5531
x, y (Weighting scheme)	0.0915, [a,b]	0.0234, 3.3758 [a,b]	0.0177, 1.4650 [a]
Hydrogen refinement			
Flack-Parameter	0.23(2)	0.350(15)	–
Parameters	281	281	406
restraints	0	0	0
$R(F_{obs})$	0.0528	0.0290	0.0304
$R_w(F^2)$	0.1426	0.0642	0.0744
S	1.050	1.050	1.037
shift/error$_{max}$	0.001	0.002	0.001
max. electron density/e Å^{-3}	1.824	0.439	0.961
min. electron density /e Å^{-3}	−1.169	−0.595	−0.788
CCDC number	1867066	1867065	1866199

[a] All H atoms were calculated in idealized positions, riding on their parent atoms. U_{iso} was always coupled to the parent atom. [b] Refined as a 2-component inversion twin.

Table 6.6: Crystallographic data of PPN[FeBr$_{3.05}$(NO)$_{0.95}$][33] (**13b**), NMe$_4$[FeCl$_2$(NO)$_2$] (**14a**), NMe$_4$[FeCl$_2$(NO)$_2$] (**14b**).

Compound	13b	14a	14b
Formula	C$_{36}$H$_{30}$Br$_{3.05}$FeN$_{1.95}$O$_{0.95}$P$_2$	C$_4$H$_{12}$Cl$_2$FeN$_3$O$_2$	C$_4$H$_{12}$Cl$_2$FeN$_3$O$_2$
M_r/g mol^{-1}	866.45	260.92	260.92
Crystal system	Monoclinic	Orthorhombic	Orthorhombic
Space group	*C2/c*	*Pbcm*	*Pbcm*
a/Å	34.6432(13)	8.7160(3)	8.6919(4)
b/Å	8.9595(3)	10.0941(4)	10.0982(5)
c/Å	22.9056(9)	12.2151(5)	12.1948(6)
α/°	90	90	90
β/°	94.8470(12)	90	90
γ/°	90	90	90
V/Å^3	7084.1(5)	1074.69(7)	1070.37(9)
Z	8	4	4
ρ/g cm^{-3}	1.625	1.613	1.619
μ/mm^{-1}	3.984	1.870	1.877
Crystal size/mm	0.08 × 0.05 × 0.02	0.251 × 0.184 × 0.015	0.100 × 0.100 × 0.020
Temperature/K	173(2)	123(2)	100(2)
Diffractometer	Bruker D8Venture	Oxford XCalibur	Bruker D8Venture
Radiation	MoKα	MoKα	MoKα
Rated input/kW	2.5	2.00	2.5
ϑ-range/°	2.50–30.60	4.369–27.465	3.341–26.35
Reflexes for metric	9916	1760	9807
Absorption correction	multi-scan	multi-scan	multi-scan
Transmissions factors	0.6454–0.7461	0.87124–1.00000	0.6780–0.7454
Reflexes measured	128288	6701	37095
Independent reflexes	10857	1291	1137
R_{int}	0.039	0.0431	0.0277
Mean σ(I)/I	0.0199	0.0306	0.0096
Reflexes with $I \geq 2\sigma$ (I)	9425	1099	1097
x, y (Weighting scheme)	0.0290, 49.7534	0.0192, 0.4566	0.0162, 0.5607
Hydrogen refinement	[a]	[a]	[a]
Parameters	406	62	62
restraints	0	0	2
$R(F_{obs})$	0.0392	0.0271	0.0155
$R_w(F^2)$	0.1049	0.0597	0.0383
S	1.148	1.069	1.060
shift/error$_{max}$	0.002	0.001	0.001
max. electron density /e Å^{-3}	0.838	0.400	0.479
min. electron density /e Å^{-3}	−1.022	−0.335	−0.256
CCDC number	1867067	1866200	1867068

[a] All H atoms were calculated in idealized positions, riding on their parent atoms. U_{iso} was always coupled to the parent atom.

Table 6.7: Crystallographic data of PPN[FeCl$_2$(NO)$_2$] (**14c**), PPN[FeCl$_2$(NO)$_2$]$^{[33,41]}$ (**14d**), PPN[FeBr$_2$(NO)$_2$] (**15b**).

Compound	14c	14d	15b
Formula	C$_{36}$H$_{30}$Cl$_2$FeN$_3$O$_2$P$_2$	C$_{36}$H$_{30}$Cl$_2$FeN$_3$O$_2$P$_2$	C$_{36}$H$_{30}$Br$_2$FeN$_3$O$_2$P$_2$
M_r/g mol^{-1}	725.32	725.32	814.24
Crystal system	Triclinic	Triclinic	Triclinic
Space group	$P\bar{1}$	$P\bar{1}$	$P\bar{1}$
a/Å	9.7798(3)	9.8240(2)	9.8449(3)
b/Å	11.3863(3)	11.4411(2)	11.5468(4)
c/Å	16.0979(5)	16.1360(4)	16.2231(5)
α/°	73.2810(10)	73.1010(10)	72.7710(10)
β/°	79.6160(10)	79.405(2)	79.1910(10)
γ/°	87.9000(10)	87.749(2)	87.3840(10)
V/Å^3	1688.48(9)	1705.55(6)	1730.10(10)
Z	2	2	2
ρ/g cm^{-3}	1.427	1.412	1.563
μ/mm^{-1}	0.737	0.730	2.875
Crystal size/mm	0.050 × 0.030 × 0.010	0.150 × 0.080 × 0.030	0.100 × 0.100 × 0.080
Temperature/K	100(2)	200(2)	100(2)
Diffractometer	Bruker D8Venture	KappaCCD	Bruker D8Venture
Radiation	MoKα	MoKα	MoKα
Rated input/kW	2.5	3.025	2.5
ϑ-range/°	3.174–26.06	3.211–27.788	2.578–27.13
Reflexes for metric	9986	7714	9307
Absorption correction	multi-scan	–	multi-scan
Transmissions factors	0.6966–0.7453	–	0.6671–0.7455
Reflexes measured	32942	14994	22285
Independent reflexes	6619	7952	7607
R_{int}	0.0296	0.0379	0.0314
Mean σ(I)/I	0.0293	0.0556	0.0347
Reflexes with $I \geq 2\sigma$ (I)	5689	5642	6410
x, y (Weighting scheme)	0.0216, 1.2942	0.0415, 0.4315	0.0205, 1.4776
Hydrogen refinement	a	a	a
Parameters	415	415	415
restraints	1	0	3
$R(F_{obs})$	0.0282	0.0419	0.0273
$R_w(F^2)$	0.0675	0.1033	0.0620
S	1.047	1.060	1.047
shift/error$_{max}$	0.001	0.001	0.002
max. electron density /e Å^{-3}	0.369	0.291	1.018
min. electron density /e Å^{-3}	−0.308	−0.321	−0.361
CCDC number	1866202	1867069	1866201

a All H atoms were calculated in idealized positions, riding on their parent atoms. U_{iso} was always coupled to the parent atom.

Table 6.8: Crystallographic data of PPN[FeI$_2$(NO)$_2$] (**16**), AsPh$_4$[FeI$_2$(NO)$_2$] (**18**), PPh$_4$[FeI$_2$(NO)$_2$] (**19**).

Compound	16	18	19
Formula	C$_{36}$H$_{30}$FeI$_2$N$_3$O$_2$P$_2$	C$_{24}$H$_{20}$AsFeI$_2$N$_2$O$_2$	C$_{24}$H$_{20}$FeI$_2$N$_2$O$_2$P
M_r/g mol^{-1}	908.22	752.99	709.04
Crystal system	Triclinic	Triclinic	Triclinic
Space group	$P\bar{1}$	$P2/n$	$P2/n$
a/Å	10.0181(4)	12.6477(5)	12.5219(6)
b/Å	11.8184(5)	7.0044(2)	7.0252(4)
c/Å	16.4001(7)	14.5910(5)	14.4356(8)
α/°	71.8584(12)	90	90
β/°	79.0522(11)	100.7490(10)	100.799(2)
γ/°	86.9932(12)	90	90
V/Å^3	1811.59(13)	1269.93(8)	1247.39(12)
Z	2	2	2
ρ/g cm^{-3}	1.665	1.969	1.888
μ/mm^{-1}	2.244	4.341	3.167
Crystal size/mm	0.100 × 0.030 × 0.030	0.1 × 0.1 × 0.05	0.100 × 0.100 × 0.080
Temperature/K	173(2)	173(2)	100(2)
Diffractometer	Bruker D8Venture	Bruker D8Venture	Bruker D8Venture
Radiation	MoKα	MoKα	MoKα
Rated input/kW	2.5	2.5	2.5
ϑ-range/°	3.057–26.44	3.339–27.13	3.340–27.52
Reflexes for metric	9674	9757	9848
Absorption correction	multi-scan	multi-scan	multi-scan
Transmissions factors	0.6787–0.7454	0.6439–0.7455	0.5930–0.7456
Reflexes measured	81396	44574	32515
Independent reflexes	7429	2744	2816
R_{int}	0.0350	0.0272	0.0312
Mean $\sigma(I)/I$	0.0192	0.0180	0.0186
Reflexes with $I \geq 2\sigma(I)$	6296	2632	2713
x, y (Weighting scheme)	0.0227, 1.3216		0.0102, 1.0101
Hydrogen refinement	[a]	[a]	[a]
Extinction parameter	.	.	0.0059(6)
Parameters	415	146	147
restraints	0	0	0
$R(F_{obs})$	0.0224	0.0152	0.0152
$R_w(F^2)$	0.0505	0.0366	0.0365
S	1.041	1.110	1.044
shift/error$_{max}$	0.002	0.001	0.004
max. electron density /e Å^{-3}	0.585	0.537	0.442
min. electron density /e Å^{-3}	−0.351	−0.588	−0.572
CCDC number	1867072	1867070	1867071

[a] All H atoms were calculated in idealized positions, riding on their parent atoms. U_{iso} was always coupled to the parent atom.

Table 6.9: Crystallographic data of $(PPN)_2[FeI_2(NO)_2]I_3$ (**17**).

Compound	**17**
Formula	$C_{72}H_{60}FeI_5N_4O_2P_4$
$Mr/g\ mol^{-1}$	1827.47
Crystal system	Orthorhombic
Space group	*Ibca*
a/Å	16.4952(6)
b/Å	28.9529(11)
c/Å	29.6363(11)
V/Å3	14153.8(9)
Z	8
ρ/g cm-3	1.715
μ/mm-1	2.532
Crystal size/mm	0.250 × 0.010 × 0.010
Temperature/K	100(2)
Diffractometer	Bruker D8Venture
Radiation	MoKα
Rated input/kW	2.5
ϑ-range/°	3.089–27.24
Reflexes for metric	9850
Absorption correction	multi-scan
Transmissions factors	0.6756–0.7455
Reflexes measured	202689
Independent reflexes	7883
R_{int}	0.0398
Mean $\sigma(I)/I$	0.0144
Reflexes with $I \geq 2\sigma (I)$	6765
x, y (Weighting scheme)	0.0212, 32.7993
Hydrogen refinement	[a]
Parameters	399
restraints	0
$R(F_{obs})$	0.0212
$R_w(F^2)$	0.0495
S	1.060
shift/errormax	0.003
max. electron density /e $Å^{-3}$	1.171
min. electron density /e $Å^{-3}$	−0.895
CCDC number	1867073

[a] All H atoms were calculated in idealized positions, riding on their parent atoms. U_{iso} was always coupled to the parent atom.

Table 6.10: Crystallographic data of [Fe(bipzpy)Cl$_2$(NO)]·MeOH (**20a, 20a*, 20b**) and Fe(bipzpy)Cl$_3$]·MeOH (**20c**).

Compound	**20a**	**20a***	**20b**	**20c**
Formula	C$_{12}$H$_{13}$Cl$_2$FeN$_6$O$_2$	C$_{12}$H$_{13}$Cl$_2$FeN$_6$O$_2$	C$_{12}$H$_{13}$Cl$_2$FeN$_6$O$_2$	C$_{12}$H$_{13}$Cl$_3$FeN$_5$O
M_r/g mol^{-1}	400.03	400.03	400.03	405.47
Crystal system	Monoclinic	Monoclinic	Monoclinic	Monoclinic
Space group	$P2_1/c$	$P2_1/c$	$P2_1/c$	$P2_1/c$
a/Å	8.1091(2)	8.1418(4)	8.1175(4)	10.0113(4)
b/Å	25.8285(7)	25.8691(10)	25.8303(13)	10.8212(4)
c/Å	7.6689(2)	7.9902(4)	7.6632(3)	14.7229(5)
α/°	90	90	90	90
β/°	100.3150(10)	99.405(2)	100.209(2)	90.6930(10)
γ/°	90	90	90	90
V/Å^3	1580.26(7)	1660.28(13)	1581.36(13)	1594.88(10)
Z	4	4	4	4
ρ/g cm^{-3}	1.681	1.600	1.680	1.689
μ/mm^{-1}	1.310	1.247	1.309	1.455
Crystal size/mm	0.100 × 0.050 × 0.020	0.050 × 0.030 × 0.020	0.050 × 0.040 × 0.020	0.100 × 0.090 × 0.050
Temperature/K	100(2)	298(2)	100(2)	100(2)
Diffractometer	Bruker D8Venture	Bruker D8Venture	Bruker D8Venture	Bruker D8Venture
Radiation	MoKα	MoKα	MoKα	MoKα
Rated input/kW	2.5	2.5	2.5	2.5
ϑ-range/°	3.001–26.43	2.985–27.13	2.998–26.03	2.034–26.39
Reflexes for metric	9990	7055	6885	9988
Absorption correction	multi-Scan	multi-scan	multi-Scan	multi-Scan
Transmissions factors	0.6745–0.7454	0.6815–0.7455	0.6910–0.7453	0.6855–0.7454
Reflexes measured	35063	31036	23456	24886
Independent reflexes	3234	3655	3095	3260
R_{int}	0.0466	0.0376	0.0400	0.0233
Mean σ(I)/I	0.0301	0.0278	0.0310	0.0178
Reflexes with $I \geq 2\sigma$ (I)	2708	2703	2536	2993
x, y (Weighting scheme)	0.0090, 2.4076	0.0337, 1.7030	0.0168, 1.8851	0.0179, 1.7977
Hydrogen refinement	[a]	[a]	[a]	[a]
Extinction parameter	.	0.0043(8)	.	.
Parameters	210	212	210	204
restraints	0	0	0	0
$R(F_{obs})$	0.0345	0.0396	0.0309	0.0238
$R_w(F^2)$	0.0645	0.1033	0.0667	0.0601
S	1.096	1.056	1.068	1.100
shift/error$_{max}$	0.001	0.001	0.001	0.001
max. electron density /e Å^{-3}	0.377	0.770	0.317	0.367
min. electron density /e Å^{-3}	−0.438	−0.395	−0.321	−0.427

[a] All H atoms were calculated in idealized positions, riding on their parent atoms. U_{iso} was always coupled to the parent atom.

Table 6.11: Crystallographic data of [Fe(bipzpy)(NO)$_2$]BF$_4$ (**21**), [Fe(bipzpy)(NO)$_2$]$_3$(BF$_4$)(NO$_3$)$_2$ (**22**), [Fe(aptz)$_2$Cl(NO)]Cl·0.5MeOH (**23**) and [Fe(CH$_3$OH)(NO)(μ$_4$-SO$_4$)]$_{n/n}$ (**A**).

Compound	**21**	**22**	**23**	**A**
Formula	C$_{11}$H$_9$BF$_4$FeN$_7$O$_2$	C$_{33}$H$_{27}$BF$_4$Fe$_3$N$_{23}$O$_{12}$	C$_{33}$H$_{32}$Cl$_4$Fe$_2$N$_{14}$O$_3$S$_4$	CH$_4$FeNO$_6$S
M_r/g mol^{-1}	413.91	1192.13	1054.46	213.95
Crystal system	hexagonal	monoclinic	monoclinic	tetragonal
Space group	$P6_5$	$C2$	$I2/c$ (non-standard setting (c$\bar{b}$a) of $I2/a$)	$P4/nmm$
a/Å	9.0102(2)	15.2797(7)	13.5945(13)	6.3962(2)
b/Å	9.0102(2)	8.8579(4)	22.587(2)	6.3962(2)
c/Å	32.7581(17)	16.7622(7)	13.8445(13)	9.3349(7)
$α$/°	90	90	90	90
$β$/°	90	101.4900(10)	98.485(8)	90
$γ$/°	120	90	90	90
V/Å^3	2303.13(16)	2223.23(17)	4204.5(7)	381.90(4)
Z	6	2	4	2
$ρ$/g cm^{-3}	1.791	1.781	1.666	1.852
$μ$/mm^{-1}	1.052	1.072	1.198	2.226
Crystal size/mm	0.100 × 0.080 × 0.050	0.050 × 0.040 × 0.010	0.030 × 0.020 × 0.010	0.080 × 0.050 × 0.020
Temperature/K	100(2)	100(2)	100(2)	100(2)
Diffractometer	Bruker D8Venture	Bruker D8Venture	Bruker D8Venture	Bruker D8Venture
Radiation	MoKα	MoKα	MoKα	MoKα
Rated input/kW	2.5	2.5	2.5	2.5
θ-range/°	3.209–26.03	3.457–25.43	3.088–26.40	5.408–25.68
Reflexes for metric	7133	9895	7654	4418
Absorption correction	multi-scans	multi-scan	multi-scan	multi-scan
Transmissions factors	0.6179–0.7453	0.6833–0.7452	0.6840–0.7454	0.6206–0.7453
Reflexes measured	34624	22784	43117	6793
Independent reflexes	2971	4066	4286	234
R_{int}	0.0801	0.0457	0.0825	0.0241
Mean σ(I)/I	0.0518	0.0446	0.0551	0.0122
Reflexes with $I ≥2σ$ (I)	2557	3980	3151	232
x, y (Weighting scheme)	0.0143, 1.6776	0.0303, 19.4329	0.0104, 21.9046	0.0642, 1.3804
Hydrogen refinement	[a,b]	[a,b]	[a]	[a]
Flack parameter	0.01(2)	0.058(15)	–	–
Parameters	236	346	286	34
restraints	1	13	0	6
$R(F_{obs})$	0.0340	0.0506	0.0473	0.041
$R_w(F^2)$	0.0642	0.1205	0.0874	0.1112
S	1.042	1.156	1.053	1.167
shift/error$_{max}$	0.001	0.001	0.001	0.030
max. electron density /e Å^{-3}	0.302	0.842	0.574	1.034
min. electron density /e Å^{-3}	−0.377	−0.891	−0.507	−0.417
				wv079

[a] All H atoms were calculated in idealized positions, riding on their parent atoms. U_{iso} was always coupled to the parent atom. [b] Refined as a 2-component inversion twin.

7 Bibliography

[1] F. Roncaroli, M. Videla, L. D. Slep, J. A. Olabe, *Coord. Chem. Rev.* **2007**, *251*, 1903–1930.

[2] M. Rößler, T. Koch, C. Janzer, M. Olzmann, *MTZ Worldw.* **2017**, *78*, 70–75.

[3] J. O. Lundberg, M. T. Gladwin, E. Weitzberg, *Nat. Rev. Drug Discovery* **2015**, *14*, 623–641.

[4] S. Mocellin, V. Bronte, D. Nitti, *Med. Res. Rev.* **2007**, *27*, 317–352.

[5] F. Wittkamp, C. Nagel, P. Lauterjung, B. Mallick, U. Schatzschneider, U.-P. Apfel, *Dalton. Trans.* **2016**, *45*, 10271–10279.

[6] J. A. McCleverty, *Chem. Rev.* **2004**, *104*, 403–418.

[7] R. F. Furchgott, P. M. Vanhoutte, *FASEB J.* **1989**, *3*, 2007–2018.

[8] L. J. Ignarro, G. M. Buga, K. S. Wood, R. E. Byrns, G. Chaudhuri, *Proc. Natl. Acad. Sci.* **1987**, *84*, 9265–9269.

[9] H.-Y. Hsiao, C.-W. Chung, J. H. Santos, O. B. Villaflores, T.-T. Lu, *Dalton Trans.* **2019**, *48*, 9431–9453.

[10] J. Bradbury, *Lancet* **1998**, *352*, 1287.

[11] D. Basudhar, L. A. Ridnour, R. Cheng, A. H. Kesarwala, J. Heinecke, D. A. Wink, *Coord. Chem. Rev.* **2016**, *306*, 708–723.

[12] S. Huerta, *Futur. Sci. OA* **2015**, *1*, fso.15.44.

[13] W. Manchot, K. Zechentmayer, *Justus Liebigs Ann. Chem.* **1906**, *350*, 368–389.

[14] W. Manchot, F. Huttner, *Justus Liebigs Ann. Chem.* **1910**, *372*, 153–178.

[15] W. Manchot, *Ber. Dtsch. Chem. Ges.* **1914**, *47*, 1601–1614.

[16] V. Kohlschütter, M. Kutscheroff, *Ber. Dtsch. Chem. Ges.* **1904**, *37*, 3044–3052.

[17] V. Kohlschütter, M. Kutscheroff, *Ber. Dtsch. Chem. Ges.* **1907**, *40*, 873–878.

[18] V. Kohlschütter, P. Sazanoff, *Ber. Dtsch. Chem. Ges.* **1911**, *44*, 1423–1432.

[19] D. Koshland, *Science* **1992**, *258*, 1861–1861.

[20] J. H. Enemark, R. D. Feltham, *Coord. Chem. Rev.* **1974**, *13*, 339–406.

[21] R. Pulukkody, M. Y. Darensbourg, *Acc. Chem. Res.* **2015**, *48*, 2049–2058.

[22] C.-H. Ke, C.-H. Chen, M.-L. Tsai, H.-C. Wang, F.-T. Tsai, Y.-W. Chiang, W.-C. Shih, D. S. Bohle, W.-F. Liaw, *J. Am. Chem. Soc.* **2017**, *139*, 67–70.

[23] S. A. T. Dillinger, H. W. Schmalle, T. Fox, H. Berke, *Dalton Trans.* **2007**, 3562–3571.

[24] W. Beck, A. Enzmann, P. Mayer, *Z. Anorg. Allg. Chem.* **2005**, *631*, 105–109.

[25] T. W. Hayton, W. S. McNeil, B. O. Patrick, P. Legzdins, *J. Am. Chem. Soc.* **2003**, *125*, 12935–12944.

[26] Z.-S. Lin, T.-W. Chiou, K.-Y. Liu, C.-C. Hsieh, J.-S. K. Yu, W. Liaw, *Inorg. Chem.* **2012**, *51*, 10092–10094.

[27]   G. Monsch, P. Klüfers, *Angew. Chem. Int. Ed.* **2019**, *58*, 8566–8571.

[28]   B. M. Aas, *Synthesis, Characterization and DFT Analysis of Stable {FeNO}[7] Compounds*, Dissertation, Ludwig-Maximilians-University Munich, **2018**.

[29]   W. Manchot, *Justus Liebigs Ann. Chem.* **1910**, *372*, 179–186.

[30]   W. Manchot, E. Linckh, *Z. Anorg. Allg. Chem.* **1924**, *140*, 37–46.

[31]   W. Manchot, *Ber. Dtsch. Chem. Ges.* **1914**, *47*, 1614–1616.

[32]   G. Monsch, A. In-Iam, X. Kästele, P. Klüfers, *Z. Anorg. Allg. Chem.* **2020**, *646*, 1–5.

[33]   A. In-Iam, M. Wolf, C. Wilfer, D. Schaniel, T. Woike, P. Klüfers, *Chem. Eur. J.* **2019**, *25*, 1304–1325.

[34]   W. P. Griffith, J. Lewis, G. Wilkinson, *J. Inorg. Nucl. Chem.* **1958**, *7*, 38–44.

[35]   N. G. Connelly, C. Gardner, *J. Chem. Soc. Dalton. Trans* **1976**, 1525.

[36]   M. Steimann, U. Nagel, R. Grenz, W. Beck, *J. Organomet. Chem.* **1983**, *247*, 171–174.

[37]   C. Wilfer, Masterthesis, Ludwig-Maximilians-University Munich, **2011**.

[38]   H. Akutsu, J. Yamada, S. Nakatsuji, S. S. Turner, *X-Ray Struct. Anal. Online* **2014**, *30*, 49–50.

[39]   E. Victor, S. Kim, S. J. Lippard, *Inorg. Chem.* **2014**, *53*, 12809–12821.

[40]   A. M. Tondreau, J. M. Boncella, *Polyhedron* **2016**, *116*, 96–104.

[41]   M. Wolf, *Synthesis, Characterization and Quantum-Chemical Analysis of {FeNO}[7] and {Fe(NO)₂}[9] Compounds*, Dissertation, Ludwig-Maximilians-University Munich, **2016**.

[42]   L. Burlamacchi, G. Martini, E. Tiezzi, *Inorg. Chem.* **1969**, *8*, 2021–2025.

[43]   T. R. Bryar, D. R. Eaton, *Can. J. Chem.* **1992**, *70*, 1917–1926.

[44]   N. G. Connelly, *Inorg. Chim. Acta Rev.* **1972**, *6*, 47–89.

[45]   H.-C. Böttcher, *Private Communication*, Ludwig-Maximilians-University Munich, **2014**.

[46]   M. G. Sauaia, R. G. De Lima, A. C. Tedesco, R. S. Da Silva, *J. Am. Chem. Soc.* **2003**, *125*, 14718–14719.

[47]   J. Liu, Q. Duan, J. Wang, Z. Song, X. Qiao, H. Wang, *J. Biomed. Opt.* **2015**, *20*, 015004.

[48]   N. Levin, J. Perdoménico, E. Bill, T. Weyhermüller, L. D. Slep, *Dalton Trans.* **2017**, *46*, 16058–16064.

[49]   P. Coppens, I. Novozhilova, A. Kovalevsky, *Chem. Rev.* **2002**, *102*, 861–884.

[50]   A. Y. Kovalevsky, G. King, K. A. Bagley, P. Coppens, *Chem. Eur. J.* **2005**, *11*, 7254–7264.

[51]   L. Cheng, I. Novozhilova, C. Kim, A. Kovalevsky, K. A. Bagley, P. Coppens, G. B. Richter-Addo, *J. Am. Chem. Soc.* **2000**, *122*, 7142–7143.

[52]   W. Manchot, *Justus Liebigs Ann. Chem.* **1910**, *375*, 308–315.

[53]   J. Maigut, R. Meier, R. Van Eldik, *Inorg. Chem.* **2008**, *47*, 6314–6321.

[54]   M. Schmeisser, R. van Eldik, *Dalton. Trans.* **2014**, *43*, 15675–15692.

[55]   S. Begel, R. Puchta, J. Sutter, F. W. Heinemann, L. Dahlenburg, R. van Eldik, *Inorg. Chem.* **2015**, *54*, 6763–6775.

[56]   R. E. Noftle, G. H. Cady, *Inorg. Chem.* **1966**, *5*, 2182–2184.

[57]   D. Gwost, K. G. Caulton, *Inorg. Chem.* **1973**, *12*, 2095–2099.

[58]   D. Gwost, K. G. Caulton, *Inorg. Chem.* **1974**, *13*, 414–417.

[59]   F. M. Paul Kubelka, *Z. Tech. Phys.* **1931**, *12*, 593–601.

[60]   T. Huxel, S. Leone, Y. Lan, S. Demeshko, J. Klingele, *Eur. J. Inorg. Chem.* **2014**, *2014*, 3114–3124.

[61]   S. Grimme, S. Ehrlich, L. Goerigk, *J Comput. Chem* **2011**, *32*, 1456–1465.

[62]   S. Sinnecker, F. Neese, L. Noodleman, W. Lubitz, *J. Am. Chem. Soc.* **2004**, *126*, 2613–2622.

[63]   C. Van Wüllen, *J. Phys. Chem. A* **2009**, *113*, 11535–11540.

[64]   T. Soda, Y. Kitagawa, T. Onishi, Y. Takano, Y. Shigeta, H. Nagao, Y. Yoshioka, K. Yamaguchi, *Chem. Phys. Lett.* **2000**, *319*, 223–230.

[65]   M. Radoń, E. Broclawik, K. Pierloot, *J. Phys. Chem. B* **2010**, *114*, 1518–1528.

[66]   B. M. Aas, P. Klüfers, *Eur. J. Inorg. Chem.* **2017**, *2017*, 2313–2320.

[67]   D. Gwost, K. G. Caulton, *Inorg. Chem.* **1973**, *12*, 2095–2099.

[68]   P. C. Ford, B. O. Fernandez, M. D. Lim, *Chem. Rev.* **2005**, *105*, 2439–2456.

[69]   K. G. Caulton, *Coord. Chem. Rev.* **1975**, *14*, 317–355.

[70]   B. B. Wayland, L. W. Olson, *J. Am. Chem. Soc.* **1974**, *96*, 6037–6041.

[71]   T. S. Piper, R. S. Drago, *J. Chem. Phys.* **1962**, *36*, 241–242.

[72]   A. L. Speelman, B. Zhang, A. Silakov, K. M. Skodje, E. E. Alp, J. Zhao, M. Y. Hu, E. Kim, C. Krebs, N. Lehnert, *Inorg. Chem.* **2016**, *55*, 5485–5501.

[73]   H. L. K. Wah, M. Postel, F. Tomi, L. Mordenti, *New J. Chem.* **1991**, *15*, 629–633.

[74]   P. Ghosh, S. Ding, M. Quiroz, N. Bhuvanesh, C. H. Hsieh, P. M. Palacios, B. S. Pierce, M. Y. Darensbourg, M. B. Hall, *Chem. Eur. J.* **2018**, *24*, 16003–16008.

[75]   K. Boguslawski, C. R. Jacob, M. Reiher, *J. Chem. Theory Comput.* **2011**, *7*, 2740–2752.

[76]   H.-Y. Cheng, S. Chang, P.-Y. Tsai, *J. Phys. Chem. A* **2004**, *108*, 358–361.

[77]   C. Kupper, A. Schober, S. Demeshko, M. Bergner, F. Meyer, *Inorg. Chem.* **2015**, *54*, 3096–3098.

[78]   J. Conradie, K. H. Hopmann, A. Ghosh, *J. Phys. Chem. B* **2010**, *114*, 8517–8524.

[79]   J. H. Rodriguez, Y. M. Xia, P. G. Debrunner, *J. Am. Chem. Soc.* **1999**, *121*, 7846–7863.

[80]   R. D. Harcourt, *Nitric Oxide* **2017**, *69*, 51–55.

[81]   M. Wolf, P. Klüfers, *Eur. J. Inorg. Chem.* **2017**, 2303–2312.

[82]   W. P. Griffith, J. Lewis, G. Wilkinson, *J. Chem. Soc.* **1958**, *2*, 3993.

[83]   C. A. Brown, M. A. Pavlosky, T. E. Westre, Y. Zhang, B. Hedman, K. O. Hodgson, E. I. Solomon, *J. Am. Chem. Soc.* **1995**, *117*, 715–732.

[84]   A. Earnshaw, E. A. King, L. F. Larkworthy, *J. Chem. Soc. A* **1969**, 2459–2463.

[85]   Z. J. Tonzetich, L. H. Do, S. J. Lippard, *J. Am. Chem. Soc.* **2009**, *131*, 7964–7965.

[86]   J. Conradie, D. A. Quarless, H. F. Hsu, T. C. Harrop, S. J. Lippard, S. A. Koch, A. Ghosh, *J. Am. Chem. Soc.* **2007**, *129*, 10446–10456.

[87]   E. Broclawik, A. Stępniewski, M. Radoń, *J. Inorg. Biochem.* **2014**, *136*, 147–153.

[88]   M. L. Tsai, C. C. Chen, I. J. Hsu, S. C. Ke, C. H. Hsieh, K. A. Chiang, G. H. Lee, Y. Wang, J. M. Chen, J. F. Lee, W. F. Liaw, *Inorg. Chem.* **2004**, *43*, 5159–5167.

[89]   R. J. Dai, S. C. Ke, *J. Phys. Chem. B* **2007**, *111*, 2335–2346.

[90]   F.-T. Tsai, T.-S. Kuo, W.-F. Liaw, *J. Am. Chem. Soc.* **2009**, *131*, 3426–3427.

[91]   C. C. Tsou, F. Te Tsai, H. Y. Chen, I. J. Hsu, W. F. Liaw, *Inorg. Chem.* **2013**, *52*, 1631–1639.

[92]   S. Ye, F. Neese, *J. Am. Chem. Soc.* **2010**, *132*, 3646–3647.

[93]   N. Y. Shmatko, D. V. Korchagin, G. V. Shilov, N. S. Ovanesyan, A. V. Kulikov, N. A. Sanina, S. M. Aldoshin, *Polyhedron* **2017**, *137*, 72–80.

[94]   A. A. Raheem, M. Wilke, M. Borgwardt, N. Engel, S. I. Bokarev, G. Grell, S. G. Aziz, O. Kuhn, I. Y. Kiyan, C. Merschjann, E. F. Aziz, *Struct. Dyn.* **2017**, *4*, 04403, 1–15.

[95]   M. L. Boillot, B. Weber, *C. R. Chim.* **2018**, *21*, 1196–1208.

[96]   A. Abhervé, M. Clemente-León, E. Coronado, C. J. Gómez-García, M. López-Jordà, *Dalton Trans.* **2014**, *43*, 9406–9409.

[97]   M. A. Halcrow, *Coord. Chem. Rev.* **2005**, *249*, 2880–2908.

[98]   M. A. Halcrow, *Coord. Chem. Rev.* **2009**, *253*, 2493–2514.

[99]   M. A. Halcrow, *Crystals* **2016**, *6*, 58.

[100]   M. del C. Giménez-López, M. Clemente-León, C. Giménez-Saiz, *Dalton Trans.* **2018**, *47*, 10453–10462.

[101]   M. W. Hlawitschka, M. Oßberger, C. Backes, P. Klüfers, H. J. Bart, *Oil Gas Sci. Technol.* **2017**, *72*, 1–11.

[102]   D. Merker, L. Böhm, M. Oßberger, P. Klüfers, M. Kraume, *Chem. Eng. Technol.* **2017**, *40*, 1391–1399.

[103]   F. Neese, *WIREs Comput. Mol. Sci.* **2012**, *2*, 73–78.

[104]   M. Sierka, A. Hogekamp, R. Ahlrichs, *J. Chem. Phys.* **2003**, 9136–9148.

[105]   O. Treutler, R. Ahlrich, *J. Chem. Phys.* **1995**, *102*, 346–354.

[106]   A. Schaefer, H. Horn, R. Ahlrich, *J. Chem. Phys.* **1992**, *97*, 2571–2577.

[107]   F. Weigend, R. Ahlrich, *Phys. Chem.* **2005**, *7*, 3297–3305.

[108]   A. D. Becke, *Phys. Rev. A* **1988**, *38*, 3098–3100.

[109]   J. P. Perdew, *Phys. Rev. B* **1986**, *33*, 8822–8824.

[110]   J. P. Perdew, Y. Wang, *Phys. Rev. B.* **1992**, *45*, 13244–13249.

[111]   V. N. Staroverov, G. E. Scuseria, J. Tao, J. P. Perdew, *J. Chem. Phys.* **2003**, *119*, 12129–12137.

[112]   J. Tao, J. P. Perdew, V. N. Staroverov, G. E. Scuseria, *Phys. Rev. Lett.* **2003**, *91*, 1464011–1464014.

[113]   Y. Takano, K. N. Houk, *J. Chem. Theory Comput.* **2005**, *1*, 70–77.

[114]   S. Grimme, J. Antony, S. Ehrlich, H. Krieg, *J. Chem. Phys.* **2010**, *132*, 154104.

[115]   T. Lu, F. Chen, *J. Comput. Chem.* **2012**, *33*, 580–592.

[116]   T. Huxel, *Low-Melting Cationic Transition Metal Complexes – Developing Spin Crossover Ionic Liquids –*, Dissertation, Albert-Ludwigs-Universität Freiburg, **2014**.

[117]   G. Zoppellaro, M. Baumgarten, *Eur. J. Org. Chem.* **2005**, *2005*, 2888–2892.

[118]   K. S. Hagen, *Inorg. Chem.* **2000**, *39*, 5867–5869.

[119]   D. Coucouvanis, in *Inorg. Synth.*, John Wiley & Sons, Inc., New York, USA, **2002**, pp. 75–121.

Publikationen:

2020   G. Monsch, A. In-Iam, X. Kästele, P. Klüfers, *Z. Anorg. Allg. Chem.* **2020**, *646*, 1–5. "Brown-Ring"-related coordination polymers of the quartet-{FeNO}[7] chromophore. DOI: 10.1002/zaac.201900352

2018   A. In-Iam, M. Wolf, C. Wilfer, D. Schaniel, T. Woike, P. Kluefers, *Chem. Eur. J.* **2019**, *25*, 1304-1325. {FeNO}[7]-Type halogenido nitrosyl ferrates: syntheses, bonding, and photoinduced linkage isomerism. DOI: 10.1002/chem.201804565.

2017   D. Beck, A. Belz, A. In-Iam, P. Mayer, P. Klüfers, *Z. Anorg. Allg. Chem.* **2017**, *643*, 1191–1194. NO(HSO$_4$), a fairly ionic solid. DOI: 10.1002/zaac.201700274.

Poster:

J. Heinnemann, A. In-Iam, P. Klüfers: Temparaturabhängige Disproportionierung eines Nitritoeisen-Komplexes, *15. Koordinationschemie-Treffen* **2019**, München.

B. M. Aas, A. In-Iam, P. Klüfers: In Multiphase Reaction Media – *in-situ* Characterizable Nitrosyl Iron Complexes with Controllable Reactivity, *Jahreskolloquium DFG SPP 1740 "Reaktive Blasenströmungen"* **2016**, Berlin.

B. M. Aas, A. In-Iam, P. Klüfers: In Multiphase Reaction Media – *in-situ* Characterizable Nitrosyl Iron Complexes with Controllable Reactivity, *Jahreskolloquium DFG SPP 1740 "Reaktive Blasenströmungen"* **2015,** Hamburg-Harburg.

Vorträge und Konferenzen:

2014 – 2017 Wissenschafliche Mitarbeiterin in "Reactive Bubbly Flows" für *DFG-SPP1740* sowie Konferenz und Posterpräsentation der Ergebnisse.

B. M. Aas, A. In-Iam, P. Klüfers: Fe–NO-Complexes in Multiphase Flows, *Workshop "Chemical Reaction Systems" DFG SPP 1740 "Reaktive Blasenströmungen"* **2014**, München.

Gallien, danke ich für die immerwährende hilfsbereite und freundschaftliche Atmosphäre und für die lustige und schöne Zeit auch außerhalb des Labors. Besonderer Dank geht dabei an meine Laborkollegen Tobias Riggenmann, Torsten Amßler, Dr. Christine Sturm und Dr. Leonie Lindner.

Besonderen Dank geht an Dr. Daniel Beck, Jens Popp, Sezen Hollweck, Torsten Ampßler, Tobias Riggenmann und Dr. Bianca Aas dafür, dass sie in schwierigen Zeiten bei meiner Seite waren und eine Umarmumg für mich hatten.

Dem Analytik-Team möchte ich für die Messung meiner Proben danken. Außerdem danke ich Herrn Dr. Peter Mayer, Sandra Albrecht, Dr. Anja Belz, Dr. Christine Sturm, Dr. Daniel Beck und Helen Funk für die zusätzlichen röntgenkristallographischen Messungen meiner Kristalle.

Herzlichen Dank auch an meine Praktikanten Aaron Gerwien, Philipp Schmidt, Stephan Blum, Ebru Durak und Korbinian Sommer für ihre gewissenhafte und fleißige Mitarbeit, vielen Dank!

Meinen beiden Familien, allen Personen aus der Familie In-Iam aber im Besonderen meinen Eltern Sukij, Watchanee und meiner Schwester Pimonporn), Famile Hägele und Familie Kiewprom, meiner Cousine Ploypailin In-Iam und Dr. Berndhard Pillep, meiner Tante Mali Drießler und dem Plaa Uan Team, danke ich für die bedingungslose Unterstützung auf dem Weg zu dieser Dissertation.

Meinen Freunden in Thailand (นางสิบสอง) und in Deutschland danke ich für das Guttun für meine Seele und die viele positive Energie, die sie mir gegeben haben.

Meinem Mann Dr. Till Hägele danke ich für die unendliche Unterstützung und seiner Liebe seit 13 Jahren. Ohne Dich wäre das alles nicht möglich gewesen. Dankeschön Jubjub.